The isotopic compositions of cadmium and other volatile trace metals in Earth and chondrites

Emeliana Maria Palk

Imperial College London
Department of Earth Science and Engineering

Thesis submitted for the degree of Doctor of Philosophy (PhD), 2017

Declaration of Originality

I declare that the work contained in this thesis is my own and that all else is appropriately referenced.

Emeliana Maria Palk

Copyright Notice

The copyright of this thesis rests with the author and is made available under a Creative Commons Attribution Non-Commercial No Derivatives licence. Researchers are free to copy, distribute or transmit the thesis on the condition that they attribute it, that they do not use it for commercial purposes and that they do not alter, transform or build upon it. For any reuse or redistribution, researchers must make clear to others the licence terms of this work.

Acknowledgements

First and foremost, I offer my heartfelt thanks and gratitude to my supervisor, Professor Mark Rehkämper, who has cheerfully and steadfastly supported me, encouraged me and assisted me throughout my research. I am truly thankful for the wisdom and knowledge Mark has passed on to me, much of which simply cannot be obtained from books, and for the immense support he has offered in helping me bring this thesis to a successful conclusion. Thank you, Mark.

I am indebted to Dr Katharina Kreissig and Mr Barry Coles for the countless times they patiently and cheerfully advised me on all manner of practical things to do with geochemistry, laboratory practice and mass spectrometry. Thanks for making the lab work so enjoyable and rewarding.

It has been a privilege to work in the MAGIC research group at Imperial College. It is hard to imagine working with a more friendly and caring bunch of colleagues, who always seem to be willing to step in and help when the need arises. Great people to work with.

I am grateful to Imperial College for placing confidence in me and giving me the opportunity to study for this PhD in the first place, and to the Science and Technology Facilities Council for making it all possible.

Finally, I am truly thankful for the love, sacrifice and support that my wife, Fameeda, and my sons, Samuel and Nathanael, have given me. I know that my working on this PhD has been hard on them sometimes, with long days (and nights) in the lab and, latterly, of course, being consumed by the writing-up. In return, therefore, I dedicate this entire work to my family, as an encouragement to my sons in their future endeavours, a recognition of the sacrifice and hard work of my wife, and, most of all, as a token of my love for them all.

Abstract

The origin of Earth's volatile elements is unresolved with different views on the extent to which volatiles were delivered during the main accretion stage or by a volatile-rich late veneer. This question is addressed here through isotopic investigations of the volatile element Cd.

New Cd isotope data were obtained for both terrestrial rocks and carbonaceous chondrites, and these yield well-constrained estimates of $\varepsilon^{114/110}Cd = -0.9 \pm 0.5$ and $+3.2 \pm 0.8$ for the Cd isotope compositions of the bulk silicate Earth and carbonaceous chondrites, respectively. Metal-silicate partitioning experiments conducted at elevated temperature and pressure, furthermore, demonstrate that partitioning of slightly siderophile Cd during segregation of Earth's core was not accompanied by Cd isotope fractionation.

Accretion modelling with these constraints suggests that Earth's main accretionary component was characterised by $\varepsilon^{114/110}Cd \approx -1.6$ for a late veneer with 0.5% of Earth's mass (M_E) and by $\varepsilon^{114/110}Cd \approx -5$ for a larger late veneer with 1.7% M_E. Volatiles condensed late in the inner solar nebula, and such material, contributing to the main accretion stage of Earth, probably featured a lighter Cd isotope composition than earlier condensates, as represented by carbonaceous chondrites. Notably, there is no evidence from meteorites that material with an unusually low $\varepsilon^{114/110}Cd$ of about –5 was ever common in the inner solar system. This renders scenarios where a large proportion of Earth's Cd and other volatiles were delivered by a large late veneer with $\geq 1.7\%$ M_E much more unlikely than accretion models that encompass only a minor addition of volatile-rich material after cessation of core formation.

An investigation into the application of the extinct ^{205}Pb – ^{205}Tl chronometer to enstatite and ordinary chondrites was also carried out and showed that such work is severely restricted by both terrestrial Pb contamination and Tl stable isotope fractionation from parent body processing.

Table of Contents

List of Tables **13**

List of Figures **14**

Chapter 1 Introduction **19**

1.1 Research background and aims **20**
1.1.1 The extinct radionuclide ^{205}Pb in the early solar system 20
1.1.1.1 The ^{205}Pb – ^{205}Tl chronometer and the search for ^{205}Pb in the early solar system 20
1.1.1.2 Research carried out in this thesis into the ^{205}Pb – ^{205}Tl systematics and Pb, Tl, and Cd behaviour in enstatite and ordinary chondrites 21
1.1.2 The Cd isotope composition of the BSE and volatile delivery to Earth 21
1.1.2.1 Volatile element delivery during Earth's main accretion and late veneer stages 21
1.1.2.2 The role of Cd in Earth's accretion 22
1.1.2.3 Research carried out in this thesis to explore Earth's main accretion and late veneer delivery of Cd 22

1.2 Outline of the thesis **23**

Chapter 2 The precise and accurate measurement of cadmium stable isotope compositions by multiple-collector ICP-MS **25**

2.1 Introduction **26**

2.2 Reagents and laboratory procedures **26**

2.3 Cd separation and purification **27**

2.4 Mass spectrometry **29**
2.4.1 Instrumentation 29
2.4.2 Reporting Cd isotope compositions 31
2.4.2.1 The epsilon notation 31
2.4.2.2 Cd zero-epsilon standard 32
2.4.2.3 Cd isotope ratio used for reporting stable isotope variations 32

2.5 Principles of the Cd double spike method **33**
2.5.1 Introduction 33
2.5.2 The double spike technique 34
2.5.2.1 Theory of the double spike technique 34
2.5.2.2 Spike-sample ratio 36
2.5.2.3 Initial Cd concentration check prior to anion exchange chemistry 37

2.5.2.4 Second Cd concentration check in preparation for IC measurements *38*

2.6 Design, preparation and calibration of the Cd double spike solution **38**
2.6.1 Cd isotopes and isobaric and molecular interferences 38
2.6.2 Double spike optimisation, preparation and calibration 40

2.7 Analytical precision **43**
2.7.1 Calculation of analytical uncertainties 43
2.7.2 Use of a secondary isotopic reference material 44
2.7.3 Assessment of analytical precision achieved 45
2.7.4 Comparison with precision attained in other Cd isotope studies 48
2.7.5 Organic residues from ion exchange and extraction chromatography 49

2.8 Conclusions **51**

Chapter 3 Variable Tl, Pb and Cd concentrations and isotope compositions in enstatite and ordinary chondrites **53**

3.1 Introduction **54**
3.1.1 The extinct ^{205}Pb – ^{205}Tl radionuclide system 54
3.1.1.1 Astrophysical context *54*
3.1.1.2 Usefulness as a high resolution chronometer *54*
3.1.1.3 Early work on ^{205}Pb *55*
3.1.1.4 Recent work *55*

3.2 Samples **57**
3.2.1 Enstatite chondrites 57
3.2.2 Ordinary chondrites 57

3.3 Analytical approach **58**

3.4 Analytical methods **60**
3.4.1 Reagents and laboratory procedures 60
3.4.2 Sample preparation and digestion 60
3.4.2.1 Meteorite crushing *60*
3.4.2.2 Acid digestion *61*
3.4.3 Isotope dilution and double spike methods for determining Pb, Tl and Cd concentrations 61
3.4.3.1 Pb and Tl ID procedures *62*
3.4.3.2 Pb and Tl ID mass spectrometry *62*
3.4.3.3 Cd ID procedures *63*
3.4.3.4 Cd ID mass spectrometry *63*
3.4.4 Separation and purification of Pb, Tl and Cd 63
3.4.4.1 Anion exchange separation of Pb, Tl and Cd *63*
3.4.5 Procedural blanks 67
3.4.6 Mass spectrometry 68

3.5 Results and discussion **70**
3.5.1 Tl, Pb and Cd concentrations 70

3.5.1.1 Enstatite chondrites 72
3.5.1.2 Ordinary L chondrites 74
3.5.1.3 Ordinary LL chondrites 74
3.5.2 Pb isotope compositions and evaluation of terrestrial Pb contamination 75
3.5.3 Pb – Pb isochrons 79
3.5.3.1 Enstatite chondrites 79
3.5.3.2 Ordinary chondrites 80
3.5.3.3 Discussion 80
3.5.4 Tl isotope compositions and $^{204}Pb/^{203}Tl$ – evidence for live ^{205}Pb in the early solar system 81
3.5.4.1 Enstatite chondrites 81
3.5.4.2 L chondrites 85
3.5.4.3 LL chondrites 86
3.5.5 Shock and thermal metamorphism in enstatite and ordinary chondrites 87
3.5.5.1 Enstatite chondrites 88
3.5.5.2 Discussion 89
3.5.5.3 Weathering and Cd isotope fractionation 92
3.5.5.4 Ordinary chondrites 92
3.5.5.5 Discussion 94

3.6 Conclusions 95

3.7 Declaration 98

Chapter 4 Accretion and core formation in Earth – insights from cadmium metal-silicate partitioning experiments 99

4.1 Introduction 100

4.2 Metal-silicate partitioning experiments samples and procedures 100
4.2.1 Experimental methods and samples 100
4.2.1.1 Starting materials and capsules 100
4.2.1.2 Experimental strategy 101
4.2.1.3 Experimental apparatus and procedures 102
4.2.2 Analytical methods 103
4.2.2.1 Reagents and laboratory procedures 103
4.2.2.2 Major element analysis and microscopy 103
4.2.2.3 Separation of metal and silicate fractions 104
4.2.2.4 Acid digestion 105
4.2.2.5 Aliquoting samples for isotope composition analysis 106
4.2.2.6 Cd separation and purification 107
4.2.2.7 Procedural blanks 107
4.2.3 Mass spectrometry 108
4.2.3.1 Instrumentation 108
4.2.3.2 Zero-epsilon standard and reporting Cd isotope compositions 109
4.2.3.3 Cd isotope composition measurements 109

4.2.4 Analytical precision 109
4.2.4.1 Test for matrix effects in metal samples 109
4.2.4.2 Long-term precision monitored by a secondary isotopic reference material 111
4.2.4.3 Analytical precision in this study 112

4.3 Results and discussion 112
4.3.1 Major element analysis 112
4.3.1.1 General observations and Fe content in the silicate phases 113
4.3.1.2 Dissolution of capsule material 113
4.3.1.3 Silicate melt polymerisation 115
4.3.2 Physical descriptions of experimental run products 116
4.3.3 Cd metal-silicate partition coefficients 120
4.3.3.1 Introduction 120
4.3.3.2 Results for time series experiments 120
4.3.3.3 Results for initial experiments using different capsule materials 122
4.3.3.4 Partition and exchange coefficients for Cd and variability with temperature 123
4.3.4 Cd isotope compositions 125
4.3.4.1 Introduction 125
4.3.4.2 Kinetic Cd isotope fractionation and volatilisation 126
4.3.4.3 Fractionation of Cd isotopes between metal and silicate during partitioning 128
4.3.4.4 Comparison with metal-silicate isotope fractionation in other stable isotope systems 129

4.4 Conclusions 130

4.5 Declaration 132

Chapter 5 The cadmium isotopic composition of Earth 133

5.1 Introduction 134

5.2 Analytical methods 136
5.2.1 Sample preparation and digestion 136
5.2.1.1 Reagents and laboratory procedures 136
5.2.1.2 Cleaning and leaching MORB samples 136
5.2.1.3 Acid hotplate digestion 138
5.2.1.4 High pressure vessel digestion 140
5.2.2 Preparation of the samples for mass spectrometry 141
5.2.2.1 Cd separation and purification 141
5.2.2.2 Procedural blanks 142
5.2.3 Mass spectrometry 142
5.2.3.1 Instrumentation 142
5.2.3.2 Zero-epsilon standard and reporting Cd isotope compositions 143
5.2.3.3 Applying the Cd double spike method 143
5.2.4 Analytical precision 144

5.2.4.1 Long-term precision monitored by a secondary isotopic reference material *144*
5.2.4.2 Analytical precision in this study *145*

5.3 Sample selection and descriptions **145**
5.3.1 Introduction 145
5.3.2 Peridotite xenoliths 146
5.3.3 Komatiites 147
5.3.4 Basalts 147
5.3.5 Loess 148

5.4 Results and discussion **149**
5.4.1 Introduction 149
5.4.2 Peridotite xenoliths 150
5.4.2.1 Metasomatism in Cameroon Line spinel lherzolites *150*
5.4.2.2 Stable isotope fractionation in the mantle *156*
5.4.3 Komatiites 158
5.4.4 Basalts 159
5.4.5 Degassing behaviour in MORBs and OIBs 161
5.4.6 Continental crust 162
5.4.7 Olivine separates 163
5.4.8 The Cd isotope composition of the bulk silicate Earth 164
5.4.9 The Cd and Zn isotopic offset between the bulk silicate Earth and carbonaceous chondrites 165

5.5 Modelling Cd behaviour during Earth's accretion and core partitioning **169**
5.5.1 The late veneer 169
5.5.2 Simple mass balance applied to the accretion of Cd and Zn to Earth 171
5.5.3 Accretion modelling strategy 173
5.5.4 Accretion modelling results and discussion 176
5.5.4.1 Accretion model elemental and isotopic constraints *176*
5.5.4.2 The Cd isotope compositions of Earth's building blocks *178*
5.5.4.3 Chondritic Earth building blocks *180*
5.5.4.4 Comparison with other isotope systems *181*
5.5.4.5 The light Cd isotope composition of the main accretionary material *182*

5.6 Conclusions **185**

5.7 Declaration **186**

Chapter 6 Summary and outlook **189**

6.1 Major research findings **190**
6.1.1 ^{205}Pb – ^{205}Tl and volatile element systematics in enstatite and L- and LL-chondrites 190
6.1.2 Cd isotope fractionation during core-mantle partitioning 190

6.1.3 The Cd isotope composition of the bulk silicate Earth 191
6.1.4 The Cd isotope composition of Earth's building blocks 191
6.2 Future directions 192
6.3 Closing remarks 193

Bibliography 195

List of Tables

Table 2.1. Column chemistry for the separation of Cd from silicate rock and meteorite samples 28

Table 2.2. Collector configuration for Cd isotope analyses and relevant isobaric and molecular interferences..... 39

Table 2.3. Cd double spike compositions used in this study measured by mass spectrometry compared to the ideal double spike composition set out in Rudge (2011)..... 40

Table 2.4. Collector configuration for Cd double spike isotope composition calibration runs 41

Table 2.5. Cd isotope compositions of Cd standards and ^{111}Cd – ^{113}Cd double spikes used in this study. The standards are normalised to a reference ratio of $^{110}Cd/^{114}Cd = 0.438564$ (Rosman, 1980; Wombacher et al., 2004) 42

Table 2.6. Internal within-run precision achieved at various sample concentrations compared to within-day precision achieved previously in other studies..... 48

Table 2.7. Precision achieved for stable NIST SRM 3108 Cd runs at various Cd concentrations during individual analytical sessions compared within-day precision in other studies 49

Table 3.1. First stage anion exchange chemistry for the separation of Tl and combined Pb – Cd fractions..... 65

Table 3.2. Second stage anion exchange chemistry for the separation of Pb and Cd..... 66

Table 3.3. Second stage anion exchange chemistry for further purification of the Tl fraction. 67

Table 3.4. Tl, Pb and Cd concentrations and isotope compositions of enstatite and ordinary chondrites..... 71

Table 3.5. 'Inverse' Pb-Pb ages for chondrite groups excluding selected samples..... 79

Table 4.1. Starting materials and experimental run conditions 101

Table 4.2. Electron microprobe (EMP) analyses of major elements in the silicate phases of selected experiments. 114

Table 4.3. Cd isotope compositions, concentrations and metal-silicate partition coefficients for experiments 119

Table 5.1. Summary of hotplate digestion stages for different categories of sample indicating, in normal font, the total acid volumes used (in ml) and, in italics, the same acid volumes stated in ml per gram of sample digested. 139

Table 5.2. Cadmium isotope compositions and concentrations for samples in this study.... 152

Table 5.3. Mass balance results for Cd and Zn during Earth's accretion under low and high mass late veneer delivery scenarios. 173

Table 5.4. Parameters and results of accretion modelling. 177

List of Figures

Figure 2.1. Graphical representation of the relationship between the Cd isotope compositions of a sample (N), a ^{111}Cd – ^{113}Cd double spike (S), and the spike-sample mixture (M) in three Cd isotope ratio space modified after Galer (1999) and Hofmann (1971). Nomenclature selected from Galer (1999) and Siebert et al. (2001): N, M and S are the true Cd isotope compositions of a sample, the spike-sample mixture and a ^{111}Cd – ^{113}Cd double spike respectively, m is the measured Cd isotope ratio of the spike-sample mixture and n is the isotope composition of a zero-epsilon standard. F_{nat} represents the mass fractionation vector of the sample and F_{ins} represents the instrumental mass fractionation vector, both of which are in reality non-linear. 35

Figure 2.2. Error propagation of F_{nat} natural fractionation relative to standard applied to the ^{111}Cd - ^{113}Cd double spike using nomenclature of Siebert et al. (2001)..... 36

Figure 2.3. Measurements of BAM-I102 Cd certified isotopic reference material in chronological order (April 2013 to June 2015; n = 48) during sample measurements sessions for samples described in Chapter 4 (Cd metal-silicate partitioning experiments) and Chapter 5 (Cd terrestrial and meteoritic samples). Error bars are shown at 2se (internal errors). The horizontal red dashed line indicates the arithmetic mean ($\varepsilon^{114/110}Cd = –13.38$) and the shaded area represents 2sd (±0.71) of these BAM-I102 measurements. The horizontal blue dashed line shows, for comparison, the weighted average ($\varepsilon^{114/110}Cd = –13.32 \pm 0.43$ 2se, n = 179) of BAM-I102 measurements carried out by the seven laboratories in the assay of Cd standard solutions published by Abouchami et al. (2013). Weighted averages have been calculated using the methods of Taylor (1982). 45

Figure 2.4. The relationship between measured beam intensities (figures a and c) and estimated sample Cd concentrations (figures b and d) and the corresponding Cd isotope composition external and internal errors (in terms of $\varepsilon^{114/110}Cd$ units). Cd concentrations comprise natural sample Cd and added Cd double spike with spike-sample ratios in the range 1 – 1.7. Symbols show individual runs for the terrestrial and meteoritic samples surveyed in Chapter 5 and the metal-silicate partitioning samples of Chapter 4, sub-categorised into the different desolvation units used – see section 2.4.1. 47

Figure 3.1. Plots of (a) Pb v Tl, (b) Cd v Tl and (c) Pb v Cd concentrations for enstatite chondrites and ordinary chondrites analysed in this study. Data for carbonaceous chondrites from Baker et al. (2010) shown for comparison. Logarithmic scaling has been used on both axes for all plots to encompass highly variable concentration data. Errors bars at the 2sd level are shown except when smaller than the symbols. 73

Figure 3.2. Plots of (a) $^{207}Pb/^{204}Pb$ v $^{206}Pb/^{204}Pb$ and (b) $^{206}Pb/^{204}Pb$ v $^{204}Pb/^{203}Tl$ (in logarithmic scale) for the enstatite and ordinary chondrites analysed in this study. Data for carbonaceous chondrites from Baker et al. (2010) is shown for comparison and has been corrected for terrestrial Pb contamination (see text). In panel (b) the yellow, green and blue fields represent the approximate isotope compositions of meteoritic, terrestrial and radiogenic Pb, respectively, and the blue and red arrows represent the radiogenic ingrowth of Pb and the addition of terrestrial Pb, respectively (see text). Error bars at the 2se level (for Pb isotope ratios) and 2sd level (for $^{204}Pb/^{203}Tl$ ratios) are shown except when smaller than the symbols. 77

Figure 3.3. Plots of $\varepsilon^{205}Tl$ versus $^{204}Pb/^{203}Tl$ for the enstatite and ordinary chondrites of this study. The carbonaceous chondrites of Baker et al. (2010) are shown for comparison and

have been corrected for terrestrial Pb (see text). Panels (a), (b) and (c) are of the same plot but use variable scaling to best reveal the structure and systematics of the data. The red and blue boxes show the coverage of the scaled up panels (b) and (c), respectively. The grey shaded areas indicate samples more likely to be perturbed by terrestrial Pb contamination ($^{204}Pb/^{203}Tl > 25$). Error bars at the 2sd level are shown except where they are smaller than the symbols. 82

Figure 3.4. Plots of $\varepsilon^{205}Tl$ versus $\varepsilon^{114/110}Cd$ for the enstatite chondrites of this study and the carbonaceous chondrites of Baker et al. (2010). Panels (a) and (b) are of the same plot but use variable scaling to best reveal the structure and systematics of the data. The red box in panel (a) shows the coverage of the scaled up panel (b). The grey dashed line in both panels is the linear regression of all the enstatite chondrite samples excluding the EL6 Khairpur. The blue dashed line is the linear regression of all enstatite chondrites excluding EL6 chondrites Khairpur and Atlanta and the EL3 PCA 91020. Linear regression equations and R^2 values are shown next to relevant lines. Error bars at the 2sd level are shown except where they are smaller than the symbols. 84

Figure 3.5. Plot of $\varepsilon^{205}Tl$ versus Tl concentrations for the enstatite and ordinary chondrites of this study. The carbonaceous chondrites of Baker et al. (2010) are shown for comparison. Shock stages are indicated for each meteorites which have been classified in the literature and the references are listed in the caption to **Table 3.4** on page 71. Error bars at the 2sd level are smaller than the symbols. 93

Figure 4.1. Results of matrix test showing measurements of a Cd solution separated and purified from a solution of digested NIST SRM 361 steel doped with NIST SRM 3108 Cd and ^{111}Cd – ^{113}Cd double spike solutions (represented by the red diamonds) and analysed in two measurement sessions. These are bracketed with measurements of NIST SRM 3108 Cd standard solutions with each bracketing group separated by vertical grey lines in the plot. Single measurements of standards used in the bracketing of two samples, one after the other, are indicated by the dark grey symbols. Standard measurements used for bracketing only one sample are marked by light grey symbols. Uncertainties are internal errors shown at the 2se level. 111

Figure 4.2. Photomicrographs of experimental run products. (a) Experiment BW1305 showing the curved interface between the quenched silicate glass sample and silica capsule. Note the ingress of capsule material into the sample. (b) Experiment BW1306 showing the quench texture of the flattened Fe metal solid. (c) Experiment BW1307 showing the quench texture exhibited by the near spherical metal ball and also silicate crystalline and glass quench textures. The curved interface between the crystalline silicate sample and the MgO capsule is visible on the left hand side. (d) Experiment BW1308 showing the almost dendritic quench texture of the spherical metal Fe ball. The blueish tinge exhibited by silicate material in panels (a) and (c) is due to Fe content. 117

Figure 4.3. Cd metal-silicate partition coefficients, $D_{Cd}^{MET/SIL}$, versus experiment duration for the graphite capsule time series experiments. $D_{Cd}^{MET/SIL}$ is calculated in accordance with Eq. 4.2 on page 120. Error bars are shown at the 2sd level, unless smaller than the symbols. ... 121

Figure 4.4. Logarithmic partition ($\log D_{Cd}^{MET/SIL}$) and exchange coefficients ($\log K_D$) for Cd versus inverse experimental temperature, 10000/T, in 10000 K^{-1} units with equivalent temperatures given in °C. The grey arrows indicate the broad linear trends in the data (see text). Literature data are for sulphur-free metal-silicate partitioning experiments in MgO capsules, except where noted: Lagos et al. (2008) in graphite capsules, experiments at 0.5 – 2.0 GPa; Ballhaus et al. (2013) starting materials doped with ~ 0.3 wt% FeS, experiments at 1

– 5 GPa; Wang et al. (2016a) experiments at 15 – 20 GPa (squares); Wood et al. (2014), experiment at 1.5 GPa. If the K_D values were not shown by these authors, they were calculated here from their published Fe contents in metal and silicate phases and the $D_{Cd}^{MET/SIL}$ values using Eq. 4.1 and Eq. 4.3 above. Error bars are shown at the 2sd level except where smaller than symbols (2sd data unavailable for Lagos et al. (2008) K_D values). 124

Figure 4.5. Cd isotope compositions (ICs) of metal and silicate phases versus Cd metal-silicate partition coefficients ($D_{Cd}^{MET/SIL}$). Panel (b) is the same plot as (a) but with a narrower scale. The blue dashed lines in panel (a) show the coverage of the scaled up panel (b). In panel (c), $\Delta\varepsilon^{114}Cd_{MET-SIL} = \varepsilon^{114}Cd_{MET} - \varepsilon^{114}Cd_{SIL}$, or the Cd isotope fractionation between the phases. Error bars for Cd ICs (including $\Delta\varepsilon^{114}Cd_{MET-SIL}$) are shown at the 2se level, for $D_{Cd}^{MET/SIL}$ at the 2sd level, unless smaller than the symbols. The red vertical lines in (a) and (b) represent the Cd IC of the Cd-doped CMAS starting material The grey shaded area represents the uncertainty on this value at the 2se level. The blue vertical line in panel (c) represents the reference value $\Delta\varepsilon^{114}Cd_{MET-SIL} = 0$. 127

Figure 5.1. Map showing sample locations for this study. The numbers cross-reference to sample details in **Table 5.2**. Map produced using Ocean Data View (Schlitzer, 2016). 151

Figure 5.2. Cd isotope compositions of the bulk silicate Earth (BSE) and chondrites. Data analysed in this study are shown as solid coloured symbols and detailed in **Table 5.2** starting on page 152 and in Chapter 3 (enstatite chondrites). Literature data are shown as light grey symbols: 2 MORBs, 2 OIBs, 3 loess and all continental sulphides are from Schmitt et al. (2009b); Global Deep Ocean Water is from Xue et al. (2013); 9 carbonaceous chondrites are from Baker et al. (2010). The BSE isotope composition (red vertical line) is based on the average Cd isotope composition for peridotites and dunite excluding an anomalous highly fractionated sample (see text); the carbonaceous chondrite average Cd isotope composition (blue vertical line) excludes the highly fractionated samples included in the lower section of the figure. Error bars for data in this study are shown at the 2se level, with adjustments for scatter as explained in section 2.7.1 on page 43. Error bars for data from Schmitt et al. (2009b) and Xue et al. (2013) are shown at the 2se level, from Baker et al. (2010) at the 2sd level. The grey shaded areas represent uncertainties at the 2se level on the BSE and CC values. 155

Figure 5.3. Plot of Cd isotope compositions expressed in $\varepsilon^{114/110}Cd$ units against Cd concentrations in ppb. Data is from this study and 2 MORBs, 2 OIBs, 3 loess are from Schmitt et al. (2009b). Error bars for $\varepsilon^{114/110}Cd$ values are at the 2se level. Uncertainties for Cd concentrations are unavailable for the data from Schmitt et al. (2009b), otherwise they are shown at the 2sd level unless smaller than the symbols. The red arrow indicates an approximate possible degassing trend and the green arrow indicates an approximate possible partial melting trend. 160

Figure 5.4. Cd and Zn isotope compositions (ICs) of bulk silicate Earth (BSE) and carbonaceous chondrites (CC) shown in ε-notation and normalised to a mass difference of 1 amu (Wombacher and Rehkämper, 2004) and with the ICs of the BSE aligned (red line) to allow direct comparison of the two isotope systems. The Zn IC of the BSE is the average of peridotites (dunite, lherzolites) and ocean island basalts, but excludes the refractory harzburgites. For the Cd IC of the BSE see **Figure 5.2**. Data from this study are plotted as solid coloured symbols, literature data as light grey symbols. Cd isotope data from this study (**Table 5.2** and **Figure 5.2**) and from Schmitt et al. (2009b) and Baker et al. (2010). Zn isotope data from Archer and Vance (2004), Barrat et al. (2012), Bigalke et al. (2010), Bridgestock et al. (2014), Chen et al. (2013), Chen et al. (2009), Chen et al. (2016), Chapman

et al. (2006), Cloquet et al. (2006), Dolgopolova et al. (2006), Doucet et al. (2016), Herzog et al. (2009), Liu et al. (2016), Luck et al. (2005), Maréchal et al. (2000), Moynier et al. (2010), Moynier et al. (2011), Sonke et al. (2008), Sossi et al. (2015), Toutain et al. (2008), Viers et al. (2007), Zhou et al. (2014). For the Lyon JMC 3-0749 zero-delta standard see Maréchal et al. (1999). The CI2 chondrite is 'Tagish Lake' which can also be classified as C2 ungrouped. Error bars for data from this study and Cd ICs for MORBs and OIBs from Schmitt et al. (2009b) are reported at the 2se level. Error bars for other literature data are at the 2sd level. The grey shaded areas represent uncertainties at the 2se level on the BSE and CC values. . 167

Figure 5.5. Estimated elemental abundances in the primitive mantle normalised to CI chondrite abundances and Mg versus elemental half-mass condensation temperatures, based on the data of Palme and O'Neill (2014) and references therein, and Lodders (2003). The more precise data of Wang and Becker (2013) has been used for the mantle abundances of S, Te and Se. Geochemical classification after McDonough and Sun (1995) modified by more recent metal-silicate partitioning data of Ballhaus et al. (2013) and Wang et al. (2016a). Lithophile elements = diamond symbols, weakly to strongly siderophile elements = circles. The 50% T_C is the temperature at which 50% of the element has condensed from a solar system composition gas at 10^{-4} bar, approximately the pressure at a solar radial distance of 1 AU (Fegley, 2000; Lodders, 2003). Refractory elements are those elements with 50% T_C > 1300 K. The blue field represents the volatility trend at 1 AU defined by lithophile elements. Error bars are shown at the 1sd level if larger than the symbols and take account of the uncertainties in mantle and CI contents for each element and in the Mg normalisation factor. 170

Figure 5.6. Results of accretion simulation (after Halliday, 2004) showing fractional mass and $\varepsilon^{182}W$ isotope evolution versus time after start of accretion for a low- and high-mass late veneer. Panels (a) and (c) show the fractional mass of bulk Earth (M_E) accreted and $\varepsilon^{182}W$ isotope evolution respectively for a late veneer of 0.5% M_E, panels (b) and (d) show the same for a late veneer of 1.7% M_E. 175

Chapter 1 Introduction

1.1 Research background and aims

The work of this thesis is designed primarily to address two main issues relating to the early Earth and solar system. Firstly, this research continues the search for evidence of the extinct radionuclide ^{205}Pb in the early solar system, and, secondly, investigations are conducted into the delivery of volatile elements such as Cd to Earth during its main accretion phase and the 'late veneer'. The second goal is addressed using two new pieces of evidence obtained in this research: (i) a reliable estimate for the Cd isotope composition of the bulk silicate Earth (BSE) based on the analysis of a comprehensive suite of rocks from a variety global tectonic settings, and (ii) constraints on whether Cd isotopes are fractionated during core-mantle partitioning.

1.1.1 The extinct radionuclide ^{205}Pb in the early solar system

1.1.1.1 The ^{205}Pb – ^{205}Tl chronometer and the search for ^{205}Pb in the early solar system

The extinct radionuclide ^{205}Pb decays by electron capture to ^{205}Tl with a half-life of 17.3 Myr (Kondev, 2004). Since Tl is more volatile than Pb in a gas of solar system composition (Lodders, 2003), and the ^{205}Pb half-life is relatively short, the ^{205}Pb – ^{205}Tl chronometer has the potential to provide high-resolution relative age information on the timing of processes which induce volatile fractionation either in the solar nebula or on planetesimals.

Early investigations of the chronometer were hampered by the inability of instruments to resolve the very small variations in Tl isotope compositions that are expected from radiogenic ingrowth of ^{205}Tl due to the decay of ^{205}Pb (Rehkämper et al., 2002). In addition, since Tl only has two isotopes, distinguishing between stable isotope fractionation and radiogenic ingrowth of ^{205}Tl will always remain challenging.

The introduction of multi-collector inductively coupled plasma mass spectrometers (MC-ICP-MS), which were able to resolve these small variations in Tl isotopes (Rehkämper et al., 2001), opened up new opportunities to study the ^{205}Pb – ^{205}Tl chronometer with initial investigations of iron meteorites (Andreasen et al., 2012; Nielsen et al., 2006a) and carbonaceous chondrites (Baker et al., 2010).

1.1.1.2 Research carried out in this thesis into the ^{205}Pb – ^{205}Tl systematics and Pb, Tl, and Cd behaviour in enstatite and ordinary chondrites

This thesis aims to extend these investigations into the ^{205}Pb – ^{205}Tl chronometer by studying two further chondrite groups: enstatite and ordinary chondrites. The technique of Baker et al. (2010) will also be employed to identify samples where Tl isotope variations due to radiogenic ingrowth might be obscured by stable isotope variations. This involves using coupled Cd stable isotope analyses to identify Tl stable isotope fractionation from nebular and parent body volatilisation and alteration processes. Both Tl and Cd are highly labile elements with similar volatilities (Lipschutz and Woolum, 1988; Lodders, 2003) and they are therefore likely to be affected similarly by such stable isotope fractionation.

Leading on from the study of the ^{205}Pb – ^{205}Tl decay system in two new meteorite groups, coupled Pb, Tl and Cd analyses offer an opportunity to investigate parent body processes which fractionate the isotopes and abundances of these volatile elements in a particularly rare and important group of meteorites: the enstatite chondrites.

1.1.2 The Cd isotope composition of the BSE and volatile delivery to Earth

1.1.2.1 Volatile element delivery during Earth's main accretion and late veneer stages

Most authors accept that a 'late veneer' consisting of a volatile-rich meteoritic influx with a composition approximately akin to CI chondrites was delivered to Earth after its main accretion and differentiation phase and this late veneer established at least part of the volatile element budget of Earth. However, the question remains how much of the volatile element budget was delivered by the 'late veneer' and how much by the main accretionary materials.

Strong evidence for a fairly small late veneer is provided by abundances of highly siderophile elements (HSEs) in the bulk silicate Earth (BSE). These elements are so siderophile that they should have been sequestered almost completely to the core during Earth's accretion, and yet they have chondritic relative abundances in the BSE. This suggests a delivery of chondritic material after core formation of 0.3 to 0.7% of Earth's mass (M_E) (Chou, 1978; Holzheid et al., 2000; Jacobson et al., 2014; Walker, 2009). With such a relatively small late veneer, Earth's compliment of volatile elements must have been primarily delivered during the main accretion phase (Palme et al., 1988; Wood et al., 2010). Other authors, however, advocate a much larger late veneer component of, for example, 1.7%

M_E, or even 4% M_E (Albarède et al., 2013; Ballhaus et al., 2013), and suggest that this was the primary mechanism for delivery of volatile elements to Earth.

Since the approximately CI-chondritic HSE abundances of the BSE were established by the late veneer, it is a reasonable assumption that the late veneer itself has a composition approximately akin to CI-chondrites (e.g. Chou, 1978). If the concentration of a particular element is known for the BSE, together with the element's core-mantle partitioning behaviour, mass balance calculations can be employed to infer the concentration of the element in the main accretionary component. Notably, the result of the mass balance hinges on the amount of material delivered to Earth by the late veneer.

1.1.2.2 The role of Cd in Earth's accretion

There is a large contrast in the abundances of Cd between the BSE (31 – 40 ng/g) and CI chondrites (710 ng/g) (e.g. McDonough and Sun, 1995; Wang et al., 2016a). As Cd is only moderately siderophile during core-mantle partitioning (e.g. Wang et al., 2016a; Wood et al., 2014), a significant part of Earth's Cd budget remains in the BSE. Thus, the Earth's budget of Cd is heavily dependent on the mass of material delivered by the volatile-rich and hence Cd-rich late veneer. Similarly, the Cd isotope composition of the BSE depends on the isotopic signatures of both the main accretionary material and the late veneer. In addition, it is also affected by any Cd isotope fractionation that occurs during the core-mantle partitioning, which accompanied the main accretion phase.

In summary, provided Cd abundances and isotope compositions of the BSE and the late veneer, and Cd isotope fractionation during core-mantle partitioning, are well-constrained, mass balance can be applied to estimate the Cd isotope composition of the main accretionary material. The only remaining variable in this mass balance is the size of the late veneer. Consequently, such results can be used to assess whether a small late veneer (0.3 to 0.7% M_E) or a large late veneer (1.7 to 4% M_E) is more reasonable.

1.1.2.3 Research carried out in this thesis to explore Earth's main accretion and late veneer delivery of Cd

The Cd isotope composition of the BSE was estimated by Schmitt et al. (2009b) based on data for seven loess and basalt samples. This estimate rested on the assumption that the mantle, mantle-derived rocks and the continental crust have essentially identical Cd isotope compositions. In this thesis, this assumption will be tested by analyses of a more

comprehensive suite of rocks from a range of global tectonic settings. This includes, vitally, mantle peridotites, which were not available in the study of Schmitt et al. (2009b) but which are likely to provide the best estimate for the Cd isotope composition of the BSE. In addition, the more comprehensive high-precision Cd isotope data presented in this thesis enable a first assessment of whether magmatic processes, such as partial melting and volcanic degassing, are associated with Cd isotope fractionation (Schönbächler et al., 2009).

The Cd isotope composition of carbonaceous chondrites was previously investigated by Baker et al. (2010), who analysed various CM2, CV3, CO3 and CR2 meteorites and the CI chondrite Orgueil. As part of the thesis research, these data were augmented by further analyses of Murchison CM2 and the very rare CI chondrite Ivuna.

Finally, experiments were carried out to determine the partitioning behaviour of Cd between metal and silicate liquids at high pressure (1.5 GPa) and elevated temperature using a range of capsule materials. Similar experiments were carried out previously by other workers, primarily to obtain metal-silicate partition coefficients for various elements (e.g. Ballhaus et al., 2013; Lagos et al., 2008). The thesis research, however, extends beyond elemental partitioning and provides the first constraints on whether Cd stable isotope fractionation is expected during core-mantle partitioning. Unlike previous metal-silicate partitioning experiments, those carried out here were specifically designed to minimise loss of Cd by volatilisation. Very few studies (e.g. Bonnand et al., 2016; Bridgestock et al., 2014; Hin et al., 2014) have hitherto focussed on stable isotope fractionation during core-mantle partitioning.

1.2 Outline of the thesis

This thesis is organised into the following chapters:

Chapter 2 provides a detailed account of the analytical techniques used for the measurement of Cd abundances and isotope compositions. The description focuses particularly on the analyses of the Cd-rich samples from metal-silicate partitioning experiments of Chapter 4 and the terrestrial and meteoritic samples of Chapter 5, which have comparatively low Cd abundances. These same analytical techniques were, however, also used for the determination of the Cd abundances and isotope compositions of the enstatite chondrites, which are discussed in Chapter 3.

The primary focus of Chapter 3 is the search for evidence of the extinct radionuclide ^{205}Pb in enstatite and ordinary chondrites. This involved Pb and Tl isotope analyses of

relevant meteorite samples in an attempt to resolve possible parent body ^{205}Pb – ^{205}Tl isochrons. This work continues previous searches for evidence of formerly live ^{205}Pb in iron meteorites (Andreasen et al., 2012; Nielsen et al., 2006a) and carbonaceous chondrites (Baker et al., 2010). In addition, Pb isotope compositions were applied to determine Pb – Pb isochrons and coupled analyses of Cd isotope compositions were used to interrogate whether Tl isotopes were possibly altered by stable isotope fractionation during parent body metamorphism. Finally, the Pb, Tl, and Cd elemental and isotope data were employed to evaluate processes that might have taken place on the respective meteorite parent bodies.

Chapter 4 covers metal-silicate partitioning experiments that were carried out to determine, for the first time, whether Cd isotopes recorded stable isotope fractionation during Earth's core-mantle segregation. Such fractionation would have had a significant impact on the Cd isotope composition of the BSE and must therefore be well-constrained to enable a discussion of the compositional relationships between the BSE, the late veneer material and the original building blocks of Earth that were assembled during the main phase of accretion.

Chapter 5 is centred on a major survey of the Cd abundances and isotope compositions of diverse terrestrial rocks from major global tectonic settings in order to characterise the Cd isotope composition of the BSE. This suite of rocks is much more comprehensive and extensive compared to the sample suites that were used previously for this purpose (e.g. Schmitt et al., 2009b). The data are also applied to assess whether magmatic processes result in the fractionation of Cd isotopes. These results and the data of Chapter 4 are finally applied together to fully explore the implications of the finding that the BSE and carbonaceous chondrites display a small but readily resolvable difference in their Cd isotope compositions. To this end, simple numerical accretion models are employed to estimate the Cd isotope composition of the main accretion building blocks of Earth for several suggested late veneer scenarios.

Finally, Chapter 6 provides a summary of the major findings of the PhD investigations and looks ahead to possible future directions for such research.

Chapter 2 The precise and accurate measurement of cadmium stable isotope compositions by multiple-collector ICP-MS

2.1 Introduction

An important part of the analysis of all the samples considered in this thesis is the precise and accurate measurement by multiple-collector inductively coupled plasma mass spectrometer (MC-ICP-MS) of Cd concentrations and isotope compositions using the double spike method. The detailed methods to achieve this, described in this chapter, are well-established and owe much to the work of Wombacher et al. (2003) and Ripperger and Rehkämper (2007).

The sample preparation and digestion methods relevant to the different types of samples handled in these studies are described in the chapters relating to those samples. However, subsequent to digestion, the same methods for Cd separation and purification, double-spiking and mass spectrometry are used for the samples from the Cd metal-silicate partitioning experiments of Chapter 4 and the terrestrial and meteoritic samples of Chapter 5. In addition, these methods also apply to the Cd analyses of the enstatite and ordinary chondrites, which are the focus of Chapter 3. However, Pb and Tl analyses of these meteorite samples are also carried out and there are therefore some differences in approach. In particular, modifications are employed to the separation and purification procedures to enable the isotopic analysis of all three elements. Full details of these modifications together with the procedures relating specifically to the analysis of Pb and Tl abundances and isotope compositions are set out in the analytical methods section of Chapter 3.

2.2 Reagents and laboratory procedures

Digestion, anion exchange separation, preparation for mass spectrometry and all critical work on samples, apart from weighing, were carried out in Class 10 laminar flow hoods within the Class 1000 MAGIC clean room facility at Imperial College London using ultrapure reagents and water.

All water used in sample processing or dilution of distilled acids was supplied through a Milli-Q® water purification system supplied by Merck Millipore providing ‘type 1’ ultrapure water with an electrical resistivity of 18.2 MΩ.cm at 25 °C. Distilled 6 M HCl and 16 M HNO_3 acids were produced from analytical grade low trace metal acids in dedicated sub-boiling quartz stills inside a Class 10 laminar flow hood in the clean room facility. Double-distilled 12 M HCl and ethanol were made from analytical grades in dedicated sub-boiling elbow-style PFA stills also in the laminar flow hood. Ultrapure 28 M HF (49%) and

8.7 M HBr (47%) were purchased from Qmx (PlasmaPURE Plus®) and Fisher Scientific (Optima®). All laboratory hotplates used for acid refluxing, digestion and drying down were Teflon® coated and situated within Class 10 laminar flow hoods in the clean room facility.

Samples were processed in Savillex® PFA (perfluoroalkoxy) vials throughout, except when centrifuging residues for which PP (polypropylene) centrifuge tubes were used. Samples diluted in 0.1 M HNO_3 were only transferred to HDPE (high-density polyethylene) and LDPE (low-density polyethylene) bottles and PP centrifuge tubes for mass spectrometry. All PFA vials were cleaned in hot analytical grade 6 M HCl, 8 M HNO_3 acids and acidified Milli-Q® water. Prior to use, vials were refluxed with a small amount of distilled acid, usually 16 M HNO_3. All HDPE, LDPE and PP bottles and centrifuge tubes were cleaned over periods of many months with 2 to 4 M HNO_3 and 1 to 3 M HCl at room temperature, the last cleaning stage using distilled acid. The molarity of the acids were chosen to suit the acid corrosion resistance of the plastic, and the bottles and centrifuge tubes were stored until use containing this distilled acid.

Powdered or crushed samples were weighed in a dedicated weighing room within the same clean room facility using a Mettler Toledo AX250 DeltaRange® analytical balance reading to the nearest 0.01 mg (0.1 mg above 82 g). Digestions, aliquots, double spike and standards were weighed in closed vials after handling in the laminar flow hoods and no liquid transfers were carried out in the weighing room to minimise blanks and cross-contamination.

Precautions were taken during weighing to minimise the effect of variations in temperature in the weighing room and build up of static electricity in PFA vials on the accuracy of sample weights, for example by using an antistatic gun and monitoring laboratory temperature.

2.3 Cd separation and purification

A clean, matrix-free fraction of Cd was extracted from the samples using the column chemistry procedures described in this section which are essentially the same as those of Wombacher et al. (2003), consisting of two stages of anion exchange chromatography followed by a final stage of extraction chromatography, as set out in Table 2.1.

Prior to separation and purification of the samples using these procedures, a precisely weighed ^{111}Cd – ^{113}Cd double spike solution was added to the digested sample in order to achieve a ratio of spike- to sample-derived Cd (also termed the spike-sample ratio in the following) of about 1.1 – 1.25, as described in sections 2.5.2.2 and 2.5.2.3 starting on page

36. This involves an initial check to determine the concentration of Cd in the sample by isotope dilution and use of this data to calculate the weight of double spike solution required to produce the desired spike-sample ratio. The sample solutions were then evaporated to dryness, re-dissolved in the matrix required for the first stage of anion exchange chemistry (Table 2.1), 10 ml 3 M HCl, and refluxed on a hotplate to ensure complete equilibration of natural and double-spike Cd.

Table 2.1. Column chemistry for the separation of Cd from silicate rock and meteorite samples

First stage anion exchange chemistry		**Second stage anion exchange chemistry**
2 ml Bio-Rad AG® 1-X8 resin *100 – 200 mesh* *50 ml quartz glass columns*		*100 µl Bio-Rad AG® 1-X8 resin* *200 – 400 mesh* *Small PTFE columns*
15 ml 2 M HNO_3	Resin cleaning – Cd eluted	750 µl 2 M HNO_3
2 ml Milli-Q H_2O		100 µl Milli-Q H_2O
26 ml 6 M HCl	Wash, conversion to Cl^- form	1300 µl 6 M HCl
12 ml 0.5 M HCl	Wash	600 µl 0.5 M HCl
6 ml 3 M HCl	Column equilibration	300 µl 3 M HCl
Sample in 10 ml 3 M HCl	Sample loading	Sample in 500 µl 3 M HCl
Sample in 1 – 2 ml 3 M HCl	Flush residual sample in vials	
2 ml 3 M HCl	Matrix elution	100 µl 3 M HCl
30 ml 0.5 M HCl	Matrix elution incl. In, Mo	1500 µl 0.5 M HCl
10 ml 1 M HCl	Matrix elution incl. Mo	500 µl 1 M HCl
10 ml 2 M HCl	Matrix elution	500 µl 2 M HCl
12 ml 6 M HCl	Matrix elution, incl. Ag	600 µl 6 M HCl
16 ml 0.1 M HBr – 0.5 M HNO_3	Zn and In elution	600 µl 0.1 M HBr – 0.5 M HNO_3
2 ml 2 M HNO_3	Column equilibration	100 µl 2 M HNO_3
13 ml 2 M HNO_3	Cd eluate collection (Remaining Sn Mo, In, Zn also eluted, Pd retained on resin)	750 µl 2 M HNO_3
Third stage extraction chromatography		
100 µl Eichrom® TRU® resin *100–150 µm particle size* *Small PTFE columns*		
10 ml 6 M HCl	Resin cleaning – Cd eluted	
Sample in 200 µl 8 M HCl	Sample loading and Cd collection, Sn and Mo retained on resin	
200 µl 8 M HCl	Cd collection, Sn and Mo retained on resin	
1400 µl 6 M HCl	Cd collection, Sn and Mo retained on resin	

Bio-Rad analytical grade AG® 1-X8 resin was used for both stages of anion exchange chromatography with wet bead sizes of 106 – 180 μm (100 – 200 mesh) for the first stage and 45 – 106 μm (200 – 400 mesh) for the second. An attempt was made to use the smaller bead size for the first stage but the column chemistry took too long owing to the slow elution rate: 7 – 10 ml/h compared to 12 – 15 ml/h with the larger bead size.

The final extraction chromatography stage used the same PTFE columns as in the second 'clean up' stage, after having been cleaned in distilled 2 M HCl, and utilized 100 μl Eichrom® TRU® resin with a particle size of 100 – 150 μl. The primary purpose of this step is to remove from the sample potential sources of isobaric and molecular interferences in mass spectrometry arising from the presence of Sn and Mo. The high distribution coefficients for Sn and Mo (Huff and Huff, 1993) ensure that these elements are retained on the resin column, whilst Cd is readily eluted. Such potential interferences are further discussed in section 2.6.1 below.

The elution characteristics of key elements indicated in the centre column of Table 2.1 are those determined from published distribution coefficients for Bio-Rad AG® 1-X8 or similar strongly basic anion exchange resins using various eluents: HCl (Kraus and Nelson, 1956; Van der Walt et al., 1985), HNO_3 (Faris and Buchanan, 1964) and HBr – HNO_3 mixtures (Strelow, 1978).

In respect of the experimental metal-silicate partitioning samples of Chapter 4 and the terrestrial and meteoritic samples of Chapter 5, the average yield of Cd from these chemical separation procedures was approximately 85%, with yields for most individual samples in the range 65 – 100% and only three samples with lower yields (32 – 50%).

2.4 Mass spectrometry

2.4.1 Instrumentation

All isotopic measurements were carried out using a Nu Plasma HR multiple-collector inductively coupled plasma mass spectrometer (MC-ICP-MS), manufactured by Nu Instruments (part of the Ametek, Inc. Materials Analysis Division) at the Imperial College London MAGIC laboratory facility. This instrument is of the double focusing Nier-Johnson design and features an array of 12 fixed Faraday collectors equipped with 10^{11} Ω resistors. It uses a system of quadrupolar zoom lenses to align the ion beams into the collectors.

The instrument was fitted with a rotary pump with a capacity of 80 L/min to evacuate the expansion chamber between the sampling and skimmer cones and was operated with a voltage of 6 kV applied to the extraction plate for the primary acceleration of the ions.

Desolvating nebuliser systems were used to introduce sample solutions in 0.1 M HNO_3 as a dry aerosol into the ICP torch with three different models operated at different times: the DSN-100 (Nu Instruments), the Aridus and the Aridus II (Teledyne CETAC Technologies). Both glass and PFA nebulisers were used with a sample uptake rate generally in the range 100 – 130 µl/min. A comparison between the performance of the Aridus and Aridus II in terms of the internal precision achieved for Cd isotope composition measurements given in section 2.7.3 and in Figure 2.4 on page 47

The instrument was operated with the source-defining slit positioned at its widest setting (0.3 mm) giving a mass resolution (M/ΔM) of about 400 and an instrumental sensitivity that generally ranged between 180 – 300 V/ppm Cd and averaged about 240 V/ppm. Higher sensitivities 350 to 400 V/ppm were obtained in a few measurement sessions using the DSN-100 nebuliser.

The instrument was allowed to warm up for a few hours before the start of an analytical session to ensure stability during runs. During the warm up time, the instrument was tuned for maximum ion beam intensity and sensitivity primarily by adjusting the plasma torch position and voltages on extraction and steering ion optics. In addition, optimum peak shape and peak-top flatness and coincidences on the channels used for isotope composition analysis were fine-tuned by adjusting the voltage on quadrupole zoom lenses in front of the static collector array and using a software program to test the effectiveness of these adjustments. Very low concentration NIST SRM 3108 Cd solutions were used for tuning, usually about 5 ppb and these were double spiked to a spike-sample ratio approximating the samples and standards to be run during the analytical session, in order to prevent the build up of Cd 'memory' in the instrument.

During analysis sessions the build up of Cd baseline 'memory' was monitored and controlled by washing out with clean 0.1 M HNO_3 for periods of about 5 to 10 minutes between sample and standard runs. Particular attention was paid to monitoring the Cd 'memory' on the beams for masses 111 and 113, since a ^{111}Cd – ^{113}Cd double spike was mixed with samples and standards in this study (see section 2.5).

2.4.2 Reporting Cd isotope compositions

2.4.2.1 The epsilon notation

All Cd isotope compositions are reported using the epsilon notation which denotes the deviation of the isotope ratio of a sample from that of a standard, in the case of this study the National Institute of Standards and Technology (NIST) standard reference material (SRM) 3108 Cd standard solution, in parts per 10,000 (Wombacher and Rehkämper, 2004), thus:

$$\varepsilon^{114/110}\mathrm{Cd} = \left(\frac{(^{114}\mathrm{Cd}/^{110}\mathrm{Cd})_{\mathrm{SAMPLE}}}{(^{114}\mathrm{Cd}/^{110}\mathrm{Cd})_{\mathrm{NIST\ SRM\ 3108\ Cd}}} - 1\right) \times\ 10{,}000 \qquad \text{Eq. 2.1}$$

In addition, it may be useful to report isotope fractionation normalised to a mass difference of 1 amu for comparison between εCd values calculated using any Cd isotope ratio (Rehkämper et al., 2011; Wombacher and Rehkämper, 2004) or even for comparison with other stable element isotope systems, thus:

$$\varepsilon\mathrm{Cd/amu} = \left(\frac{(^{114}\mathrm{Cd}/^{110}\mathrm{Cd})_{\mathrm{SAMPLE}}}{(^{114}\mathrm{Cd}/^{110}\mathrm{Cd})_{\mathrm{NIST\ SRM\ 3108\ Cd}}} - 1\right) \times\ 10{,}000/(m_{114} - m_{110}) \qquad \text{Eq. 2.2}$$

In Eq. 2.2, m_{114} and m_{110} are the exact atomic masses of ^{114}Cd and ^{110}Cd respectively.

However, εCd/amu values calculated using Eq. 2.2 need to used with caution: such values calculated from different Cd isotope ratio measurements for the same degree of fractionation will not be exactly the same. The difference is dependent on the mass difference between the isotopes used in the ratios compared and the mass fractionation law governing isotope variation in the sample and increases with the degree of fractionation, although the difference is negligible for $\varepsilon^{114/110}$Cd values between about –10 and +10 (Rehkämper et al., 2011; Wombacher and Rehkämper, 2004).

An accurate method for converting measurements in one isotope ratio to another, which overcomes the drawbacks described in the previous paragraph requires an assumption to be made for the mass fractionation law. The relationship between two Cd isotope ratios, for example the ^{114}Cd/^{110}Cd ratio used throughout this study and the ^{112}Cd/^{110}Cd ratio used by other authors (e.g. Schmitt et al., 2009b) is described by the following equation (Wombacher and Rehkämper, 2004):

$$\varepsilon^{114/110}\mathrm{Cd} = \left[\left(\frac{\varepsilon^{112/110}\mathrm{Cd}}{10{,}000} + 1\right)^{\beta} - 1\right] \times 10{,}000 \qquad \text{Eq. 2.3}$$

In Eq. 2.3, the β function describes the relevant mass fractionation law. In most cases, the kinetic law would be appropriate, thus:

$$\beta = \ln\left(m_{114}/m_{110}\right)/\ln(m_{112}/m_{110}) \qquad \text{Eq. 2.4}$$

In Eq. 2.4, m_{114}, m_{112} and m_{110} are the exact atomic masses of ^{114}Cd, ^{112}Cd and ^{110}Cd respectively.

2.4.2.2 Cd zero-epsilon standard

The NIST SRM 3108 Cd solution has been adopted as the zero-epsilon reference material in this study as it is now finding wide acceptance in Cd isotopic studies (e.g. Georgiev et al., 2015; Kruijer et al., 2013; Lambelet et al., 2013; Lee et al., 2013; Xue et al., 2013). Abouchami et al. (2013) reported that NIST SRM 3108 Cd yielded reproducible $\varepsilon^{114/110}$Cd values between seven laboratories, was found to contain only negligible amounts of elements known to produce isobaric and polyatomic interferences on Cd isotopes, and had a $\varepsilon^{114/110}$Cd value close to that of the bulk silicate Earth. They thus recommended NIST SRM 3108 Cd as a zero-epsilon standard for Cd isotopic studies and it is therefore adopted in this study.

2.4.2.3 Cd isotope ratio used for reporting stable isotope variations

Most Cd isotopic studies report Cd stable isotope variations in terms of the ^{114}Cd/^{110}Cd ratio following the reasoning set out in Wombacher and Rehkämper (2004), although Schmitt et al. (2009a) advocated the use of ^{112}Cd/^{110}Cd, preferring to use a 2 amu offset as this offers more comparability with the (2 amu mass difference) ratios that are commonly used to report stable isotope variations for many other elements.

Wombacher and Rehkämper (2004) argued against using ^{106}Cd, ^{108}Cd and ^{116}Cd which are low abundance isotopes of natural Cd with major isobaric interferences (see Table 2.2 below), but noted that, in the range of major isotopes from ^{110}Cd to ^{114}Cd which only have minor isobaric interferences, ^{114}Cd/^{110}Cd has the largest mass difference. The small isobaric

interferences on ^{110}Cd and ^{114}Cd (^{110}Pd and ^{114}Sn) are easily removed during chemical separation, as indicated in Table 2.1 and, in the case of Sn, further correction is made to the data to remove any residual interference as explained in section 2.6.1 below. Thus, in this study, the $^{114}Cd/^{110}Cd$ ratio will be used throughout to report Cd isotope variations, except when comparing with other elements, when all such variations will be converted to an epsilon value per amu using Eq. 2.2.

2.5 Principles of the Cd double spike method

2.5.1 Introduction

The mathematical techniques of the double spike method were first described by Dodson (1963) and further developed and used to correct for the instrumental mass fractionation encountered during the analysis of the isotopes of Pb and other elements by mass spectrometry (e.g. Boelrijk, 1968; Compston and Oversby, 1969; Dodson, 1970; Hamelin et al., 1985; Hofmann, 1971; Krogh and Hurley, 1968).

The double spike technique uses a solution artificially enriched in two isotopes of an element which is admixed and equilibrated with a sample solution in precise amounts before ion exchange chemistry and requires the measurements of three isotope ratios with a common isotope as a denominator, involving four isotopes of an element in all.

Isotope fractionation can occur during the chemical separation of an element from a sample by ion exchange chromatography and other methods (e.g. Maréchal and Albarède, 2002; Russell and Papanastassiou, 1978; Taylor and Urey, 1938). In relation to Cd separation using an anion exchange resin column, some workers (e.g. Cloquet et al., 2005; Schmitt et al., 2009a; Wombacher et al., 2003) have found that the Cd isotope composition of the eluate becomes lighter as elution progresses. This is possibly due to different Cd species with distinct isotope compositions forming in the stationary and mobile phases, which, upon elution, fractionate differently between eluent and resin (Wombacher et al., 2003).

When a double spike is mixed and equilibrated with a sample prior to chemical separation, it effectively tracks any isotope fractionation during chemistry enabling the original natural fractionation in the sample to be derived using the mathematical techniques described briefly in section 2.5.2 below. Thus the addition of a double spike obviates the need to obtain a 100% yield of a target element during ion exchange chemistry (Schönbächler and Fehr, 2014). In addition, instrumental mass bias is corrected without the need for external normalisation (Rudge et al., 2009).

One of the first uses of a ^{106}Cd and ^{111}Cd double spike for the correction of mass discrimination was by Rosman and De Laeter (1975) who used the mathematical solutions of Russell (1971) in their study of Cd isotopes in Cd-bearing minerals. Ripperger and Rehkämper (2007) later established techniques for use of the double spike technique for the analysis of Cd isotopes by MC-ICP-MS and their techniques have been relied upon in most of the recent Cd isotopic work (e.g. Lambelet et al., 2013; Xue et al., 2013; Xue et al., 2012) and in this study, as described in the section 2.6 below.

2.5.2 The double spike technique

2.5.2.1 Theory of the double spike technique

The double spike technique employed in this study uses the geometric principles and numerical solutions set out in Galer (1999) and Siebert et al. (2001). These principles are illustrated in Figure 2.1 below which uses the four isotopes ^{111}Cd, ^{112}Cd, ^{113}Cd and ^{114}Cd in three ratios with the common denominator ^{111}Cd to describe the Cd isotope compositions of the sample, double spike and spike-sample mixture.

The primary goal of this technique is to determine the fractionated true isotope composition of a sample in terms of $\varepsilon^{114/110}$Cd, as defined in Eq. 2.1, which is equivalent to the natural fractionation vector, F_{nat} in Figure 2.1, and which determines the fractionation of the sample, N, from a Cd zero-epsilon standard, n. This is achieved by measuring four isotopes ^{111}Cd, ^{112}Cd, ^{113}Cd and ^{114}Cd of a mixture of known quantities of the sample and a ^{111}Cd – ^{113}Cd double spike, denoted by m in the figure. The reasons behind measuring these four isotopes and the choice of double spike isotopes are described further in section 2.6.1 below.

The true isotope compositions of the standard, n, and the double spike, S, are known as a result of double spike calibration procedures described in section 2.6.2 on page 40. The true isotope composition of the spike-sample mixture, M, is not known because the measurement, m, is fractionated by an unknown instrumental mass fractionation vector, F_{ins}. However, the true isotope composition of this spike-sample mixture (M) lies on the plane P_n (red in the diagram) in three isotope ratio space defined by the isotope compositions of the sample (N), standard (n) and double spike (S). Similarly the isotope measurement of the spike-sample mixture, m, and the isotope compositions of the double spike (S) and spike-sample mixture (M) all lie on the plane P_m (green in the diagram).

Applying the iterative techniques described by Siebert et al. (2001) to these planes, after making reasonable initial assumptions about the values of the fractionation vectors f_{nat} and f_{ins}, and utilising the mixing line N-M-S, it is possible to determine the fractionation vectors and hence the isotope compositions of the sample (N) and the spike-sample mixture (M). This is achieved by an offline data reduction spreadsheet applied to measurements of ion beam intensities of the spike-sample mixture, after adjusting for isobaric interferences of In and Sn, explained further in section 2.6.1 below. If the correct calibrated isotope compositions of the standard (n) and the double spike (S) are used together with reasonable initial assumptions in the iteration, the values of F_{nat} and F_{ins} will converge to their true values.

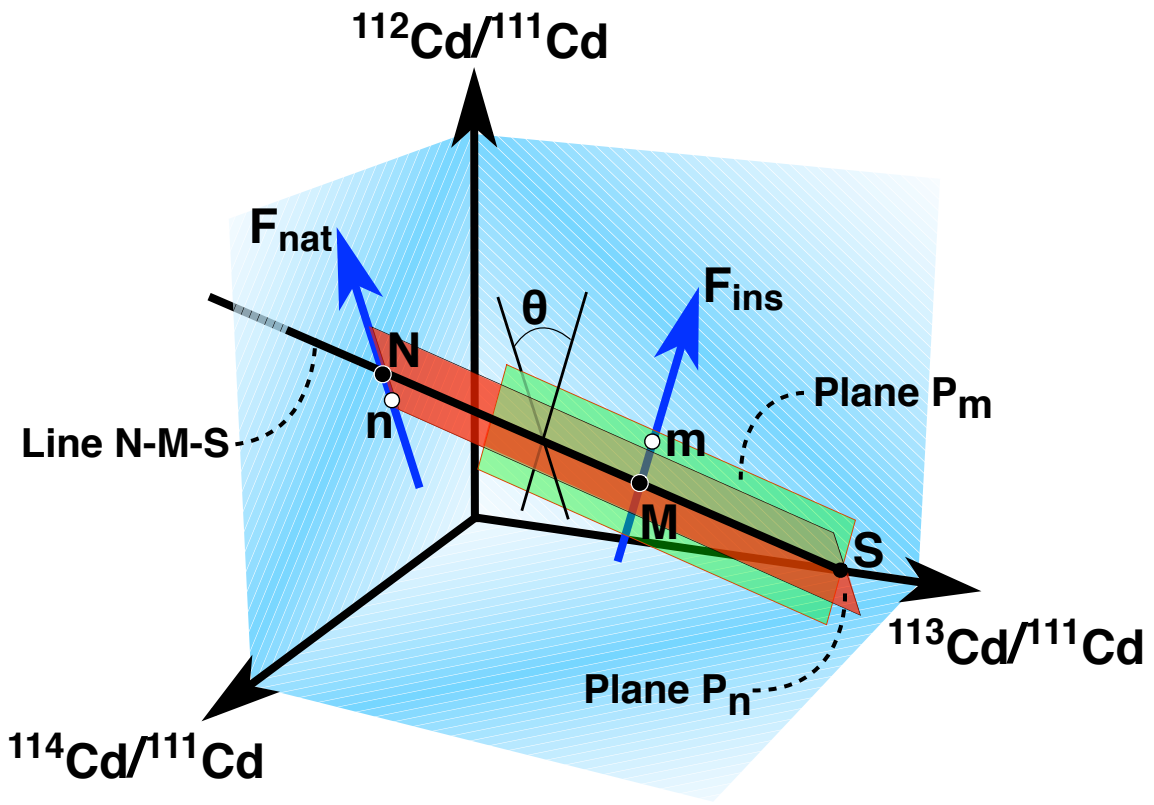


Figure 2.1. Graphical representation of the relationship between the Cd isotope compositions of a sample (N), a ^{111}Cd – ^{113}Cd double spike (S), and the spike-sample mixture (M) in three Cd isotope ratio space modified after Galer (1999) and Hofmann (1971). Nomenclature selected from Galer (1999) and Siebert et al. (2001): N, M and S are the true Cd isotope compositions of a sample, the spike-sample mixture and a ^{111}Cd – ^{113}Cd double spike respectively, m is the measured Cd isotope ratio of the spike-sample mixture and n is the isotope composition of a zero-epsilon standard. F_{nat} represents the mass fractionation vector of the sample and F_{ins} represents the instrumental mass fractionation vector, both of which are in reality non-linear.

2.5.2.2 Spike-sample ratio

The spike-sample ratio is the ratio of the molar amounts of Cd from the double spike and natural Cd from the sample. Thus, if Q = molar fraction of natural Cd in a mixture of sample and double spike, then the spike-sample ratio is (1 – Q)/Q.

The choice of mixture is critical in controlling precision of data produced by the double spike method. In Figure 2.1, a spike-sample mixture (M) composition too close to the sample (N) compositions will produce a small angle of incidence θ between the two planes P_n (red) and P_m (green), due to the rotation of the fractionation vector F_{ins}. A spike-sample mixture (M) composition too close to the double spike (S) composition results in the degradation of plane P_m (green) to a line. Both extremes would prevent the mixing line N-M-S from being well defined (Galer, 1999).

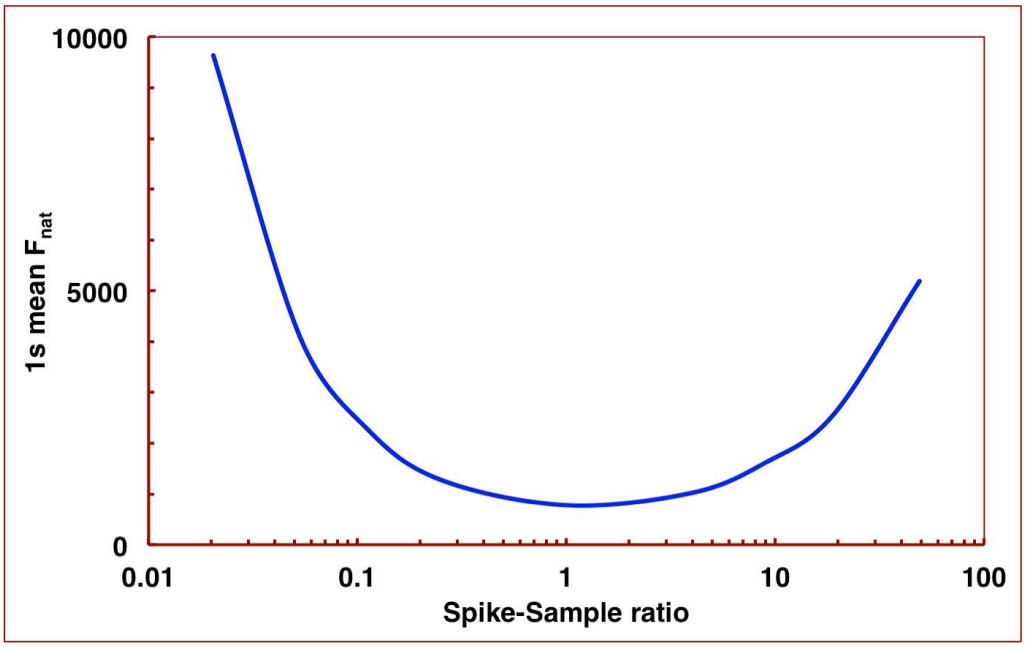


Figure 2.2. Error propagation of F_{nat} natural fractionation relative to standard applied to the ^{111}Cd - ^{113}Cd double spike using nomenclature of Siebert et al. (2001)

Based on the results of error propagation analyses on test data set out in Figure 2.2, the optimum spike-sample ratio, producing the lowest error in F_{nat}, is ≈1. Uncertainties increase exponentially as spike-sample ratios decrease below 1 (under-spiked) but degrade more gradually as ratios increase above 1 (over-spiked). Thus, it is better for the spike-sample mixtures to be slightly over-spiked than under-spiked.

For this reason, due to the likelihood of small uncertainties in weighing an amount of double spike solution to add to a sample to produce a specific spike-sample ratio, it was

decided to target a spike-sample ratio of 1.1 to avoid ratios falling below 1. For some samples with very low Cd contents or where very small amounts of sample were available for digestion, a spike-sample ratio of 1.5 or 1.7 was chosen as a way of artificially increasing the amount of Cd in a sample to be measured in order to improve beam intensities and thus precision during mass spectrometry.

2.5.2.3 Initial Cd concentration check prior to anion exchange chemistry

In order to determine the weight of Cd double spike solution to add to a digested sample to produce a specific spike-sample ratio, it is necessary first to determine the Cd content of the sample. Thus, an aliquot of 1 to 5% v/v of the digested sample was taken and weighed, and a weighed amount of Cd double spike was added to the aliquots based on estimated sample Cd contents.

The double-spiked aliquots were evaporated to dryness, taken up in 500 µl 3M HCl, refluxed to ensure complete equilibration of the double spike with sample Cd, and then purified using only the second stage anion exchange chemistry and third stage extraction chromatography as set out in Table 2.1 on page 28. The Cd isotope compositions of the spiked sample aliquots were measured on the mass spectrometer, the raw data was processed using offline data reduction methods described in section 2.5.2.1 above and the results were used to calculate sample Cd concentrations by the isotope dilution (ID) method.

It is not critical to achieve a spike-sample ratio close to 1 in the sample aliquots, or even accurate and precise isotope composition measurements, since the ID method is still robust enough to produce sufficiently accurate sample Cd concentrations. Therefore, the measurements can be done quickly without the need for extensive instrument tuning, sample-standard bracketing or washout procedures during the measurements sessions. In practice, the concentration check aliquots had spike-sample ratios of between 0.35 and 7.76 and, diluted in 1 ml 0.1 M HNO_3 for analysis on the mass spectrometer, had concentrations of about 1 to 11 ppb. The Cd contents calculated by ID from these measurements were accurate to within approximately ± 1% of the final concentrations calculated from measurements taken from the isotope composition (IC) runs.

The weight of double spike solution required to produce a specific spike-sample ratio in a sample can be determined using simple mixing calculations using the sample Cd concentration calculated by ID and Cd double spike concentration derived during calibration, as described in section 2.6.2 below and detailed in Table 2.3. The calculated amount of

double spike solution is weighed and fully equilibrated with the sample solution before separation and purification of Cd from the sample by ion exchange chemistry and extraction chromatography, as described in section 2.3 starting on page 27.

2.5.2.4 Second Cd concentration check in preparation for IC measurements

An aliquot of 1 to 5% v/v of the sample eluate after chemical separation was taken and analysed on the mass spectrometer to determine Cd abundances, the exact spike-sample ratio achieved and the approximate yield of Cd from chemistry. This data was used to make up solutions of the samples in 0.1 M HNO_3 to a specific concentration for Cd isotope composition analysis on the mass spectrometer, usually 50 to 70 ppb. The NIST SRM 3108 Cd standard solutions were made up to match the concentrations and spike-sample ratios of the samples for sample-standard bracketing during analysis so that ion beam intensities are similar for samples and bracketing standards. This ensures that instrumental conditions are, as far as possible, similar for samples and standards helping to reduce systematic errors (Wombacher et al., 2003).

The beam intensities for ^{111}Cd measured for all the sample runs of this study (covering the samples of Chapters 3 to 5), and for BAM-I102 secondary isotopic reference solutions (section 2.7.2), were compared to those for associated bracketing standards (NIST SRM 3108 Cd). The results were that, in 63% of cases, the sample ion beam intensities were within 5% of the ion beam intensities measured for the matching standards and, in 97% of cases, they were within 20% of the ion beam intensities measured for the matching standards.

2.6 Design, preparation and calibration of the Cd double spike solution

2.6.1 Cd isotopes and isobaric and molecular interferences

Determining which Cd isotopes to use for the double spike requires knowledge of the relative natural abundances of Cd isotopes and isobaric nuclides of other elements and these are summarised in Table 2.2 below, along with the mass spectrometer collector configuration and double spike isotopes used in this study.

Ripperger and Rehkämper (2007) concluded that the isotopes ^{106}Cd, ^{108}Cd and ^{116}Cd were not suitable for analysis using a double spike because of the major isobaric interferences from Pd and Sn. They suggested that the isotopes ^{110}Cd, ^{111}Cd, ^{112}Cd, and ^{114}Cd were suitable candidates for analysis for the following reasons. Firstly, ^{111}Cd has no isobaric interferences,

secondly, ^{110}Cd has only a minor isobaric interference from ^{110}Pd, which should be readily removable during ion exchange chemistry (Table 2.1), and, thirdly, ^{112}Cd and ^{114}Cd have minor interferences from Sn, which can be adjusted for by simultaneously monitoring ^{117}Sn or ^{118}Sn and applying an interference correction to the data.

During their analyses using thermal ionisation mass spectrometry, Rosman and De Laeter (1975) established methods for determining the effect of likely isobaric interferences on Cd isotopes by monitoring the ^{104}Pd, ^{105}Pd, ^{115}In, ^{120}Sn ion beams. This study follows more recent practice (e.g. Lambelet et al., 2013; Xue et al., 2013; Xue et al., 2012) and adopts the ^{113}Cd isotope for analysis instead of ^{110}Cd. Although ^{113}In is a minor isobaric interference, ^{115}In can be easily monitored during analyses using the collector configuration set out in Table 2.2 and applying an interference correction for ^{113}In to the data in a similar fashion to the correction for Sn.

Table 2.2. Collector configuration for Cd isotope analyses and relevant isobaric and molecular interferences

Mass	106	107	108	109	110	111	112	113	114	115	116	117
Collectors monitored						L4	L3	L2	Ax	H2		H5
Cd isotopes monitored						^{111}Cd	^{112}Cd	^{113}Cd	^{114}Cd			
Isobaric interferences monitored										^{115}In		^{117}Sn
										^{115}Sn		
Double spike isotopes						^{111}Cd		^{113}Cd				
Isotope abundances (%):												
Cd	1.25		0.89		12.5	12.8	24.1	12.2	28.7		7.49	
Isobaric nuclides (%):												
Pd	27.3		26.5		11.7							
Ag		51.8		48.2								
In								4.3		95.7		
Sn							0.97		0.65	0.36	14.5	7.68
Major molecular interferences:												
$M^{40}Ar^+$	^{66}Zn	^{67}Zn	^{68}Zn	^{69}Ga	^{70}Ge	^{71}Ga	^{72}Ge	^{73}Ge	^{74}Ge	^{75}As	^{76}Ge	^{77}Se
					^{70}Zn						^{76}Se	
$M^{16}O^+$	^{90}Zr	^{91}Zr	^{92}Zr	^{93}Nb	^{94}Zr	^{95}Mo	^{96}Zr	^{97}Mo	^{98}Mo	^{99}Ru	^{100}Mo	^{101}Ru
			^{92}Mo		^{94}Mo		^{96}Mo		^{98}Ru		^{100}Ru	
							^{96}Ru					

In practice, adjustments for the In and Sn interferences are very minor (typically <1 ppm for In and <100 ppm for Sn) as the three stage ion exchange and extraction chromatography is designed to remove these elements from the sample (Table 2.1). Thus, the

four Cd isotopes measured during mass spectrometry are ^{111}Cd, ^{112}Cd, ^{113}Cd and ^{114}Cd and the double spike isotopes are ^{111}Cd and ^{113}Cd.

2.6.2 Double spike optimisation, preparation and calibration

The ^{111}Cd – ^{113}Cd double spike used in this study was prepared from concentrated single spike ^{111}Cd (15.73 μg/g) and ^{113}Cd (35.667 μg/g) solutions previously prepared from the digestion of pure single isotope Cd metal in 2 M HNO_3.

The composition of the double spike itself is a major control on the precision of data produced using the double spike method, in particular the precision of the most important variable: the natural fractionation between a zero-epsilon standard and the sample, or F_{nat} using the terminology introduced in section 2.5.2 above (Rudge et al., 2009). According to Galer (1999) and Johnson and Beard (1999) who produced geometric solutions for the double spike method, described further in section 2.5.2, the optimal double spike composition is the one which produces the maximum angle of incidence θ between the two planes P_n (red) and P_m (green), and hence best defines the sample-spike mixing line N-M-R, illustrated in Figure 2.1.

Rudge et al. (2009) produced software to calculate optimal double spike compositions which minimise the error propagation on F_{nat}, and using this software have created a 'cocktail list' of double spike compositions (Rudge, 2011) for the thirty-three elements with four or more natural isotopes. Thus, the composition of the ^{111}Cd – ^{113}Cd double spike using the four inversion isotopes ^{111}Cd, ^{112}Cd, ^{113}Cd and ^{114}Cd has been made up using the proportions of single spikes set out in Rudge (2011), as detailed in Table 2.3.

Table 2.3. Cd double spike compositions used in this study measured by mass spectrometry compared to the ideal double spike composition set out in Rudge (2011)

Preparation date:	Ideal Cd double spike composition (Rudge, 2011)	Imperial Cd double spike no. 2 28/11/2009	Imperial Cd double spike no. 3 3/7/2013	Imperial Cd double spike no. 4 8/4/2015
^{111}Cd	60.73%	59.51%	60.94%	61.33%
^{112}Cd	1.67%	1.69%	1.66%	1.67%
^{113}Cd	35.53%	36.73%	35.40%	34.99%
^{114}Cd	1.39%	1.46%	1.39%	1.39%
Cd concentration		100.16 ng/g	100.59 ng/g	101.23 ng/g

Using this optimum double spike composition and an overall Cd concentration of 100 ng/g as target values for a double spike solution, a simple mixing calculation was employed

to determine the proportions of single spikes required. The spikes were weighed individually and mixed with a predetermined volume of 2 M HCl, which was allowed to equilibrate fully for 10 days with occasional agitation and ultrasonication.

Double spike calibration was achieved using procedures previously described by Ripperger and Rehkämper (2007). The isotope composition of the double spike was measured using external normalisation to Ag which was achieved by first measuring a mixed solution of 40 ppb NIST SRM 3108 Cd and 20 ppb Alfa Aesar Specpure Ag with the collector configurations in Table 2.4. The isotopes ^{111}Cd to ^{114}Cd were measured with Ag normalisation for eight repeated runs with a washout after every run using the collector configuration set out in the top section of Table 2.4. An additional sequence was added to every alternate run using the collector configuration in the lower section of Table 2.4 in order to monitor masses 115 and 118, enabling corrections to be made for isobaric interferences of In on ^{113}Cd and Sn on ^{112}Cd and ^{114}Cd.

Table 2.4. Collector configuration for Cd double spike isotope composition calibration runs

Mass	107	108	109	110	111	112	113	114	115	116	117	118
Ag normalisation run:												
Collectors monitored	L4	L3	L2	Ax	H2	H4	H5	H6				
Cd and Ag isotopes	^{107}Ag		^{109}Ag	^{110}Cd	^{111}Cd	^{112}Cd	^{113}Cd	^{114}Cd				
Interference run:												
Collectors monitored				L5	L4	L3	L2	Ax	H2			H6
Cd isotopes				^{110}Cd	^{111}Cd	^{112}Cd	^{113}Cd	^{114}Cd				
Interferences									^{115}In			^{118}Sn
									^{115}Sn			

The mass bias characteristics determined during the runs of mixed NIST SRM 3108 Cd and Alfa Aesar Ag solutions were then used to correct for mass bias during runs of a mixed solution of 40 ppb Cd double spike and 20 ppb Aesar Specpure Ag, conducted immediately afterwards. A total of 8 to 10 runs of the mixed Cd double spike–Alfa Aesar Ag solution were carried out using the two-sequence Ag normalisation and interference runs detailed in Table 2.4, again ensuring adequate washout after each run to minimise memory effects, particularly due to the relatively high ^{111}Cd and ^{113}Cd ion beams.

The Ag normalisation applied to the double spike measurements uses the exponential (kinetic) law for correction of mass discrimination (Wombacher and Rehkämper, 2003; Young et al., 2002). An appropriate ^{107}Ag/^{109}Ag ratio is determined (Wombacher and Rehkämper, 2003) so that the ^{107}Ag/^{109}Ag normalised ^{110}Cd/^{111}Cd, ^{112}Cd/^{111}Cd, ^{113}Cd/^{111}Cd

and $^{114}Cd/^{111}Cd$ ratios measured during the runs of mixed NIST SRM 3108 Cd and Alfa Aesar Ag solutions produce results which are as close as possible to the same Cd ratios internally normalised to the reference ratio of $^{110}Cd/^{114}Cd$ = 0.438564 (Rosman, 1980; Wombacher et al., 2004). This reference $^{107}Ag/^{109}Ag$ ratio is then deemed to be suitable for the mass bias conditions of the entire session and therefore the same $^{107}Ag/^{109}Ag$ ratio is also applied in the external Ag normalisation of the Cd isotope ratios for the mixed Cd double spike–Alfa Aesar Ag solution.

The calibration sessions described above were repeated and the results of both sessions were averaged or the most precise sessions or results were selected and used to characterise the Cd isotope composition of the standard and double spike, denoted by n and S in the double spike data reduction procedures described in section 2.5.2 on page 34. The results for the three Cd double spikes used for measurements in this study are set out in Table 2.5 below. Note that the uncertainties are relatively large for the $^{111}Cd/^{114}Cd$ and $^{113}Cd/^{114}Cd$ ratios of the double spike. This is due to the rapid build-up of memory on the ^{111}Cd and ^{113}Cd ion beams during the double spike measurements sessions.

Table 2.5. Cd isotope compositions of Cd standards and ^{111}Cd – ^{113}Cd double spikes used in this study. The standards are normalised to a reference ratio of $^{110}Cd/^{114}Cd$ = 0.438564 (Rosman, 1980; Wombacher et al., 2004)

Solution	n	$^{110}Cd/^{114}Cd$	$^{111}Cd/^{114}Cd$	$^{112}Cd/^{114}Cd$	$^{113}Cd/^{114}Cd$
Imperial Cd DS no. 4:					
NIST SRM 3108 Cd	22	0.438564	0.448984 (135)	0.843225 (70)	0.426530 (97)
^{111}Cd – ^{113}Cd double spike	8	0.328414 (115)	44.0737 (412)	1.199680 (341)	25.1481 (221)
Imperial Cd DS no. 3:					
NIST SRM 3108 Cd	16	0.438564	0.448966 (171)	0.843244 (44)	0.426510 (97)
^{111}Cd – ^{113}Cd double spike	16	0.324262 (226)	43.8038 (491)	1.193351 (332)	25.4443 (298)
Imperial Cd DS no. 2:					
Alfa Cd Zürich	17	0.438564	0.448934 (202)	0.843250 (112)	0.426491 (75)
^{111}Cd – ^{113}Cd double spike	9	0.317378 (2086)	40.8168 (12524)	1.155540 (9546)	25.1911 (7224)

After calibration of the isotope compositions of the double spike, it is necessary to determine the concentration of the double spike solution so that it can be used to prepare optimum spike-sample mixtures as described in section 2.5.2.2 above. This is achieved by measuring the isotope composition of a JMC Cd Zürich standard solution admixed with Cd double spike using normal Cd data reduction techniques described in section 2.5.2 above.

The concentration of this dilution of the JMC Cd Zürich standard (6.71378 μg/g) was previously accurately determined gravimetrically and therefore the concentration of the

double spike could be derived using a reverse isotope dilution calculation with the double spike's calibrated isotope composition. Several different solutions were prepared with different spike-sample ratios, in order to provide different leveraging points for the reverse isotope dilution calculation, and the results were averaged.

2.7 Analytical precision

2.7.1 Calculation of analytical uncertainties

Where possible, sample Cd isotope measurements were repeated up to five times across different measurement sessions in order to assess reproducibility and further constrain precision. Table 5.2 indicates the number of analyses carried out for each sample under the heading 'N'. The weighted average of these measurements, and the 2x standard deviation of the weighted average, are calculated to give the Cd isotope composition and associated uncertainty, respectively, for a sample in accordance with the definitions and equations of Taylor (1982), set out below in Eq. 2.5, Eq. 2.6 and Eq. 2.7.

The weighted average of the individual Cd isotope compositions measured for a sample, denoted by x_i, is given by:

$$\bar{x}_{WAV} = \frac{\sum w_i x_i}{\sum w_i} \qquad \text{Eq. 2.5}$$

In Eq. 2.5, the weighting for each measurement, w_i, is calculated as follows from the internal errors for each measurement, expressed as σ in Eq. 2.6:

$$w_i = \frac{1}{{\sigma_i}^2} \qquad \text{Eq. 2.6}$$

The standard deviation of the weighted average statistic calculated in Eq. 2.6, is given by the reciprocal square root of the sum of the weights, w_i, for individual measurements calculated as follows:

$$\sigma_{WAV} = \frac{1}{\sqrt{\sum w_i}} \qquad \text{Eq. 2.7}$$

Where scatter in the isotope compositions of individual measurements for a sample is particularly marked, such that the overall uncertainty calculated using Eq. 2.7 clearly understates the true uncertainty, the 2se value has been increased by a suitable value to reflect this scatter. Horner et al. (2010) used instrumentation similar to that applied here to measure the Cd isotope compositions of ferromanganese crusts and they also reported their uncertainties at the 2se level based on within-run internal errors. However, they issued a caution about the use of this statistic in assessing data quality, remarking that "they often underestimate the true uncertainty" and suggested that the external uncertainty, as given by the 2sd statistic applied to bracketing standards and referred to in section 2.7.4, was a better reflection of reproducibility as suggested by Ripperger and Rehkämper (2007).

In response to this, it was found in this study that the 2sd statistic based on bracketing standards might underestimate reproducibility simply because samples were generally run after bracketing standards had stabilised. The solution offered in this study, explained above, uses the 2se internal errors as a basis for the uncertainties but adjusts the value when multiple measurements of the same sample run in different sessions shows that the 2se statistic underestimates reproducibility.

2.7.2 Use of a secondary isotopic reference material

In order to test the accuracy of analytical and data reduction procedures during a sample measurement session, the BAM-I102 certified isotopic reference material (IRM) solution, manufactured by the Bundesanstalt für Materialforschung und -prüfung, Berlin, Germany, was measured usually at the beginning and end of sample measurement sessions. BAM-I102 has a fractionated isotope composition relative to NIST SRM 3108 Cd (and natural terrestrial materials) and is thus ideal for use as a secondary IRM, rather than as a zero-delta standard in its own right (Abouchami et al., 2013)

The measured BAM-I102 solutions were usually made up to approximately the same concentration and spike-sample ratio as the corresponding samples and NIST SRM 3108 Cd standard solutions. They were subsequently measured as an additional sample, bracketed with measurements of NIST SRM 3108 Cd standard solution in the same way as the samples. The Cd isotope compositions of these measurements are plotted in chronological order in Figure 2.3.

The arithmetic mean of the BAM-I102 measurements is $\varepsilon^{114/110}$Cd = –13.38 (± 0.71 2sd; n = 48), almost identical to the weighted average of BAM-I102 measurements ($\varepsilon^{114/110}$Cd

= –13.32 ± 0.43 2se, n = 179) from seven laboratories in the assay of Cd standard solutions published by Abouchami et al. (2013), as illustrated in Figure 2.3.

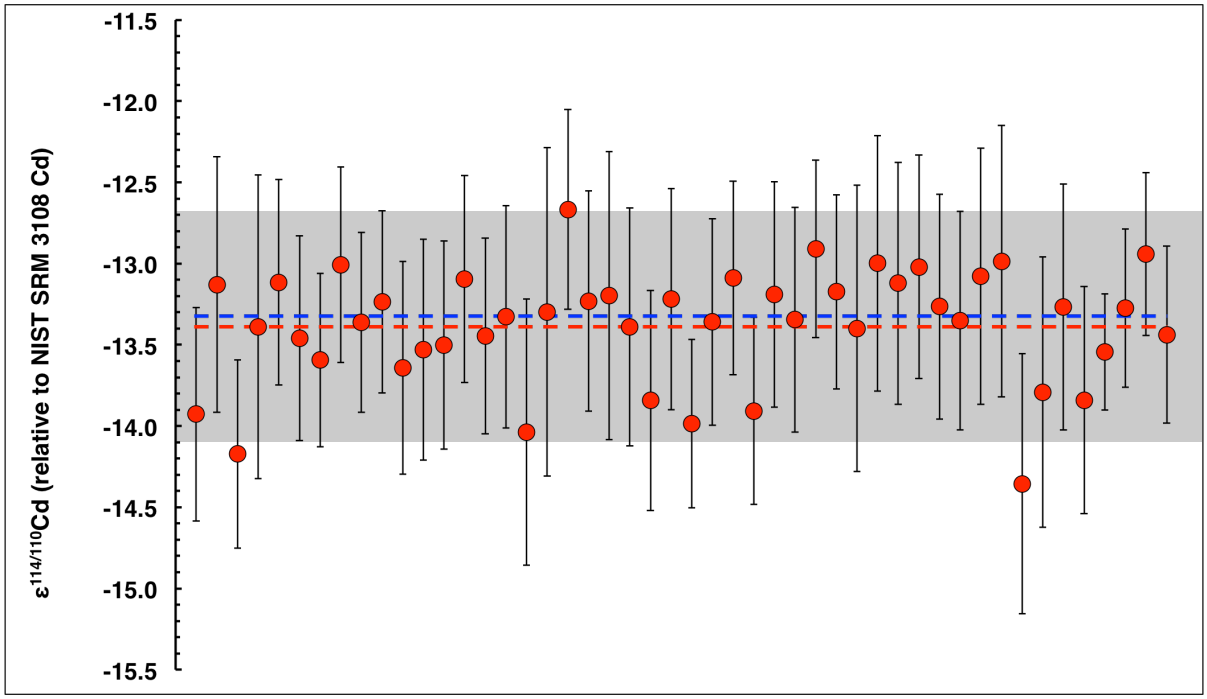


Figure 2.3. Measurements of BAM-I102 Cd certified isotopic reference material in chronological order (April 2013 to June 2015; n = 48) during sample measurements sessions for samples described in Chapter 4 (Cd metal-silicate partitioning experiments) and Chapter 5 (Cd terrestrial and meteoritic samples). Error bars are shown at 2se (internal errors). The horizontal red dashed line indicates the arithmetic mean ($\varepsilon^{114/110}$Cd = –13.38) and the shaded area represents 2sd (±0.71) of these BAM-I102 measurements. The horizontal blue dashed line shows, for comparison, the weighted average ($\varepsilon^{114/110}$Cd = –13.32 ± 0.43 2se, n = 179) of BAM-I102 measurements carried out by the seven laboratories in the assay of Cd standard solutions published by Abouchami et al. (2013). Weighted averages have been calculated using the methods of Taylor (1982).

The overall conclusion from this is that Cd isotope measurements, both in the study of terrestrial and meteoritic samples (Chapter 5) and metal-silicate partitioning experiments (Chapter 4), are reproducible from one measurement session to another and can be readily compared with measurements from other laboratories.

2.7.3 Assessment of analytical precision achieved

Analytical uncertainties for measurements of Cd isotope composition of the samples in this study are based on the internal errors for each sample run on the mass spectrometer. More specifically, they are calculated as twice the standard error of the mean (2se) of the 60 measurement cycles comprising the run. All 60 measurements were used without any

systematic exclusion of any outliers, which can introduce an element of subjectivity into the results obtained for a run.

In order to assess the analytical precision attainable under different mass spectrometer run conditions, the internal (within-run) and external (calculated from bracketed standards) precisions were plotted in Figure 2.4 against the average beam intensity measured on mass 114 during sample runs and the Cd content (natural and double spike) of the sample as diluted in 0.1M HNO_3 for analysis. The plots in Figure 2.4 give some insight into the internal precision attainable for the instrumental set-up used for measurements in this study (see section 2.4.1 above), for comparison with other laboratories.

It is known that higher Cd concentrations in analysed samples tend to yield better measurement precision, although it has been noted that any improvement in analytical precision tails off for Cd concentrations above 60 ppb (Ripperger and Rehkämper, 2007; Xue et al., 2012). The terrestrial and meteoritic samples described in Chapter 5, were mostly diluted to between 50 and 70 ppb total Cd concentration, with lower concentrations than that only in samples with low Cd contents where insufficient material was available for analysis. At concentrations of 50 to 70 ppb, about 35 to 48 ng total Cd (sample and double spike) is consumed during a 6 minute analysis run, assuming a typical sample flow rate of 115 µl/min. This equates to approximately 17 to 23 ng natural Cd per run based on a typical spike-sample ratio of 1.1.

The samples from the metal-silicate partitioning experiments described in Chapter 4 were made up to higher total Cd concentrations of 80 to 100 ppb and during typical analysis runs about 55 to 69 ng total Cd is consumed, or approximately 24 to 30 ng natural Cd, assuming a typical spike sample ratio of 1.3. It is clear from Figure 2.4 that there is considerable scatter in the plots, which provides an indication that, inevitably, factors other than beam intensity or Cd concentration influence precision. Nevertheless, it can be seen from Figure 2.4 charts (c) and (d), that internal precision generally improves with increasing beam intensity or Cd concentration, although the same trend seems to be less evident for external precision.

Also quite noticeable is the difference in internal precision achieved simply by using different desolvation units for sample introduction. The internal precisions of measurements using the Aridus system (Teledyne CETAC Technologies) are generally worse than those produced when using the newer version of this unit, the Aridus II, although the same pattern is not seen for external precision in charts (a) and (b). The difference between the units may result from the older Aridus producing a noisier signal in comparison to the Aridus II.

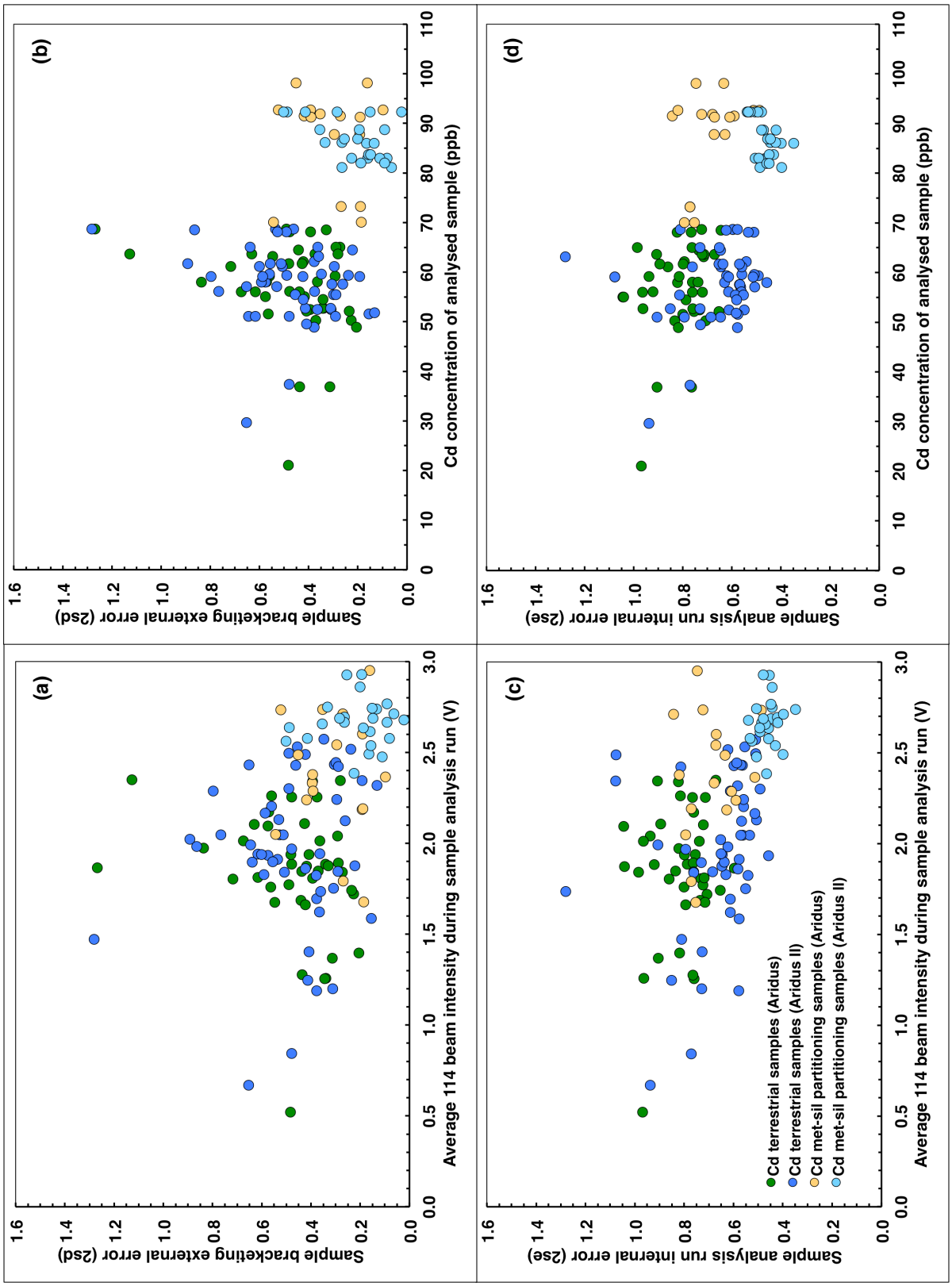


Figure 2.4. The relationship between measured beam intensities (figures a and c) and estimated sample Cd concentrations (figures b and d) and the corresponding Cd isotope composition external and internal errors (in terms of $\varepsilon^{114/110}$Cd units). Cd concentrations comprise natural sample Cd and added Cd double spike with spike-sample ratios in the range 1 – 1.7. Symbols show individual runs for the terrestrial and meteoritic samples surveyed in Chapter 5 and the metal-silicate partitioning samples of Chapter 4, sub-categorised into the different desolvation units used – see section 2.4.1.

The greater scatter seen for external precision may be due to the more subjective nature of this measurement compared to internal precision. The external precision statistic for a sample is calculated from the standard deviation (2sd) of the $\varepsilon^{114/110}$Cd values for associated bracketing standards. If a bracketing standard measurement is clearly imprecise or inaccurate, perhaps due to temporary instrumental instabilities, it is normally excluded from the calculation of the $\varepsilon^{114/110}$Cd value, provided there are no gaps between standard runs and provided at least one standard measurement directly before and after the sample measurement remains. In practice, no fewer than three standard measurements and usually more were used for bracketing. Due to the greater subjectivity inherent in the external error statistic (2sd), the internal error (2se) was used in this study instead to express the precision of the Cd isotope composition for a sample. A further advantage of this approach is that Schmitt et al. (2009b) also use the internal error as a measure of precision in their dataset of Cd isotope compositions of rocks, sulphide minerals and marine deposit, some of which have been used to supplement the terrestrial Cd dataset of Chapter 5, as detailed in Table 5.2.

2.7.4 Comparison with precision attained in other Cd isotope studies

Table 2.6. Internal within-run precision achieved at various sample concentrations compared to within-day precision achieved previously in other studies.

Total Cd concentration (sample + spike) (ppb)	This study: samples and standards					Ripperger and Rehkämper (2007)	Xue et al. (2012)
	Internal errors (within-run)			Average spike-sample ratio	Natural Cd consumed per run (ng)	Within-day (2sd) ($\varepsilon^{114/110}$Cd units)	Within-day (2sd) ($\varepsilon^{114/110}$Cd units)
	2se (in $\varepsilon^{114/110}$Cd units)						
	Range	Average	N			Range	Range
1	n.a.	n.a.	n.a.	n.a.	n.a.		~5
2	*2.3 – 5.3*	*4.1*	*15*	*1.12*	*~0.7*		
3	*1.8 – 4.5*	*2.9*	*85*	*1.23*	*~0.9*		~2 – 3
4	*2.3 – 3.2*	*2.8*	*11*	*1.11*	*~1.3*		
5	*1.5 – 4.2*	*2.3*	*47*	*0.93*	*~1.8*		
10	*1.0 – 2.1*	*1.4*	*41*	*1.09*	*~3.3*	~2 – 4	
20	*0.7 – 1.2*	*0.9*	*27*	*0.92*	*~7.2*	~1.2 – 2.8	1.0 – 1.4
30	*0.7 – 1.0*	*0.9*	*18*	*1.04*	*~10*	~0.7 – 2.1	
40	n.a.	n.a.	n.a.	n.a.	n.a.	0.5 – 1.5	0.5 – 0.8
50	0.6 – 1.0	0.7	21	1.14	~16	~1.0	
60	0.4 – 1.5	0.7	577	1.13	~19		0.4 – 0.7
80	0.3 – 1.1	0.6	172	1.28	~24		
90	0.4 – 0.8	0.6	20	1.29	~27		
120	n.a.	n.a.	n.a.	n.a.	n.a.		0.4 – 0.7

Range and average values of 2se internal errors at for samples and associated standards are drawn from the metal-silicate partitioning dataset (Chapter 4) and the Cd terrestrial dataset (Chapter 5). 'N' refers to the number of individual measurements in the subset for a particular concentration and 'n.a.' indicates there were no samples in this study for the Cd concentration shown. Low concentration measurements shown in italics are taken from concentration check runs (see sections 2.5.2.3 and 2.5.2.4). Natural Cd consumed per analysis run is calculated from the spike-sample ratio shown, and assumes a sample uptake rate of 115 µl/min and total measurement time of 6 minutes.

A compilation of internal within-run precision data (2se of the $\varepsilon^{114/110}$Cd values for the 60 cycles for each run) for the Cd metal-silicate partitioning samples of Chapter 4 and the Cd terrestrial and meteoritic samples of Chapter 5 is shown in Table 2.6 above. Particularly evident from this data, are the same trends seen in Figure 2.4, whereby precision improves with Cd concentration. The internal errors shown for this study are similar to published within-day reproducibilities (2sd) from two other studies which use similar instrumental set-ups, although it is acknowledged that a direct comparison between the "within-run" and "within-day" statistics cannot made. Nevertheless, this evidence does support the use of internal errors as a basis for estimating measurement uncertainties in this study.

For a more direct comparison between this study and the other two studies cited in Table 2.6, a survey of precision (2sd) for NIST SRM 3108 Cd stable and bracketed standards for individual sample analysis sessions for the same samples is set out in Table 2.7 below.

Table 2.7. Precision achieved for stable NIST SRM 3108 Cd runs at various Cd concentrations during individual analytical sessions compared within-day precision in other studies

Total Cd concentration (sample + spike) (ppb)	This study: stable and bracketed standards					Ripperger and Rehkämper (2007)	Xue et al. (2012)
	Within-session			Average spike-sample ratio	Natural Cd consumed per run (ng)	Within-day (2sd) (in $\varepsilon^{114/110}$Cd units)	Within-day (2sd) (in $\varepsilon^{114/110}$Cd units)
	2sd (in $\varepsilon^{114/110}$Cd units)						
	Range	Average	N			Range	Range
5-9		~2	19 (2)	1.02	~2 – 3		
10	n.a.	n.a.	n.a.	n.a.	n.a.	~2 – 4	
20	n.a.	n.a.	n.a.	n.a.	n.a.	~1.2 – 2.8	1.0 – 1.4
30	0.6 – 0.8	0.7	15 (2)	1.40	~9	~0.7 – 2.1	
40	n.a.	n.a.	n.a.	n.a.	n.a.	0.5 – 1.5	0.5 – 0.8
50	n.a.	n.a.	n.a.	n.a.	n.a.	~1.0	
60	0.5 – 1.6	0.8	572 (37)	1.15	~19		0.4 – 0.7
80	0.3 – 1.0	0.5	172 (11)	1.30	~24		

Within-day 2sd values for consecutive stable NIST SRM 3108 Cd runs (including bracketed standards before and after sample analyses) during analysis sessions for the same samples covered by **Table 2.6**. 'N' refers to the number of individual measurements of standards in the subset for a particular concentration with the number of analysis sessions shown in brackets. Natural Cd consumed per analysis run calculated as in **Table 2.6**. 'n.a.' indicates there were no samples in this study for the Cd concentration shown.

From this it is possible to conclude that the precisions achieved in this study are in line with those achieved by Ripperger and Rehkämper (2007) and Xue et al. (2012). Both used the same type of instrument (Nu Plasma MC-ICP-MS, large capacity rotary pump 80 L/min) and same double spike technique as in this study (see sections 2.4.1 and 2.5.2).

2.7.5 Organic residues from ion exchange and extraction chromatography

Organic contaminants, thought to be derived from resins, or coatings leached from resins during chemical separation, have been attributed by some workers to anomalous and

inaccurate Cd isotope measurements during MC-ICP-MS analyses. Although the double spike method adopted in this study will correct for all instrumental mass dependent fractionation (sections 2.5.1 and 2.5.2 above), anomalous analytical artefacts of this type are not corrected for (Gault-Ringold and Stirling, 2012; Murphy et al., 2015).

A procedure adopted in this study to address this problem was to oxidise organic contaminants prior to analysis by refluxing the final purified Cd eluate from column chemistry in 500 µl 15 M HNO_3 for about 3 days at a high temperature, up to 170 °C. Although some workers have reported that this method removed the organic residues (Shiel et al., 2009), others contend that the instabilities still remain after such chemical treatment (Murphy et al., 2015)

Therefore, the main strategy adopted in this study to address the problem was to dilute the samples, and hence organic residue content, sufficiently to render any destabilising effects insignificant. Murphy et al. (2015) reported that increasing dilution of the solution for Cd isotope analysis reduced adverse analytical effects attributed to the presence of organic residues from the Eichrom® TRU® resin (Table 2.1 on page 28) and that these effects were insignificant with dilutions of 3 ml or more.

This approach was a very simple matter for the Cd metal-silicate partitioning samples of Chapter 4 since these samples had very high Cd concentrations compared to terrestrial samples (up to 1.8 wt%) and required aliquoting and dilution to reduce concentrations to manageable levels (see section 4.2.2.5 on page 106). Therefore most of these samples were diluted in 15 to 47 ml 0.1 M HNO_3 for analysis. Two silicate samples had relatively low concentrations due to volatilisation of Cd and low recovery of silicate material but were still diluted to about 3 ml 0.1 M HNO_3 for analysis.

Turning to the terrestrial and meteoritic samples of Chapter 5, in most cases it was possible to digest sufficient sample to enable dilution in 3 to 19 ml 0.1 M HNO_3. One mid-ocean ridge basalt (MORB) and two olivine samples were diluted in only 1ml 0.1 M HNO_3 for analysis. The MORB sample, however, was part of a large suite of MORBs that were analysed and both olivine samples were analysed twice as separate dilutions (of 1 ml each). Significant anomalous isotopic shifts were not detected in the results for these few low concentration samples diluted in 1ml 0.1 M HNO_3, when compared to the anomalous isotopic offset of $\varepsilon^{114/110}Cd = 4.6 \pm 3.4$ for a zero-epsilon reference material reported by Murphy et al. (2015).

2.8 Conclusions

The analytical techniques described in this Chapter have been applied to the precise and accurate determination of Cd isotope compositions for the terrestrial and meteoritic samples with relatively low Cd contents of Chapters 3 and 5 and the Cd-rich samples from the metal-silicate partitioning experiments of Chapter 4. Any procedures specific to a particular sample set, such as digestion protocols, are described in the analytical methods section of the relevant chapter. The mass spectrometry, double spike preparation, data reduction and chemical separation techniques used in these studies are based on the pioneering work of Wombacher et al. (2003) and Ripperger and Rehkämper (2007) for the analysis of Cd isotope compositions as well as Galer (1999) and Siebert et al. (2001) for the application of the double spike method.

This study uses an ε-notation to report Cd isotope compositions and ε-data are referenced to the now widely adopted zero-epsilon standard NIST SRM 3108 Cd (Abouchami et al., 2013). Isotopic variations are thereby reported for the $^{114}Cd/^{110}Cd$ ratio that is also used by most other workers, as it has a relatively large mass difference and avoids low natural abundance isotopes. The double spike method applied in this study employs a ^{111}Cd – ^{113}Cd double spike with a composition designed to minimise error propagation, when geometric and numerical methods are used to derive the natural sample isotope composition (Galer, 1999; Rudge et al., 2009; Siebert et al., 2001). Accordingly, masses 111 to 114 are monitored during mass spectrometer runs to cover the isotopes ^{111}Cd, ^{112}Cd, ^{113}Cd, and ^{114}Cd, together with masses 115 and 117, which are used to monitor minor isobaric interferences from Sn and In. Chemical separation and purification are designed to remove most of the Sn and In from sample solutions and the offline data reduction procedure then corrects for the presence of any small residual amounts of these elements.

Emphasis has been placed in this study on the monitoring and maintenance of data quality. Examples of this include the following. Firstly, a secondary Cd isotope reference material with a well-defined isotopic offset was used to monitor the accuracy of measurements. Secondly, the spike-sample ratios and Cd concentrations of zero-epsilon standards were carefully matched to the samples that are being bracketed. Thirdly, the most suitable Cd concentrations for sample analyses were selected to optimise precision whilst minimising the build-up of instrumental memory.

Also essential to maintaining data quality are the strict clean room laboratory procedures and rigorous labware cleaning protocols employed to keep contaminants to a minimum in all stages of sample preparation for mass spectrometry. The very low blank levels that are reported for Cd in sections 3.4.5 and 4.2.2.7 and 5.2.2.2, attest to the success of these procedures.

The potential problem of matrix effects, arising for samples solutions containing small amounts of organic material leached from the resins used in the chemical separation of Cd, was addressed primarily by ensuring that the solutions employed for the isotope analyses were adequately diluted, whilst maintaining sufficient Cd concentrations to ensure precise measurements.

The internal error (2se) of each run was used in this study to express the uncertainty attached to a Cd stable isotope measurement, instead of the external error statistic (2sd), as calculated from repeated measurements of bracketing matching standards. A disadvantage of the latter approach is that 2sd values can change, depending on the number of matching standards used in the calculation. However, the internal 2se statistics can underestimate the true uncertainty of a sample analysis. Therefore, in this study, account is taken of the spread of results obtained for multiple runs of a sample, to ensure that the quoted uncertainties for a single run are in accord with data obtained for multiple measurements of a sample.

Overall, the precision obtained for the Cd isotope measurements in this study, both in terms of the internal within-run errors (Table 2.6) and the external errors determined from multiple standard analyses in a measurements session (Table 2.7), is comparable to that achieved by other workers (Ripperger and Rehkämper, 2007; Xue et al., 2012) using similar instrumental and analytical techniques.

Chapter 3 Variable Tl, Pb and Cd concentrations and isotope compositions in enstatite and ordinary chondrites

3.1 Introduction

3.1.1 The extinct ^{205}Pb – ^{205}Tl radionuclide system

3.1.1.1 Astrophysical context

^{205}Pb is produced purely by the s-process (slow neutron capture) in nucleosynthesis, unlike other short-lived radionuclides which involve other processes in their production (Blake et al., 1973; Burbidge et al., 1957; Yokoi et al., 1985), and decays by electron capture to ^{205}Tl with a half-life of 17.3 Myr (Kondev, 2004). Although Blake and Schramm (1976) suggested that ^{205}Pb might be destroyed if retained in a star long enough at certain temperatures before incorporation into the solar nebula, Yokoi et al. (1985) presented calculations indicating high s-process yields of ^{205}Pb under a wide variety of conditions, enhancing the possibility for finding evidence of extinct ^{205}Pb in astromaterials. That ^{205}Pb is unique amongst short-lived radionuclides in being only produced by the s-process, enhances its usefulness as a method for identifying sources of materials injected into the nascent solar system with calculations indicating significant surface enrichment of ^{205}Pb in 3 $M_{\odot}$ Asymptotic Giant Branch stars at their advanced stage (Mowlavi, 1998) and possibly Wolf-Rayet stars (Arnould et al., 2000; Arnould et al., 1997).

3.1.1.2 Usefulness as a high resolution chronometer

Aside from the ability of ^{205}Pb to provide constraints on the late injection of s-process material into the solar nebula, the ^{205}Pb – ^{205}Tl system has the potential to provide relative age information on early solar system processes that change Pb/Tl ratios. Since Pb and Tl have different volatilities, with a 50% T_C of 727 K and 532 K respectively at 10^{-4} bar (Lodders, 2003), the ^{205}Pb – ^{205}Tl chronometer has the potential to provide useful information on the timing of volatile loss from thermal processing or shock in the solar nebula or on planetesimals. Furthermore, under the probable conditions of Earth's core formation, Pb is moderately siderophile, Tl is only weakly siderophile and both metals have similar chalcophile affinities (Wood et al., 2008) indicating that the ^{205}Pb – ^{205}Tl chronometer could also provide insight on the timing of planetary differentiation and core crystallisation.

3.1.1.3 Early work on ^{205}Pb

The search for ^{205}Pb in chondrites and iron meteorites started with the work of Anders and Stevens (1960) and Ostic et al. (1969), at a time when only two other extinct natural radionuclides were known (^{129}I and ^{244}Pu), and continued with the work of Huey and Kohman (1972) on lunar soils and chondrites and Arden (1983) on Allende matrix separates. Unfortunately, these workers had only limited success and found that these astromaterials had $^{205}Tl/^{203}Tl$ ratios indistinguishable from terrestrial values within error. Rehkämper et al. (2002) observed two things concerning this. Firstly, Tl has only two naturally-occurring isotopes, ^{203}Tl and ^{205}Tl, with a mass difference of only 1%, thus any changes in isotope composition due to stable isotope fractionation are likely to be small. Secondly, early studies of Tl isotopes, such as those mentioned above, used thermal ionisation mass spectrometry (TIMS), which, was simply unable to resolve permil variations in Tl isotope ratios.

Chen and Wasserburg (1987) directed the search at two iron meteorites chosen from their previous work (Chen and Wasserburg, 1983) for their high abundance of primordial Pb allowing easier monitoring of terrestrial contamination. They reported a slight but reproducible isotopic shift in $^{205}Tl/^{203}Tl$ for the sulphide in one of the iron meteorites (Type IIICD Nantan).

They also noted that measuring $^{205}Tl/^{203}Tl$ was problematic due to mass-dependant fractionation during analysis in the mass spectrometer resulting in enrichment of the heavier isotope over time. In addition, Wombacher et al. (2008) commented that fractionation of highly volatile elements could frustrate attempts to analyse short-lived radionuclides with a volatile daughter element which had only had two stable isotopes, such as with the ^{205}Pb – ^{205}Tl and ^{107}Pd – ^{107}Ag decay systems. In such cases, they argued, an isotopic shift due to in situ decay of the parent isotope might not be distinguishable from isotopic shifts due to kinetic evaporation and condensation.

3.1.1.4 Recent work

The advent of multiple-collector inductively coupled plasma mass spectrometry (MC-ICP-MS), which, unlike TIMS, is able to resolve small variations in isotope ratios of ‘heavy’ elements such as Tl (Rehkämper et al., 2001), provided a new impetus in the search for Tl isotope variation in meteorites.

Nielsen et al. (2006a) used this technique to analyse metal and troilite in type IAB, IIAB and IIIAB iron meteorites, chosen for their large variations in Pb/Tl, enhancing the

prospect of detecting Tl isotope variations from in situ decay of ^{205}Pb. From this data, they were able to construct an isochron for the IAB meteorites, despite stable isotope fractionation of Tl in some troilite samples thought to be the result of diffusion, together with a potential isochron for the IIIAB group. This lead to the conclusion that the isochrons represented the in situ decay of ^{205}Pb, thus demonstrating the existence of 'live' ^{205}Pb in the early solar system. However, due to the lack of a simultaneous 'long-lived' radiogenic chronometer they were unable to link the isochron for the short-lived ^{205}Pb – ^{205}Tl system to an absolute timescale, therefore their calculation of the initial solar system abundance of ^{205}Pb remained uncertain.

Since the short-lived ^{205}Pb – ^{205}Tl chronometer provides high resolution but relative age data, linking these relative ages to an absolute timescale is desirable to enable application of the ^{205}Pb – ^{205}Tl system as a chronometer of early solar system events. This link was first established by Baker et al. (2010) who found a strong correlation between Tl isotope composition and ^{204}Pb/^{203}Tl in a suite of carbonaceous chondrites. This isochron was interpreted as recording volatile fractionation in the early solar nebula at close to 4,567 Ma and defined the initial ^{205}Pb abundance of the solar system as $^{205}Pb/^{204}Pb_{SS,0} = (1.0 \pm 0.4) \times 10^{-3}$.

In dealing with terrestrial Pb contamination of meteorites, a common problem particularly in meteorite 'finds', they noted that whilst most samples plotted on a linear trend of ^{206}Pb/^{204}Pb against Tl concentrations due to the link between volatile depletion of Tl and higher U/Pb ratios, some samples plotted above this line. They attributed these abnormally radiogenic Pb isotope compositions to terrestrial contamination (Göpel et al., 1985) and were able to use mass balance calculations to correct for this (Baker et al., 2010 supplement).

Baker et al. (2010) recognised that the variability of Tl isotope composition in carbonaceous chondrites might be caused by stable isotope fractionation possibly in the solar nebula or during accretion, differentiation or metamorphism on the meteorite parent bodies or even as a result of terrestrial weathering. They referred to a previous study by Wombacher et al. (2008) who found that the isotope compositions of Cd, which is almost as volatile as Tl, were readily affected by volatilisation processes. Thus, in their study, Baker et al. (2010) used Cd isotope compositions of the carbonaceous chondrites to determine which samples had Tl compositions altered by secondary processes (evidenced by elevated Cd isotope fractionation) and excluded these samples from the isochron along with a heavily Pb contaminated sample.

Further evidence for radiogenic variations in Tl isotope compositions were provided by Andreasen et al. (2012) in their study of IIAB and IIIAB iron meteorites. Notably, these

authors also re-evaluated the carbonaceous chondrite isochron of Baker et al. (2010) in the light of their iron meteorite results and concluded that some of the data that were originally applied in the isochron calculations were questionable due to Pb contamination, despite the above-mentioned correction for terrestrial Pb contamination. Following elimination of possibly questionable results, they determined a revised carbonaceous chondrite isochron, which provided a higher initial solar system $^{205}Pb/^{204}Pb_{SS,0}$ of $(2 \pm 1) \times 10^{-3}$.

This study applies the techniques of Baker et al. (2010) in an investigation of whether Tl variations in bulk rock samples of EL and EH enstatite chondrites and L and LL ordinary chondrites derive from in situ decay of ^{205}Pb. Additional Pb isotope analyses were carried out on all samples to extract absolute age data and determine whether the samples had been contaminated by terrestrial Pb. Cadmium isotope analyses were also performed on the suite of enstatite chondrites to determine the extent of Tl and Cd stable isotope fractionation resulting from mobilisation of these labile elements during thermal and shock metamorphism on the meteorite parent body (Lipschutz and Woolum, 1988).

3.2 Samples

3.2.1 Enstatite chondrites

The enstatite chondrites are a rare group of chondrites, with only 274 classified samples compared to 1,387 carbonaceous chondrites and 42,650 ordinary chondrites (Krot et al., 2014). Consequently they are one of the least studied groups of meteorites.

The enstatite chondrites consist mainly of FeO-poor pyroxene (enstatite $MgSiO_3$) with metal, sulphides and other minerals, some of which are unusual, formed under highly reducing conditions in the early solar system (e.g. Brearley and Jones, 1998; Franchi, 2008; Keil, 1989; Krot et al., 2014).

A total of nine enstatite chondrites were analysed in this study covering the main petrological types (Table 3.4): six samples from the low Fe content EL3 and EL6 groups, two of which are falls, and three samples from the high Fe content EH4 and EH5 groups, all of which are falls.

3.2.2 Ordinary chondrites

A total of 20 ordinary chondrites were analysed, again spanning the main petrological groups, and comprising 10 ordinary chondrites from the groups L3.7 to L6, which have low

iron content, and 10 ordinary chondrites from the groups LL3.1 to LL6, which not only have low iron content, but also low metallic iron content. All of the ordinary chondrite samples in this study are falls, which minimises the exposure of the meteorite to terrestrial weathering, a possible source of Pb contamination – a critical factor in this study.

3.3 Analytical approach

The three most recent ^{205}Pb – ^{205}Tl isochron studies referred to in section 3.1.1.4 above highlighted that two particular problems beset the application of this decay system to early solar system chronology.

Firstly, Tl shows significant variability in isotope compositions within some terrestrial environments (Coggon et al., 2014; Nielsen et al., 2006c; Rehkämper et al., 2004; Rehkämper et al., 2002), although, despite these localised variations, the overall Tl isotope composition in most natural Earth environments is near to the bulk silicate Earth value of ε^{205}Tl = –2 (Nielsen and Rehkämper, 2012; Nielsen et al., 2007; Nielsen et al., 2006b; Nielsen et al., 2005; Nielsen et al., 2006c). Since small differences in thermodynamic properties between isotopes of the same element result in fractionation but such effects generally diminish with elements of increasing atomic weight (Urey, 1947), the extent of variability in natural Tl isotope compositions is surprising, considering its relatively high atomic weight.

Schauble (2007) conducted first principles calculations suggesting that equilibrium Tl isotope fractionation is dominated by mass-independent nuclear volume, or nuclear field shift effects instead of mass-dependent effects determined by bond vibrational frequencies, which predominantly control fractionation in lighter elements (Wasylenki, 2012). More specifically, nuclear field shift effects involve changes in the *distribution* of nuclear charge for a given number of protons in the nucleus resulting from differing numbers of neutrons, i.e. different isotopes (Bigeleisen, 1996; Fujii et al., 2009). Moreover, Fujii et al. (2013) demonstrated this theory experimentally by investigating Tl isotope fractionation in a liquid-liquid exchange system in which the nuclear field shift effect was calculated to be >1‰ in Tl(I) – Tl(III) redox reactions and Tl(III) ligand exchanges.

Since Tl has only two stable isotopes, ^{203}Tl and ^{205}Tl, it is not possible to differentiate between stable isotope fractionation, including the mass-independent effects discussed above, and the radiogenic ingrowth of ^{205}Tl from the decay of formerly live ^{205}Pb. Furthermore, stable isotope fractionation of Tl during nebular and parent body processes is enhanced by its highly volatile and labile nature (Lipschutz and Woolum, 1988), and evidence for such effects

have been found in carbonaceous chondrites by Baker et al. (2010). These authors tackled this problem by employing stable isotope measurements of Cd, an element slightly less volatile than Tl (Lodders, 2003) and also known to readily display stable isotope effects from volatilisation and mobilisation (Rehkämper et al., 2011; Wombacher et al., 2008), to monitor such effects. Such analyses are also applied to the enstatite chondrites in this study whilst previous work has already shown that Cd stable isotope fractionations are very common but not ubiquitous in ordinary chondrites (Wombacher et al., 2008; Wombacher et al., 2003).

Secondly, both stony and iron meteorites, including observed falls, are known to be pervasively contaminated by modern terrestrial Pb. Such contamination has an impact on ^{205}Pb – ^{205}Tl chronology because it may be difficult or even impossible to recover the original 'meteoritic' $^{204}Pb/^{203}Tl$ ratios needed for the successful construction of an isochron. Lead contamination can be detected and even corrected for using Pb isotope analyses, for example in the iron meteorite study of Nielsen et al. (2006a), but corrections for such effects can be problematic if contamination is severe or the original 'meteoritic' composition is not precisely defined, or both.

The effects of Pb contamination can be mitigated but not completely eliminated in the case of iron meteorites by aggressive leaching with aqua regia (Nielsen et al., 2006a), however such an approach was not attempted with the chondrite samples in this study for two reasons. Firstly, samples were small, about 1.5 to 2 g, and aggressive leaching removes too much of the outer layers of the sample most affected by Pb contamination. Secondly, other elements of interest in this study, Tl and Cd, are highly labile (Lipschutz and Woolum, 1988) and likely to be lost or isotopically fractionated by leaching acids (Zhang et al., 2016), particularly since chondrite samples are more friable and porous than iron meteorites.

In this study, the correction of measured $^{204}Pb/^{203}Tl$ ratios in samples affected by terrestrial Pb contamination requires knowledge of 'pristine meteoritic' Pb isotope compositions of those samples. Accordingly, Pb isotope measurements were carried out on all samples in this study in order to assess terrestrial Pb contamination and attempts were made to correct for Pb contamination in accordance with the method of Baker et al. (2010) – supplementary material, in which primordial Pb isotope compositions of uncontaminated meteorites from the same class as the contaminated meteorite were used as a proxy.

3.4 Analytical methods

3.4.1 Reagents and laboratory procedures

A full description of reagents and laboratory procedures used in this study is set out in section 2.2 starting on page 26, except that there are two major differences.

Firstly, although hotplate digestion was carried out inside a Class 10 laminar flow hood, standard household hotplates were used with the heated surfaces covered in aluminium foil, instead of the laboratory Teflon®-coated hotplates later used for the digestion of samples described in Chapter 5. It is thought that the hotplates used for the digestion of samples in this study might have contributed to the level of Pb procedural blanks (section 3.4.5 below). The Teflon®-coated hotplates were, however, used for all refluxing and drying down of samples solutions after their digestion.

Secondly, meteorite preparation, cleaning and crushing were carried out in a dedicated meteorite clean room at the Natural History Museum, London. All other critical work on samples, apart from weighing, was carried out in Class 10 laminar flow hoods within the Class 1000 MAGIC clean room facility at Imperial College London using ultrapure reagents and water.

3.4.2 Sample preparation and digestion

3.4.2.1 Meteorite crushing

All meteorite samples were received as small rock chips from the collection at the Natural History Museum, London, apart from Indarch and Daniel's Kuil, which had already been powdered, and apart from EL6 chondrite NWA 3134, which was purchased from a collector.

The meteorite chips were initially prepared by carefully sanding down sawn surfaces and labels with silicon carbide paper, after which they were cleaned in distilled ethanol in an ultrasonic bath and dried in a Class 10 laminar flow hood. The meteorite chips were crushed and ground gently to a fine powder with a cleaned alumina pestle and mortar using an aluminium foil wrap around the mortar to prevent sample spillage. The alumina pestle and mortar was cleaned thoroughly prior to use on each sample by grinding acid-washed high-purity quartz sand in the mortar wetted with distilled ethanol and flushing away ground particles with 18.2 MΩ.cm grade Milli-Q® water and distilled ethanol.

Approximately 1.5 to 2 g of meteorite powder was transferred to 60 ml Savillex® PFA (perfluoroalkoxy) vials, which had been acid-cleaned, refluxed and dried using the procedures detailed in section 2.2 on page 26. The vials were weighed accurately with and without the samples in a dedicated weighing room within the Class 1000 clean room facility using a Mettler Toledo AX250 DeltaRange® analytical balance reading to the nearest 0.01 mg (0.1 mg above 82 g).

3.4.2.2 Acid digestion

The acid digestion steps for these meteorites are similar to those used for terrestrial silicate samples as detailed in section 5.2.1.3 on page 138, except that the general approach for the potentially more reactive meteorite powders was to leave the samples in acid at room temperature for a few days prior to heating on a hotplate.

For the initial silicate digestion, 5 ml 15 M HNO_3 (2.5 to 3.3 ml acid per g sample) was gradually added to the sample powders in the PFA vials after which up to 6 to 7 ml 28 M HF (3 to 4.4 ml/g sample) was gradually added. After a few days at room temperature, the mixture was heated on a hotplate for two days and dried down.

The second and third acid digestion steps involved the addition of 5 to 10 ml 6 M HNO_3 and 6 M HCl respectively (2.5 to 6.7 ml/g sample), and leaving the sample for a few days at room temperature. The vials were heated for 2 days for the HNO_3 step and agitated in an ultrasonic bath without heating for the HCl step.

The sample digests were centrifuged in acid-cleaned 15 ml polypropylene centrifuge tubes and any residue transferred to PFA vials and subjected to a second round of acid digestion using the same three steps described above but using approximately half the volume of acid in the HF – HNO_3 step and 5 ml acid in each of the 6 M HNO_3 and 6 M HCl steps.

3.4.3 Isotope dilution and double spike methods for determining Pb, Tl and Cd concentrations

The following aliquots were taken from the digested and centrifuged sample solutions in 6 M HCl. Firstly a 2.5% (all aliquots in % w/w except where noted) aliquot was taken for Pb and Tl isotope dilution (ID) chemistry and mass spectrometry. Secondly, a 5% reserve aliquot for some of the samples was taken for further ID work, if necessary. Finally, a 1% aliquot was taken for Cd ID chemistry and mass spectrometry. The remaining 91.5% (96.5%

for samples without the 5% reserve aliquot) of the solutions was reserved for isotope composition (IC) measurements.

3.4.3.1 Pb and Tl ID procedures

This aliquot was spiked with about 48 to 56 µl single isotope ^{208}Pb (1002.0221 ng/g) and ^{203}Tl (10.2654 ng/g) tracer solutions with accurate weights recorded for both the aliquot itself and the tracer solution. All work with the single isotope spikes was carried out in a separate clean room laboratory to the one used for processing the aliquots for IC measurements to avoid any cross-contamination of the IC aliquot with the spikes.

In order to produce separate eluates of Pb and Tl free from matrix elements for analysis, the spike aliquot was evaporated to dryness and taken up in 1 ml 0.2 HBr – 1%Br_2, after which it was passed through the same anion exchange elution sequence used by Baker et al. (2009) for their ID aliquots. The purpose of adding Br_2 in the form of saturated $Br_2 – H_2O$, which oxidises the Tl in solution to its trivalent form, is explained fully in section 3.4.4.1 below.

3.4.3.2 Pb and Tl ID mass spectrometry

The Pb and Tl eluates were evaporated to dryness and, after refluxing with a drop of 15 M HNO_3 and drying down again, the Pb aliquot was taken up in 1 ml 0.1 M HNO_3 and the Tl aliquot 1ml 0.1 M HNO_3 – 0.1% H_2SO_4 for mass spectrometry. A small aliquot of 5% (v/v) was taken from each solution and analysed to check ion beam intensities: this is particularly important for the Pb aliquot since potentially large Pb abundances from terrestrial contamination might saturate collectors on the mass spectrometer. The remainder of the Pb solutions were diluted so to produce a ^{208}Pb beam intensity of about 7 V, whereas the Tl solutions required no dilution due to low Tl abundances.

The ID analyses were carried out using an Nu Plasma HR multiple-collector inductively coupled plasma mass spectrometer (MC-ICP-MS) described more fully in section 2.4.1 on page 29. Mass bias correction for the Pb ID analyses used the $^{205}Tl/^{203}Tl$ ratio of admixed NIST SRM 997 Tl solution. However, a similar approach was not possible for the Tl aliquots since they were likely to contain residual Pb preventing the use of $^{208}Pb/^{206}Pb$ from admixed NIST SRM 981 Pb as a means of mass bias correction. To overcome this problem, Nielsen et al. (2004) doped the ID samples with Pt as well as NIST SRM 981Pb, monitoring the $^{208}Pb/^{206}Pb$ and $^{198}Pt/^{196}Pt$ ratios independently to correct for mass bias. The same

approach was adopted in this study by adding 50 ng Pt–β standard to the aliquot, which was increased to 100 ng when instrumental sensitivity was low.

3.4.3.3 Cd ID procedures

This aliquot was spiked with about 0.5 ng ^{113}Cd – ^{111}Cd double spike, with accurate weights recorded for both the aliquot itself and the double spike, and thereafter evaporated to dryness before being taken up in 500 µl 3 M HCl. The sample was then passed through just the second stage anion exchange chemistry for Cd separation set out in Table 2.1 on page 28, which, without a further stage of separation using TRU® resin, normally left a significant amount of Sn in the aliquot. Since the purpose of these Cd ID measurements was to obtain a reasonable estimate of Cd abundance to determine the optimum Cd double spike to add to the IC aliquot, it was not deemed necessary at this stage to remove this isobaric interference.

3.4.3.4 Cd ID mass spectrometry

The Cd eluate was dried down and, after refluxing with a drop of 15 M HNO_3 and drying down again, was taken up in 1 ml 0.1 M HNO_3 for mass spectrometry. The Cd abundances were simply calculated from the beam intensities measured using the Cd double spike data reduction procedures described in section 2.5.2 on page 34 with one notable exception. Normally Cd ID calculations using the double spike method are performed using the measured ratios $^{111}Cd/^{114}Cd$ and $^{112}Cd/^{114}Cd$. However, the offline data reduction spreadsheets were reworked to enable the calculations to be performed using the measured ratios $^{111}Cd/^{110}Cd$ and $^{114}Cd/^{110}Cd$ in order in order to minimise the effect of the Sn isobaric interferences on ^{112}Cd and ^{114}Cd (see Table 2.2 on page 39). The isobaric interference of Pd on ^{110}Cd would have been largely eliminated during chemistry since Pd is retained on the resin during Cd elution (see Table 2.1).

3.4.4 Separation and purification of Pb, Tl and Cd

3.4.4.1 Anion exchange separation of Pb, Tl and Cd

The key objective of the chemical separation of the enstatite chondrite samples is to obtain separate fractions of the elements Pb, Tl, and Cd free from matrix elements present in samples, particularly isobaric or molecular interferences, sufficiently pure for accurate and precise measurements of isotope compositions.

Separation and purification of these elements has previously been achieved by Baker et al. (2010) in their study of the Pb, Tl, and Cd isotope compositions of carbonaceous chondrites. They used a first stage anion exchange chemistry producing separately eluted fractions of Pb, Tl, and Cd which were then purified using a further 'clean-up' stage of anion exchange chemistry. A third stage of extraction chromatography was required for Cd to remove significant isobaric interference elements.

The first stage chemistry of Baker et al. (2010) required the sample to be dissolved in 0.1 M HCl for loading onto the resin column. Using this eluent, Pb is eluted immediately upon loading the sample along with matrix elements such as Al, alkali metals, alkaline earth metals, rare earth elements, and many transition metals such as Ti, Mn, Fe and Ni (Kraus and Nelson, 1956). There are several possible disadvantages centred on using 0.1 M HCl as the loading acid. Firstly, the low acid molarity may result in incomplete dissolution of the samples and, secondly, elution of Pb along with the bulk of the matrix elements present in meteorites places heavy reliance on the second 'clean-up' stage to produce a pure matrix-free fraction of Pb for analysis.

Thus the first stage anion exchange chemistry used in this study was broadly based on the separation procedures of Baker et al. (2010) but, instead, allowed for some elution of major matrix elements to take place before collection of combined Pb – Cd and Tl fractions, as shown in Table 3.1 below. In addition, the sample is dissolved in 1 M HCl (+2% Br_2 – H_2O) for loading onto the resin column, instead of in 0.1 M HCl. This improves sample dissolution and results in the elution of matrix elements without the elution of Pb, which has a distribution coefficient of more than 10 for the 1 M HCl eluent (Korkisch, 1989; Trémillon, 1965).

A feature of this anion exchange chemistry, and that of Baker et al. (2010), is the addition of a 'holding oxidant' in the form of saturated bromine water (Br_2 – H_2O) to the sample solution and to all elution stages prior to the elution of Tl. This ensures that all Tl present in sample solutions is oxidised to its trivalent form, Tl(III), and held in that form on the resin bed until reduction and subsequent elution. Trivalent Tl is adsorbed onto strongly basic anion exchange resin from HCl and HBr solutions and has a moderately high distribution coefficient (~10) in aqueous HNO_3. The elution of Tl from the resin bed is effected using 0.1 M HCl with ~5% dissolved SO_2 (w/w) as eluent. This reduces Tl(III) to its monovalent form, Tl(I), which is only slightly adsorbed (Andersen and Knutsen, 1962; Faris and Buchanan, 1964; Korkisch, 1989; Kraus and Nelson, 1956; Trémillon, 1965).

The saturated Br_2 – H_2O oxidant was prepared by equilibrating ~5 ml cleaned bromine (99.998% Alfa-Aesar®) in 100 ml Milli-Q in accordance with the method of Rehkämper and Halliday (1999). Before use, the Br_2 – H_2O preparation was agitated to ensure proper equilibration and saturation of the water with bromine, as the two phases separate when left to stand. The reductant 0.1 M HCl – 5% SO_2 (w/w) was prepared by bubbling SO_2 gas from a pressurized cylinder of liquid SO_2 (Sigma-Aldrich Corporation) through a Teflon® bottle containing a sufficient volume of 0.1 M HCl for the chemistry, and monitoring the weight of the solution until the weight had increased by about 5%, as described by Rehkämper and Halliday (1999). The 0.1 M HCl – 5% SO_2 solutions were always prepared fresh on the day before use.

Table 3.1. First stage anion exchange chemistry for the separation of Tl and combined Pb – Cd fractions.

First stage anion exchange chemistry	**Elution stages**
1 ml Bio-Rad AG® 1-X8 resin *200 – 400 mesh* *50 ml quartz glass columns*	
18 ml 2 M HNO_3	Resin cleaning (Cd, Pb eluted)
2 ml Milli-Q H_2O	
18 ml 0.1 M HCl – 5% SO_2 (w/w)	Resin cleaning (Tl eluted)
11 ml 0.1 M HCl	Conversion of resin to Cl^- form
4 ml 1 M HCl – 2% Br_2 (v/v)	Column equilibration
Sample in 20 – 25 ml 1 M HCl – 2% Br_2	Sample loading, matrix elution
10ml 0.03 M HBr – 0.5 M HNO_3 – 1% Br_2	Pb – Cd fraction collected
20 ml 0.03 M HBr – 1 M HNO_3 – 1% Br_2	Pb – Cd fraction collected (matrix elements also eluted)
10 ml 0.01 M HCl – 1% Br_2	Pb – Cd fraction collected (matrix elements eluted, Zn, In, Mo)
15 ml 0.1 M HCl – 5% SO_2	Tl eluate collection

For an explanation of the addition of the oxidant Br_2 and reductant SO_2 to eluents see text below. The elution characteristics of the various elements indicated, including matrix elements, have been determined from published distribution coefficients for the following eluents and using Bio-Rad® AG 1-X8 or similar strongly basic anion exchange resins: HNO_3 (Faris and Buchanan, 1964); HCl (Korkisch, 1989; Kraus and Nelson, 1956; Trémillon, 1965); and HBr – HNO_3 mixtures (Strelow, 1978).

Tests on the anion exchange chemistry of Table 3.1 indicated that Cd was being eluted during the 0.03 M HBr – 0.5 M HNO_3 – 1% Br_2 (about 25 to 40%), and 0.03 M HBr – 1 M HNO_3 – 1% Br_2 stages (about 60 to 75%), but not during sample loading in 1 M HCl – 2% Br_2. This elution is not expected based on published distribution coefficients (Strelow, 1978) and there are a number of possible reasons for this unexpected behaviour. Firstly, the Br_2 itself may have been adsorbed onto the resin thus reducing the capacity of the resin bed to

adsorb elements such as Cd (Korkisch, 1989). This is unlikely, however, as very low concentrations of Br_2 – H_2O were used and no loss of Cd was observed during the sample loading stage. Secondly, the addition of bromine may also have affected the performance of the resin in other unknown ways resulting in selective loss of Cd. Thirdly, the distribution coefficient of Cd may not be high enough (at 14.4) during the 0.03 M HBr – 1M HNO_3 elution stage, resulting in partial elution of Cd. Furthermore, the distribution coefficient of Cd is fairly sensitive to changes in the acid molarities in the HBr – HNO_3 mixtures. In particular, a slight reduction in HBr molarity, or increase in HNO_3 molarity, will lead to a decrease in the Cd distribution coefficient (Strelow, 1978).

Table 3.2. Second stage anion exchange chemistry for the separation of Pb and Cd

Second stage anion exchange chemistry (Pb – Cd separation)	
1 ml Bio-Rad AG® 1-X8 resin *200–400 mesh* *50 ml quartz glass columns*	
10 ml 2 M HNO_3	Resin cleaning (Cd, Pb eluted)
0.5 ml Milli-Q H_2O	
20 ml 6 M HCl	Resin cleaning (Pb eluted) and conversion of resin to Cl^- form
7 ml 0.2 M HBr	Column equilibration
Sample in 20 – 25 ml 0.2 M HBr	Sample loading (Pb – Cd fraction from first stage), matrix elution
6 ml 0.2 M HBr – 0.5 M HNO_3	Matrix elution, incl In, Zn
3 ml 0.03 M HBr – 0.5 M HNO_3	Matrix elution, incl. In, Zn
8 ml 0.03 M HBr – 0.5 M HNO_3	Pb eluate collection
10 ml 0.5 M HCl	Matrix elution incl. In, Mo
5 ml 2 M HCl	Matrix elution
10 ml 6 M HCl	Matrix elution incl. Ag
1 ml 2 M HNO_3	Column equilibration
10 ml 2 M HNO_3	Cd eluate collection
	(Remaining Sn Mo, In, Zn also eluted, Pd retained on resin)

The elution characteristics of the various elements indicated, including matrix elements, have been determined from published distribution coefficients for HNO_3, HCl and HBr – HNO_3 mixtures using Bio-Rad® AG 1-X8 or similar strongly basic anion exchange resins detailed in the caption to **Table 3.1** above. In addition, the elution characteristics of HBr have been taken from Andersen and Knutsen (1962) and Marsh et al. (1978).

Consequently, the matrix elution stages were collected as a combined Pb – Cd fraction, as shown in Table 3.1 for further separation and purification in a second stage as set out in Table 3.2. Once separate fractions of Pb, Tl and Cd are obtained, a further clean-up anion exchange chemistry stage is required for Tl, as shown in Table 3.3 below. This employs

the same principle, described above, whereby Br_2 – H_2O is added to act as a holding oxidant to maintain Tl in the strongly resin-adsorbed trivalent form during matrix elution.

Further purification of Cd is achieved by using the second stage anion exchange chemistry and third stage extraction chromatography set out in Table 2.1, and described more fully in section 2.1 on page 26. The Pb fraction from the second stage Pb – Cd separation in Table 3.2 has undergone two stages of matrix removal and therefore requires no further purification.

Table 3.3. Second stage anion exchange chemistry for further purification of the Tl fraction.

Second stage anion exchange chemistry (Tl clean-up)	
100 µl Bio-Rad AG® 1-X8 resin *200–400 mesh* *Small PTFE columns*	
3.1 ml 0.1 M HCl – 5% SO_2	Resin cleaning (Tl eluted)
3.1 ml 6 M HCl	Resin cleaning (Pb eluted) and conversion of resin to Cl^- form
0.4 ml 6 M HCl – 2% Br_2	Column equilibration
Sample in 0.5 to 1 ml HCl – 2% Br_2	Sample loading (Tl fraction from first stage), matrix elution
3.1 ml 6 M HCl – 2% Br_2	Matrix elution
0.5 ml 12 M HCl – 2% Br_2	Matrix elution, incl. Pb
3.1 ml 0.01 M HCl – 2% Br_2	Matrix elution, incl. Pb
1.6 ml 0.1 M HCl – 5% SO_2	Tl eluate collection

The elution characteristics of HCl are derived from published distribution coefficients detailed in the captions to **Table 3.1**.

3.4.5 Procedural blanks

Generally, one acid blank for every six samples was processed through digestion and chemical separation. After chemical separation, the blanks collected along with Pb, Tl and Cd eluates from chemistry were dissolved in 1ml 0.1 M HNO_3 (Pb and Cd) and 0.1 M HNO_3 – 0.1% H_2SO_4 (Tl) and analysed on the mass spectrometer by scanning masses appropriate for each element and generally using the ion-counting multiplier.

For the enstatite chondrite samples, the accumulated procedural blanks averaged 5 pg for Tl and 50 pg for Cd which had a negligible effect on the concentrations of those elements. However, Pb blanks varied between 900 pg and 2800 pg, probably attributable mostly to the use of standard metal household hotplates for drying down and refluxing during digestion compared to laboratory Teflon®-coated hotplates which were used during chemistry and mass spectrometry. The USGS rock standard AGV-2, analysed alongside the enstatite chondrites (Table 3.4 below), was, however, digested on the Teflon®-coated hotplates and the

corresponding Pb blanks averaged only 90 pg. The blanks for Tl and Cd were also considerably lower: about 2 pg and 22 pg, respectively.

The influence of the high Pb blanks on Pb concentrations was limited since the Pb and Tl concentrations were based on isotope dilution analyses of 2% (v/v) aliquots of the digested solutions. Therefore, on the basis that most of the Pb and Tl blanks arose during digestion, only a small portion of the blank (75 ± 50 pg for Pb and 0.3 ± 0.2 pg for Tl) needed to be factored into the calculations of Pb and Tl concentrations and $^{204}Pb/^{203}Tl$ ratios.

It is clear that Tl and Cd blanks have had a negligible effect on the isotope compositions of those elements. However, the Pb blanks have likely contributed to the Pb isotope compositions of some low Pb content samples, which may have been skewed towards a more terrestrial Pb composition. A full assessment of the terrestrial Pb content of samples and the effect on isotope composition is set out in the discussion in section 3.5.2 below.

3.4.6 Mass spectrometry

All isotope measurements were carried out using a Nu Plasma HR MC-ICP-MS (Nu Instruments, part of the Ametek, Inc. Materials Analysis Division) at the Imperial College London MAGIC laboratory facility. Desolvating nebulisers were used to introduce sample solutions in 0.1 M HNO_3 and 0.1 M HNO_3 – 0.1% H_2SO_4 as a dry aerosol into the ICP torch with three different models operated at different times: the DSN-100 (Nu Instruments), the Aridus and the Aridus II (Teledyne CETAC Technologies). Both glass and PFA nebulisers were used with a sample uptake rate generally in the range 100 – 130 µl/min. Further details of how the instrument was set-up are contained in section 2.4.1 on page 29.

All sample Pb, Tl and Cd fractions purified using chemical separation as described in section 3.4.4.1 above were evaporated to dryness and, after refluxing with about 2 to 3 drops of 15 M HNO_3 and drying down again, were taken up in 1ml 0.1 M HNO_3 (Pb and Cd fractions) or 1ml 0.1 M HNO_3 – 0.1% H_2SO_4 (Tl fractions) for mass spectrometry. The reason for the different acid matrix for the Tl fractions is that the elution of Tl with the reductant SO_2 results in this fraction having some H_2SO_4 content which cannot be driven off by drying down the sample due to the relatively high boiling point of H_2SO_4 (~340 °C).

Prior to the Tl and Pb IC analyses, an aliquot of 2% (v/v) to determine Tl and Pb concentrations was analysed to allow for correct admixing of standards for mass spectrometry. The aliquots were doped with 10 ppb NIST SRM 960 U solution and, in order to determine the concentrations of Tl and Pb, the beam intensities for ^{205}Tl and ^{208}Pb were

measured, for *both* the Tl and Pb fractions, and normalised to the beam intensity for ^{238}U in order to correct for fluctuations in sensitivity during the measurement session.

The concentration data was primarily used to prepare solutions for IC analysis: Pb fractions were admixed with NIST SRM 997 Tl solution to produce known $^{205}Tl/^{204}Pb$ ratios and Pb concentrations. Admixed NIST SRM 981 Pb and 997 Tl solutions were made up with the same $^{205}Tl/^{204}Pb$ ratios and Pb concentrations for sample standard bracketing. Similarly for Tl fractions, sample solutions were admixed with NIST SRM 981 Pb to produce known $^{208}Pb/^{205}Tl$ ratios and Tl concentrations and admixed standards made up with the same characteristics for bracketing. The Pb content of the Tl fractions was also assessed in order to evaluate the effectiveness of its removal by anion exchange chemistry: any significant Pb content would interfere with mass bias correction with NIST SRM 981 Pb.

The Tl IC measurements themselves followed the procedures of Baker et al. (2009) utilising external normalisation to admixed NIST SRM 981 Pb solution and standard-sample bracketing for mass bias correction. All results are reported in ε-notation as defined by:

$$\varepsilon^{205}\mathrm{Tl} = \left(\frac{(^{205}\mathrm{Tl}/^{203}\mathrm{Tl})_{\mathrm{SAMPLE}}}{(^{205}\mathrm{Tl}/^{203}\mathrm{Tl})_{\mathrm{NIST\ SRM\ 997\ Tl}}} - 1 \right) \times 10{,}000 \qquad \text{Eq. 3.1}$$

The NIST SRM 997 Tl isotope reference solution, characterised by Dunstan et al. (1980) with the value $^{205}Tl/^{203}Tl = 2.38710$, was used as the zero-epsilon $\varepsilon^{205}Tl = 0$ standard for all samples. A Tl standard manufactured by Aldrich with a isotope composition relative to NIST SRM 997 Tl of $\varepsilon^{205}Tl = -0.81 \pm 0.33$ (2sd n=133), according to a compilation by Nielsen and Rehkämper (2012), was used as a secondary isotopic reference standard in each Tl measurement session. The values obtained for this secondary standard averaged –1.15 ± 0.42 (2sd, n=3) which are in accord with the published values.

The Pb IC measurements were conducted using standard-sample bracketing and external normalisation relative to admixed NIST SRM 997 Tl for mass bias correction. The analytical methods were similar to those outlined in Rehkämper and Mezger (2000) and all results are reported relative to the NIST SRM 981 Pb data of Galer and Abouchami (1998).

All Cd isotope compositions are reported using ε-notation as defined by Eq. 2.1 on page 31 and relative to the NIST SRM 3108 Cd zero-epsilon standard described further in section 2.4.2.2 on page 32. The Cd isotope measurements were carried out using broadly the same double spike analytical and data reduction methods described fully in section 2.5 starting on page 33. Briefly, the stages in this process were as follows. The Cd concentration

data obtained from the initial ID procedures described in sections 3.4.3.3 and 3.4.3.4 above were used to calculate the weight of ^{111}Cd – ^{113}Cd double spike to add to the IC aliquot before anion exchange chemistry to achieve a spike-sample ratio of about 1. This was to minimise error propagation in the mass fractionation vector of the sample (F_{nat}) in the double spike method as described more fully in section 2.5.2.2 on page 36.

For most of the enstatite chondrite samples, spike-sample ratios were between 0.9 and 1.1, with one low concentration sample having a ratio of 1.7. One sample had a spike sample ratio of 0.6 due to inaccurate results from the initial concentration check. However, subsequent aliquots of the same sample digestion were run with spike-sample ratios of about 1 and there were no significant differences in the isotope compositions measured at the different spike-sample ratios despite the ratio of 0.6 being sub-optimal (section 2.5.2.2).

An aliquot of 5% (v/v) was taken from the Cd fraction in order to measure Cd concentrations and spike-samples ratios of the samples and yield from chemistry. This data was used to make up solutions for IC analysis to a specific concentration, usually about 60 ppb, and to make up NIST SRM 3108 Cd standard solutions to match the concentrations and spike-sample ratios. This ensures that beam intensities are broadly similar for samples and bracketed standards to minimise systematic errors (Wombacher et al., 2003).

3.5 Results and discussion

3.5.1 Tl, Pb and Cd concentrations

Table 3.4 below summarises the Tl, Pb and Cd concentrations and isotope compositions of the enstatite and ordinary chondrites analysed in this study. The Tl, Pb and Cd contents are briefly discussed in this section, with a more detailed discussion of Tl and Cd contents in the context of shock and thermal metamorphism in section 3.5.5 on page 87.

Overall, the enstatite and ordinary chondrites display greater variability in Pb and Tl contents than the carbonaceous chondrites of groups CI, CM, CO, CR and CV analysed by Baker et al. (2010). These workers did not publish the Cd content of their samples but previous studies indicate that the Cd content of these carbonaceous chondrite groups typically vary between 300 and 690 ng/g for the CI, CM, CV and CR groups, although the CO group has an anomalously low average Cd content of 8 ng/g (Lodders and Fegley, 1998).

Table 3.4. Tl, Pb and Cd concentrations and isotope compositions of enstatite and ordinary chondrites

Sample name	Class	Fall/ Find	Year	Location	Shock	Tl ng/g	2sd ng/g	Pb ng/g	2sd ng/g	Cd ng/g	2sd ng/g	204Pb/ 203Tl	2sd	ε^{205}Tl	2sd	$\varepsilon^{114/110}$Cd	2sd	206Pb/ 204Pb	2se	207Pb/ 204Pb	2se	208Pb/ 204Pb	2se
																	(b)						
EH chondrites																							
Abee	EH4	Fall	1952	Canada	S2-S4	73.2	1.5	2,497	50	857	17	2.16	0.01	-3.3	1.0	2.9	0.5	10.336	0.001	10.972	0.001	30.481	0.001
Indarch	EH4	Fall	1891	Azerbaijan	S3	104	2	31,528	631	659	13	13.9	0.1	-2.7	0.5	4.2	0.5	18.137	0.001	15.143	0.001	38.076	0.002
St Marks	EH5	Fall	1903	S Africa	S3	3.78	0.08	205	5	12.5	0.7	2.63	0.07	0.8	0.5	9.7	1.0	16.625	0.001	14.794	0.001	36.424	0.002
EL chondrites																							
MAC 02839	EL3	Find	2002	Antarctica	S3 (a)	44.5	0.9	1,653	33	286	6	2.44	0.01	-1.3	0.5	7.6	0.6	9.584	0.001	10.480	0.001	29.765	0.001
PCA 91020	EL3	Find	1991	Antarctica	S5	36.7	0.7	1,234	25	486	10	2.21	0.01	22.2	0.5	72.9	0.6	9.609	0.001	10.496	0.001	29.842	0.001
Atlanta	EL6	Find	1938	USA	S2	1.60	0.03	469	9	5.65	0.70	13.6	0.1	-1.8	0.5	10.4	1.3	17.868	0.001	15.320	0.001	38.028	0.003
Daniel's Kuil	EL6	Fall	1868	S Africa	S2	8.58	0.17	7,978	160	4.85	0.97	42.4	0.1										
Khairpur	EL6	Fall	1873	Pakistan	S2	5.78	0.12	251	5	21.7	1.0	2.67	0.04	-1.0	0.5	65.7	0.9	10.976	0.001	11.339	0.001	31.364	0.002
NWA 3134	EL6	Find	2004	Morocco		0.756	0.015	47	7	1.76	0.86	1.88	0.26	-1.4	0.5	6.9	2.1	28.085	0.002	21.977	0.002	52.917	0.004
L chondrites																							
Mezö-Madaras	L3.7	Fall	1852	Romania	S3	25.6	0.5	617	12	7.0	0.7	1.48	0.21	-1.0	0.3			11.292	0.001	11.518	0.001	31.313	0.001
Saratov	L4	Fall	1918	Russia	S2-S3	0.45	0.01	81	2	1.8	0.2	6.7	0.9	1.0	0.8			25.530	0.001	20.426	0.001	44.199	0.001
Tennasilm	L4	Fall	1872	Estonia	S2-S3	4.84	0.10	484	10	6.6	0.7	5.3	0.7	-21.3	0.5			14.616	0.001	13.555	0.001	34.643	0.001
Ausson	L5	Fall	1858	France	S3	1.55	0.03	4,850	97	4.9	0.5	144	20	-4.2	0.5			18.415	0.001	15.703	0.001	38.456	0.001
Alfianello	L6	Fall	1883	Italy	S5	19.2	0.4	1,645	33			4.1	0.6	-2.1	0.5			17.15	0.01	15.72	0.01	36.97	0.01
New Concord	L6	Fall	1860	USA	S4	0.35	0.01	597	12			76.3	10.7	-9.9	0.9			19.60	0.01	16.42	0.01	39.67	0.01
Mocs 54773	L6	Fall	1882	Romania	S3	0.10	0.002	59	1	0.4	0.04	15.6	2.2					41.616	0.001	30.012	0.001	58.962	0.001
Mocs 54647	L6	Fall	1882	Romania	S3	0.11	0.002	55	1	0.4	0.04	13.7	1.9	0.3	5.9			39.190	0.001	28.432	0.001	59.271	0.001
Barwell	L6	Fall	1965	England	S3	0.15	0.003	100	2	0.52	0.05	24.8	3.5	-3.9	1.1			26.449	0.001	21.223	0.001	45.830	0.001
Marion (Iowa)	L6	Fall	1847	USA		0.49	0.01	21,598	432	0.7	0.07	2,030	284	-2.6	0.6			18.379	0.001	15.640	0.001	38.405	0.001
LL chondrites																							
Bishunpur	LL3.1	Fall	1895	India	S2	19.1	0.4	1,239	25	291	29	3.3	0.5	-7.5	0.5			15.435	0.001	13.996	0.001	35.458	0.001
Parnallee	LL3.6	Fall	1857	India	S3	0.56	0.01	265	5	1.4	0.1	28.1	3.9	7.1	1.6			11.85	0.01	11.93	0.01	31.95	0.01
Benares	LL4	Fall	1798	India		0.57	0.01	1,899	38	1.4	0.1	152	21	-2.7	1.7			18.21	0.01	15.76	0.01	38.77	0.01
Soko-Banja	LL4	Fall	1877	Serbia		1.28	0.03	564	11	3.6	0.4	24.9	3.5	2.7	0.5			13.057	0.001	12.608	0.001	33.108	0.001
Khanpur	LL5	Fall	1932	India		1.50	0.03	656	13	16	2	20	3	-6.0	0.6			18.752	0.001	16.375	0.001	38.223	0.001
Olivenza	LL5	Fall	1924	Spain	S3	16.0	0.3	486	10	40	4	1.71	0.24	14.9	0.4			13.17	0.01	12.62	0.01	33.18	0.01
Tuxtuac	LL5	Fall	1975	Mexico	S2	18.5	0.4	267	5	6.9	0.7	0.66	0.09	-12.5	0.3			18.089	0.001	15.465	0.001	38.870	0.001
Appley Bridge	LL6	Fall	1914	England	S3	0.38	0.01	714	14	0.84	0.08	90.2	12.6	0.1	2.8			17.37	0.01	15.25	0.01	37.21	0.01
Dhurmsala	LL6	Fall	1860	India	S3	0.34	0.01	694	14	11	1	90.1	12.6	-10.9	0.6			19.411	0.001	16.344	0.001	39.317	0.001
Mangwendi	LL6	Fall	1934	Zimbabwe		10.8	0.2	503	10	3.1	0.3	2.35	0.33	-1.4	0.4			15.87	0.01	14.58	0.01	35.80	0.01
Terrestrial																							
AGV-2				USGS						67.7	2.3			-2.4	0.5	1.5	0.8	18.867	0.001	15.622	0.001	38.551	0.004
AGV-2 - literature values				USGS						66.6 (c)				-1.9 (d)	0.5	1.1 (c)	1.1	18.864-		15.609-		38.501-	
														-3.0 (e)	0.6			18.874 (g)		15.621 (g)		38.552 (g)	
														-2.7 (f)	0.4								

Notes: (a) MAC 02839 and MAC 02837 are paired (NASA Johnson Space Centre, 2004); (b) Estimated from internal 2se uncertainties of runs (typically similar to 2sd of multiple standard runs) using a minimum value of 0.5. Literature values: (c) Wiggenhauser et al. (2016); (d) Baker et al. (2009); (e) Prytulak et al. (2013); (f) Hettmann et al. (2014); (g) selected values from GeoReM database v.19 accessed 13 May 2016 (Jochum et al., 2005). Shock stages from Bennett and McSween (1996); Friedrich et al. (2004); Gattacceca et al. (2005); Izawa et al. (2011); Rubin (1994); Rubin (2004); Rubin et al. (1997); Stöffler et al. (1991)

The enstatite chondrites and ordinary chondrites analysed in this study also display greater variability in Cd content. The higher variability of Tl, Pb and Cd contents in enstatite and ordinary chondrites in comparison to the main carbonaceous chondrite groups is confirmed by literature data, although this is normally only available for individual samples with only scarce high quality paired analyses of Tl, Pb and Cd contents for meteorites in these groups.

3.5.1.1 Enstatite chondrites

The Tl concentrations of the enstatite chondrites vary by more than two orders of magnitude from less than 1 ng/g to more than 100 ng/g (Table 3.4, Figure 3.1 (a) and (b)). The Cd contents of these meteorites are even more variable with concentrations from about 1.8 ng/g to nearly 860 ng/g. Similar systematics seem to be controlling the concentrations of both elements. First, the analysed EH and EL chondrites display a similar range of concentrations for both elements. Second, the less metamorphosed group of each clan (EH4 and EL3) generally has higher Tl and Cd contents compared to the more strongly metamorphosed meteorites (EH5 and EL6).

Similar trends are also seen for Pb, with concentrations in the enstatite chondrites ranging from less than 50 ng/g to more than 31,000 ng/g, and the less metamorphosed EH4/EL3 samples generally displaying higher Pb contents than the most equilibrated samples of groups EH5 and EL6. However, the EL6 Daniel's Kuil has a higher Pb content (of about 8 μg/g) than the two analysed EL3 samples (with <1.7 μg/g Pb), whilst the EH4 Indarch has an unusually high Pb abundance of more than 31 μg/g.

These latter observations may be due to significant contamination of the meteorites with terrestrial Pb, even though they were documented falls and would thus have probably avoided significant weathering. In particular, such contamination is expected to be far more severe for Pb than for Tl, Cd and other elements since Pb contamination is far more pervasive in the environment than Tl or Cd, largely contributed by tetraethyl lead antiknock additives in petrol from the 1920's to the 1970's and non-ferrous metal production (e.g. Falahi-Ardakani, 1984; Nriagu, 1990; Nriagu and Pacyna, 1988; Pacyna and Pacyna, 2001; Wolff and Peel, 1985).

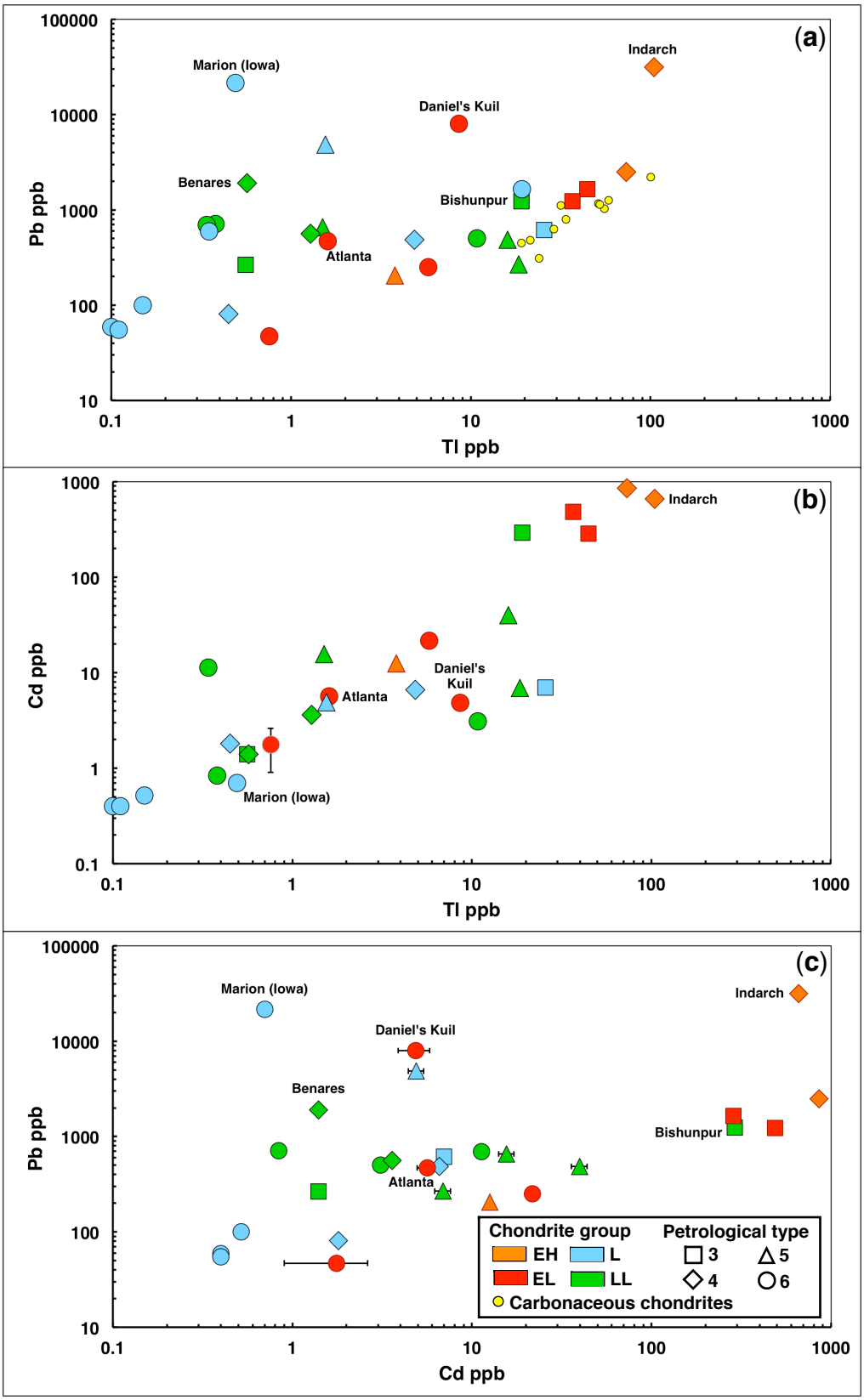


Figure 3.1. Plots of (a) Pb v Tl, (b) Cd v Tl and (c) Pb v Cd concentrations for enstatite chondrites and ordinary chondrites analysed in this study. Data for carbonaceous chondrites from Baker et al. (2010) shown for comparison. Logarithmic scaling has been used on both axes for all plots to encompass highly variable concentration data. Errors bars at the 2sd level are shown except when smaller than the symbols.

Furthermore, the combined enstatite chondrite dataset reveals rather well correlated Cd and Tl concentrations (R^2 = 0.83; Figure 3.1 (b)) with a mean Cd/Tl ratio of about 8. The plots of Pb content versus Tl and Cd reveal that all but three of the samples are in accord with strongly correlated behaviour between these elements with regression coefficients of R^2 = 0.99 and 0.88 for the Pb versus Tl and Cd trends, respectively. This correlation suggests that these elements are possibly concentrated in similar phases in these meteorites. The same Pb contaminated samples Indarch and Daniel's Kuil, together with the EL6 chondrite Atlanta, are clearly offset from these correlations in both plots, most likely as a result of recent terrestrial Pb contamination.

3.5.1.2 Ordinary L chondrites

The range of Tl and Cd contents for the L chondrites is similar to the enstatite chondrites (Table 3.4, Figure 3.1). Specifically, the Tl content varies by just over two orders of magnitude, namely from about 0.1 to 26 ng/g, and the Cd content varies from 0.4 to 7 ng/g respectively, just over one order of magnitude. For both elements, the less metamorphosed samples (of types L3 and L4) also tend to have higher concentrations of both elements than the more equilibrated L5 and L6 chondrites.

The Pb concentrations of the L chondrites are similarly highly variable with values from 55 ng/g up to 21,600 ng/g for the L6 Marion (Iowa), which clearly stands out as having an unusually high Pb content (Figure 3.1 (a) and (c)). There is no clear correlation between petrological type and Pb concentration. Rather, it is apparent that the samples with the lowest Tl and Cd contents have the most variable Pb content. Most likely, this reflects that samples with low indigenous volatile contents (as shown by Tl and Cd) are most susceptible to contamination by modern terrestrial Pb. Given these elemental systematics, it is unsurprising that Cd and Tl are somewhat correlated in L chondrites, whilst there is no correlated distribution for Pb with either Tl or Cd in these meteorites.

3.5.1.3 Ordinary LL chondrites

The Tl content of LL chondrites varies by just under two orders of magnitude, between about 0.3 and 19 ng/g, with Cd content varying between about 0.8 and 290 ng/g, just over two orders of magnitude (Table 3.4, Figure 3.1). In contrast to the enstatite chondrites and L chondrites, the LL chondrites show only a trace of a correlation between the Tl and Cd contents with no systematic variation of the concentrations with petrological type.

In comparison to this, the Pb content varies by less than a factor of 10, between about 270 and 1,900 ng/g. No correlation is apparent between the Pb content and either Tl or Cd concentrations. For example, the highest Pb concentrations of about 1,200 and 1,900 ng/g in the LL chondrites Bishunpur and Benares are coupled with the highest and one of the lowest Tl and Cd contents respectively. The apparent random nature of Pb concentrations is most likely due to alteration of the 'meteoritic' Pb budgets by terrestrial contamination.

3.5.2 Pb isotope compositions and evaluation of terrestrial Pb contamination

The samples were not leached prior to dissolution, to prevent the loss of Tl and Cd and the generation of possible isotope fractionations in those labile elements during the leaching process (Zhang et al., 2016). It is therefore not surprising that the concentration data of Figure 3.1 suggest that a number of the enstatite and ordinary chondrites samples are clearly contaminated with significant terrestrial Pb. This conclusion is reinforced by an evaluation of the Pb isotope data in this section.

Attempts were made to correct for terrestrial Pb contamination of the enstatite chondrites using the methods outlined in the supplement of Baker et al. (2010). Based on these calculations, three enstatite chondrites had significant Pb contamination: St Marks (EH5) had a molar fraction of primitive Pb of only 12.2%, for Indarch (EH4) it was less at 7.6%, and Atlanta (EL6) had just 4.3%. Furthermore, calculated uncertainties, which included uncertainties in the composition of terrestrial Pb and procedural blanks, amounted to more than 40% of the values of absolute Pb contents and $^{204}Pb/^{203}Tl$ ratios. Consequently, it was determined that the corrected values for these three meteorites were not reliable and therefore they were not used, even though the 'corrected' $^{204}Pb/^{203}Tl$ ratios were within the range of values of carbonaceous chondrites.

The plot of $^{207}Pb/^{204}Pb$ versus $^{206}Pb/^{204}Pb$ (Figure 3.2 (a)) for the enstatite and ordinary chondrites of this study demonstrates that the Pb isotope data fall into three broad groups. Firstly, samples with $^{206}Pb/^{204}Pb \leq 13.5$ have primitive or near primitive meteoritic Pb, similar to that seen in the carbonaceous chondrites analysed by Baker et al. (2010). These samples encompass four enstatite chondrites, a single L chondrite, and three LL chondrites. Secondly, four L chondrites and an EL chondrite, NWA 3134, have radiogenic Pb isotope compositions with $^{206}Pb/^{204}Pb \geq 25$. Thirdly, the largest group of samples have intermediate Pb isotope ratios with $^{206}Pb/^{204}Pb$ between 14.5 and 19.5. Whilst such isotope compositions could well reflect indigenous meteoritic Pb produced in meteorites with intermediate μ

($^{238}U/^{204}Pb$), there are several lines of evidence which demonstrate that the majority of samples from this group are pervasively contaminated with modern terrestrial Pb, characterised by $^{206}Pb/^{204}Pb$ of about 16.0 to 19.5 (Göpel et al., 1985). In particular, many of the samples with intermediate, terrestrial-like Pb isotope compositions also feature atypical, elevated Pb concentrations. This includes, for example, the enstatite chondrites Indarch and Atlanta, the L5 and L6 chondrites Ausson, New Concord, and Marion (Iowa), as well as the LL4 to LL6 meteorites Benares, Khanpur, Appley Bridge and Dhurmsala (Figure 3.1).

A diagram of $^{206}Pb/^{204}Pb$ versus $^{204}Pb/^{203}Tl$ is also useful for distinguishing between the components of Pb present in the samples and to help identify contamination effects (Figure 3.2 (b)). This diagram reveals two separate trends of data emanating from near-primordial meteoritic Pb characterised by $^{206}Pb/^{204}Pb$ ratios of between 9.5 and 10.5.

A very steep trend linear toward a composition characterised by $^{206}Pb/^{204}Pb > 40$ and $^{204}Pb/^{203}Tl$ of between about 2 and 20 (blue arrow in Figure 3.2 (b)) appears to reflect ingrowth of radiogenic Pb formed in high-μ environments. In contrast, a shallower curved trend towards $^{206}Pb/^{204}Pb \approx 18$ and high $^{204}Pb/^{203}Tl$ values of >100 (red arrow in Figure 3.2 (b)) likely reflects the addition of terrestrial Pb.

Combining the information from Pb concentrations (Figure 3.1) and isotope compositions (Figure 3.2) results in the suggestion that $^{204}Pb/^{203}Tl$ ratios of greater than 75 are most likely an artefact of terrestrial Pb contamination and are therefore unsuitable for application in isochron diagrams that attempt to exploit the extinct ^{205}Pb – ^{205}Tl decay system for chronology.

The recent study of Baker et al. (2010) also encountered problems with terrestrial Pb contamination, although less severe than in this study in that a smaller proportion of samples were affected (4 out of 11). Furthermore, using simple techniques, these authors were able to estimate the extent of contamination and correct for these effects using mass balance calculations. These showed that two of the four samples were pervasively (60 – 80%) contaminated, and the other two less so (about 10%). These authors excluded one of the less contaminated samples, Allende CV3 Smithsonian, from the isochron, along with two samples, Kainsaz CO3 and Leoville CV3, which exhibited significant Cd isotope fractionation ($\varepsilon^{114/110}Cd > +15$).

The question remains whether the corrections applied by Baker et al. (2010) to the data for the three remaining Pb contaminated carbonaceous chondrite samples are accurate enough for use in constructing a ^{205}Pb – ^{205}Tl isochron.

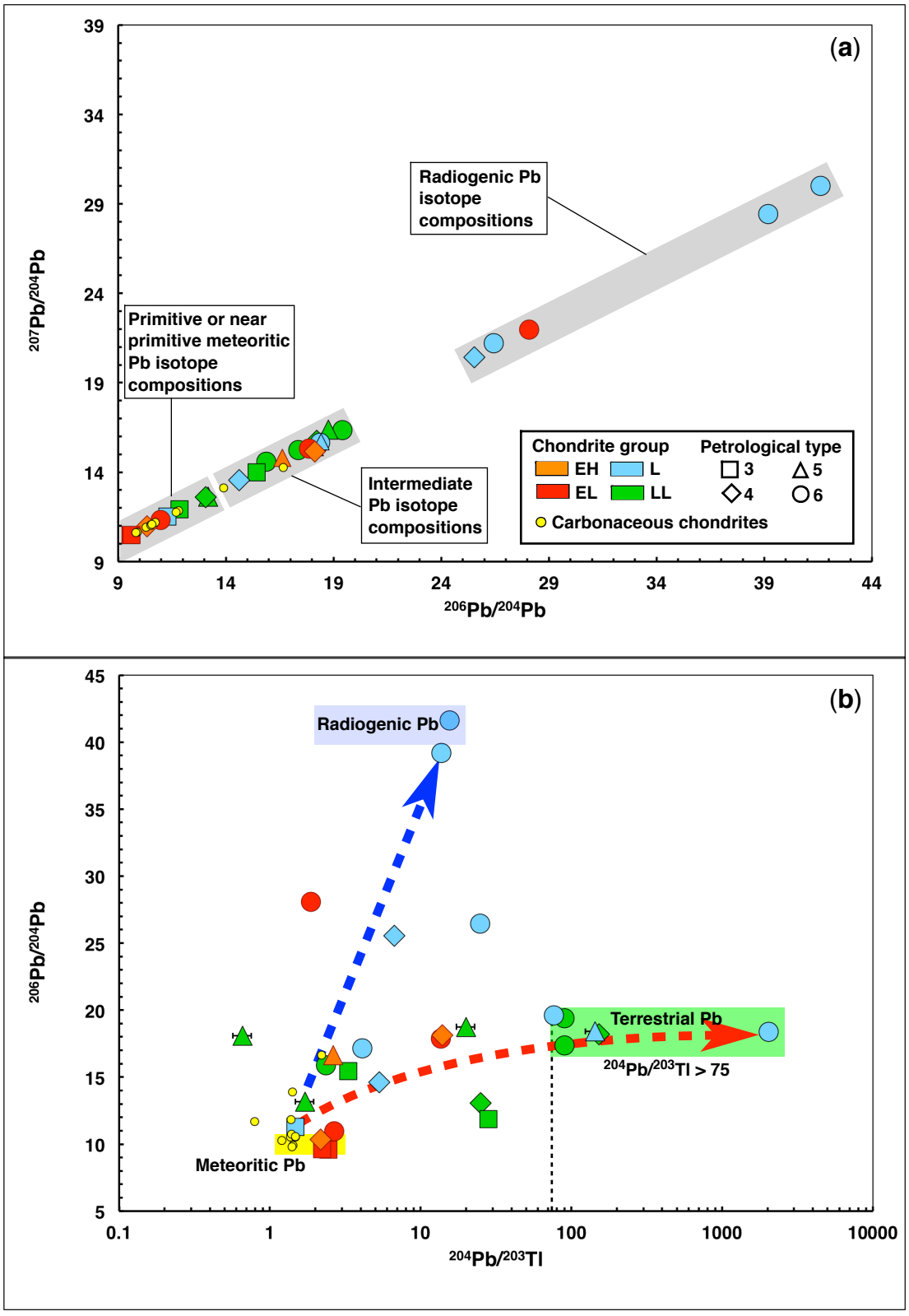


Figure 3.2. Plots of (a) $^{207}Pb/^{204}Pb$ v $^{206}Pb/^{204}Pb$ and (b) $^{206}Pb/^{204}Pb$ v $^{204}Pb/^{203}Tl$ (in logarithmic scale) for the enstatite and ordinary chondrites analysed in this study. Data for carbonaceous chondrites from Baker et al. (2010) is shown for comparison and has been corrected for terrestrial Pb contamination (see text). In panel (b) the yellow, green and blue fields represent the approximate isotope compositions of meteoritic, terrestrial and radiogenic Pb, respectively, and the blue and red arrows represent the radiogenic ingrowth of Pb and the addition of terrestrial Pb, respectively (see text). Error bars at the 2se level (for Pb isotope ratios) and 2sd level (for $^{204}Pb/^{203}Tl$ ratios) are shown except when smaller than the symbols.

The mass balance calculations require knowledge of the original Pb isotope compositions of the meteorite, now unknown, and the only estimates of this composition are based on a pristine uncontaminated sample of the same meteorite or, failing that, samples from the same group and petrological type. They also assume that the contaminant has a Pb isotope composition akin to the terrestrial composition defined by Göpel et al. (1985) and make the assumption that the final contaminated composition of the meteorite results from a simple two-component mixing model, albeit constrained in four-isotope space.

The modern terrestrial Pb field defined by Göpel et al. (1985) is wide, with $^{206}Pb/^{204}Pb$ values ranging from 16 – 19.5, based on global ore deposits and industrial pollutants as well as laboratory reagents and saw blades (for cutting iron meteorites). Nevertheless, actual environmental Pb varies considerably both temporally and spatially (Bollhöfer and Rosman, 2000; Bollhöfer and Rosman, 2001) and a composite value or a one-component value for Pb contamination of a particular meteorite may not be appropriate, and cannot be known with any degree of certainty without leaching. Baker et al. (2010) deal with this by building into the mass balance calculations a fairly large uncertainty arising from the Pb isotope composition of the contaminant.

Thus, the significant uncertainties inherent in these assumptions about unknown factors make it impossible to assess the accuracy of the corrections. Baker et al. (2010) acknowledged this issue by commenting that excluding the most contaminated CO3 chondrite Colony from the isochron as well as Allende CV3 Smithsonian made no significant difference to the calculated initial solar system $^{204}Pb/^{204}Pb_{SS,0}$ and $\varepsilon^{205}Tl_{SS,0}$ values.

Andreasen et al. (2012), however, went further in their assessment of the reliability of the carbonaceous chondrite ^{205}Pb – ^{205}Tl isochron of Baker et al. (2010), because it still included a slightly Pb contaminated desert find, the CR2 chondrite NWA 801 known to have "moderate to extensive weathering" (Connolly Jr et al., 2005), and the aforementioned very contaminated CO3 chondrite Colony. Following elimination of these two samples from the complete dataset of 11 carbonaceous chondrites together with the Allende (Smithsonian) sample already excluded by Baker et al. (2010), the inferred initial solar system $^{204}Pb/^{204}Pb_{SS,0}$ ratio changed from $(1.0 \pm 0.4) \times 10^{-3}$ to $(2 \pm 1) \times 10^{-3}$ and the $\varepsilon^{205}Tl_{SS,0}$ value changed from -7.6 ± 2.1 to -13 ± 6. Andreasen et al. (2012) found that these revised values were in excellent accord with their ^{205}Pb – ^{205}Tl isochron data for IIAB iron meteorites.

A point to note is that the two samples showing heavy Cd compositions of $\varepsilon^{114/110}Cd > +15$, Kainsaz CO3 and Leoville CV3, which may also record stable isotope fractionation of Tl, were included in the revised isochron. However, excluding these two samples, as well as

the above-mentioned three Pb contaminated samples, makes very little difference, producing an isochron with $^{204}Pb/^{204}Pb_{SS,0}$ = (1.8 ± 0.7) x 10^{-3} and an $\varepsilon^{205}Tl_{SS,0}$ value of –12.5 ± 4.0. Thus the only sample which seems to make a significant difference to the outcome is the desert find NWA 801, which is included by Baker et al. (2010) but excluded by Andreasen et al. (2012).

3.5.3 Pb – Pb isochrons

Based on the above criteria to evaluate the contamination of meteorite specimens, the enstatite and ordinary chondrite sample suites were filtered to eliminate samples with clear signs of terrestrial Pb contamination, prior to the calculation of Pb – Pb isochrons in 'inverse' $^{207}Pb/^{206}Pb$ versus $^{204}Pb/^{206}Pb$ isotope space. All $^{207}Pb/^{206}Pb$ ages were calculated using regression algorithms of the Isoplot Visual Basic 'add-in' (v3.41b) designed by Ludwig (2003) for the Microsoft Excel® program and are shown in Table 3.5:

Table 3.5. 'Inverse' Pb-Pb ages for chondrite groups excluding selected samples

Chondrite class	Samples included in regression calculation	n	Age Ma	+2sd Ma	–2sd Ma
Enstatite chondrites	All samples	8	4490	83	88
Enstatite chondrites	All except Atlanta, Indarch	6	4547	18	18
EH chondrites	All except Indarch	2	4521	n.a.	n.a.
EL chondrites	All except Atlanta	4	4553	6	6
Ordinary L chondrites	All samples	10	4529	76	81
Ordinary L chondrites	All except Ausson, New Concord, Marion (Iowa)	7	4538	84	90
Ordinary L chondrites	All except Ausson, New Concord, Barwell, Marion (Iowa)	6	4529	103	111
Ordinary LL chondrites	All samples	10	4512	97	105
Ordinary LL chondrites	All except Benares, Appley Bridge, Dhurmsala	7	4536	156	176

Regression calculated using Isoplot v3.41b using the 'Model 2' fit which assigns equal weights and zero error correlations to each point (Ludwig, 2003). 'Inverse' Pb – Pb ages derived using present day $^{238}U/^{235}U$ = 137.88, and decay constants $\lambda^{235}U$ = 0.98571 Ga^{-1} (Mattinson, 2010) and $\lambda^{238}U$ = 0.155125 Ga^{-1} (Jaffey et al., 1971).

3.5.3.1 Enstatite chondrites

When all enstatite chondrites are considered, a $^{207}Pb/^{206}Pb$ age of 4490 +83/–88 Ma was obtained, whilst exclusion of two clearly Pb contaminated samples (Indarch and Atlanta) yielded a much more precise result of 4547 ± 18 Ma. Although some early investigations suggested a common parent body for EH and EL chondrites (e.g. Kaczaral et al., 1988; Kong et al., 1997), a number of petrological, elemental and isotopic studies, however, provide firm evidence for a developing consensus that the EH and EL chondrites are derived from two separate parent bodies (e.g. Keil, 1989; Lin and Goresy, 2002; Savage and Moynier, 2013; Sears et al., 1982). Hence, separate isochrons were established here. Following elimination of

the aforementioned clearly contaminated samples, this yielded an isochron age of 4553 ± 6 Ma for the EL chondrites and a two-point isochron age of 4521 Ma for the EH chondrites. Overall, these results are similar to the published ^{53}Mn – ^{53}Cr isochron ages of about 4560 Ma for EL6 (Khairpur) and about 4565 Ma for EH4 (Abee and Indarch) chondrites (Shukolyukov and Lugmair, 2004) and Pb – Pb ages of 4582 Ma for EH5 (St Marks) and 4588 Ma for EL6 chondrites (Manhès and Allègre, 1978).

3.5.3.2 Ordinary chondrites

Using the data for all L chondrites, the $^{207}Pb/^{206}Pb$ isochron age is 4529 +76/–81 Ma. When three (Marion (Iowa), Ausson and New Concord) and four (aforementioned plus Barwell) samples with the most obvious terrestrial Pb contamination are excluded, similar ages of 4538 +84/–90 Ma and 4529 +103/–111 Ma, respectively, are obtained. These results are in agreement with published Pb – Pb ages: 4552 ± 1 Ma and 4553 ± 1 Ma for L5 chondrites Knyahinya and Homestead, respectively (Manhès and Allègre, 1978); a mean age of 4550 Ma for L5 and L6 chondrites (Unruh, 1982); ages ranging from 4511 – 4543 Ma for L5 and L6 chondrite phosphates (Göpel et al., 1994); and two-point isochron ages of 4530 – 4544 Ma for L5 chondrites (Bouvier et al., 2007).

Data for all LL chondrites yield a $^{207}Pb/^{206}Pb$ isochron age of 4512 +97/–105 Ma whilst excluding Benares, Appley Bridge and Dhurmsala yields a result of 4536 +156/–176 Ma. In both cases, removal of the more radiogenic and Pb contaminated samples increases the uncertainty of the results. In general, these data are consistent with published Pb – Pb ages: 4543 ± 19 Ma for the LL6 Saint Séverin (Manhès et al., 1978); and two-point isochron ages of 4532 Ma for L/LL4 and 4548 – 4576 Ma for LL5 – 6 chondrites (Bouvier et al., 2007).

3.5.3.3 Discussion

Given the large uncertainties of the results, the agreement seen with previously published ages for enstatite and ordinary chondrites is not surprising. These large uncertainties are largely a reflection that this study made no particular attempt to obtain high-precision ages through thorough leaching of the samples or separation and preparation of the phases (e.g. phosphates, leachates) that feature radiogenic Pb, or both, to improve the precision of the $^{207}Pb/^{206}Pb$ isochron ages.

3.5.4 Tl isotope compositions and $^{204}Pb/^{203}Tl$ – evidence for live ^{205}Pb in the early solar system

In comparison to the carbonaceous chondrites, the enstatite and particularly the ordinary chondrites display significantly greater variability in both Tl isotope compositions and $^{204}Pb/^{203}Tl$ ratios (Figure 3.3). Despite this large variability, it is difficult to apply the results to demonstrate evidence for the existence of live ^{205}Pb at the time the meteorite parent bodies formed and cooled in the early solar system or apply the ^{205}Pb – ^{205}Tl decay system for chronometry. In part, this reflects that at least some of the Tl isotope variability is due to stable isotope fractionation, as suggested by the relatively large variability in Cd stable isotope compositions observed in this study for the enstatite chondrites and published by Wombacher et al. (2008) who reported less precise $\varepsilon^{114/110}Cd$ values from about –110 to +150 for ordinary chondrites. The latter data further indicate similar variability in H, L and LL chondrites and particularly large isotope effects for unequilibrated Type 3 ordinary chondrites.

3.5.4.1 Enstatite chondrites

For the enstatite chondrites, the Tl isotope compositions of all but one sample show variability similar to that seen in carbonaceous chondrites, with $\varepsilon^{205}Tl$ values of between –3.0 to +0.8, the exception being the unequilibrated EL3 chondrite PCA 91020 with an anomalously heavy composition of $\varepsilon^{205}Tl$ = +22.2 (Figure 3.3, Figure 3.4). Turning to the $^{204}Pb/^{203}Tl$ ratios, most samples fall within a narrow range of between about 1.9 and 2.7, but one each from the EH and EL groups have $^{204}Pb/^{203}Tl \approx 14$. In addition, the EL6 chondrite Daniel's Kuil is characterised by $^{204}Pb/^{203}Tl \approx 42$ but this sample is not plotted in either Figure 3.3 or Figure 3.4 because Tl and Cd isotope data are not available.

The $\varepsilon^{114/110}Cd$ values of the enstatite chondrites display more variability with the main group (6 out of 8 samples) showing results of between +2.9 and +10.4 and the other two, the EL6 Khairpur and the aforementioned EL3 PCA 91020, showing extremely heavy compositions of +65.7 and +72.9, respectively. The main group of carbonaceous chondrites (7 out of 9 samples) show a more restricted range of $\varepsilon^{114/110}Cd$ values of between +1.1 and +5.3 with the other anomalous samples, Kainsaz (CO3) and Leoville (CV3), showing compositions of +15.6 and +32.7, respectively. The generally larger Cd isotope variability of the enstatite chondrites is an indication that they have undergone significant stable isotope fractionation due to parent body processes.

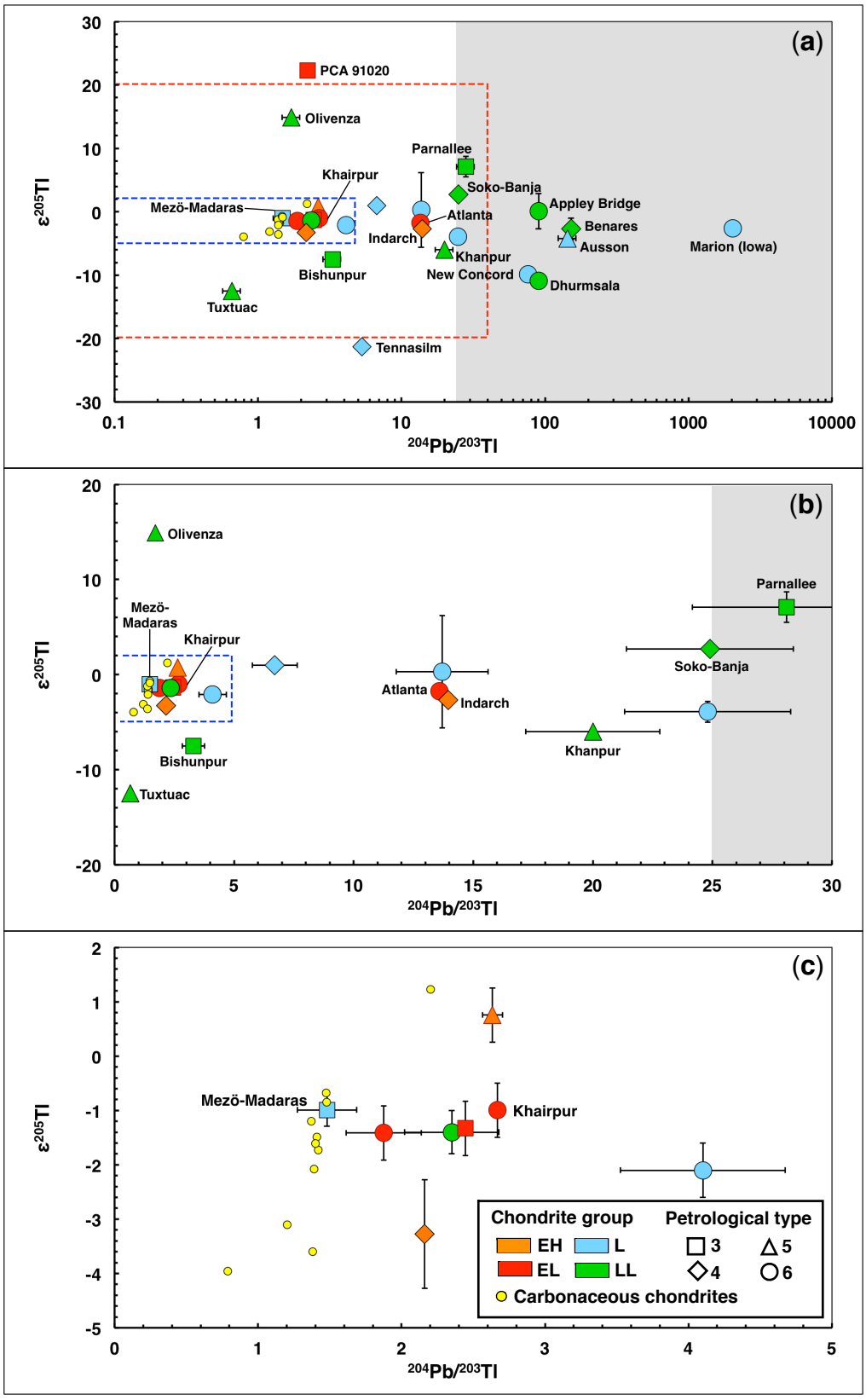


Figure 3.3. Plots of $\varepsilon^{205}Tl$ versus $^{204}Pb/^{203}Tl$ for the enstatite and ordinary chondrites of this study. The carbonaceous chondrites of Baker et al. (2010) are shown for comparison and have been corrected for terrestrial Pb (see text). Panels (a), (b) and (c) are of the same plot but use variable scaling to best reveal the structure and systematics of the data. The red and blue boxes show the coverage of the scaled up panels (b) and (c), respectively. The grey shaded areas indicate samples more likely to be perturbed by terrestrial Pb contamination ($^{204}Pb/^{203}Tl > 25$). Error bars at the 2sd level are shown except where they are smaller than the symbols.

The high $^{204}Pb/^{203}Tl$ ratios of Indarch (EH4) and Atlanta (EL6) are almost certainly a product of terrestrial Pb contamination rendering them unsuitable for isochron calculations. Similarly, the high, and hence possibly radiogenic, $\varepsilon^{205}Tl$ of +22.2 for the EL3 PCA 91020 is accompanied by an extremely fractionated Cd isotope composition with a $\varepsilon^{114/110}Cd$ value of +72.9. This suggests that the heavy Tl isotope composition is almost certainly perturbed by stable isotope fractionation, most likely by vaporisation from impact shock (section 3.5.5 below).

The remaining five enstatite chondrites display a far more restricted range of Tl isotope compositions and $^{204}Pb/^{203}Tl$ ratios, which might be interpreted to define a correlation that is essentially sub-parallel to the data array of the carbonaceous chondrites (Figure 3.3 (c)). If this correlation is interpreted as defining an isochron, this would provide estimates for the initial ^{205}Pb abundance and Tl isotope composition of about $^{205}Pb/^{204}\,Pb \approx (1 – 2) \times 10^{-3}$ and $\varepsilon^{205}Tl \approx -8$ to -10.

Unfortunately, this interpretation is very unlikely to be realistic, however, given that significant Cd stable isotope fractionation is revealed by the enstatite chondrites. Seven out of eight enstatite chondrite samples define a strong linear correlation ($R^2 = 0.99$) between $\varepsilon^{205}Tl$ and $\varepsilon^{114/110}Cd$ values (grey dashed line in Figure 3.4). The excluded sample is the EL6 chondrite Khairpur, which has unusual characteristics with a very heavy Cd isotope composition but relatively unfractionated Tl isotopes. However, the identified $\varepsilon^{205}Tl$ – $\varepsilon^{114/110}Cd$ correlation must be treated with some caution: extreme values will tend to exert undue influence on least-squares regression statistics and, accordingly, PCA 91020 exerts a controlling influence on the slope of the linear regression due to its extreme $\varepsilon^{205}Tl$ and $\varepsilon^{114/110}Cd$ values.

Re-casting the linear regression to exclude the EL3 chondrite PCA 91020 together with the EL6 chondrites, Khairpur and Atlanta, which exhibit heavy Cd isotope compositions with relatively little Tl fractionation still produces a strong regression (blue dashed line in Figure 3.4, $R^2 = 0.95$). However, this regression has a significantly different slope ($\varepsilon^{205}Tl \approx 0.56 \times \varepsilon^{114/110}Cd$) compared to the regression produced when only excluding Khairpur ($\varepsilon^{205}Tl \approx 0.36 \times \varepsilon^{114/110}Cd$), and this is an indication that there is a degree of decoupling in the Cd and Tl isotope systematics of PCA 91020, Atlanta and Khairpur. Possible reasons for this are considered further in section 3.5.5 below, which explores the effects of shock and thermal metamorphism.

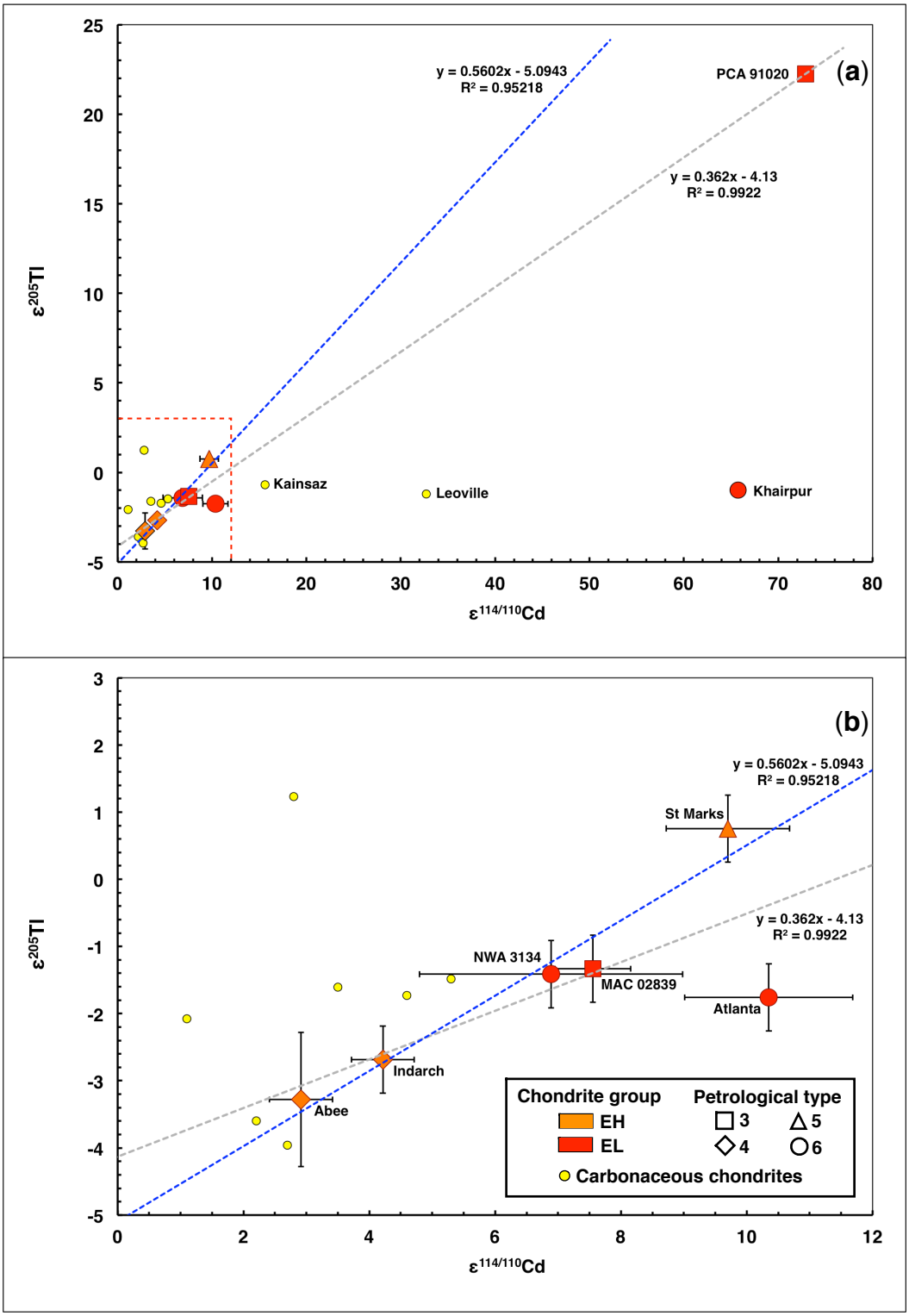


Figure 3.4. Plots of ε^{205}Tl versus $\varepsilon^{114/110}$Cd for the enstatite chondrites of this study and the carbonaceous chondrites of Baker et al. (2010). Panels (a) and (b) are of the same plot but use variable scaling to best reveal the structure and systematics of the data. The red box in panel (a) shows the coverage of the scaled up panel (b). The grey dashed line in both panels is the linear regression of all the enstatite chondrite samples excluding the EL6 Khairpur. The blue dashed line is the linear regression of all enstatite chondrites excluding EL6 chondrites Khairpur and Atlanta and the EL3 PCA 91020. Linear regression equations and R^2 values are shown next to relevant lines. Error bars at the 2sd level are shown except where they are smaller than the symbols.

In summary, these observations indicate that the Tl isotope compositions may well show some variability that reflects in situ decay of ^{205}Pb but this cannot be convincingly separated from stable isotope effects that are also likely to have affected, and possibly dominated, Tl isotope compositions. A detailed evaluation of possible radiogenic variations of ε^{205}Tl is furthermore complicated by the terrestrial Pb contamination of the meteorites, which perturbed the ^{204}Pb/^{203}Tl ratios of some, if not all, samples to some extent.

3.5.4.2 L chondrites

In the case of the L chondrites, ε^{205}Tl varies between –21.3, the lowest value measured for this isotope system to date, and +1.0. The ^{204}Pb/^{203}Tl ratios range from a carbonaceous chondrite-like value of 1.5 for the L3.7 Mezö-Madaras up to a highly anomalous ratio of 2030 for the L6 Marion (Iowa). The latter result almost certainly reflects contamination by terrestrial Pb (Figure 3.3). The high ^{204}Pb/^{203}Tl ratios of L5 Ausson (^{204}Pb/^{203}Tl = 144) and L6 New Concord (^{204}Pb/^{203}Tl = 76.3) are similarly also probably affected by such contamination.

Overall, Mezö-Madaras plots close to the carbonaceous chondrites both in terms of ^{204}Pb/^{203}Tl ratio and ε^{205}Tl, which is in agreement with it being volatile rich, and not having been significantly thermally processed. In contrast, the most anomalous Tl isotope compositions are displayed by the L4 Tennasilm (ε^{205}Tl = –21.3) and the L6 New Concord (ε^{205}Tl = –9.9), even though these meteorites have Tl concentrations which are a magnitude apart at 4.84 ng/g and 0.35 ng/g. Given that large Cd stable isotope fractionations have been documented by Wombacher et al. (2008) for L chondrites, it is likely that the Tl isotope compositions of Tennasilm and possibly also New Concord were altered by stable isotope effects and this cannot be ruled out for other L chondrites.

When considering only those samples which are least likely to be perturbed by terrestrial Pb contamination (with ^{204}Pb/^{203}Tl ratios ≤ 25) and Tl stable isotope fractionation (ε^{205}Tl ≥ –20 to exclude Tennasilm), the L chondrites show little or no evidence of live ^{205}Pb. Focussing on the two most reliable and weakly metamorphosed meteorites, Mezö-Madaras (L3.7) and Saratov (L4), these define a two-point isochron which provides an initial ratio of ^{205}Pb/^{204} Pb ≈ (1.0 ± 0.4) x 10^{-4} (Andreasen et al., 2009). Assuming an initial solar system ^{205}Pb/^{204}Pb$_{SS,0}$ in the range (1 – 2) x 10^{-3} as defined by the carbonaceous chondrites (Andreasen et al., 2012; Baker et al., 2010), this is equivalent to a Pb – Tl cooling age for L chondrites of about 50 to 93 Ma.

3.5.4.3 LL chondrites

Amongst the chondrites studied to date, the LL chondrites have the most variable Tl isotope compositions, with ε^{205}Tl values of between –12.5 and +14.9. In contrast, the ^{204}Pb/^{203}Tl ratios are less variable than for L chondrites, with results ranging from 0.66 to 152. Notably, the three samples with the highest ^{204}Pb/^{203}Tl ratios of between 90 and 152, the LL4 Benares and the LL6s Appley Bridge and Dhurmsala, are characterised by ^{206}Pb/^{204}Pb ratios of between 17.4 and 19.4 and, therefore, are likely to feature significant terrestrial Pb contamination. Similarly the LL4 Khanpur and LL5 Tuxtuac have Pb isotope compositions with ^{206}Pb/^{204}Pb ratios of 18.1 and 18.8, respectively, and are consequently also likely to have been contaminated. Hence, the original meteoritic ^{204}Pb/^{203}Tl ratios of these samples are essentially unconstrained.

The results for the two samples with the most extreme Tl isotope compositions, Tuxtuac (ε^{205}Tl = –12.5) and Olivenza (ε^{205}Tl = +14.9), are also suspect. Notably, both are heavily metamorphosed LL5 chondrites. Tuxtuac has a low Pb content (267 ppb) and a ^{204}Pb/^{203}Tl ratio that is lower (at 0.66) than found in any of the carbonaceous chondrites analysed by Baker et al. (2010). As it also has a terrestrial Pb isotope composition with ^{206}Pb/^{204}Pb = 18.1, the Pb content of this meteorite most likely reflects exchange with terrestrial Pb and overall Pb loss. In contrast, Olivenza features a much higher Pb concentration coupled with relatively high Tl content, which produces a ^{204}Pb/^{203}Tl ratio similar to that of carbonaceous chondrites. In addition it has a relatively low ^{206}Pb/^{204}Pb ratio of 13.2, indicative of a mostly primitive Pb content. Given its comparatively low Pb/Tl ratio and ε^{205}Tl of +14.9, Olivenza plots far above the carbonaceous chondrite isochron, regardless of the exact slope of the latter. For this positive ε^{205}Tl to be of radiogenic origin, Olivenza would need to be derived from a parent body originally characterised by a very high Pb/Tl ratio, after which the parent asteroid or meteorite lost significant quantities of Pb. Whilst possible, such an evolution is considered less likely than a scenario whereby the high ε^{205}Tl is due to stable isotope fractionation, for example from redistribution and concentration of isotopically heavy Tl derived, perhaps, from volatilisation, during parent body metamorphism.

Considering only the least metamorphosed and least contaminated samples, Bishunpur (LL3.1), Parnallee (LL3.6), and Soko-Banja (LL4), there is a hint of a correlation between ^{204}Pb/^{203}Tl and ε^{205}Tl. In detail, Bishunpur has low Pb/Tl and low ε^{205}Tl of –7.5, whilst Soko-Banja and Parnallee have higher ^{204}Pb/^{203}Tl ratios and positive ε^{205}Tl values of

+2.7 and +7.1 respectively. The correlation defined by these samples is equivalent to an initial $^{205}Pb/^{204}Pb = (1.3 \pm 0.2) \times 10^{-4}$, which, if interpreted as an isochron, is equivalent to an age of about 48 to 73 Ma, assuming an initial solar system $^{205}Pb/^{204}Pb_{SS,0} \approx (1 - 2) \times 10^{-3}$ defined by the carbonaceous chondrites (Andreasen et al., 2012; Andreasen et al., 2009; Baker et al., 2010).

This age must be treated with caution, however, given the high degree of uncertainty as to whether the $^{204}Pb/^{203}Tl$ ratios are indeed unaffected by Pb terrestrial contamination. A key observation is that the LL chondrite Pb – Tl isochron plots below the original isochron of Baker et al. (2010) for carbonaceous chondrites with an initial $\varepsilon^{205}Tl$ of –9.3 ± 0.7. This is not, however, problematic in the light of the revised carbonaceous chondrite isochron discussed in section 3.5.2 above and the IIAB iron meteorite isochron of Andreasen et al. (2012), which feature initial solar system $\varepsilon^{205}Tl_{SS,0}$ values of –13.1 ± 6.0 and –12.3 ± 1.0 respectively.

In summary, it is likely that the least metamorphosed LL chondrites show evidence for the presence of live ^{205}Pb but the metamorphic cooling age of about 48 to 73 Ma after carbonaceous chondrite formation is, nevertheless, still fairly speculative.

3.5.5 Shock and thermal metamorphism in enstatite and ordinary chondrites

Volatilisation and isotope fractionation may accompany heating and melting from impacts on meteorite parent bodies. In their study of L chondrites, Friedrich et al. (2004), showed that volatile elements were depleted in strongly-shocked compared to mildly-shocked meteorites. Moynier et al. (2010) found that heavier Zn isotope compositions in ureilites were broadly correlated with a higher degree of shock in those meteorites and concluded that isotope fractionation resulted from heating and volatilisation driven by impact shocks. The enrichment of heavy Zn, Cu and Fe isotopes in lunar soils (Moynier et al., 2006) and of heavy Zn and Cu isotopes in shocked sandstones from a large terrestrial impact crater (Albarède et al., 2007) have also been attributed to volatilisation of those elements. Similarly, the heavy Zn and Cd isotope composition of terrestrial tektites has been attributed to the evaporation of those elements during impact volatilisation (Moynier et al., 2009; Wombacher et al., 2003).

Stöffler et al. (1991) presented a classification scheme for shock metamorphism in ordinary chondrites, based on shock effects on olivine and plagioclase grains as seen in thin section, and ranging from S1 (unshocked) to S6 (very strongly shocked). Rubin et al. (1997)

extended this classification to enstatite chondrites by using orthopyroxene instead of olivine due to the rarity of olivine in this meteorite type.

3.5.5.1 Enstatite chondrites

The trends in Cd and Tl concentrations are broadly linked to petrological type within the EH and EL classes, with higher contents in the less metamorphosed meteorites, controlled by the degree to which these similarly volatile elements are driven off by thermal metamorphism, thus, generally for Cd and Tl contents EL3 > EL6 and EH4 > EH5. As mentioned in section 3.5.1.1, there is a good correlation (R^2 = 0.83; Figure 3.1 (b) above) between Cd and Tl contents across the entire enstatite chondrite dataset. However, looking at these results in more detail, the EH5 and EL6 chondrites, apart from Daniel's Kuil (possibly because of the high uncertainty attached to its Cd content), are very strongly correlated (R^2 = 0.99), in line with the argument that these elements are systematically volatilised by thermal metamorphism. However, the picture is more complex when considering the less metamorphosed EL3 and EH4 chondrites: PCA 91020 (EL3) is more *enriched* in Cd but more *depleted* in Tl than MAC 02839 (EL3) and Abee (EH4) is similarly more enriched in Cd and more depleted in Tl than Indarch (EH4). In fact, Abee has the highest Cd content of all enstatite chondrites analysed in this study (857 ng/g) and the second highest Tl content (73.2 ng/g) after Indarch.

Further complexities arise from the correlation between the Cd and Tl isotope compositions of the enstatite chondrites, as discussed in section 3.5.4.1 on page 81, and plotted in Figure 3.4. An observation from this analysis was that there was some degree of decoupling in the Cd and Tl isotope systematics for the EL3 PCA 91020, and the EL6 meteorites Khairpur and Atlanta. The remaining enstatite chondrites (Abee, Indarch, St Marks, MAC 02839 and NWA 31340) exhibit a strong linear correlation between Cd and Tl isotope compositions, defined by the blue line of Figure 3.4. The three aforementioned meteorites, however, exhibit Tl isotope compositions that are lighter than would be expected if they were to conform to the linear correlation of the remaining five.

Thus, processes other than systematic volatilisation by thermal metamorphism appear to have influenced the Cd and Tl contents and isotope systematics, particularly of the enstatite chondrites PCA 91020, Khairpur, Atlanta and Abee, and it is worth exploring whether shock metamorphism may have played a role in creating these complexities. The remaining enstatite chondrites (Indarch, St Marks, MAC 02839 and NWA 3134) were only

very weakly or weakly shocked (S2 or S3), and they also have relatively unfractionated Cd and Tl isotope compositions ($\varepsilon^{114/110}$Cd ≈ +4 to +10; ε^{205}Tl ≈ –3 to +1), so they will not be considered further here.

The most heavily shocked enstatite chondrite analysed in this study is the unequilibrated EL3 chondrite PCA 91020, assigned a shock stage of S5 (Rubin et al., 1997). PCA 91020 was observed to have foliations due to impact-induced shearing (Rubin et al., 2009) and plagioclase that was transformed to maskelynite (Rubin et al., 1997), a dense glass produced by melting and quenching induced by high pressure shock waves (Chen and El Goresy, 2000). This meteorite also has the heaviest Tl and Cd isotope compositions recorded in this study (ε^{205}Tl = +22.2 and $\varepsilon^{114/110}$Cd = +72.9), which is consistent with other evidence outlined above, whereby heavy isotope enrichment is associated with heating and volatilisation due to impact shock.

Although Khairpur and Atlanta have a final observed shock stage of S2 (very weakly shocked) they contain clasts and veins that indicate relatively high levels of impact shock in their histories. It has been suggested that these meteorites, as well as other EL6 chondrites, were shocked to S3 to S5 levels prior to thermal metamorphism, whereby the latter would have erased many petrological shock features by annealing. Hence, their recorded shock levels become S2, most likely due to subsequent less violent impacts (Rubin, 1983; Rubin et al., 1997).

The EH4 chondrite Abee (S2 to S4) is an impact melt breccia which had undergone an episode of impact melting according to Rubin and Scott (1997), followed by brecciation due to bombardment, followed by further impact melting.

In summary, all four enstatite chondrites exhibiting unusual Cd and Tl concentrations and isotope systematics show evidence of high-pressure shocks from impacts in their petrological histories.

3.5.5.2 Discussion

The evidence from the EL6 chondrites Khairpur and Atlanta is that proto EL6 material underwent impact metamorphism followed by annealing of the impact features by thermal metamorphism followed by, most likely, further weaker shock events, resetting the shock grade to S2. In this context, it is worth exploring whether the ‘onion shell’ model, which has been applied to the H-chondrite parent body (Trieloff et al., 2003), can account for the petrological and isotopic features of EL3 and EL6 chondrites. In this scenario, thermal

metamorphism could have taken over from impact metamorphism after the proto EL6 material was buried by further accreting material, eventually raising the material to petrological type EL6. EL3 material would have remained at or near the surface, subject to impact heating and melting without the subsequent annealing, such as with PCA 91020, although the EL3 MAC 02839 clearly was not subject to the same degree of bombardment.

Quirico et al. (2011) suggested that the 'onion shell' model could apply to the enstatite chondrite parent bodies based on a correlation of petrological types with the closure temperatures of opaque minerals. Patzer and Schultz (2002), however, dismissed the onion shell model on account of the distribution of noble gases in enstatite chondrites. Furthermore, there is no clear support for this model from Ar – Ar and I – Xe ages (Hopp et al., 2016; Hopp et al., 2014). Therefore, application of this model to enstatite chondrites remains highly speculative.

A number of workers have reported a correlation between petrological type and shock classification in ordinary and enstatite chondrites. This assumes that some higher petrological types were shocked to a high grade and subsequently annealed, leading to the conclusion that collisions were possibly the major source of heat on the parent bodies in addition to the decay of short-lived radionuclides such as ^{26}Al. (Rubin, 2004; Rubin, 2015; Rubin and Wasson, 2011; Stöffler et al., 1991). The number of samples in this study is insufficient to enable any firm conclusions to be drawn about a correlation between shock stage and petrological type. Tentatively, however, if EL6 chondrites are reset from their original high shock stage, as is almost certainly the case with Khairpur and Atlanta, then they would have had a higher shock stage than the EL3 MAC 02839. The exception, of course, is that the EL3 PCA 91020 is a clearly highly shocked too.

The proto-EL6 material in this scenario would have been originally shocked during an early sustained episode of bombardment, which resulted in heating and melting forming the EL6 petrological type and annealing early shock features. EL3 material could have formed either by subsequent accretion, avoiding the early collisional heating and melting which affected proto-EL6 material, or simply buried under a blanket of early proto-EL6 accreted material and protected from thermal metamorphism from impacts. Thus, PCA 91020 could have possibly been impacted or even excavated by a late massive collision which left MAC 02839 untouched.

This would be consistent with the highly Cd and Tl fractionated PCA 91020 and unfractionated MAC 02839 compositions. The EL3 PCA 91020 most likely has undergone open system volatilisation of Cd and Tl, resulting from heating and melting following violent

impacts, whereby lighter isotopes are removed leaving a residue with heavy isotope compositions of both elements. However, both Cd and Tl would have been depleted by volatilisation, but when compared to MAC 02839, which is the relatively unfractionated, PCA 91020 is enriched in Cd but depleted in Tl. The same enrichment and depletion in Cd and Tl applies to Abee when compared to Indarch, but Abee has relatively unfractionated Cd and Tl isotope compositions. In addition there is evidence for the decoupling of Cd and Tl isotope compositions in PCA 91020, whereby the Tl isotope composition of PCA 91020 is heavy, but not as heavy as might be expected from its Cd isotope composition.

Whilst a redistribution of impact melt enriched in heavy Cd isotopes might have caused this, it is not clear how the depletion of Tl, nor the decoupled isotope compositions, might have arisen. It is possible that fractionation between the two elements may have been influenced by the slightly higher volatility or mobility of Tl compared to Cd (Schaefer and Fegley, 2010) or it may have simply been the result of multiple episodes of impact excavation and redistribution of the PCA 91020 material.

The EL6 chondrites Khairpur and Atlanta are enriched in heavy Cd isotopes but Tl isotopes are unfractionated. Kinetic evaporation of Cd and Tl from impacts or thermal metamorphism would have produced a heavy isotopic signature for both elements, such as with PCA 91020. It might be suggested that a heavy Tl isotopic signature from metamorphism was altered afterwards by, for example, equilibration with isotopically light Tl produced by kinetic Rayleigh condensation of a vapour containing Tl (e.g. Davis and Richter, 2014). However, this scenario is unlikely for the following reasons: (i) all of the EL6 chondrites have near identical Tl isotope compositions (ε^{205}Tl $\approx$ –1 to –2); (ii) they are not particularly enriched in their Tl content; (iii) most likely Cd content and isotope composition would have been similarly affected since Cd and Tl have only slightly different condensation temperatures and labilities (Lodders, 2003; Schaefer and Fegley, 2010); and (iv) as mentioned earlier in this section, the Cd and Tl contents of all EL6 chondrites are strongly correlated.

In summary, there is significant decoupling of Cd and Tl concentrations and isotope compositions in the heavily shocked enstatite chondrites, however, the exact mechanism or mechanisms causing this remain elusive, probably due to their complex thermal and shock metamorphic histories.

3.5.5.3 Weathering and Cd isotope fractionation

A final word on the enstatite chondrites concerns the meteorite PCA 91020 which has been assigned a weathering grade of "Ce", indicating severe rustiness and presence of evaporite minerals and described as considerably weathered (NASA Johnson Space Centre, 1993). It is not known, however, to what extent the fragment analysed in this study might have been affected by such weathering. Leaching experiments on Pb – Zn ore samples and analysis of soil samples have suggested that Cd isotope fractionation might take place during weathering whereby the Cd content of run-off fluids has a heavy isotope composition leaving the source rocks and soils with a lighter Cd composition (Zhang et al., 2016). Potentially this could also affect the Cd isotope composition of meteorite finds, however, this is not likely to have affected PCA 91020 since it has an extremely heavy Cd isotope composition.

3.5.5.4 Ordinary chondrites

Most L and LL chondrites in this study are very weakly (S2) or weakly shocked (S3) (Table 3.4, Figure 3.5), however notable exceptions to this are the L6 chondrites New Concord (S4 – moderately shocked) and Alfianello (S5 – strongly shocked). The Tl content of Alfianello is highly enriched (19.2 ng/g) compared to other L6 chondrites, which have Tl contents in the range 0.11 to 0.49 ng/g and is even greater than the Tl contents in the lower L chondrite petrological types, apart from the L3.7 Mezö-Madaras (S3), which has a Tl content of 25.6 ng/g. New Concord, however, has a depleted Tl content of 0.35 ng/g, similar to the other L6 chondrites, apart from Alfianello, which have Tl contents of below 0.5 ng/g.

There seems to be no trend between shock grades and Tl contents in this dataset, in line with a previous study (Neal et al., 1981), although these workers found such trends in other volatile elements. Contrary to this, subsequent workers have found correlations between increasing shock grade and decreasing contents of highly volatile elements such as Tl (Friedrich et al., 2004; Huston and Lipschutz, 1984; Walsh and Lipschutz, 1982). It is conceivable that such a trend cannot be discerned in the dataset of this study because the higher shock grades are relatively underrepresented.

The L5 Ausson and L4 Tennasilm have intermediate Tl contents of 1.55 and 4.84 ng/g respectively, although the L4 Saratov is depleted like most of the L6 chondrites with a Tl content of 0.45 ng/g. As noted before in section 3.5.1.2, there is a general pattern, ignoring Alfianello and Saratov, of increasing Tl content with decreasing petrological type in the L chondrites, a trend also found by other workers (Keays et al., 1971; Schaefer and Fegley,

2010). The L3.7 Mezö-Madaras and L6 Alfianello stand out as enriched in Tl by about two orders of magnitude compared to the most depleted of the L6 chondrites.

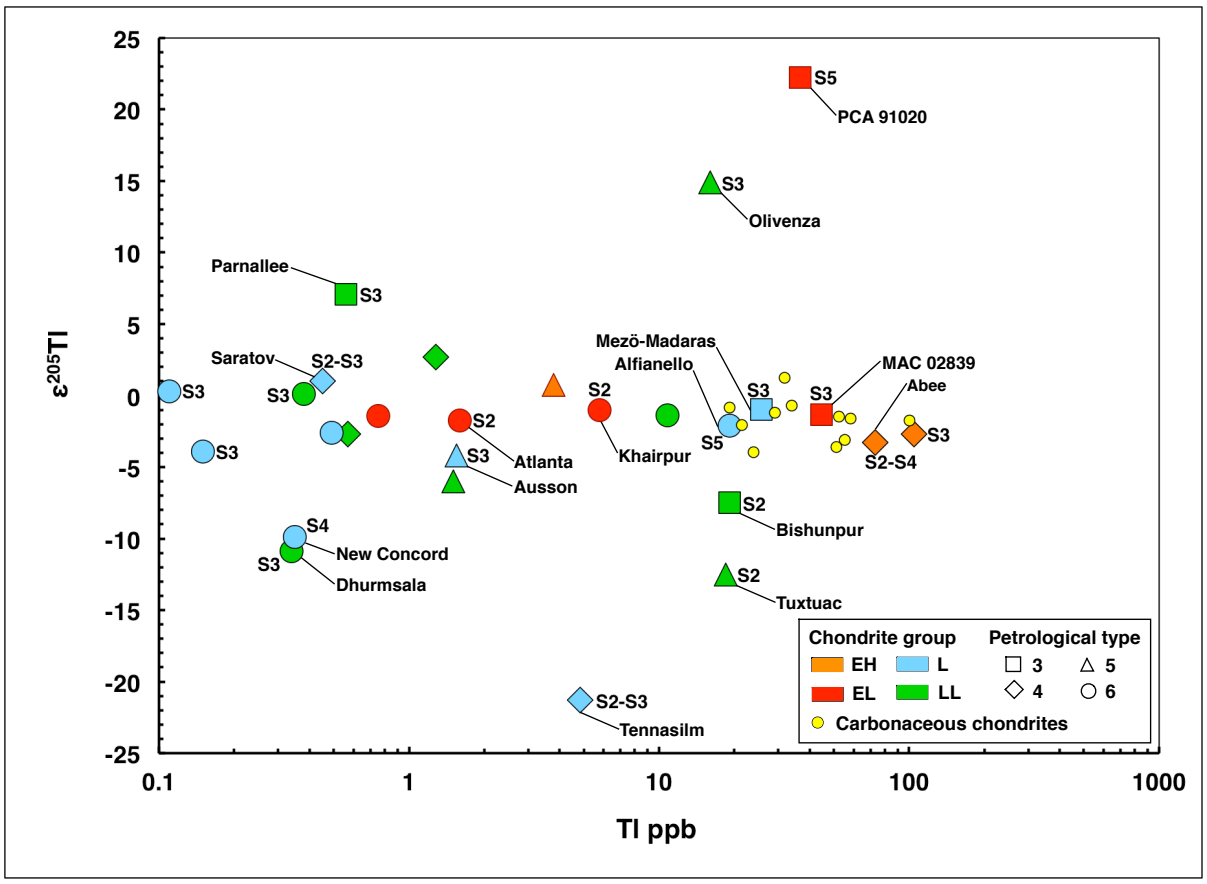


Figure 3.5. Plot of ε^{205}Tl versus Tl concentrations for the enstatite and ordinary chondrites of this study. The carbonaceous chondrites of Baker et al. (2010) are shown for comparison. Shock stages are indicated for each meteorites which have been classified in the literature and the references are listed in the caption to **Table 3.4** on page 71. Error bars at the 2sd level are smaller than the symbols.

In contrast, there is considerable variability in both equilibrated and unequilibrated LL chondrites. They display depleted Tl contents of ≤ 1.5 ng/g for all petrological types (L3.6 – L6) and enriched contents of > 10 ng/g for petrological types LL3, LL5 and LL6. The highest Tl content is found in the LL3.1 Bishunpur (19.1 ng/g), but the second highest is found in the more equilibrated LL5 Tuxtuac (18.5 ng/g). Whilst the two meteorites with the highest Tl contents are only weakly shocked at S2, there is no clear correlation between Tl content and shock grade for LL chondrites. However, shock grades have not been determined for some of the LL chondrites of our sample suite.

It is interesting that eight of the ordinary chondrites record Tl isotope compositions which are lighter than the enstatite chondrites. However, there is no apparent correlation between Tl isotope composition and petrological type or shock grade, other than perhaps the observation that most L6 and LL6 chondrites record isotope compositions within a fairly

narrow range of ε^{205}Tl from –3.9 to 0.3, including the strongly shocked L6 Alfianello (ε^{205}Tl = –2.1). The type 6 meteorites outside of this range are the moderately shocked L6 New Concord (ε^{205}Tl = –9.9) and the weakly shocked LL6 Dhurmsala (ε^{205}Tl = –10.9). Other petrological types are scattered over a wider range from ε^{205}Tl from –21.3 to +14.9, with the majority recording values of between ε^{205}Tl = –12.5 and +7.1.

There is also little correlation between Tl content and isotope composition and possibly the only observation of note is that the most depleted samples (≤ 1.5 ng/g) exhibit a fairly limited range of ε^{205}Tl values between –10.9 and +7.1.

3.5.5.5 Discussion

In comparison to the relatively narrow field of Tl isotope compositions and abundances exhibited by the carbonaceous chondrites (Figure 3.5), data for the ordinary chondrites are considerably more scattered. Ignoring the highly fractionated EL3 chondrite PCA 92010, the L and LL chondrites exhibit a far wider range of Tl isotope compositions than the enstatite chondrites, including many with very light Tl isotope compositions. The case of the strongly shocked L6 chondrite Alfianello is interesting: whilst it has an unfractionated Tl isotope composition, it is highly enriched in Tl compared to other L6 chondrites and even more enriched compared to lower petrological types. This unusual case, together with the widely scattered Tl isotope compositions in the L and LL chondrite dataset, including very light values, points to widespread redistribution of isotopically light and heavy Tl, possibly produced in numerous episodes of volatilisation and condensation during sustained and destructive impact events.

Further to this, Rubin (2004) concluded from his extensive study of equilibrated ordinary chondrites (types 4 – 6 with observed shock stages S1 – S2) that, based on a range of petrological indicators such as chromite veinlets, they were originally shocked by impacts to stages S3 – S6 and subsequently annealed, erasing conventional shock indicators. Subsequent to annealing, the ordinary chondrite material was re-shocked to the observed shock stage. This author painted a scenario from this evidence whereby the originally highly-shocked material was buried under a hot ejecta blanket, annealed and subsequently excavated by further impacts, thereby possibly undergoing multiple episodes of shock and annealing. An impact history such as this could account for the widely-scattered Tl isotope compositions and abundances for the L and LL chondrites observed in this study, as this element is highly labile and easily mobilised (e.g. Lipschutz and Woolum, 1988; Schaefer and Fegley, 2010).

Furthermore, that equilibrated ordinary chondrites are likely to have been subject to high levels of impact shock, possibly in multiple episodes, may also explain the apparent lack of correlation between shock grade and Tl content in the ordinary chondrite dataset of this study.

As discussed in sections 3.5.1.2 and 3.5.1.3 above, a tenuous negative correlation was found between Tl content and petrological type in L chondrites but there was no similar correlation amongst the LL chondrites. It is possible, therefore, that the initial budget of volatile elements in the L chondrite parent body were redistributed from the hotter interior, characterised by the higher petrological types, to the cooler outer layers, characterised by the lower petrological types (Dreibus and Wänke, 1980; Schaefer and Fegley, 2010). Such an 'onion shell' model would probably have been disrupted by large-scale impact heating as is suggested by the evidence that ordinary chondrites experienced high shock levels which were later annealed (Rubin, 1995; Rubin, 2004). The observation that correlations between Tl content and petrological type and shock grade are fairly weak or non-existent for the L and LL chondrites dataset is an indication that both internal parent body and impact heating processes probably played a part the evolution of the L and LL ordinary chondrite parent bodies.

3.6 Conclusions

This investigation carried out Tl and Pb concentration and isotope analyses for a comprehensive suite of enstatite chondrites and L- and LL-type ordinary chondrites. In addition, Cd concentration results were obtained for all samples but Cd isotope data only for the enstatite chondrites.

The Pb, Tl, and Cd abundances of the enstatite chondrites display considerable and systematic variability. In particular, the EL3 and EH4 enstatite chondrites have much higher volatile element contents (by 1 – 2 orders of magnitude) than the EH5 and EL6 chondrites. The Pb abundances show a similar offset between samples of petrological types 3 and 4 versus 5 and 6, but some meteorites defy this trend, presumably due to pervasive contamination by terrestrial Pb, as evidenced by Pb isotope compositions plotting in the terrestrial field. Following elimination of patently contaminated samples, the data indicate inverse Pb – Pb isochron ages of 4521 Ma and 4553 Ma for the EH and EL chondrites, respectively, in agreement with previous work.

The Cd isotope compositions of the enstatite chondrites are highly variable with $\varepsilon^{114/110}$Cd values of between +3.0 and +72.9, presumably due to stable isotope fractionation

during episodes of parent body thermal or impact shock metamorphism, or probably both. In contrast, the Tl isotope compositions are less variable, with all but one sample showing ε^{205}Tl values of between –3.3 and +0.8. The anomalous sample with ε^{205}Tl = +22.2 also has an extremely heavy Cd isotope composition.

Considering the ^{204}Pb/^{203}Tl ratios, most samples have values of between about 1.9 and 2.7, but three of the enstatite chondrites show ^{204}Pb/^{203}Tl ratios of >14, presumably due to terrestrial Pb contamination. The five remaining enstatite chondrites with primarily 'meteoritic' Pb might be interpreted to define a ^{205}Pb – ^{205}Tl isochron, in accord with an initial ^{205}Pb abundance similar to that of the carbonaceous chondrites. This interpretation is questionable, however, as a strong correlation of ε^{205}Tl with $\varepsilon^{114/110}$Cd is supported by all but one of the samples. This suggests that the Tl isotope variability may be dominated by stable isotope effects rather than radiogenic ingrowth.

Turning to the L chondrites, the Tl and Cd contents vary by up to nearly two orders of magnitude whereby the less metamorphosed meteorites (of types L3 and 4) tend to have higher concentrations of both of these volatile elements than the more equilibrated type L5 and L6 chondrites. The Pb concentrations are also highly variable but there is no clear correlation with petrological type, most likely as a result of terrestrial Pb contamination, which is particularly evident for samples with low indigenous volatile contents.

The Pb isotope compositions of the L chondrites are highly variable, with samples displaying near-primordial, terrestrial and somewhat radiogenic isotope ratios. When the three meteorites with the most obvious terrestrial Pb contamination are excluded, the remaining results define a Pb – Pb isochron age of 4538 Ma, in accord with published data. The Tl isotope compositions of most samples range between ε^{205}Tl values of between –4.2 and +1.0 but there are two meteorites with anomalous ε^{205}Tl values of –9.9 and –21.3, which most likely reflect stable isotope fractionation. Similarly, three samples have very high ^{204}Pb/^{203}Tl ratios of > 75, most probably due to terrestrial Pb contamination. Considering only those L chondrites which are least likely to have been contaminated by terrestrial Pb or affected by stable Tl isotope fractionation, there is only limited evidence for live ^{205}Pb. Speculatively, data for volatile-rich Mezö-Madaras (L3.7) and Saratov (L4), combined as a two-point isochron would indicate an initial ^{205}Pb/^{204}Pb $\approx (1.0 \pm 0.4) \times 10^{-4}$, equivalent to a cooling age of 50 to 93 Ma.

The Tl and Cd contents of LL chondrites show no systematic variation with petrological type, unlike the L chondrites. In addition, the Pb contents of the LL chondrites shows less variability than for the L chondrites, only varying by less than a factor of 10, most

likely as a result of Pb contamination, particularly of originally Pb-poor meteorites. This conclusion is supported by the Pb isotope compositions of the samples, which vary between near-primordial and terrestrial values. When the most clearly contaminated meteorites are excluded from the dataset, the results yield a Pb – Pb isochron age of 4536 Ma, albeit with a high uncertainty of +156/–176 Ma.

The LL meteorites display the most variable Tl isotope compositions seen in this study, with ε^{205}Tl values of between –12.5 and +14.9, indicative of stable isotope fractionation. An evaluation of the extent to which this variability reflects radiogenic ingrowth from ^{205}Pb decay is not straightforward. The highest observed ^{204}Pb/^{203}Tl ratios are thought to reflect terrestrial Pb contamination whereas the most extreme Tl isotope compositions are most likely an artefact of stable isotope fractionation. Considering, then, only the least metamorphosed (LL3 and 4) and least contaminated samples, there is a hint of a correlation between ε^{205}Tl and ^{204}Pb/^{203}Tl, indicative of in situ decay of ^{205}Pb. If this correlation is speculatively interpreted as an isochron, it yields an initial ^{205}Pb/^{204}Pb $\approx$ (1.3 ± 0.2) x 10^{-4}, equivalent to a cooling age of 49 to 73 Ma for LL chondrites, relative to carbonaceous chondrites.

Although the Cd and Tl isotope compositions of most enstatite chondrites are well correlated, consistent with episodes of open system thermal metamorphism, one EL3 and two EL6 chondrites, which have indications of high pressure shock in their petrological histories, show significant decoupling of Cd and Tl isotope compositions, by exhibiting Tl isotope compositions lighter than would be expected when compared to the remaining correlated enstatite chondrites. In addition, the aforementioned EL3 chondrite, together with an EH4 impact breccia, exhibit enriched Cd and depleted Tl contents when compared to other enstatite chondrites of the same class. The exact mechanisms responsible for the decoupling of Cd and Tl concentrations and isotope compositions in these four enstatite chondrites remain elusive, however, it seems that there may be a link to episodes of high impact shock, which may have resulted in multiple redistributions of labile elements such as Cd and Tl.

In summary, these analyses revealed highly variable ‘meteoritic’ Tl and Cd contents in enstatite and ordinary chondrites, whilst Pb concentrations are strongly affected by terrestrial Pb contamination. In addition, the Tl isotope compositions of at least some but possibly many meteorites were affected by stable isotope fractionation. Together, the issues severely restrict the search for evidence of live ^{205}Pb in enstatite and ordinary chondrites, as well as the application of the ^{205}Pb – ^{205}Tl decay system to chronological investigations. With more basic understanding, the sensitivity with which both Tl and Cd concentrations and isotope

compositions react to secondary mobilisation and alteration processes might be exploited, however, to improve understanding of both nebular and parent body processes that affect element budgets and distributions.

3.7 Declaration

The study detailed in this chapter was completed as part of collaborative research efforts to which the author of this thesis contributed all of the Tl, Pb and Cd isotope measurements and Cd concentrations measurements of the enstatite chondrites together with the data reduction for the Tl and Pb ID measurements for these samples. The author was primarily responsible for developing the interpretations that are presented here for both the enstatite and ordinary chondrites data. Mrs Alison Stunt prepared the enstatite chondrite samples for digestion and carried out Tl and Pb ID measurements and initial rough Cd concentration checks for these samples. Dr Rasmus Andreasen carried out the Tl and Pb concentration and isotope analyses of the ordinary chondrites and supported data interpretation. Mr Barry Coles, Dr Katharina Kreissig and Dr Rasmus Andreasen introduced the author to the use of the clean room laboratory, sample preparation techniques and mass spectrometry. Dr Caroline Smith from the Natural History Museum, London, advised on sample selection and provided all but one of the samples for this work.

Chapter 4 Accretion and core formation in Earth – insights from cadmium metal-silicate partitioning experiments

4.1 Introduction

The work of this chapter is centred on addressing the question of whether Cd isotopes were fractionated when Cd was partitioned between mantle and core during Earth's accretion and concomitant core formation. Metal-silicate partitioning experiments containing silicate, Fe metal and small quantities of Cd were performed at high pressure and temperature using different capsule materials and in a time series. Cadmium isotope analyses of the phases produced in the experiments were then carried out to establish whether Cd isotope fractionation between silicate and metal is an expected result of Earth's core formation, or not.

A number of studies have used techniques of experimental petrology similar to those applied here to determine the quantitative partitioning of various elements between metal and silicate and thereby constrain the behaviour of these elements during core formation (e.g. Ballhaus et al., 2013; Wood et al., 2014). In addition, studies such as, for example, Righter (2011), have attempted to draw together this wealth of published data on metal – silicate partition coefficients to derive a coherent view of the conditions of core formation. However, very few investigations to date have focussed on stable isotope fractionation between metal and silicate phases at conditions relevant for terrestrial core segregation. In particular, no study to date has specifically investigated Cd isotope fractionation during core formation.

4.2 Metal-silicate partitioning experiments samples and procedures

4.2.1 Experimental methods and samples

4.2.1.1 Starting materials and capsules

The compositions of the starting materials, the types of capsule into which the starting materials are loaded, and the run conditions for the metal-silicate partitioning experiments in this study are detailed in Table 4.1. Experimental starting materials consisted of intimate mixtures of Fe (metal and in some experiments also oxide) and a synthesised silicate component with added CdO (between 0.4 and 1.0 wt%), with the metal and silicate components in approximately equal proportions by weight.

Three types of capsule composition were used in the initial experiments: silica, polycrystalline MgO and graphite, with internal capsule diameters of 4.0 mm, 2.5 mm and 2.6 mm respectively. There are advantages and disadvantages in using each of these capsule

types. Silica capsules have a tendency to crack at the applied high experimental temperatures which may result in melt and volatile elements such as Cd being lost, although erosion of capsule material during longer experimental runs is unlikely to affect the basaltic silicate component of the sample as much as other capsule materials.

Table 4.1. Starting materials and experimental run conditions

Experiment	Starting material composition in wt%	Capsule	T °C	P GPa	Dur-ation mins
Initial experiments using different capsule materials					
BW1305 (A299)	49% CMAS + 50% Fe + 1% CdO	Silica	1565	1.5	58
BW1306 (B159)	49% CMAS + 50% Fe + 1% CdO	Graphite	1440	1.5	56
BW1307 (A301)	49% CMAS + 50% Fe + 1% CdO	MgO	1570	1.5	63
BW1308 (A303)	26% CMAS + 26% $Na_2Si_2O_5$ + 50% Fe + 1% CdO	Graphite	1370	1.5	70
Time series experiments					
BW1521 (A643)	20% CMAS + 30% $Na_2Si_2O_5$ + 44% Fe + 5% FeO + 0.4% CdO	Graphite	1235	1.5	4
BW1518 (A640)	20% CMAS + 30% $Na_2Si_2O_5$ + 44% Fe + 5% FeO + 0.4% CdO	Graphite	1235	1.5	12
BW1520 (A642)	20% CMAS + 30% $Na_2Si_2O_5$ + 44% Fe + 5% FeO + 0.4% CdO	Graphite	1235	1.5	30
BW1517 (B251)	20% CMAS + 30% $Na_2Si_2O_5$ + 44% Fe + 5% FeO + 0.4% CdO	Graphite	1235	1.5	66
BW1519 (B252)	20% CMAS + 30% $Na_2Si_2O_5$ + 44% Fe + 5% FeO + 0.4% CdO	Graphite	1235	1.5	200

CMAS (CaO-MgO-Al_2O_3-SiO_2) is a composition close to the eutectic at 1.5 GPa in the system $An_{50}Di_{28}Fo_{22}$ (anorthite-diopside-forsterite) as demonstrated experimentally by Presnall et al. (1978).

Polycrystalline MgO capsules will densify during the experiment and this will help to contain sample material, however erosion of capsule material may transform the basaltic starting material into an MgO-rich ultramafic silicate melt (Righter et al., 2014). Graphite capsules contain the sample materials well during the experiments, however increasing dissolution of carbon from the capsule into the melt is known to reduce Cd and Pb metal-silicate partition coefficients (Marin et al., 2013; Wood and Halliday, 2010) and also reduce significantly the melting point of Fe metal from 1550 °C at 1.5 GPa to around 1200 °C (e.g. Chabot et al., 2008; Chipman, 1972; Liu and Bassett, 1975; Wood, 1993). The C content of the metal component can reach 6 – 7 wt% in experiments using graphite capsules (Righter et al., 2014).

4.2.1.2 Experimental strategy

The initial experiments BW1305 to BW1308 (Table 4.1) were carried out using different capsule compositions and temperatures to determine the effect, if any, of these different run conditions on the volatile loss of Cd and fractionation of Cd isotopes during melting and equilibration of the metal and silicate components. Of additional interest was the effect of capsule composition on the metal and silicate products of the experiments.

Based on the results of those initial experiments, a time series (BW1517 to BW1521; Table 4.1) was then conducted using graphite capsules under consistent run conditions with

run duration being the only variable. The primary goal of the time series experiments was to determine whether there was any equilibrium Cd isotope fractionation during metal-silicate partitioning. In order to do this, it was necessary to achieve full isotopic equilibrium for Cd between the liquid silicate and metal fractions during the experiments in a near closed system, and a time series was the best method to determine if and when such equilibrium was attained. Since the experiments were not primarily used to determine the metal-silicate distribution coefficient of Cd, it was therefore less important that the coefficient was likely to be depressed as a result of C addition to the melt from the graphite capsules (Marin et al., 2013).

Since Cd is highly volatile, it is possible (and was observed) that Cd is lost during the initial experiments run at higher temperatures of 1370 – 1570 °C, which normally ensure that silicate and metal fractions are fully molten. Such volatile loss of Cd would likely result in open system Cd isotope fractionations (Wombacher et al., 2004). It may also hinder isotopic equilibrium, which is required for these experiments. Therefore, in order to minimise volatile loss of Cd from the capsule and any consequent kinetic isotope fractionation, the time series experiments were run at a lower temperature (1235 °C). This was achieved by the addition of a minor component of FeO and a major component of Na_2O, in the form of sodium disilicate ($Na_2O.2SiO_2$), to the starting material, which have the effect of lowering the liquidus of CMAS (Gudfinnsson and Presnall, 2000; Heber et al., 2007; Walter and Presnall, 1994). As explained above, the melting point of the Fe metal component is lowered by the dissolution of carbon from the graphite capsule. The addition of FeO to the starting material also acts to mitigate to some extent the reducing effect of the dissolved C which imposes a very low oxygen fugacity on the melt below that of terrestrial mantle conditions (Holloway et al., 1992; Jakobsson, 2012; Matsukage and Kubo, 2003; Médard et al., 2008; Wood et al., 2014).

4.2.1.3 Experimental apparatus and procedures

The experiments were largely conducted in accordance with the methods and procedures detailed in Wood et al. (2014) which are summarised below. The silicate component CMAS (CaO-MgO-Al_2O_3-SiO_2) was made up close to the eutectic composition in the system anorthite-diopside-forsterite at a pressure of 1.5 GPa which was determined experimentally by Presnall et al. (1978) to be $An_{50}Di_{28}Fo_{22}$. The three individual components forming the eutectic composition were prepared by grinding together reagent-grade SiO_2, MgO, Al_2O_3 and $CaCO_3$ in appropriate proportions. The anorthite and diopside mixtures were

decarbonated at 800 °C for approximately 24 hours after which all three component mixtures were pelletised, fired at 1300 °C and reground. This step was repeated twice to ensure homogeneity. The sodium disilicate component used in the lower temperature experiments was synthesised by combining reagent-grade Na_2CO_3 and SiO_2 using methods similar to those described above.

The experiments themselves used an end-loaded piston-cylinder apparatus at the Department of Earth Sciences, University of Oxford, of the type described by Boyd and England (1960) and containing the internal cell, graphite furnace and thermocouple configurations specified in Wood et al. (2014). However, in this study a pyrophyllite sleeve and SiO_2 glass inner sleeve assembly was used to contain the sample capsule instead of the $BaCO_3$ and SiO_2 sleeve and inner sleeve combination applied previously. Experiments were conducted at a pressure of 1.5 GPa over a range of temperatures from 1235 – 1570 °C (Table 4.1). Since the thermocouples were positioned above the capsule containing the sample, the indicated temperatures were adjusted upwards by 25 °C in order to better reflect the true temperature of the sample inside the capsule. Pressure corrections were made in accordance with McDade et al. (2002). Experiment run times ranged from 4 minutes to 200 minutes and the samples were quenched by cutting the power to the graphite furnace whilst maintaining pressure, which was then released slowly.

4.2.2 Analytical methods

4.2.2.1 Reagents and laboratory procedures

Digestion, anion exchange separation, preparation for mass spectrometry and all critical work on samples, apart from separation of metal and silicate fractions, described in section 4.2.2.2 below and weighing, were carried out in Class 10 laminar flow hoods within the Class 1000 MAGIC clean room facility at Imperial College London using ultrapure reagents and water. Further details of reagents used, cleaning procedures for Savillex® PFA (perfluoroalkoxy) vials for digestion and HDPE and LDPE (high- and low-density polyethylene) bottles for mass spectrometry, procedures for weighing samples and other laboratory procedures and precautions are set out in section 2.2 on page 26.

4.2.2.2 Major element analysis and microscopy

It is a known issue that capsule materials dissolve in the melt during an experiment and therefore have a direct impact on the compositions of the silicate and metal phases (e.g.

Righter et al., 2014). In order to assess the impact of capsule material on the silicate melt, and determine if there were any significant contaminants, such as sulphur, small samples of the silicate fractions of experiments BW1305 to BW1308 (initial experiments using different capsule materials) and BW1317 (time series) were analysed using a JEOL JXA8600 electron microprobe at the Department of Archaeology, University of Oxford using similar configurations and methods to those described in Wood et al. (2014). The following elements were analysed: Na, Mg, Al, Si, P, S, Ca, Ti, Mn, Fe and the results are set out in Table 4.2 on page 114.

In addition, photomicrographs were taken of the initial experiments in reflected light with a Leitz Ortholux II POL-BK microscope using a 2 mm stage micrometer for scale. Quenched products from experiments generally consisted of a solidified Fe metal ball surrounded by a silicate crystalline mass or glass embedded in capsule material, evident in the photomicrographs in Figure 4.2 on page 117.

4.2.2.3 Separation of metal and silicate fractions

Separation of the experimental products was carried out in a Bassaire benchtop laminar flow workstation in laboratories separate from the Class 1000 clean room facility due to the risk of dust contamination, particularly with potentially high Cd content, during separation procedures. In addition, a personal respirator was worn due to the risk of inhaling airborne particles (with possibly relatively high contents of toxic Cd) from the samples.

The sample pellets, comprising solidified metal balls in a silicate crystalline or glass mass sometimes also still embedded in capsule material, were initially easily split into a number of glass fragments, capsule material and (usually) one metal ball by very gently tapping the samples using a small porcelain pestle and mortar. A thin spatula blade cleaned with double-distilled ethanol was used to further separate any components stuck together or stuck to capsule material. The pestle and mortar was thoroughly cleaned prior to use on each sample by grinding high-purity quartz sand in the mortar wetted with double-distilled ethanol and flushing away ground particles with 18.2 MΩ.cm grade Milli-Q® water and double-distilled ethanol and repeating the grinding and cleaning process twice. Ground particles were not reused to avoid cross-contamination.

The glass fragments and metal ball were picked with the aid of a 10x glass hand lens and transferred to acid-cleaned 60 ml Savillex® PFA (perfluoroalkoxy) vials, one for metal and one for silicate. The vials were weighed accurately with and without the samples using

either a Sartorius AX224 or a Mettler Toledo AX250 DeltaRange® analytical balance reading to the nearest 0.1 mg. Sample material recovered ranged from 10 mg to 35 mg for the metal fraction and 2 mg to 17 mg for the silicate fraction.

4.2.2.4 Acid digestion

Different digestion protocols, employing 60 ml Savillex® PFA vials, were used for metal and silicate fractions. The metal fractions were digested in aqua regia comprising 2 ml 16 M HNO_3 and 6 ml 6 M HCl (1:3 ratio) and the silicate fractions, which included a sample of the Cd-doped CMAS starting material, were digested in 2 ml 16 M HNO_3 and 4 ml 28 M HF (1:2 ratio). Matrix test samples comprising two aliquots of NIST 361 steel, one with added Cd NIST 3108 and one without, were also digested using the same method applied for metal fractions. Acid blanks were also included for both digestion methods. All digested samples were refluxed in closed vials on a hotplate for 3 to 7 days at temperatures increasing to 130 °C and in most cases this was sufficient to digest the samples completely without leaving a residue. Temperatures were increased gradually and vials opened periodically in the laminar flow hood to minimise build up of pressure within the vials from reaction gases, particularly from the aqua regia solutions.

A few samples had a tiny amount of fluoride or very fine carbon residues left over from the HF digestion and graphite capsules respectively. Several metal samples had a few tiny residual specks of translucent material, assumed to be residual silicate glass lodged in the metal balls, which were very difficult to remove completely by physical separation. The advantage of the digestion method used is that any unwanted silicate material in the metal fractions is not digested.

All sample solutions were evaporated to dryness, re-dissolved in 20 ml 6 M HCl and refluxed in closed vials on a hotplate for 3 to 4 days at temperatures of 120 °C to 160 °C. All laboratory hotplates used for acid refluxing, digestion and drying down were Teflon® coated and situated within Class 10 laminar flow hoods in the clean room facility although, due to the potentially high concentrations of Cd in these samples, digestion work was purposely done in a laboratory separate from the one used for low concentration Cd work.

The few samples with tiny amounts of residue were centrifuged in acid-cleaned 15 ml polypropylene tubes although it was found that this made little difference due to the fineness of the residues. Most samples did not require centrifuging, however.

4.2.2.5 Aliquoting samples for isotope composition analysis

A major problem posed by this suite of samples is that most had such high Cd concentrations so that substantial dilution or aliquoting of the samples was needed to ensure that the ion beam intensities during mass spectrometry analyses did not saturate the Faraday collectors of the instrument during analysis. For example, several of the metal fractions had as much as 1.1 to 1.2% Cd and the Cd-doped CMAS starting material contained 1.8% Cd. The first step was to establish the true Cd concentration of the samples by analysing a very small aliquot.

Based on estimates of the likely concentrations of Cd in the samples derived from estimating the metal-silicate partition coefficients and loss of Cd from volatilisation and applying these factors to the original weighed proportion of CdO in the starting materials, aliquots of 0.25% to 1% (v/v) were taken from the samples for an initial 'concentration check'.

These aliquots were doped with 500 to 900 µl of the ^{111}Cd – ^{113}Cd double spike solution (101 µg/g see section 2.6.2 on page 40) and weighed accurately, before and after. Thereafter, the aliquots were evaporated to dryness and taken up in 500 µl 3M HCl, after which Cd was isolated using only the second stage anion exchange chemistry described in Table 2.1 on page 28. A further stage of extraction chromatography to remove Sn and Mo, which may cause isobaric and molecular interferences (Table 2.1), was considered unnecessary since the starting materials for the experiments were made from reagent grade materials and therefore unlikely to contain significant trace elements. The Cd concentrations of these aliquots were determined using the double spike data reduction methods described in section 2.5.2.1 on page 34 and isotope dilution calculations.

Based on the initial measured concentrations of Cd in each sample, aliquots for isotope composition (IC) analysis ranging from 30% to 100% (v/v) were taken for samples with lower Cd concentrations from experiments in silica and MgO capsules, which featured significant loss of Cd by volatilization. Aliquots of 0.6% to 18% (v/v) were taken from samples with higher Cd contents, which were from experiments in graphite capsules at generally lower temperatures, such that volatile loss of Cd was significantly reduced. Aliquots were chosen so that the final sample solutions for analysis on the mass spectrometer (in up to 50 to 55 ml 0.1 M HNO_3) had a total Cd concentration of about 80 ppb (including added Cd double spike) to produce maximum ion beam intensities of about 5 – 7 V for ^{111}Cd.

A precisely weighed ^{111}Cd – ^{113}Cd double spike solution, prepared and calibrated as described in section 2.6 starting on page 38, was added to the aliquots, to produce a spike sample ratio of 1.2 to 1.25. The optimum spike-sample ratio is about 1, based on the results of error propagation analyses as described in section 2.5.2.2 on page 36, but excellent results can be obtained for all samples with spike-sample ratios of between 1 and 2 (see Figure 2.2 on page 36). However, uncertainties associated with the double spike data reduction increase exponentially as spike-sample ratios fall below 1. Therefore, a spike-sample ratio calculated to be well over 1 was chosen to avoid the actual spike-sample ratio falling below 1, perhaps due to uncertainties in the weighing of sample, aliquots and double spike and in the Cd concentrations determined by ID.

Before separation and purification of the element, described in the next section, the double-spiked aliquots were evaporated to dryness, re-dissolved in 10 ml 3 M HCl, and refluxed on a hotplate to ensure complete equilibration of natural and spike-derived Cd.

4.2.2.6 Cd separation and purification

The sample aliquots for IC analysis were passed through exactly the same anion exchange and extraction chromatography protocols described in section 2.1 on page 26 and summarised in Table 2.1. Although, as mentioned in section 4.2.2.5 above, the samples were unlikely to have a significant trace element content, the extraction chromatography with Eichrom TRU® resin was considered necessary to remove any traces of Mo, and particularly Sn, which may be in the samples or in the acids used for digestion and chemistry. No significant isobaric interferences from Sn and In on ^{112}Cd, ^{113}Cd and ^{114}Cd were detected from the monitoring of ^{117}Sn and ^{115}In during analysis runs, attesting to the efficiency of the chemical separation procedures in removing traces of these elements. The Cd yield of the chemical separation procedures for these samples averaged 87%, and ranged from 70 to 100%, with the exception of one sample, which had a lower yield (40%).

4.2.2.7 Procedural blanks

Acid blanks were processed through the digestion and chemical separation procedures in the same way as samples. The subsequent measurements of their cumulative Cd content were carried out in accordance with the techniques outlined in section 5.2.2.2 on page 142, by scanning masses 110 to 114 using the electron multiplier (fitted with an ion counting system) and comparing the ion beam intensities to background levels.

The acid blanks relating to the samples for the initial experiments (BW1305 – BW1308) had approximately 1 pg Cd whereas those relating to the time series experiments (BW1517 – BW1521) contained around 20 pg Cd. The blank content of the samples as a proportion of indigenous Cd present was approximately 10 to 12 ppm (0.0010 to 0.0012%) for the initial experiments, about 1 to 9 ppm (0.0001 to 0.0009%) for the time series experiments, including the analyses Cd-doped CMAS starting material. The blank content of the matrix test (section 4.2.4.1 below) was approximately 35 ppm (0.0035%) of the Cd content derived from the added NIST SRM 3108 Cd.

These results are remarkably low considering the acid blanks were processed alongside samples with Cd contents as high as 1.8% and thereby confirm that there was unlikely to have been any significant cross-contamination of samples. Furthermore, the blank content of the samples was negligible so that no blank correction of the isotopic and concentration data was needed.

4.2.3 Mass spectrometry

4.2.3.1 Instrumentation

All isotope measurements were carried out using a Nu Plasma HR MC-ICP-MS (Nu Instruments, part of the Ametek, Inc. Materials Analysis Division), at the Imperial College London MAGIC laboratory facility. Desolvating nebulisers were used to introduce sample solutions in 0.1 M HNO_3 as a dry aerosol into the ICP torch with three different models operated at different times: the DSN-100 (Nu Instruments), the Aridus and the Aridus II (Teledyne CETAC Technologies). Both glass and PFA nebulisers were used with a sample uptake rate generally in the range 90 – 125 µl/min. Further details of how the instrument was set-up are given in section 2.4.1 on page 29.

The source-defining slit was positioned at the widest setting of 0.3 mm giving a mass resolution (M/ΔM) of about 400 and an instrumental sensitivity generally between 200 and 280 V/ppm Cd (averaging approximately 230 V/ppm) during the measurement sessions for the these samples.

Tuning procedures were exactly as described in section 2.4.1: the mass spectrometer was tuned for maximum beam intensity and optimum peak shape, peak-top flatness and coincidences on the collectors monitoring Cd isotopes ^{111}Cd to ^{114}Cd. Table 2.2 on page 39 shows the full collector configuration including those used for monitoring the isobaric interferences Sn and In. A detailed explanation of the rationale for choosing these specific Cd

isotopes to analyse in the context of avoiding isobaric interferences such as Pd, Sn and In is set out in section 2.6.1 on page 38.

4.2.3.2 Zero-epsilon standard and reporting Cd isotope compositions

All Cd isotope compositions are given using epsilon notation, which reports deviations of the measured isotope ratio from the standard NIST SRM 3108 Cd in parts per 10,000 using Eq. 2.1. A full explanation of this notation, the reasons for using the NIST SRM 3108 Cd standard and the selection of which Cd isotope ratio to use for reporting Cd isotope variations are set out in section 2.4.2 starting on page 31.

4.2.3.3 Cd isotope composition measurements

An aliquot of 1 to 5% v/v of the sample eluate after chemical separation was analysed on the mass spectrometer to determine Cd content, the spike-sample ratio, and the approximate yield of Cd from chemistry. This data was used to make up solutions of the samples to concentrations of 80 to 100 ppb for Cd isotope composition analysis by diluting with 20 to 50 ml 0.1M HNO_3. Appropriate NIST SRM 3108 Cd standard solutions were made up to match the concentrations and spike-sample ratios of the samples for sample-standard bracketing during analysis in order to reduce systematic errors (Wombacher et al., 2003). The spike-sample ratios achieved were: 1.31 to 1.35 for samples from the initial experiments (BW1305 – BW1308) and 1.26 to 1.35 for samples from the time-series experiments, near to the optimum spike-sample ratio illustrated in Figure 2.2.

4.2.4 Analytical precision

4.2.4.1 Test for matrix effects in metal samples

So-called ‘matrix effects’ refer to various instabilities during sample measurements by ICP-MS, which are due to residual matrix in the sample solution, and result in, for example, fluctuations in the instrumental mass bias or the ion beam intensity, isotope data with large uncertainties, a systematic isotopic offset between samples and bracketing standards, or a combination of these anomalies. The matrix could be derived from sample material other than the element of interest still remaining after chemical separation and purification procedures or (organic) material leached from the resins used in such procedures. Such matrices are absent from bracketing standards since these are essentially solutions of highly pure metals

which have not passed through any resins used in chemical separation and purification (e.g. Nielsen and Rehkämper, 2012; Pietruszka and Reznik, 2008; Poirier and Doucelance, 2009; Shiel et al., 2009).

The reliability and reproducibility of Cd isotope composition measurements of silicate samples has been well established, however metal samples have not been tested before with the chemical separation and purification procedures used in this study (sections 4.2.2.6 and 2.1 and Table 2.1). To this end, two samples of NIST standard reference material (SRM) 361 AISI 4101 steel were analysed. This SRM is a low alloy steel containing 0.383 wt% C and 95.6 wt% Fe, the remaining approximately 3 wt% consisting mainly of Ni, Cr and Mo (NIST analysis). In detail, two aliquots of the SRM, weighing approximately 120 mg each, were digested in aqua regia consisting of 2 ml 16 M HNO_3 and 6 ml 6 M HCl (1:3 ratio) and refluxed for 3 days at increasing temperatures from 70 °C to 130 °C.

The dissolved samples were then evaporated to dryness before being re-dissolved in 9 ml 6 M HCl and refluxed at 140 °C to 150 °C for 4 days and dried down again. One of these samples acted as a 'blank' to determine the Cd content of NIST SRM 361, and this was kept away from any other samples containing Cd. The second sample was doped with NIST SRM 3108 Cd and ^{111}Cd – ^{113}Cd double spike solutions, resulting in a total Cd content of 1400 ng at a spike-sample ratio of 1.25. Both samples were evaporated to dryness, re-dissolved in 10 ml 3 M HCl and passed through the same steps of chemical separation and purification as the samples from the experiments described in this chapter (see sections 4.2.2.6 and 2.1 and Table 2.1).

The NIST SRM 361 steel sample without Cd added was analysed in the same way as the procedural blanks referred to in section 4.2.2.7 above. The total Cd content of this sample was 26 pg, similar to the Cd content of 20 pg for the procedural blank. This is an indication that there is no significant Cd content in the NIST SRM 361 steel itself (< 50 pg/g based on these results) and thus the Cd isotope composition of the Cd-doped NIST SRM 361 steel should be identical to the zero-epsilon standard NIST SRM 3108 Cd.

The results of analysing the separated and purified Cd-doped NIST SRM 361 steel solution are shown in Figure 4.1. There is a very slight drift in the Cd isotope compositions of the standards (light and dark grey circles) towards lighter values in both analysis sessions. There appears to be no clear systematic isotopic offset of the sample measurements (red diamonds) compared to standards, nor any reduction in the precision of the sample measurements and subsequently measured standards, either of which might indicate

instrumental instability caused by residual matrix in the sample delivery system of the instrument.

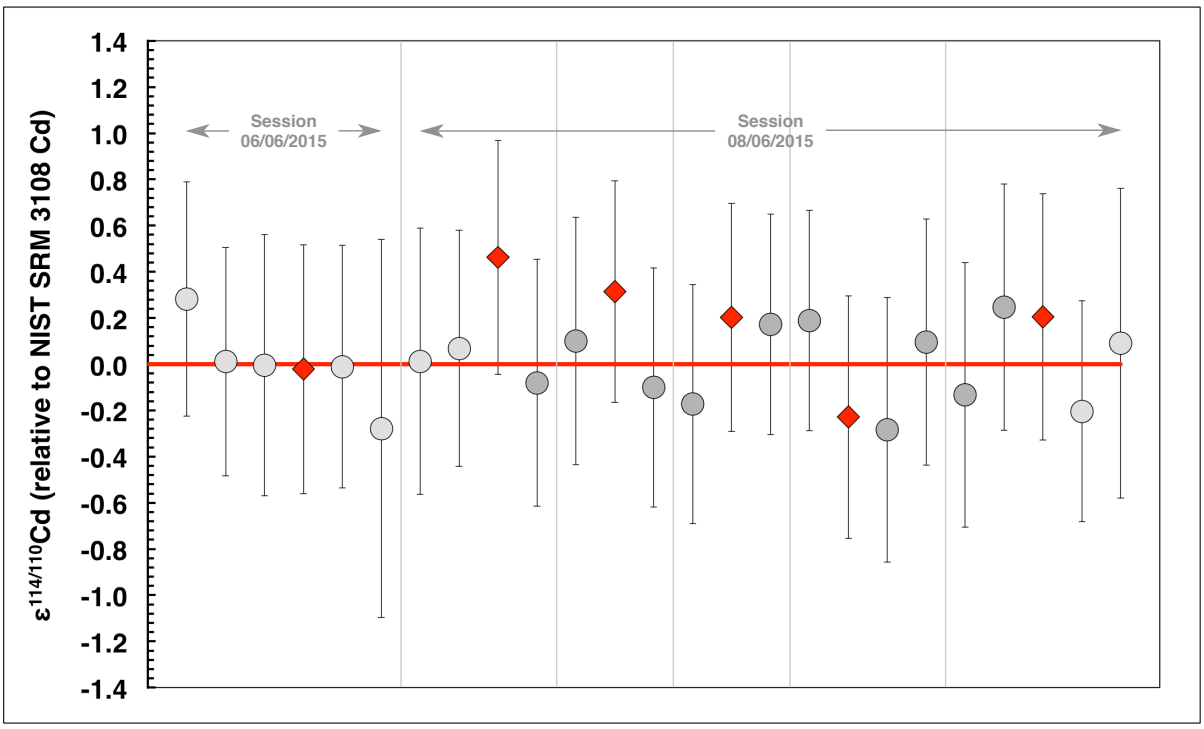


Figure 4.1. Results of matrix test showing measurements of a Cd solution separated and purified from a solution of digested NIST SRM 361 steel doped with NIST SRM 3108 Cd and ^{111}Cd – ^{113}Cd double spike solutions (represented by the red diamonds) and analysed in two measurement sessions. These are bracketed with measurements of NIST SRM 3108 Cd standard solutions with each bracketing group separated by vertical grey lines in the plot. Single measurements of standards used in the bracketing of two samples, one after the other, are indicated by the dark grey symbols. Standard measurements used for bracketing only one sample are marked by light grey symbols. Uncertainties are internal errors shown at the 2se level.

Further, the average isotope composition of the Cd-doped NIST SRM 361 steel in the test is ε^{114}Cd = +0.17 ± 0.21 (2se, n=6) which is identical within error to the isotope composition of the NIST SRM 3108 Cd dopant of ε^{114}Cd = 0.00. The conclusion from this matrix test is that the separation and purification procedures described in section 4.2.2.6 above appear to be effective in removing residual matrices in metal samples which might cause instrumental instabilities.

4.2.4.2 Long-term precision monitored by a secondary isotopic reference material

As explained in section 2.7.1 on page 43, solutions of the BAM-I102 certified isotopic reference material, made up to approximately the same concentrations and spike-sample ratios as the samples, were routinely measured, usually at the beginning and end of sample measurement sessions, in order to assess the accuracy of analytical and data reduction procedures during that session.

The results of all measurements of BAM-I102 used to assess the accuracy of sample measurements described in this study and in Chapter 5 are summarised in Figure 2.3 on page 45. The arithmetic mean of these measurements ($\varepsilon^{114/110}$Cd = –13.38 ± 0.71 2sd; n = 48) is almost identical to the weighted average of BAM-I102 measurements from seven laboratories ($\varepsilon^{114/110}$Cd = –13.32 ± 0.43 2se, n = 179) compiled by Abouchami et al. (2013). The overall conclusion from this is that Cd isotope measurements for the samples both in this Chapter and in Chapter 5 are reproducible from one measurement session to another and can be readily compared with measurements from other laboratories.

4.2.4.3 Analytical precision in this study

The Cd isotope composition analytical uncertainties are based on the weighted averages of the internal errors for individual runs (2se), the calculation of which is fully explained in section 2.7.1 on page 43.

An assessment of the analytical uncertainties achieved for the Cd isotope composition measurements relating to the Cd metal silicate partitioning samples described here and the Cd terrestrial and meteoritic samples of Chapter 5 are set out in section 2.7.3 on page 45. A comparison is also made in section 2.7.4 starting on page 48 between the analytical uncertainties achieved for the samples covered in this chapter and Chapter 5 and those achieved by Ripperger and Rehkämper (2007) and Xue et al. (2012), the former using the same type of instrument and the latter using the exact same instrument as in this study (section 2.4.1). Both studies cited also used the same Cd double spike method as this study (section 2.5.2). The conclusion from this is that the analytical precisions achieved in this study are in line with the precisions reported by those workers in their studies.

4.3 Results and discussion

4.3.1 Major element analysis

Data from major element analyses of the silicate phases from experiments BW1305 to BW1308 (initial experiments using different capsule materials) and BW1517 (time series) are set out in Table 4.2 below together with the compositions of the silicate portion of the starting materials of the experiments for comparison.

4.3.1.1 General observations and Fe content in the silicate phases

The major element analyses indicate that there are no significant contaminants (S, P, Ti, Mn) either in the starting materials or from the capsules or apparatus. Although the silicate portions of the starting materials have no Fe content (Table 4.2), the analyses indicate that some Fe has partitioned into the silicate phases from the Fe metal portion of the starting material during the experiment. The FeO content of the silicate phases varies approximately from 5 to 18 wt%, which equates to a range of Fe concentrations of between 4 and 14 wt%, and is particularly high in the graphite capsule experiments (FeO: 8 to 18 wt%). The concentration of Fe in the metal phase was not measured but is reasonably approximated as 100% for the silica and MgO capsules and as 95% (± 5%) for the graphite capsules, since it is known that some C from the graphite capsules dissolves in the metal phase (e.g. Righter et al., 2014).

The Fe metal-silicate partition coefficients, $D_{Fe}^{MET/SIL}$, can then be calculated using Eq. 4.1 from the measured concentrations of Fe in the silicate phases and the approximate Fe contents of the metal phases, with square brackets denoting concentrations:

$$D_{Fe}^{MET/SIL} = \frac{[Fe]_{METAL}}{[Fe]_{SILICATE}} \quad \text{Eq. 4.1}$$

The $D_{Fe}^{MET/SIL}$ data, shown in Table 4.3 below, are high for the silica and MgO capsule experiments at about 25 to 26, but lower and more variable for the graphite capsule experiments (at about 7 to 16) indicating a greater propensity for Fe in the melt to partition to the silicate phase in the graphite capsule experiments.

4.3.1.2 Dissolution of capsule material

The silicate phase from the silica capsule experiment (BW1305) has a high SiO_2 content of 63 wt%, compared to about 40 wt% for the graphite and MgO capsule experiments (BW1306 and BW1307), carried out using exactly the same starting material (49% CMAS + 50% Fe + 1% CdO). Since this starting material only has 47 wt% SiO_2 (Table 4.2), it is clear that silica capsule material has dissolved in the silicate melt of experiment BW1305. Similarly, the silicate phase from the MgO capsule experiment shows variable and high levels of MgO: 14 to 54 wt% with an average of 28 wt%, compared to 11 and 14 wt% for the silica and graphite experiments using the same composition of starting materials.

Table 4.2. Electron microprobe (EMP) analyses of major elements in the silicate phases of selected experiments.

Experiment	Starting material composition	Capsule	Temp (°C)	Duration (mins)	n		Na_2O	MgO	Al_2O_3	SiO_2	P_2O_5	S	CaO	TiO_2	MnO	FeO	CdO	Total	NBO/T (estimated)
BW1305 (A299)	49% CMAS + 50% Fe + 1% CdO	Silica	1565	58	25	wt%	0.03	11.2	10.4	63.4	0.01	0.01	10.1	0.01	0.01	5.20		100.3	0.6 - 0.7
						σ	*0.02*	*0.1*	*0.1*	*0.4*	*0.01*	*0.02*	*0.1*	*0.01*	*0.02*	*0.14*			
BW1306 (B159)	49% CMAS + 50% Fe + 1% CdO	Graphite	1440	56	34	wt%	0.04	14.8	15.5	41.5	0.02	0.01	15.5	0.01	0.01	10.7		98.0	1.0 - 1.3
						σ	*0.02*	*1.2*	*0.8*	*0.7*	*0.02*	*0.02*	*0.8*	*0.02*	*0.02*	*0.6*			
BW1307 (A301)	49% CMAS + 50% Fe + 1% CdO	MgO	1570	63															
Overall results					35	wt%	0.06	28.2	10.3	39.9	0.02	0.01	15.9	0.01	0.01	4.89		99.3	2.0 - 2.2
						σ	*0.03*	*14.0*	*5.7*	*0.7*	*0.01*	*0.01*	*8.7*	*0.01*	*0.01*	*0.61*			
Low Mg phases (14 - 40% MgO)					27	wt%	0.08	21.2	13.2	39.7	0.01	0.01	20.4	0.02	0.01	5.19		99.7	1.6 - 1.8
						σ	*0.01*	*5.6*	*1.9*	*0.4*	*0.01*	*0.01*	*3.2*	*0.01*	*0.01*	*0.23*			
High Mg phases (50 - 54% MgO)					8	wt%	0.00	51.9	0.40	40.8	0.02	0.01	1.06	0.00	0.01	3.85		98.1	>3.7
						σ	*0.00*	*1.4*	*0.19*	*0.8*	*0.01*	*0.01*	*0.16*	*0.00*	*0.01*	*0.09*			
BW1308 (A303)	26% CMAS + 26% $Na_2Si_2O_5$ + 47% Fe + 1% CdO	Graphite	1370	70	20	wt%	14.9	8.42	7.90	53.0	0.01	0.01	7.48	0.01	0.01	7.72		99.5	1.0 - 1.2
						σ	*0.5*	*0.14*	*0.09*	*0.5*	*0.02*	*0.02*	*0.10*	*0.02*	*0.02*	*0.12*			
BW1517 (B251)	20% CMAS + 30% $Na_2Si_2O_5$ + 44% Fe + 5% FeO + 0.4% CdO	Graphite	1235	66		wt%	9.42	5.31	5.18	48.0	n.m.	0.01	5.00	n.m.	n.m.	17.8		90.7	0.8 - 1.3
						σ	*0.03*	*0.04*	*0.05*	*0.1*		*0.01*	*0.03*			*0.1*			
Composition of the silicate portion of starting material for different experiments:																			
BW1305 - 1307	97.9% CMAS + 2.1% CdO						0.00	17.4	17.2	47.0	0.00	0.00	16.2	0.00	0.00	0.00	2.13	100.0	
BW1308	49.4% CMAS + 48.7% $Na_2Si_2O_5$ + 1.9% CdO						15.9	8.78	8.66	56.6	0.00	0.00	8.18	0.00	0.00	0.00	1.92	100.0	
BW1517 - 1521	39.3% CMAS + 59.8% $Na_2Si_2O_5$ + 0.9% CdO						19.5	7.01	6.91	59.2	0.00	0.00	6.53	0.00	0.00	0.00	0.86	100.0	

Major element analyses showing average wt% and standard deviation (σ) of the EMP runs (n). In analysing the silicate phase of experiment BW1307 (MgO capsule) a wide range of compositions, particularly of MgO, were encountered. The results were divided between low and high MgO runs as shown in order to reflect this heterogeneity better. NBO/T (see section 4.3.1.3) is calculated according to the method of Mills et al. (2011) and is estimated as proportions of FeO and Fe_2O_3 are unknown (indicated FeO = total Fe). n.m. = not measured.

In Table 4.2, the individual results for the electron microprobe analyses on the MgO capsules were divided into two broad phases: low Mg (14 to 40 wt%) and high Mg (50 to 54 wt%). The 'high MgO' phase has very low Al_2O_3 and CaO contents (1 wt% or less) compared to the 13 and 20 wt% in the 'low MgO' phase, partly due to the significant dilution of the melt in the former with dissolved MgO capsule material. These data may indicate that there has been considerable yet seemingly unequilibrated dissolution of MgO from the capsule wall into the experimental melt, particularly when the high MgO concentrations of the silicate phase (averaging 28 wt% overall) are compared to the original MgO content of the starting material of 17 wt%.

Another factor may be the tendency for experimental products in the MgO capsules to form a mixture of glass and quench crystals in the silicate phases, as indicated by Wood and Halliday (2010). These authors also reported heterogeneity in major element compositions for those capsules compared to the less scattered major element data for the graphite capsule experiments in which a homogeneous quenched glass was formed.

4.3.1.3 Silicate melt polymerisation

A measure of the extent of polymerisation in a silicate melt is the ratio of the number of non-bridging oxygen atoms to the number of oxygen atoms in tetragonal coordination in a silicate structure, abbreviated to NBO/T (e.g. Mysen, 1990). This parameter has been calculated in accordance with the formula of Mills et al. (2011), for the experimental silicate phases for which major element data has been measured by electron microprobe, and the results shown in Table 4.2.

Calculation of NBO/T requires knowledge of the proportions Fe ions in the divalent FeO and trivalent Fe_2O_3 forms in a silicate melt, however electron microprobe analysis cannot distinguish between these forms, and simply expresses total Fe in the form FeO. Therefore, in this study, the NBO/T parameter can only be estimated and hence has been expressed as a range of possible values in Table 4.2 by calculating NBO/T for a range of possible FeO and Fe_2O_3 contents in the melt. The NBO/T value is relevant to the quenched silicate glasses analysed here because the structures of the silicates in the glass are not significantly altered by quenching and thus are substantially the same as in the melt (Mysen, 1983; Seifert et al., 1981; Taylor et al., 1980).

The essential building block in a silicate structure is the SiO_4^{2-} tetrahedron, which, at one extreme, forms a fully polymerised three-dimensional structure in pure SiO_2 with an

NBO/T parameter of 0. As metal cations are added to the structure, Si – O bonds are broken and the silicate structure is depolymerised until, at the other extreme, the SiO_4^{2-} combines on its own with a cation such as Mg^{2+} or Fe^{2+} to form forsterite or fayalite respectively. This fully depolymerised silicate has an NBO/T parameter of 4. Cations such as Al^{3+} and Fe^{3+} can also substitute for the Si^{4+} ion in the structure, provided there is another charge-balancing cation (e.g. Mills et al., 2014; Mysen, 1983; Mysen, 1990). As a guide, approximate NBO/T values for basalt, komatiite and peridotite are 1.0, 1.7 and 2.8 respectively (Righter et al., 2014).

Turning to the results in Table 4.2, experiment BW1305 has an abnormally high SiO_2 content (63 wt%), most likely from the dissolution of silica capsule material, and also the lowest of the NBO/T values calculated, 0.6 to 0.7, indicating the silicate phase is nearly fully polymerised. The high Mg phase in experiment BW1307 has a very high NBO/T value of above 3.7, indicating the melt was almost completely depolymerised, consisting probably of isolated monomers, such as forsterite. Even the low Mg phase in this experiment has an NBO/T value higher (1.6 to 1.8) than those for the silica and graphite capsule experiments, suggesting generally a greater degree of depolymerisation in the Mg-rich melt.

These data suggest that the dissolution of the silica and MgO capsule wall had a profound effect on the structure and composition of the silicate melts. The MgO capsule, in particular, produced an MgO-rich ultramafic melt and, whilst this feature may be useful to model partitioning in such a silicate melt as an analogue for Earth's mantle (Wood et al., 2008), these experiments show that it is difficult to control the composition of the melt using silica and MgO capsules.

4.3.2 Physical descriptions of experimental run products

The metal and silicate products from each experiment were examined carefully using a hand lens (x10) during separation (section 4.2.2.2 above) to determine whether the phases had melted completely. Examples of the experimental products for the initial experiments using different capsule materials are shown in the photomicrographs of Figure 4.2 below which were taken in reflected light.

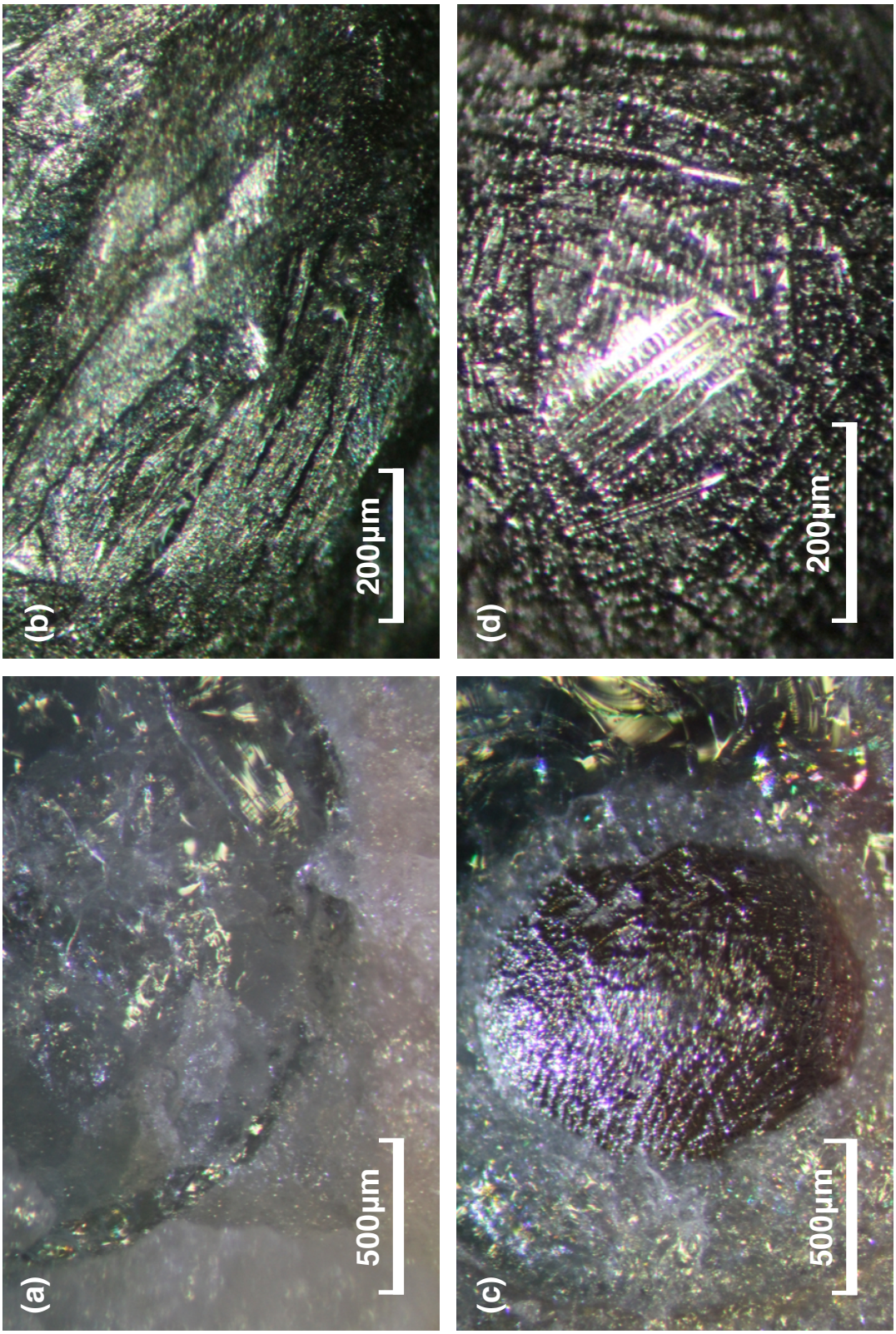


Figure 4.2. Photomicrographs of experimental run products. (a) Experiment BW1305 showing the curved interface between the quenched silicate glass sample and silica capsule. Note the ingress of capsule material into the sample. (b) Experiment BW1306 showing the quench texture of the flattened Fe metal solid. (c) Experiment BW1307 showing the quench texture exhibited by the near spherical metal ball and also silicate crystalline and glass quench textures. The curved interface between the crystalline silicate sample and the MgO capsule is visible on the left hand side. (d) Experiment BW1308 showing the almost dendritic quench texture of the spherical metal Fe ball. The blueish tinge exhibited by silicate material in panels (a) and (c) is due to Fe content.

All samples except for experiment BW1521 (duration 4 minutes, graphite capsule) had a well-defined metal fragment or ball, which had clearly quenched from a liquid phase. The experiment with the longest duration, BW1519 (200 minutes), contained a perfectly spherical metal ball, similar to the one in Figure 4.2 (c), whereas the metal phase was kidney-shaped in experiment BW1305 (duration 58 minutes, silica capsule) and more flattened in experiment BW1306 (duration 56 minutes, graphite capsule). Figure 4.2 (c) and (d) illustrates some very interesting almost dendritic quench textures found on the surface of the metal balls in experiments BW1507 and BW1508. The exception was experiment BW1521 (duration 4 minutes, graphite capsule) where the metal phase was very friable and broke into small pieces of metal mixed with possibly unequilibrated powdery starting material. Although experiment BW1518 (duration 12 minutes, graphite capsule) had a clearly defined metal phase, there were some small silicate particles embedded in the metal, which were impossible to remove during the separation process.

All experiments, including BW1521, had clear or translucent silicate glass, which broke into small shards during the separation process, indicating that the silicate fraction had quenched from the liquid phase. Some silicate and metal fractions from the graphite capsule experiments exhibited contamination from eroded capsule material evident in the form of embedded graphite particles or silicate shards with black outer edges. The metal fragment in experiment BW1518 (duration 12 minutes) had an encircling ring of graphite, which was later seen undigested in the aqua regia solution of this sample along with some undigested silicate particles (section 4.2.2.4 above). Interestingly, the experiment with the longest duration, BW1519 (200 minutes), showed very little physical evidence of graphite contamination possibly indicating that most of the eroded carbon capsule material had dissolved in the metal phase.

The overall conclusion to these observations is that all experiments had molten metal and silicate phases. The melting and equilibration of phases was almost certainly incomplete in the 4 minute experiment (BW1521) and may have also been incomplete in the 12 minute experiment (BW1518). This is consistent with the findings of Tuff et al. (2011) who reported that chemical equilibrium in 2 to 3 mm internal diameter MgO capsules was approached within 15 minutes.

Table 4.3. Cd isotope compositions, concentrations and metal-silicate partition coefficients for experiments

Experiment	Starting material composition	Capsule	Temp (ºC)	Duration (mins)	Phase	$\varepsilon^{114/110}$Cd (relative to NIST SRM 3108 Cd	$\varepsilon^{114/110}$Cd (relative to Cd-doped CMAS)	2se	$\Delta\varepsilon^{114}Cd_{MET-SIL}$ ($\varepsilon^{114}Cd_{MET} - \varepsilon^{114}Cd_{SIL}$)	2se	[Cd] (µg/g) (a)	2sd	$D_{Cd}^{MET/SIL}$ (b)	2sd	$D_{Fe}^{MET/SIL}$ (c)	2sd	K_D (d)	2sd
Initial experiments using different capsule materials																		
BW1305 (A299)	49% CMAS + 50% Fe + 1% CdO	Silica	1565	58	Metal	10.27	11.31	0.46	0.41	0.71	32.5	0.5	1.8	0.1	24.8	1.4	0.07	0.01
					Silicate	9.87	10.90	0.55			18.1	1.1						
BW1306 (B159)	49% CMAS + 50% Fe + 1% CdO	Graphite	1440	56	Metal	-0.52	0.52	0.48	0.43	0.69	11,416	240	1.7	0.1	11.4	1.4	0.15	0.02
					Silicate	-0.95	0.09	0.50			6,605	185						
BW1307 (A301)	49% CMAS + 50% Fe + 1% CdO	MgO	1570	63	Metal	28.34	29.38	0.48	-0.28	0.73	164	3	3.5	0.7	26.3	6.5	0.13	0.04
					Silicate	28.62	29.66	0.55			47.2	9.9						
BW1308 (A303)	26% CMAS + 26% $Na_2Si_2O_5$ + 47% Fe + 1% CdO	Graphite	1370	70	Metal	-0.84	0.20	0.32	-0.18	0.56	12,018	397	3.7	0.3	15.8	0.9	0.23	0.02
					Silicate	-0.66	0.38	0.45			3,283	269						
Time series experiments																		
BW1521 (A643)	20% CMAS + 30% $Na_2Si_2O_5$ + 44% Fe + 5% FeO + 0.4% CdO	Graphite	1235	4	Metal	n.m.	n.m.	n.m.	n.m.	n.m.	3,554	178	1.1	0.3				
					Silicate	n.m.	n.m.	n.m.			3,304	991						
BW1518 (A640)	20% CMAS + 30% $Na_2Si_2O_5$ + 44% Fe + 5% FeO + 0.4% CdO	Graphite	1235	12	Metal	-0.90	0.13	0.26	-0.52	0.41	3,452	69	0.82	0.16				
					Silicate	-0.39	0.65	0.31			4,193	834						
BW1520 (A642)	20% CMAS + 30% $Na_2Si_2O_5$ + 44% Fe + 5% FeO + 0.4% CdO	Graphite	1235	30	Metal	-1.01	0.03	0.31	-0.11	0.44	2,256	79	0.46	0.03				
					Silicate	-0.89	0.14	0.32			4,889	240						
BW1517 (B251)	20% CMAS + 30% $Na_2Si_2O_5$ + 44% Fe + 5% FeO + 0.4% CdO	Graphite	1235	66	Metal	-1.37	-0.33	0.33	-0.89	0.48	2,258	84	0.52	0.03	6.86	0.3	0.08	0.01
					Silicate	-0.47	0.56	0.35			4,307	228						
BW1519 (B252)	20% CMAS + 30% $Na_2Si_2O_5$ + 44% Fe + 5% FeO + 0.4% CdO	Graphite	1235	200	Metal	-0.67	0.37	0.31	-0.39	0.44	1,265	61	0.26	0.02				
					Silicate	-0.28	0.75	0.32			4,911	255						
Cd-doped CMAS (~ 2% CdO)	Used to make up the starting materials for all of the above experiments					-1.04	0.00	0.26			18,239	1,824						

The $\varepsilon^{114/110}$Cd values are shown both relative to NIST SRM 3108 Cd and the Cd-doped CMAS starting material n.m. = not measured. (a) [Cd] = Cd concentrations, (b) Metal-silicate partition coefficient $D_{Cd}^{MET/SIL} = [Cd_{MET}] / [Cd_{SIL}]$, (c) $D_{Fe}^{MET/SIL} = [Fe_{MET}] / [Fe_{SIL}]$ where $[Fe_{MET}] \approx 95$ wt% (±5%), $[Fe_{SIL}] = 0.7773$ x [FeO] (from **Table 4.2**), (d) $K_D = D_{Cd}^{MET/SIL} / D_{Fe}^{MET/SIL}$. Uncertainties for Cd isotope compositions are internal errors (2se). Uncertainties for Cd concentrations (2sd) are mainly due to measurement errors for the low sample weights.

4.3.3 Cd metal-silicate partition coefficients

4.3.3.1 Introduction

The Cd metal-silicate partition coefficient, $D_{Cd}^{MET/SIL}$, is the ratio of the concentration of Cd in the metal and silicate phases as defined by Eq. 4.2:

$$D_{Cd}{}^{MET/SIL} = \frac{[Cd]_{METAL}}{[Cd]_{SILICATE}} \quad \text{Eq. 4.2}$$

It therefore provides an indication of the chemical affinity of Cd under the conditions of the experiment: a $D_{Cd}^{MET/SIL} > 1$ indicates siderophile behaviour whereby Cd prefers to partition in the metal phase and $D_{Cd}^{MET/SIL} < 1$ indicates lithophile behaviour with a preference for the silicate phase. In addition, for comparison, the two-component exchange coefficient, K_D, where $D_{Cd}^{MET/SIL}$ is normalised to $D_{Fe}^{MET/SIL}$, was calculated in accordance with Eq. 4.3 for those experiments for which electron microprobe analyses of the Fe content of the silicate phases was available (Table 4.3).

$$K_D = \frac{D_{Cd}{}^{MET/SIL}}{D_{Fe}{}^{MET/SIL}} \quad \text{Eq. 4.3}$$

4.3.3.2 Results for time series experiments

The graphite capsule time series experiments were carried out using the same starting material compositions and run conditions (1235 °C, 1.5 GPa) so that the only variable was the duration of the experiments which ranged from 4 – 200 minutes. The main objective of the time series was to identify the point at which Cd isotope fractionation between metal and silicate phases reached equilibrium.

Figure 4.3 plots the Cd metal-silicate partition coefficients, $D_{Cd}^{MET/SIL}$, for the time series experiments versus experiment duration, and a decline in $D_{Cd}^{MET/SIL}$ values is evident for the first 30 minutes of the experiment. Thereafter, the $D_{Cd}^{MET/SIL}$ values display very little change with an average result of $D_{Cd}^{MET/SIL} = 0.41 \pm 0.16$ (2se, n=3). The variation of $D_{Cd}^{MET/SIL}$ values with experiment duration might be the result of either (a) a change in the melt composition as the experiments progressed, or (b) slow Cd partitioning between metal

and silicate phases such that a full equilibrium was only achieved in the experiments of longer duration.

Regarding (a), it is known that carbon dissolves in the metal phase of experiments conducted in graphite capsules. Lagos et al. (2008) indicated levels of about 5 to 7 wt% carbon in the metal phase of their experiments in graphite capsules run at 1400 °C and 0.5 to 2 GPa. Wood and Halliday (2010) predicted that carbon saturation in graphite capsule experiments would lower the exchange coefficient (K_D) values for Pb by about an order of magnitude when compared to non carbon-saturated MgO capsule experiments, however, Siebert et al. (2011) reported that, while C had the effect of decreasing K_D values for some elements (P, Zn, Ga), they were increased for others (V, Nb, Mo, Ta, W). Specifically in the case of Cd, however, Marin et al. (2013) reported depressed $D_{Cd}^{MET/SIL}$ values for experiments in graphite capsules compared to those in MgO capsules at the same temperature across the range 1500 – 1900 °C.

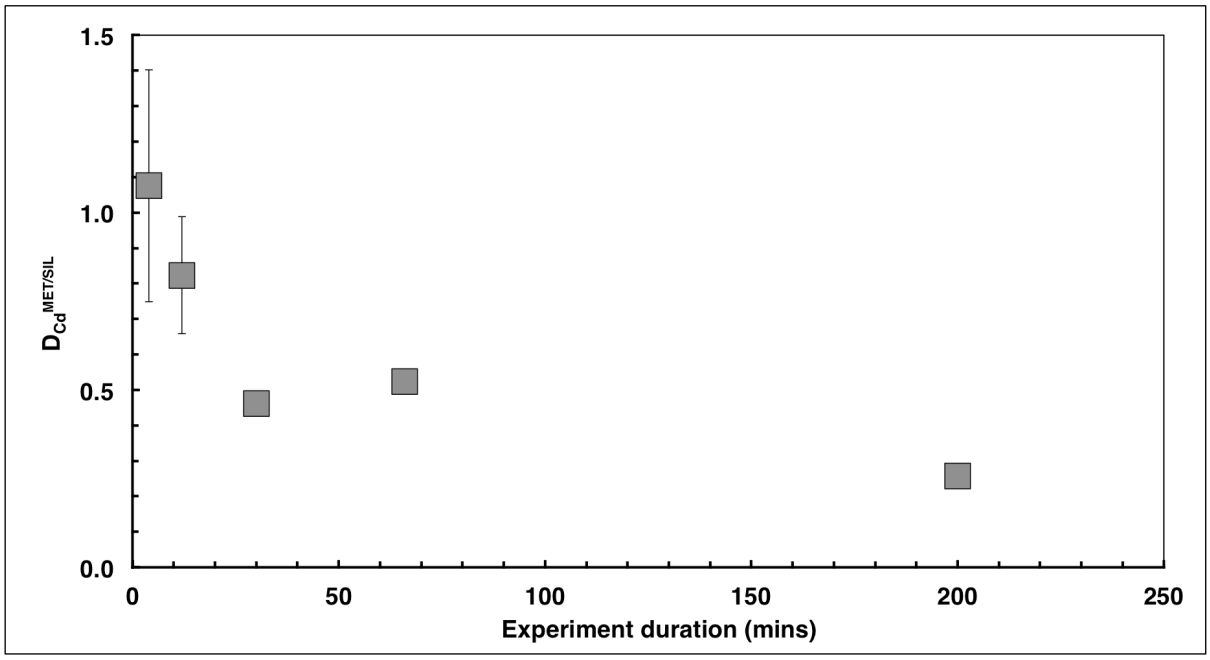


Figure 4.3. Cd metal-silicate partition coefficients, $D_{Cd}^{MET/SIL}$, versus experiment duration for the graphite capsule time series experiments. $D_{Cd}^{MET/SIL}$ is calculated in accordance with Eq. 4.2 on page 120. Error bars are shown at the 2sd level, unless smaller than the symbols.

Possibly in the case of the time series, experiments of longer duration might generate higher C contents until C saturation is achieved. If this were the case, higher carbon content in the metal phase may act to depress $D_{Cd}^{MET/SIL}$ values until the saturation point, and this may explain the initial $D_{Cd}^{MET/SIL}$ decline seen in Figure 4.3. In the context of steelmaking, Pb solubility in Fe – C melts is known to decrease with increasing C content and decreasing temperature (Malhotra et al., 1998) which provides a hint of a mechanism whereby increasing

C content could result in reducing partition coefficients. However, the data of Lagos et al. (2008) reveal no relationship between increasing experiment duration and decreasing $D_{Cd}^{MET/SIL}$ values or higher C concentrations in the metal, thereby questioning this mechanism.

Turning to (b), the physical inspection of the experimental run products from the shorter experiments, detailed in section 4.3.2 above, indicated that the phases of BW1521 (4 minutes) were almost certainly unequilibrated and the same likely applied to run BW1518 (12 minutes). Therefore ignoring the $D_{Cd}^{MET/SIL}$ values for the two experiments that were likely not fully equilibrated, Figure 4.3 shows a fairly narrow band of values for $D_{Cd}^{MET/SIL}$ of 0.26 to 0.52. Notably, these data are consistent with the results of Lagos et al. (2008) who obtained $D_{Cd}^{MET/SIL}$ values in the range of 0.2 to 0.4 for five of their graphite capsule experiments, with only one result of $D_{Cd}^{MET/SIL} = 0.06$ outside this range.

4.3.3.3 Results for initial experiments using different capsule materials

The $D_{Cd}^{MET/SIL}$ values for the initial experiments in different capsules range from 1.7 to 3.7 (Table 4.3) indicating slightly siderophile behaviour. The experiments in silica and MgO capsules (BW1305 and BW1307) have $D_{Cd}^{MET/SIL}$ coefficients of 1.8 and 3.5 respectively. These two experiments had exactly the same starting materials and had very similar durations and run conditions (58 to 63 minutes, 1565 to 1570 °C, 1.5 GPa). However, due to dissolution of capsule wall material in the melt, the silicate phases had radically different compositions when quenched, as revealed by their major element compositions and NBO/T values of 0.6 to 0.7 for the silica capsule and above 3.7 for the MgO capsule experiments. It is possible that the difference in $D_{Cd}^{MET/SIL}$ coefficients is due to slightly differing Cd partitioning behaviour in the silica-rich and Mg-rich melts.

The initial graphite capsule experiments BW1306 and BW1308 utilised different starting material compositions and temperatures. The former experiment featured the same starting material as the MgO and silica capsule experiments and was run at 1440 °C. In contrast, experiment BW1308 used a silicate portion of the starting material comprising about 50 wt% each of CMAS and $Na_2Si_2O_5$ and it was run at a lower temperature of 1370 °C. The higher temperature experiment produced a $D_{Cd}^{MET/SIL}$ coefficient of 1.7, whilst the lower temperature experiment yielded a $D_{Cd}^{MET/SIL}$ value of 3.7. The major element analyses of the silicate phase for the two experiments (Table 4.2) approximately reflect the silicate compositions of the respective starting materials, apart from some addition of Fe from the

metal component of the starting material (about 8 to 11 wt%). The extent of silicate polymerisation for the two silicate melts is identical with NBO/T values of 1.0 to 1.3.

4.3.3.4 Partition and exchange coefficients for Cd and variability with temperature

Figure 4.4 below shows (a) log $D_{Cd}^{MET/SIL}$ and (b) log K_D values for the results from this study and literature data versus inverse experimental temperature, 10000/T. A number of studies have set out equations in which the D or K_D values of specific elements are expressed as functions of experimental variables such as temperature, pressure, oxygen fugacity and melt composition and used such expressions to model partitioning behaviour (e.g. Kiseeva and Wood, 2013; Kiseeva and Wood, 2015; Mann et al., 2009; Righter, 2015; Righter et al., 1997; Siebert et al., 2011; Wade and Wood, 2005).

An example of such an expression which formulates the partition coefficient of element M, D_M, in terms of oxygen fugacity (fO_2), temperature (T), pressure (P), contents of S, C, and Si in the metal phase (X), and silicate polymerisation (nbo/t) is set out in Eq. 4.4 (Righter et al., 2014; Righter et al., 1997):

$$\ln D_M = a \ln fO_2 + \frac{b}{T} + \frac{cP}{T} + d \ln(1 - X_S) + e \ln(1 - X_C) + f \ln(1 - X_{Si}) + h(\text{nbo/t}) + g \quad \text{Eq. 4.4}$$

Experimental data can then be used to derive coefficients a – h by multiple linear regression (see e.g. Righter, 2011) allowing the expression to be used to model core-mantle segregation. A similar expression can be used to predict ln K_D values however, since, K_D is independent of oxygen fugacity (Takahashi and Irvine, 1981), the ln fO_2 term is excluded.

In this section, the emphasis is on the relationship between $D_{Cd}^{MET/SIL}$ and K_D values and temperature. From Figure 4.4, both log $D_{Cd}^{MET/SIL}$ and log K_D increase broadly in proportion to inverse experimental temperature (10000/T), with a slightly less scattered linear relationship between these two variables observed for log K_D versus 10000/T. Unsurprisingly, there will be some scatter in the data when combining the results from different laboratories, particularly due to the use of different capsule and starting material compositions. However, the linear regression is most striking for the $D_{Cd}^{MET/SIL}$ and log K_D results from Ballhaus et al. (2013) (diamond symbols) which forms the largest single dataset in Figure 4.4 (n = 11). These observations support Eq. 4.4, which indicates a linear relationship between the logarithmic (log or ln) $D_{Cd}^{MET/SIL}$ (and K_D) values and the inverse temperature.

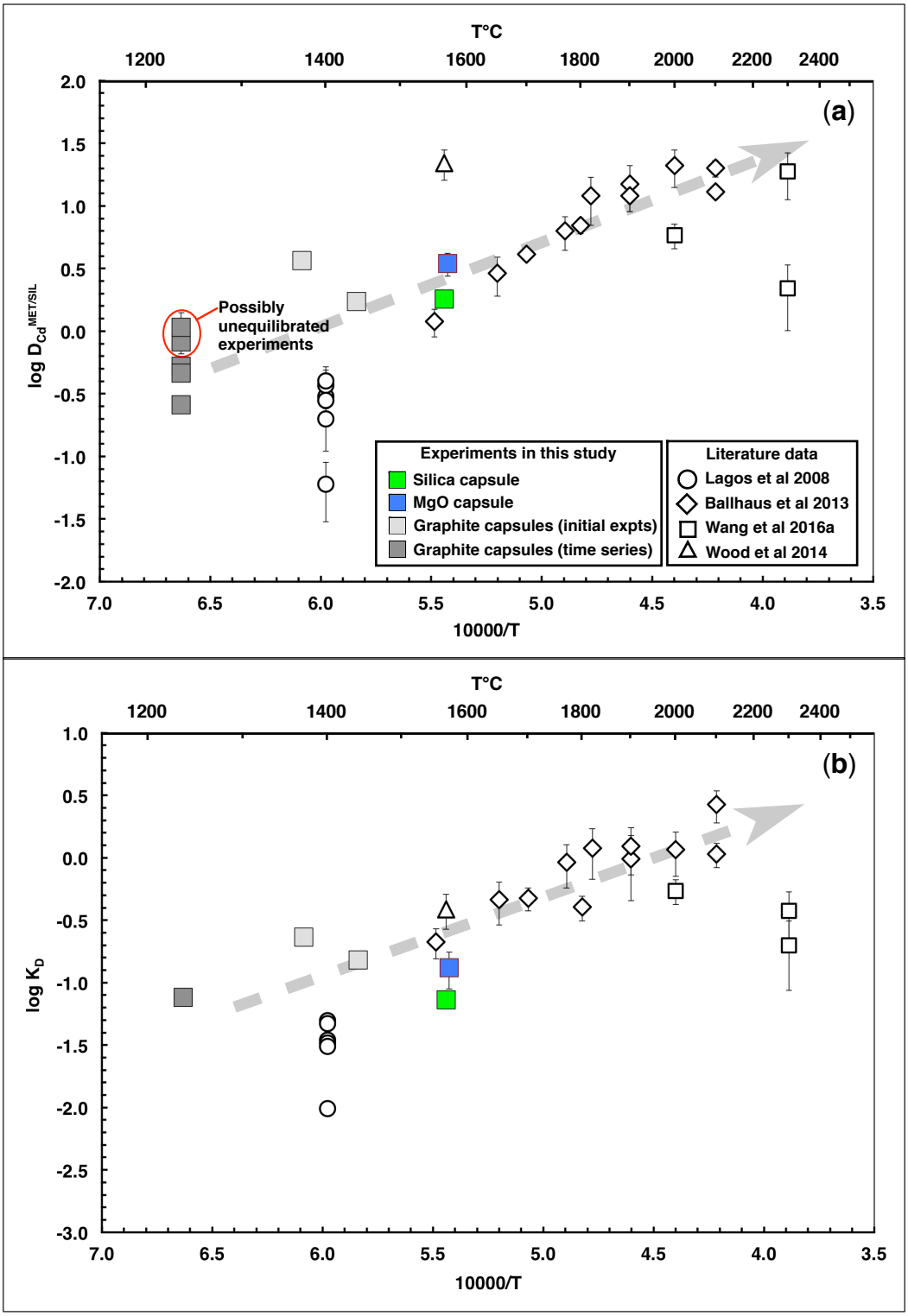


Figure 4.4. Logarithmic partition (log $D_{Cd}^{MET/SIL}$) and exchange coefficients (log K_D) for Cd versus inverse experimental temperature, 10000/T, in 10000 K^{-1} units with equivalent temperatures given in °C. The grey arrows indicate the broad linear trends in the data (see text). Literature data are for sulphur-free metal-silicate partitioning experiments in MgO capsules, except where noted: Lagos et al. (2008) in graphite capsules, experiments at 0.5 – 2.0 GPa; Ballhaus et al. (2013) starting materials doped with ~ 0.3 wt% FeS, experiments at 1 – 5 GPa; Wang et al. (2016a) experiments at 15 – 20 GPa (squares); Wood et al. (2014), experiment at 1.5 GPa. If the K_D values were not shown by these authors, they were calculated here from their published Fe contents in metal and silicate phases and the $D_{Cd}^{MET/SIL}$ values using Eq. 4.1 and Eq. 4.3 above. Error bars are shown at the 2sd level except where smaller than symbols (2sd data unavailable for Lagos et al. (2008) K_D values).

The data for log $D_{Cd}^{MET/SIL}$ (panel (a), Figure 4.4) has an almost identical structure to the data for log K_D (panel (b) Figure 4.4) which points to oxygen fugacity having a minimal influence on log $D_{Cd}^{MET/SIL}$ values, since K_D values are independent of fO_2 and D values (for some elements at least) are not (Takahashi and Irvine, 1981). This is to be expected since Cd is generally not multi-valent, existing in most minerals and phases in the divalent state only, therefore its partitioning behaviour is unlikely to be affected by the redox state of the melt in the experiments.

The data from this study (filled symbols) form a broadly linear trend (grey arrows in Figure 4.4) of increasing log $D_{Cd}^{MET/SIL}$ values with decreasing inverse temperature, particularly if the data for the two possibly unequilibrated experiments indicated is ignored (see section 4.3.3.2 above), although the trend is less evident for log K_D values. Moreover, the data from this study is generally in line with the overall linear trend in $D_{Cd}^{MET/SIL}$ and log K_D values from the literature confirming that the experimental techniques and outcomes of this study are in line with those of other laboratories.

In summary, the $D_{Cd}^{MET/SIL}$ values for the experiments in this study are broadly controlled by two main factors: (i) $D_{Cd}^{MET/SIL}$ values generally increase with experimental temperature in a fairly predictable manner, and (ii) $D_{Cd}^{MET/SIL}$ values are lowered in graphite capsule experiments due to the dissolution of C from the capsule material in the metal phase as explained in section 4.3.3.2. The influence of silicate polymerisation (NBO/T see section 4.3.1.3) on the $D_{Cd}^{MET/SIL}$ values is uncertain and would require further experiments in which NBO/T values are more controlled using different starting and capsule materials.

4.3.4 Cd isotope compositions

4.3.4.1 Introduction

The results of the Cd isotope composition measurements and isotope dilution calculations for all experiments are set out in Table 4.3 above together with calculated Cd and Fe metal-silicate partition coefficients, D_{Cd} and D_{Fe}, and the two-component exchange coefficient, K_D.

The primary purpose of these experiments is to assess the extent of Cd isotope fractionation between the metal and silicate phases at equilibrium and the Cd isotope compositions detailed in Table 4.3 are therefore plotted in Figure 4.5 below. Figure 4.5 (a) and (b) show the metal-silicate partition coefficients for Cd, $D_{Cd}^{MET/SIL}$, in each experiment versus the Cd isotope compositions of the individual metal and silicate phases. Figure 4.5 (c)

shows the $D_{Cd}^{MET/SIL}$ values for each experiment versus the difference between the Cd isotope compositions of the metal and silicate phases, $\Delta\varepsilon^{114/110}Cd_{MET-SIL}$ (= $\varepsilon^{114/110}Cd_{MET}$ – $\varepsilon^{114/110}Cd_{SIL}$), representing the extent of Cd isotope fractionation between metal and silicate phases during the experiments.

4.3.4.2 Kinetic Cd isotope fractionation and volatilisation

The Cd isotope compositions of the metal and silicate fractions separated from the experimental run products are, within error, approximately equal to or heavier than the original starting material. Notably, the experiments carried out in silica and MgO capsules exhibited significantly heavier Cd isotope compositions than the starting material for both metal and silicate phases, with $\varepsilon^{114/110}$Cd values of about +10 and +28 for the silica and MgO capsules respectively. In comparison, the Cd isotope compositions for both phases in the graphite capsule experiments fell within the range of $\varepsilon^{114/110}Cd \approx -1.4$ to –0.3, indicating little isotope fractionation, compared to the $\varepsilon^{114/110}$Cd value for the Cd-doped CMAS starting material of -1.04 ± 0.26.

Furthermore, the concentrations of Cd in metal and silicate phases from the silica capsule experiment (BW1305) were 33 and 18 μg/g, respectively, considerably lower than the original Cd content of the CMAS starting material of about 18,000 μg/g (equivalent to about 0.9 wt% Cd in the whole starting material including metal), indicating a significant loss of Cd during the experiments.

Similarly, the Cd concentrations for the metal and silicate phases of the MgO capsule experiment (BW1307) were 164 and 47 μg/g using the same starting material, also indicating a significant loss of Cd. In comparison, the concentrations of Cd in the metal and silicate fractions of the graphite capsule experiments ranged from about 1,200 to 12,000 μg/g (Table 4.3), significantly higher than the concentrations in the silica and MgO capsules and thereby exhibiting a far lower degree of Cd loss compared to the starting material.

It is very likely that some of this ‘loss’ simply reflects dilution of the melt during the experiments due to dissolution of silica and MgO capsule wall material. However, since the experiments were conducted at temperatures well above the melting point of Cd, which is 388 °C at 1.5 GPa (Errandonea, 2010), significant loss of Cd is most likely the result of volatilisation, producing Cd vapour which permeates the capsule material and escapes.

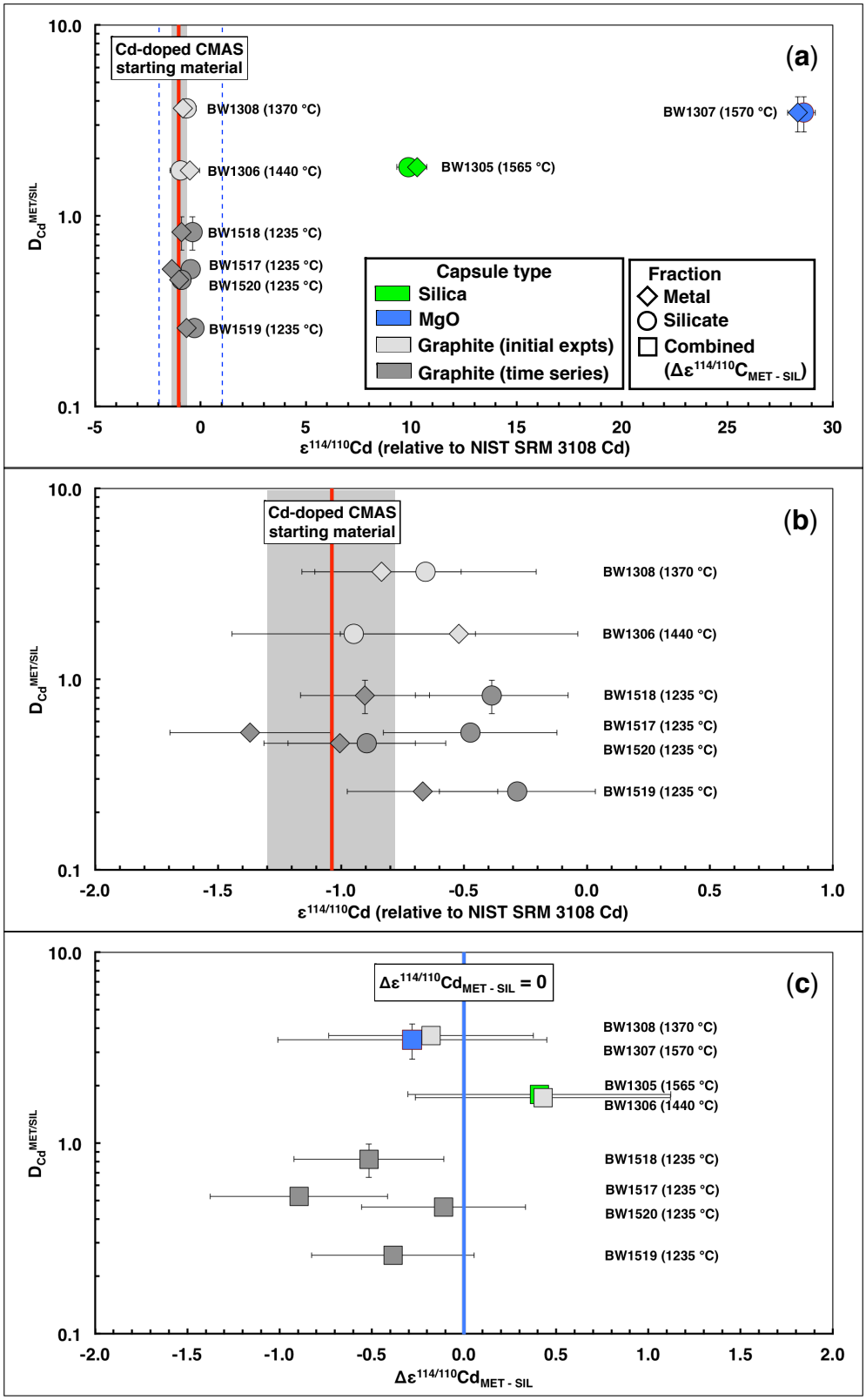


Figure 4.5. Cd isotope compositions (ICs) of metal and silicate phases versus Cd metal-silicate partition coefficients ($D_{Cd}^{MET/SIL}$). Panel (b) is the same plot as (a) but with a narrower scale. The blue dashed lines in panel (a) show the coverage of the scaled up panel (b). In panel (c), $\Delta\varepsilon^{114}Cd_{MET-SIL} = \varepsilon^{114}Cd_{MET} - \varepsilon^{114}Cd_{SIL}$, or the Cd isotope fractionation between the phases. Error bars for Cd ICs (including $\Delta\varepsilon^{114}Cd_{MET-SIL}$) are shown at the 2se level, for $D_{Cd}^{MET/SIL}$ at the 2sd level, unless smaller than the symbols. The red vertical lines in (a) and (b) represent the Cd IC of the Cd-doped CMAS starting material The grey shaded area represents the uncertainty on this value at the 2se level. The blue vertical line in panel (c) represents the reference value $\Delta\varepsilon^{114}Cd_{MET-SIL} = 0$.

The heavy Cd isotope compositions recorded by the experiments in silica and MgO capsules are therefore likely the result of kinetic isotope fractionation due to the preferential loss of light isotopes of Cd during volatilisation in a partially open system. The isotope fractionation is greater in the experiment with an MgO capsule rather than a silica capsule, which points to a greater loss of Cd vapour from the MgO capsule. This is reasonable since the polycrystalline MgO capsules tend to be more porous than those made of silica even though the former densify during heating.

However, the Cd concentrations for the metal and silicate phases of the silica capsule experiment are significantly lower than the concentrations in the phases of the MgO capsule experiment and this appears to contradict the view that the loss of Cd vapour is greater for polycrystalline MgO capsules. Bridgestock et al. (2014) observed the same apparent contradiction when conducting similar experiments in silica and MgO capsules in order to determine the partitioning behaviour of Zn. These authors attributed the apparent greater loss of Zn from a silica in comparison to an MgO capsule to dissolution of the silica capsule material, producing a greater volume of silica melt and hence lower concentrations of the target element.

4.3.4.3 Fractionation of Cd isotopes between metal and silicate during partitioning

Determining whether Cd isotopes fractionate during metal-silicate partitioning and hence during core formation in the early Earth is the primary aim for which the experiments were designed in this study. The degree of Cd metal-silicate isotope fractionation is represented by the difference between the measured Cd isotope compositions of the metal and silicate phases of the experiments, or $\Delta\varepsilon^{114/110}Cd_{MET-SIL}$ in Table 4.3.

Reviewing the $\Delta\varepsilon^{114/110}Cd_{MET-SIL}$ data for the experiments, most have negative values indicating a silicate phase with a slightly heavier Cd isotope composition than the metal phase. The exceptions are experiments BW1305 (silica capsule) and BW1306 (graphite capsule) where the metal phase is slightly heavier with a $\Delta\varepsilon^{114/110}Cd_{MET-SIL}$ value of about +0.4.

In calculating the average $\Delta\varepsilon^{114/110}Cd_{MET-SIL}$ values, the potentially unequilibrated 12 minute graphite time series experiment (BW1518 see sections 4.3.2 and 4.3.3.2 above) was excluded. Accordingly, the average $\Delta\varepsilon^{114/110}Cd_{MET-SIL}$ value is –0.14 ± 0.35 (2se, n=7) for all experiments together, –0.23 ± 0.43 (2se, n=5) for all experiments in graphite capsules including the initial experiments, and –0.46 ± 0.46 (2se, n=3) for all time series experiments

in graphite capsules with the same starting material and experimental conditions. Most experiments (n=6) exhibited slightly negative $\Delta\varepsilon^{114/110}Cd_{MET-SIL}$ values which ranged from about –0.1 to –0.9. Therefore, an argument could be made to support a very slight Cd isotope fractionation with heavier isotopes favouring the silicate phase. However, taking into account uncertainties and looking at the results as a whole, the most reasonable conclusion is there is no significant Cd isotope fractionation between the metal and silicate phases during equilibrium partitioning.

Indeed it is remarkable that, whilst the silica and MgO capsule experiments have experienced significant kinetic Cd isotope fractionation as a whole due to volatile loss ($\varepsilon^{114/110}Cd \approx +10$ to $+28$), there is still no significant difference in the Cd isotope compositions of the metal and silicate phases, which exhibit $\Delta\varepsilon^{114/110}Cd_{MET-SIL}$ values of $+0.41 \pm 0.71$ (silica capsule) and -0.28 ± 0.73 (MgO capsule). Furthermore, the lack of Cd isotope fractionation between metal and silicate for experiments that exhibited significant loss of Cd, is an indication that the remaining Cd was in equilibrium between the phases.

4.3.4.4 Comparison with metal-silicate isotope fractionation in other stable isotope systems

To date very few studies have focussed on stable isotope fractionation between metal and silicate phases, whilst many investigations have determined elemental partition coefficients for such systems at various experimental conditions.

Bridgestock et al. (2014) carried out experiments very similar to those described in this study in silica and MgO capsules including a time series in MgO capsules (n=3), to determine if Zn isotopes fractionate during partitioning between metal and silicate. Comparison of the Cd and Zn studies is particularly relevant since the two elements are chemically very similar: both are in Group 12 (IUPAC classification) of the Periodic Table, they are divalent in most compounds and have similar volatilities. Notably, Bridgestock et al. (2014) reported heavier Zn isotope compositions for experimental products in comparison to the starting materials, likely the result of preferential loss of light isotopes during volatilisation, similar to the findings in this study, particularly for the silica and MgO capsules. Moreover, as with Cd isotopes in this study, they recorded no significant Zn isotope fractionation within analytical uncertainties between metal and silicate phases.

Wood et al. (2008) found that there was no significant fractionation of Tl isotopes during the separation of both metal and sulphide from silicate phases in their partitioning experiments carried out in silica and MgO capsules at 2 GPa and 1650 to 1750 °C (n=4).

Thallium is slightly more volatile than Cd or Zn and these authors reported, as with this study and that of Bridgestock et al. (2014), that the experimental products were isotopically heavier than the starting materials and attributed this to kinetic isotope fractionation due to volatile loss of Tl during the experiments.

Nielsen et al. (2014) and Bonnand et al. (2016) found no significant fractionation of V and Cr isotopes respectively between metal and silicate phases in their experiments, however the latter did find a well correlated series of heavier Cr isotope compositions for both the metal and silicate run products with increasing experimental duration, which they attributed to preferential loss of light Cr isotopes as the experiments progressed.

Hin et al. (2013), however, established that Mo isotope fractionation took place between metal and silicate with light isotopes favouring the metal phase. They also found that the extent of fractionation decreased with increasing temperature but was constant over a range of melt compositions and oxygen fugacities and also seemingly unaffected by graphite capsule-induced carbon content in the metal.

Experiments have also been carried out on the stable isotope fractionation of major mantle- and core-forming elements. Experiments conducted by several workers have determined that light Si isotopes are enriched in the metal phase with the degree of fractionation decreasing with increasing temperature (Hin et al., 2014; Shahar et al., 2011), consistent with the Si isotope fractionation between metal and silicate phases in aubrites observed by Ziegler et al. (2010). However, partitioning experiments have not detected significant stable isotope fractionation of Fe between metal and silicate phases (Hin et al., 2012; Poitrasson et al., 2009), despite calculations indicating that Fe isotope fractionation is expected between lower mantle silicates and core metal (Polyakov, 2009).

4.4 Conclusions

Metal-silicate partitioning experiments were conducted for Cd and the run products were analysed by MC-ICP-MS using the double spike technique to determine the Cd isotope composition of the separate metal and silicate and thus the degree of fractionation between the metal and silicate phases. The experiments were conducted using a Boyd-England piston-cylinder apparatus at 1.5 GPa and at temperatures ranging from 1235 to 1570 °C in capsules made from different materials (silica, MgO and graphite).

Firstly, the overall conclusion from the experiments is that there is no significant stable Cd isotope fractionation, within analytical uncertainties, between the metal and silicate

phases. In detail, most experiments (n=6) exhibited slightly negative $\Delta\varepsilon^{114/110}Cd_{MET-SIL}$ values ranging from about –0.1 to –0.9, which could hint at possibly a very slight preference of heavy Cd isotopes for the silicate phase. However, the average $\Delta\varepsilon^{114/110}Cd_{MET-SIL}$ value for all equilibrated experiments was –0.14 ± 0.35 (2se, n=7) and when only considering those experiments in graphite capsules it was –0.23 ± 0.43 (2se, n=5). The $\Delta\varepsilon^{114/110}Cd_{MET-SIL}$ value for the equilibrated time series experiments in graphite at constant conditions of 1.5 GPa and 1235 °C was –0.46 ± 0.46 (2se, n=3). Hence, a clear negative $\Delta\varepsilon^{114/110}Cd_{MET-SIL}$ value is not supported by the data considering the uncertainties.

The experiments conducted in silica and MgO capsules show significant kinetic Cd isotope fractionation due to volatile loss from the metal and silicate phases, which exhibit Cd isotope compositions of $\varepsilon^{114/110}Cd \approx +10$ to +28. In comparison, the results for phases produced in the graphite capsule experiments only ranged between $\varepsilon^{114/110}Cd$ values of –1.4 and –0.3, thereby showing no significant Cd isotope fractionation compared to the Cd-doped CMAS starting material ($\varepsilon^{114/110}Cd = -1.04 \pm 0.26$). Despite the large overall Cd isotope fractionation in metal and silicate phases from the silica and MgO capsule experiments, there is no significant fractionation *between* metal and silicate in those two experiments ($\Delta\varepsilon^{114/110}Cd_{MET-SIL} \approx -0.3$ to +0.4), in accord with the findings of the essentially unfractionated graphite capsule experiments.

In summary, these results show that Cd partitioning between the primitive mantle and the core of the early Earth was most likely not accompanied by any significant Cd isotope fractionation.

Secondly, the log $D_{Cd}^{MET/SIL}$ values for the experiments of this study, excluding the two above-mentioned unequilibrated time series runs, increase in a broadly linear fashion with decreasing inverse temperature. This trend fits well with findings of other workers (Figure 4.4) and confirms that temperature has a significant effect on $D_{Cd}^{MET/SIL}$ values. The log K_D data for the experiments of this study show less variability versus inverse temperature than the log $D_{Cd}^{MET/SIL}$ results, but they are still in accord with the broadly increasing linear trend in log K_D values versus 10000/T found by other workers. In addition, the graphite capsule experiments provide evidence that C dissolved in the metal phase has a depressing effect on $D_{Cd}^{MET/SIL}$ values, in line with the findings of previous studies.

4.5 Declaration

The study detailed in this chapter was completed as part of collaborative research efforts to which the author of this thesis contributed all of the Cd isotope composition measurements, data reduction and analysis. The author was primarily responsible for developing the interpretations that are presented here. Professor Bernard Wood carried out the metal-silicate partitioning experiments and electron microprobe analyses using the facilities at Oxford University after which the author separated and digested the experimental run products and prepared them for analysis on the mass spectrometer.

Chapter 5 The cadmium isotopic composition of Earth

5.1 Introduction

The origin of volatile elements and their mode of delivery to Earth and other terrestrial planets remains a largely unanswered question with several competing theories having been put forward to explain their abundances. On the one hand it has been suggested that volatile elements were delivered to Earth primarily during a 'late' accretion of volatile-rich chondritic material after core formation had been completed (Albarède, 2009; Albarède et al., 2013; Ballhaus et al., 2013); on the other hand others maintain that the volatile element budget of the Earth was primarily established during its initial accretion and core formation stage (Palme et al., 1988; Wood et al., 2010). Both accretion scenarios require a 'late veneer' to deliver volatile-rich material, consistent with the requirement of a late veneer to account for the relative chondritic abundances of highly siderophile elements (HSEs) in the mantle without which most of the Earth's budget of HSEs would have been 'lost' to the core during core partitioning (Chou, 1978). The key difference is that the late veneer is the primary mechanism for delivery of volatile elements to Earth in the first-mentioned model, whereas it is a minor contribution to the volatile element budget of Earth in the second.

The equilibrium condensation sequence of the solar nebula (Grossman, 1972; Grossman and Larimer, 1974; Larimer, 1967) indicates that in the cooling inner solar system, refractory elements and minerals condensed first, followed by metallic Fe – Ni and then Mg-silicates, and that these constituents formed the bulk of material accreting to Earth (Ganapathy and Anders, 1974). The abundances of refractory lithophile elements with condensation temperatures above those of the major rock-forming elements, Mg, Fe and Si, in the bulk silicate Earth (BSE) are fairly close to bulk solar system abundances, as represented by those measured in the solar photosphere and in CI chondrites (Lodders, 2003; Lodders, 2010).

This is in contrast to the more volatile elements, condensing below about 1300 K, which are depleted in the BSE, chondrites, and other terrestrial bodies relative to the CI chondrites. Volatile element depletion in CV carbonaceous chondrites follows a trend which is largely dependant on the 50% condensation temperature (50% T_C) of the element. However, the volatile depletion trend of the BSE depends not only on the 50% T_C of the elements but also their chemical affinities, whereby siderophile and chalcophile elements are also variously depleted by entrainment with Fe – Ni metal during core formation (e.g. O'Neill and Palme, 2008; Palme et al., 1988; Palme and O'Neill, 2014; Wood et al., 2010).

This study will explore the Cd isotope compositions of the BSE and carbonaceous chondrites to determine which method of delivery of volatile elements to Earth was more likely, during or after main accretion and core formation (Schönbächler et al., 2009). This is based on a very simple premise. If volatile elements were delivered primarily during a late chondritic addition, the isotope composition of the BSE will reflect that late added material. If volatile elements were delivered primarily during the main accretion and core formation stage, the isotope composition of the BSE will reflect material accreted when the solar nebula was cool enough for volatile elements to condense.

Cadmium is an ideal element to test this hypothesis. It is highly volatile with a 50% T_C = 652 K (Lodders, 2003) and thus will be enriched in any late chondritic veneer. It is also slightly siderophile, and therefore any Cd delivered during Earth's main accretion phase, would have been partly, but not completely, removed from Earth's mantle during core partitioning. Thus the Cd abundance in the bulk silicate Earth is very sensitive to the amount of material delivered during the 'late veneer': whether it is relatively minor, 0.3 – 0.7% of Earth's mass (M_E) (e.g. Jacobsen et al., 2008), or more substantial, 1.7 – 4% M_E (Albarède, 2009; Albarède et al., 2013; Ballhaus et al., 2013).

Zinc is also highly volatile, with a 50% T_C = 726 K (Lodders, 2003), but less so than Cd, and, unlike Cd, Zn is lithophile. Its lower volatility than Cd and lithophile chemical affinity ensures that it is less enriched in a chondritic 'late veneer' relative to Cd and not significantly depleted in the primitive mantle during core formation. Thus Zn is not as sensitive to the amount of material delivered by a late veneer as Cd. A review will be carried out of Zn isotope data in the literature to determine if there is any indication of how Zn was delivered to Earth and whether that indication is consistent with Cd.

In order to test whether Cd is delivered primarily during the main accretion phase or during a late volatile accretion, the Cd isotope compositions of the BSE and carbonaceous chondrites need to be well-characterised. Schmitt et al. (2009b) published an extensive dataset of Cd isotope compositions of mainly marine hydrogenic and hydrothermal ferromanganese deposits and continental sulphides. They also analysed three loess deposits from Germany and China, two ocean island basalts (OIBs) from Hawaii and St Helena, and two mid-ocean ridge basalts (MORBs) from the East Pacific Rise. These seven measurements were used to estimate the Cd isotope composition of the BSE, on the assumption that there was little difference between the isotope compositions of mantle-derived basalts and crustal rocks.

In order to better characterise the Cd isotope composition of the silicate Earth, fifty-five samples (including repeat analyses of the same sample carried out at different times or in different laboratories) from a wide range of tectonic settings are analysed in this study. These samples include peridotites and komatiites, which should provide a better indication of the Cd isotope composition of the Earth's primitive mantle and hence the BSE but which were not present in the dataset published by Schmitt et al. (2009b). Since the dataset in this study is far more extensive for terrestrial rocks than previously published, it should also be possible to distinguish any subtle differences in isotope composition between rocks from different tectonic settings.

The carbonaceous chondrites Ivuna (CI1) and Murchison (CM2) have been also been measured for Cd content and isotope composition and will be used, along with the carbonaceous chondrite data of Baker et al. (2010), to characterise the mean Cd isotope composition of carbonaceous chondrites.

5.2 Analytical methods

5.2.1 Sample preparation and digestion

5.2.1.1 Reagents and laboratory procedures

Hotplate digestion, chemical separation, preparation for mass spectrometry and other critical work on samples were carried out in Class 10 laminar flow hoods within the Class 1000 MAGIC clean room facility at Imperial College London using ultrapure reagents and water. Handpicking of samples (section 5.2.1.2) and weighing were done inside the Class 1000 clean room but away from the laminar flow hoods to avoid spreading dust contamination from the samples.

Full details of the ultrapure reagents and water, analytical balance and hotplate apparatus used for the samples are set out in section 2.2 starting on page 26, along with other laboratory procedures and precautions, including the protocols for cleaning vials and bottles used for sample digestion and mass spectrometry.

5.2.1.2 Cleaning and leaching MORB samples

A total of ten MORB samples are presented in this study (see Table 5.2 on page 152), of which six samples (indicated by * in Table 5.2) were in the form of raw unprocessed chips from dredges from the Mid-Atlantic and Pacific Antarctic Ridges and the Pukao Seamount.

The remaining samples had previously been processed using similar methods to those described in this section.

The six raw samples had varying degrees of surface alteration. Two samples (SO157 54 DS-1 and SO157 63 DS-1 from the Pacific Antarctic Ridge) consisted of black vitreous chips with little or no visible surface grey mottling, but the remaining four samples had many dull black chips with varying degrees of grey or light brown mottling, some with extensive dusty surfaces and very few pristine black vitreous surfaces. The grey or light brown dusty surfaces or mottling are zeolite and smectite clays resulting from contact with seawater. Brown ferromanganese coatings were also present in some of the samples but far less abundant than the clay alterations.

Schmitt et al. (2009b) measured the Cd contents and isotope compositions of surface scrapings from 32 ferromanganese hydrogenic deposits covering the major ocean reservoirs. Cd contents ranged from 1.0 ppm to 21.6 ppm and averaged 5.2 ppm. This is in line with range of Cd concentrations of Atlantic, Pacific, Indian and Southern Ocean ferromanganese crusts reported by Horner et al. (2010).

Measurements of MORB glasses carried out in this study and by Schmitt et al. (2009b) indicate their Cd content to be approximately 150 ppb. Thus there is the potential for contamination from ferromanganese coatings to exaggerate the Cd content of MORB samples and affect the measured Cd isotope composition, although the argument against this would be that any coatings present would contribute very little to the overall mass balance of the MORB glass sample.

In order to minimise the influence of any alteration or coatings on measurements MORB glasses, the samples were leached using procedures similar to those described in Rehkämper et al. (1999). The cleanest MORB glass chips were picked using a hand lens from each sample and transferred to a 22 ml acid-cleaned PFA vial, covered with ultrapure Milli-Q® water and placed in an ultrasonic bath for 10 – 15 minutes for relatively clean chips and 30 minutes for the dirtier chips. The water containing dust and surface contamination from the samples was poured away and the chips were rinsed a few times with Milli-Q® water. The process was repeated another two times after which the vials were filled with double-distilled ethanol covering the chips and agitated for a few minutes. The dirty ethanol was discarded and the step was repeated with fresh ethanol. The chips were then dried in a laminar flow hood at room temperature and on a hotplate at low temperature.

After inspecting the samples using a hand lens, the samples from the Pacific-Antarctic Ridge (SO157 54 DS-1 and SO157 63 DS-1), which were relatively clean to start with, were

pristine and required no further cleaning. The dirtier chips from other samples displayed grey mottled surfaces and brown ferromanganese coatings. These samples were further cleaned by cycles of mild acid leaching. The chips were covered with distilled 0.1 M HCl and ultrasonicated for 15 minutes, after which the dirty acid was discarded and the chips rinsed with Milli Q® water. This step was repeated twice using distilled 0.5 M HCl. After the final leaching and rinsing cycle, the chips were rinsed with double distilled ethanol and dried in a laminar flow hood at room temperature and on a hotplate at low temperature.

The dried chips were inspected with a hand lens, which revealed that they were significantly cleaner than before leaching. Although some grey mottling and a few coatings remained, it was decided against further leaching, which might degrade the samples, because any remaining coatings were not significant. For all samples, approximately 1 to 2 g of the cleanest chips were handpicked with the aid of a hand lens for weighing and digestion. The chips were small enough to digest in HF – HNO_3 directly without crushing beforehand.

5.2.1.3 Acid hotplate digestion

Most rock and meteorite samples were digested in closed 22 ml or 60 ml acid-cleaned PFA vials on a hotplate using three or four acid digestion stages, as summarised in Table 5.1 and, if necessary a high pressure vessel digestion stage as described in section 5.2.1.4 below. Olivine separates were digested in acid-cleaned 180 ml and 240 ml beakers, since the larger quantity of material for these low Cd content samples required greater volumes of acid, as explained below.

After weighing samples in the vials, the samples were wetted with approximately 1 ml 6 M HCl before working with them in a laminar flow hood. This was to prevent particles from the samples contaminating the Class 10 laminar flow hoods by action of static electricity or airflow.

The addition of 16 M HNO_3 before 28 M HF ensures it acts as a ‘buffer’ to mitigate strong reactions as the HF is pipetted to the sample usually 500 µl or 1 ml at a time. In addition, the presence of acids other than HF assists with the digestion of non-silicates (Chao and Sanzolone, 1992) and, since HF has a lower boiling point than HNO_3, helps to convert fairly insoluble metal fluorides formed by action of HF into more soluble salts when the digestion is dried down (Twyman, 2005).

The samples in the HF – HNO_3 (and HCl) mixture were refluxed in closed PFA vials on a hotplate for between 4 and 10 days at temperatures of 80 to 120 °C and thereafter

evaporated to dryness at 80 to 100 °C, leaving a block of white or grey sample material. Higher temperatures and ultrasonication were sometimes employed to assist with the breakdown and digestion of MORB glass chips and meteorite samples which were not crushed to powder prior to digestion.

Table 5.1. Summary of hotplate digestion stages for different categories of sample indicating, in normal font, the total acid volumes used (in ml) and, in italics, the same acid volumes stated in ml per gram of sample digested.

				Acid digestion stages				
Sample categories	**Sample Weights (g)**	**Cd content (ng/g)**	**n**	**HF–HNO_3 (+ minor HCl)**	**Ratio HF : HNO_3 (+HCl)**	**6 M HCl (+1% Br – H_2O)**	**6 M HCl – HNO_3 (Ratio 1 : 1)**	**6 M HCl**
Peridotites, komatiites, BIR-1a	2.6 – 2.8	28 – 93	5	16.5 *5.8 – 6.4*	2.7 : 1	10 *3.5 – 3.9*		15 – 30 *5.3 – 11.7*
MORBs, basalts, loess, andesite	1.0 – 1.7	68 – 262	7	13.5 *8.1 – 13.1*	2 : 1	10 *6.0 – 9.7*	10 *6.0 – 9.7*	15 *9.0 – 14.6*
MORBs, basalts, loess, komatiite	1.1 – 2.3	48 – 302	17	12 – 15 *6.4 – 11.9*	2 – 2.5 :1		10 – 30 *7.2 – 15.5*	15 – 25 *7.7 – 15.5*
MORB small samples	0.2 – 0.4	118 – 132	2	6 – 9 *25.0 – 30.3*	2 : 1		15 –20 *42 – 101*	10 – 15 *42 – 51*
Olivine separates	5.3 – 8.7	5 – 22	2	60 *6.9 – 11.3*	2 : 1		60 – 90 *10.3 – 11.3*	30 – 60 *3.4 – 11.3*
Meteorite: Murchison	1.0	401	1	14 *14.2*	2.5 : 1		15 *15.2*	20 *20.3*
Meteorite: Ivuna	0.3	702	1	14 *54*	2.5 : 1		30 *117*	20 *78*

Modified aqua regia was employed for the second digestion stage. The dried residues were digested in equal volumes of 6 M HCl and 16 M HNO_3 and then were refluxed in closed vials for 5 to 9 days at temperatures of 90 to 130 °C. Temperatures were increased gradually because the reaction of the acids produced fumes of nitrosyl chloride, chlorine and nitric oxide which results in the build up of pressure within the vials. The vials were opened periodically in a laminar flow hood to release the pressure. The samples were then dried down at 80 to 110 °C, with higher temperatures occasionally being employed.

The samples were finally digested in 6 M HCl and refluxed at 100 to 140 °C for 1 to 2 weeks to ensure that the sample is in chloride form ready for anion exchange chemistry. All samples were centrifuged in 15 ml acid-cleaned PP centrifuge tubes to remove the small amount of insoluble fluorides remaining.

Ahrland et al. (1958) developed a classification of metal cations as ‘soft’ or ‘hard’ acids and ligands as ‘soft’ or ‘hard’ bases according to the relative affinities of Lewis acids and bases in forming compounds. From their studies, the Cd^{2+} cation is classed as a ‘soft’ acid and the F^- ligand is a ‘hard’ base. According to Pearson (1968), ‘hard’ acids prefer to

bind with ‘hard’ bases and ‘soft’ acids with ‘soft’ bases. Accordingly, any insoluble fluoride residue remaining after sample digestion is unlikely to bind any Cd^{2+}, which prefer to bind with Cl^- and other halogens, thus it is likely that all of the Cd in the sample would contained in the final 6 M HCl solution, rather than any residual insoluble fluorides.

The first few batches of samples had a fourth digestion stage after treatment with 28 M HF and 16 M HNO_3. The samples were taken up in 10 ml 6 M HCl to which was added 100 µl Br_2 – H_2O (1%) as an oxidising agent. These samples were refluxed for up to 9 days and dried down. It was considered that this digestion step did not add significantly to the efficacy of the digestion and was therefore omitted from the digestion protocol for the remaining samples.

5.2.1.4 High pressure vessel digestion

Although hotplate digestion is likely to recover all of the Cd in a sample, future work on a small aliquot of the samples may include the analysis of Zn concentrations and isotope compositions, and it is known that Zn is hosted in spinel phases in ultramafic rocks (Horn et al., 1994; O'Reilly et al., 1991). The following samples, referred to in Table 5.2 on page 152 contained significant amounts of spinel or chromite and were therefore further digested using a large capacity steel acid digestion vessel (Part number 4748, Parr Instrument Company):

P3 Cameroon Line peridotite xenolith (sample no. 49)

P13 Cameroon Line peridotite xenolith (sample no. 50)

M657 Alexo (Canada) komatiite (sample no. 75)

CM2 Murchison carbonaceous chondrite (sample no. 83)

CI1 Ivuna carbonaceous chondrite (sample no. 92)

Centrifuged residues from these samples were transferred to acid-cleaned 15 ml or 22 ml PFA vials and dried on a hotplate, after which 6 to 9 ml 12 M HCl was added to each vial. Residues for samples P3 and P13 were split between two 15 ml vials, the remaining samples, including a repeat digestion for P13, were digested in one 22 ml vial.

One 22 ml or two 15 ml vials were placed in a 125 ml acid-cleaned PTFE (polytetrafluoroethylene) liner and lid with some Milli-Q® water to provide a buffer in case of leakage from the vial. The closed PTFE liner was loaded into the acid digestion vessel and the screw cap assembled and closed in accordance with Parr Instrument Company instructions. The loaded vessels were placed in a Gallenkamp bench top laboratory oven at

130 °C (samples P3 and P13) or 150 °C (remaining samples plus repeat digestion for P13) for 3 to 5 days.

The resulting sample digests were dried down on a hotplate at 130 to 150 °C and taken up in 7.5 to 9 ml 28 M HF and 16 M HNO_3 in a 2:1 ratio. The samples were refluxed on a hotplate in closed PFA vials at 120 to 160 °C for 2 to 6 days and dried down at 130 °C. Thereafter the dried samples were taken up in 6 M or 12 M HCl and refluxed at 120 to 160 °C for a day, after which the 12 M HCl samples were diluted with Milli-Q® water to 6 M HCl. The samples were centrifuged and the liquid recombined with the previously centrifuged main aliquot of the sample. The centrifuged residues were examined with the aid of a hand lens and although there were a few particles of spinel or chromite present they were much reduced. The carbonaceous chondrite residues also contained very fine carbon particles in their residues.

Sample number 52 MT20 Monroe Township (Canada) komatiite was not subjected to any high-pressure vessel digestion even though it is expected to contain spinel. The residues of this sample were examined and found to contain some black material likely to be undigested spinel but not a significant amount considering the original sample weight was high (2.8 g). Thus, the undigested spinel may have a slight impact on Zn content but no effect on Cd content.

5.2.2 Preparation of the samples for mass spectrometry

A clean and matrix-free fraction of natural Cd from the sample with admixed ^{111}Cd – ^{113}Cd double spike made up to a specific spike-sample ratio, suitable for analysis on the mass spectrometer, was obtained from the sample digests by following the procedures and protocols described in detail in Chapter 2 and briefly summarised here.

5.2.2.1 Cd separation and purification

The three-stage anion exchange and extraction chromatography protocols set out in Table 2.1 on page 28 and described in section 2.3 were used to remove matrix elements from the sample, particularly those that might cause isobaric or molecular interferences, such as Mo, In, Pd and Sn (section 2.6.1). No significant isobaric interferences from Sn and In on ^{112}Cd, ^{113}Cd and ^{114}Cd were detected from the monitoring of ^{117}Sn and ^{115}In during analysis runs, attesting to the efficiency of the chemical separation procedures in removing traces of these elements, particularly the removal of Sn by the third Eichrom TRU® resin stage.

The Cd yield of the chemical separation procedures for these samples averaged 84% and mostly varied between 65 and 100%, with the exception of two samples which had lower yields of 32 and 48%.

5.2.2.2 Procedural blanks

The acid hotplate digestions described in 5.2.1.3 were generally carried out in groups of six, five samples and an acid blank. Chemical separations by anion exchange and extraction chromatography were then carried out in groups of twelve, ten samples and two acid blanks. After chemical separation, the acid blanks were dissolved in 1 ml 0.1 M HNO_3 and analysed on the mass spectrometer by scanning masses 110 to 114 using the ion-counting multiplier (discrete dynode type) which is far more sensitive than the Faraday cups and hence ideal for measuring the very low Cd abundances found in blanks. A clean 0.1 M HNO_3 wash solution was also analysed in the same way to obtain the Cd memory in the instrument and the beam intensities for the memory are then deducted from those measured for the blanks to obtain the true Cd content of the acid blanks. These blank analyses were carried out after a basic and fairly quick tuning of the instrument and before analyses of samples so that any background Cd 'memory' in the instrument was kept to a minimum.

Six out of the eight acid blanks relating to the suite of samples discussed in this study contained between 0.2 and 1.1 pg Cd. Depending on the sample weight and Cd content, this represents about 1 to 40 ppm (0.0001% – 0.004%) as a proportion of the indigenous Cd present in the samples. One blank contained 3.9 pg and another 15.1 pg Cd representing between about 11 and 168 ppm (0.0011% – 0.0168%) of the indigenous Cd in the samples. Since it is likely that most of the Cd content of the blank arose during chemical separation, in view of the volumes of acid used for elution, the Cd concentrations of samples derived by isotope dilution were adjusted for the Cd content of the blanks associated with those samples during chemical separation. The blank corrections to the Cd concentrations were negligible due to the low Cd content of the blanks and therefore no corresponding corrections to the Cd isotope content of the samples were considered necessary.

5.2.3 Mass spectrometry

5.2.3.1 Instrumentation

All isotope composition measurements were carried out on a Nu Plasma HR MC-ICPMS (Nu Instruments, part of the Ametek, Inc. Materials Analysis Division) at the

Imperial College London MAGIC laboratory facility. Sample solutions in 0.1 M HNO_3 were introduced into the mass spectrometer, using at various times two different models of desolvating nebuliser, the Aridus and Aridus II (Teledyne CETAC Technologies). Both glass and PFA (perfluoroalkoxy) nebulisers were used with a sample uptake rate generally between 100 and 140 µl/min. Nebuliser gas pressure was generally set at 30 psi but on occasion was increased to 32.5 psi to increase sample uptake rate and hence sensitivity. Further details of the instrumental set-up and operation are given in section 2.4.1 on page 29.

The source-defining slit was positioned at the widest setting of 0.3 mm giving a mass resolution (M/ΔM) of about 400 and an instrumental sensitivity generally between 175 and 300 V/ppm Cd (and averaging approximately 240 V/ppm) during the measurement sessions. Tuning procedures were performed using low concentration double-spiked NIST SRM 3108 Cd solutions prior to measurement runs in order to optimise sensitivity and stability, peak shape, peak-top flatness and coincidences on the collectors monitoring ^{111}Cd to ^{114}Cd. The full collector configuration showing which Cd isotopes and isobaric interferences are monitored is shown in Table 2.2. The rationale for choosing these isotopes in the context of minimising isobaric interferences is explained in section 2.6.1 starting on page 38.

5.2.3.2 Zero-epsilon standard and reporting Cd isotope compositions

All Cd isotope compositions are expressed in this study using epsilon notation, which reports deviations of the measured isotope ratio from the standard NIST SRM 3108 Cd in parts per 10,000 using Eq. 2.1. When comparing Cd isotope compositions with those of other elements a variation on this notation will be used which normalises the epsilon value in terms of 1 amu (Eq. 2.2). A full explanation of this notation, the reasons for using the NIST SRM 3108 Cd standard and the selection of which Cd isotope ratio to use for reporting Cd isotope variations are set out in section 2.4.2 starting on page 31.

5.2.3.3 Applying the Cd double spike method

The double spike technique, which is explained in detail in section 2.5 starting on page 33, is used in this study to obtain precise and accurate Cd isotope measurements. The technique requires the Cd double spike to be admixed with the sample prior to Cd separation and purification so that Cd fractionation known to take place during anion exchange chemistry (e.g. Cloquet et al., 2005; Schmitt et al., 2009a; Wombacher et al., 2003) can be monitored and corrected for. In order to do this, an initial Cd concentration check is carried

out on a 1 to 5 % (v/v) aliquot of the digested sample prior to Cd separation and purification in order to determine the natural Cd content of the sample and hence to be able to calculate the all-important spike-sample ratio (see section 2.5.2.2). The concentration check involves passing the aliquot, to which an accurately weighed amount of Cd double spike was added, through the second and third stages of chemical separation and purification (Table 2.1) and, analysing the final eluate on the mass spectrometer to determine the Cd content of the sample by isotope dilution.

The weight of double spike solution required to produce a specific spike-sample ratio in a sample can then be determined using simple mixing calculations and a spike-sample ratio of 1.0 – 1.1 for most of the samples described in this chapter or 1.7 for samples with low Cd content was targeted. In practice, the spike-sample ratios achieved were 0.98 – 1.00 for the first batch of samples processed, 1.09 – 1.17 for remaining batches and 1.68 – 1.71 for the low Cd content samples. The calculated amount of double spike solution is weighed and fully equilibrated with the digested sample solution before separation and purification of Cd in the sample by ion exchange chemistry and extraction chromatography described in section 2.3 starting on page 27.

A further concentration check is performed on a 5% (v/v) aliquot, as described in section 2.5.2.4 to determine the yield of Cd from chemical separation and purification in each sample and the actual spike-sample ratio. This data is used to make up solutions of the samples in 0.1 M HNO_3 to 50 – 70 ppb for Cd isotope composition analysis on the mass spectrometer. NIST SRM 3108 Cd standard solutions are then made up to match the concentrations and spike-sample ratios of the samples for sample-standard bracketing during analysis so that that ion beam intensities are similar for samples and bracketed standards. This ensures that instrumental conditions are, as far as possible, similar for samples and standards, which help to reduce systematic errors (Wombacher et al., 2003).

5.2.4 Analytical precision

5.2.4.1 Long-term precision monitored by a secondary isotopic reference material

Solutions of the BAM-I102 certified isotopic reference material, which is offset isotopically compared to NIST SRM 3108 Cd, were made up to approximately the same concentrations and spike-sample ratios as samples and standards and analysed routinely usually at the beginning and end of measurement sessions. This was used to monitor the accuracy of analytical and data reduction procedures during that session.

The results of all measurements of BAM-I102 associated with measurement sessions for the samples described in this chapter and in Chapter 4 are plotted in Figure 2.3 on page 45. The arithmetic mean of these measurements ($\varepsilon^{114/110}$Cd = –13.38 ± 0.71 2sd; n = 48) is almost identical to the weighted average of BAM-I102 measurements from seven laboratories ($\varepsilon^{114/110}$Cd = –13.32 ± 0.43 2se, n = 179) compiled by Abouchami et al. (2013). Thus, the Cd isotope measurements for the samples described in this chapter and in Chapter 4 are reproducible from measurement session to the next and can be confidently compared with measurements made by other laboratories.

5.2.4.2 Analytical precision in this study

The analytical uncertainties achieved for the Cd isotope composition measurements relating to the samples described in this chapter and the metal-silicate partitioning samples of Chapter 4 are fully discussed and assessed in section 2.7.3 on page 45. The assessment presents a justification for basing the Cd isotope composition analytical uncertainties on the weighted averages of the internal errors for individual runs (2se), the calculation of which is explained fully in section 2.7.1 on page 43. A comparison is also made in section 2.7.4 between the analytical uncertainties for these samples and those achieved by Ripperger and Rehkämper (2007) and Xue et al. (2012), the former using the same type of instrument and the latter using the exact same instrument as in this study (section 2.4.1). Both studies cited also used the same Cd double spike method as this study (section 2.5.2). The conclusion from this is that the analytical precisions for the samples of this study are in accord with those produced by those workers in their studies.

5.3 Sample selection and descriptions

5.3.1 Introduction

Sample locations are shown in Figure 5.1 below and sample descriptions, Cd isotope compositions and Cd concentrations are detailed in Table 5.2 which starts on page 152. Samples were selected to ensure that the main silicate reservoirs of the Earth, the mantle, and continental crust are adequately characterised by a sufficient number of rock samples from major tectonic settings.

5.3.2 Peridotite xenoliths

Peridotite xenoliths are particularly important to this study as they are samples of the sub-continental lithospheric mantle (e.g. Menzies et al., 1987), having been entrained in rapidly-ascending magmas, and accordingly they can provide direct evidence of the isotope composition of the upper mantle (e.g. Lee et al., 1996; McDonough and Sun, 1995). Furthermore, spinel lherzolites are thought to be near to the composition of the primitive mantle (Hart and Zindler, 1986; Jagoutz et al., 1979; Palme and Nickel, 1985) and, compared to garnet lherzolites, they are less depleted (Maaløe and Aoki, 1977).

The question remains, however, whether upper mantle samples, such as the spinel lherzolite xenoliths studied here, are representative of the composition of the mantle as a whole and, therefore, representative of the bulk silicate Earth, ignoring the very minor contribution from the continental crust.

Firstly, the upper mantle contains refractory lithophile elements in approximate proportions relative to those in CI chondrites (e.g. Hart and Zindler, 1986; McDonough and Sun, 1995; Palme and O'Neill, 2014), which have a composition very close to that of the Sun (Asplund et al., 2009; Lodders, 2003; Lodders, 2010). Experimental studies (Corgne et al., 2005; Corgne and Wood, 2002; Kato et al., 1988; McFarlane et al., 1994) have shown that refractory lithophile element ratios would change from their chondritic values during fractional crystallisation of high-pressure mineral phases in the magma ocean phase of the early Earth arguing against pervasive layering in the present day mantle.

Furthermore, seismic tomography supports convective flow throughout the entire depth of the mantle with some subducted slabs sinking to the core-mantle boundary (Helffrich and Wood, 2001; van der Hilst et al., 1997) and that mixing in the mantle is efficient enough for there to be no isolated portion or layers in the mantle (van Keken and Zhong, 1999).

Finally, several recent studies have concluded that the lower mantle is of a primitive ‘pyrolitic’ (Ringwood, 1962) composition, similar to the upper mantle. Hyung et al. (2016) used seismic shear wave velocity modelling, geochemical and magma ocean modelling to conclude that the lower mantle was likely to be pyrolitic and that the mantle as a whole ‘need not be chemically stratified’. Wang et al. (2015) performed ‘first-principles’ calculations involving lattice dynamics to conclude that the whole mantle has a uniform chemical composition.

Therefore, Cd abundances and isotope compositions are presented for a suite of spinel lherzolites from the Cameroon Line, West Africa, and Kilbourne Hole, New Mexico, USA. The Cameroon Line is a chain of intra-plate alkali basaltic volcanic centres 1,600 km long straddling an oceanic and continental margin thought to have been derived from an extinct mantle plume (e.g. Fitton and Dunlop, 1985; Halliday et al., 1990; Halliday et al., 1988; Lee et al., 1994; Matsukage and Oya, 2010), although other formation mechanisms have been suggested (e.g. Milelli et al., 2012; Reusch et al., 2011; Reusch et al., 2010; Temdjim, 2012). The spinel lherzolite xenoliths studied are from the continental section of the Cameroon Line and therefore sample the sub-continental lithospheric mantle. The petrology and precise sample locations of these samples have been extensively described by Lee et al. (1996), who published major and trace element data, and Rehkämper et al. (1997), who reported platinum group elements (PGE) abundances.

5.3.3 Komatiites

Komatiites are ultramafic rocks derived from Archean mantle which has undergone a high degree of partial melting. For example, Munro-type komatiites result from 50% partial melting (Arndt, 2003; Herzberg, 1992). The komatiites included in this study, from Munro Township and Alexo in Canada and Belingwe in Zimbabwe have all been dated at ca. 2.7 Ga (Corfu, 1993; Nisbet et al., 1987; Walker et al., 1988) and major, trace elements and PGE abundances for the same samples were included in a study by Rehkämper et al. (1999).

Mantle-derived partial melts, such as komatiites, which have not undergone a large degree of fractional crystallisation nor contamination from the continental crust, can also be used to derive the Cd isotope composition of the upper mantle (McDonough and Sun, 1995), thus also providing evidence for the Cd isotope composition of the bulk silicate Earth alongside the peridotite xenoliths.

5.3.4 Basalts

Mid-ocean ridge basalts (MORB) and ocean island basalts (OIB) have undergone a number of processes: partial melting of the mantle, fractional crystallisation, possible contamination by the ocean crust for the OIBs and, particularly for subaerial volcanism, degassing. Samples from these tectonic settings can also inform on the Cd isotope composition of the mantle. When compared to peridotites and komatiites, they can furthermore yield information on the effect of these processes on Cd isotope compositions.

MORB samples in this study have been collected from dredges of mid-ocean ridges in the Atlantic, Pacific and Indian Oceans during cruises of the research vessels *Poseidon, Meteor, Moana Wave, Sonne* and *Marion Dufresne* and from the FAZAR survey cruise. Major, trace elements and PGE abundances for the MORB samples POS 221 604 DS-1G and MW87/2 87-6, and the OIB samples SNS 24 and RE114 were also included in the above-mentioned study by Rehkämper et al. (1999) and osmium isotopes were measured for sample MD57 D'10-1 by Gannoun et al. (2007).

5.3.5 Loess

Loess deposits are usually widespread and sometimes thick accumulations of mostly silt-sized particles – predominantly 20 – 60μm (e.g. Smalley and Leach, 1978) – resulting from the aeolian transport of the products of weathering, glacial erosion or fluvial erosion (Pye, 1995). There is much discussion amongst workers involved in the study of loess about which processes are essential in its formation. For example, Smalley (1966) and Smalley and Leach (1978) emphasised the importance of glacial erosion and transportation in the formation of loess in the Danube basin, whereas, more recently, Smalley et al. (2009) stated that fluvial transportation was critical and glacial action less important. Pécsi (1990) argued that loess formation required accumulation of the wind-blown dust in a specific environmental area (the steppes or semi-arid grassland) where the deposits acquired some of the characteristics of loess by diagenesis. Smalley et al. (2011), on the other hand, contended that aeolian transportation was the critical factor required in the formation of loess deposits with other processes purely optional, returning to the simple definition provided by Pye (1987) that loess was “a terrestrial windblown silt deposit”.

Whichever processes are important in the formation of loess, the issue for this study is its use by many workers as a proxy for the average composition of the upper continental crust due to the natural widespread mechanical averaging processes involved in its formation (e.g. Peucker-Ehrenbrink and Jahn, 2001; Taylor et al., 1983). Recent studies have established that mountain terranes ultimately provide most of the material for loess deposits (Smalley et al., 2009; Stevens et al., 2010) enhancing its usefulness as a natural sampler of the continental crust.

There is a question that compositional differences between loess deposits from different regions (e.g. China and Europe) due to dilution by quartz, evaporites and carbonate (Gallet et al., 1998; Liu et al., 1993) might detract from its value as a proxy for the average

upper continental crust. However, this effect is unlikely to alter Cd abundances and isotope compositions significantly and can be largely overcome anyway by the selection of loess samples from different terranes, for example from different loess deposits in Europe and Asia. Accordingly, data for a comprehensive suite of samples from some of the main loess deposits of Europe and Asia are presented here, coupled with other crustal rocks and literature values for continental sulphides from Schmitt et al. (2009b) to fully characterise the Cd isotope composition and Cd abundances in the upper continental crust.

The Chinese Loess Plateau (CLP) formed from eroded material from arid regions to the north and northwest transported by winter monsoon winds and spring dust storms (e.g. Gylesjö and Arnold, 2006; Liu et al., 1994; Pye and Zhou, 1989; Stevens et al., 2010; Sun, 2002), although some of these processes have been questioned (Roe, 2009). Included in this study are samples from three strata in the Lingtai loess sequence in the central part of the CLP and described by Ding et al. (1999), and three samples from Jingyuan towards the north-western margin of the CLP (Shi et al., 2013).

Further to the west, a sample of loess from the Tajik Depression at Karamaidan, Tajikistan, Central Asia, and thought to have formed through similar climactic conditions as the CLP (Forster and Heller, 1994), is included in the dataset.

Finally, samples of loess deposits from Germany, Switzerland, Hungary and Moldova are included in order to sample the loess deposits found in widespread locations from Northern France across Europe and into Ukraine and Russia to the north of the Black Sea (Haase et al., 2007) and formed by fluvial and alluvial erosion processes and Quaternary glaciation (e.g. Buggle et al., 2008; Frechen et al., 2003; Smalley and Leach, 1978).

5.4 Results and discussion

5.4.1 Introduction

Several studies have attempted to estimate the Cd isotope composition of the bulk silicate Earth. Based on measurements of the Icelandic basalt BIR-1 (U.S. Geological Survey), and the assertion that isotope fractionation was unlikely during the formation of mantle-derived igneous rocks, Wombacher et al. (2003) concluded that the Cd isotope composition of the bulk silicate Earth was indistinguishable from the JMC Cd Münster standard (Johnson Matthey Co. ICP standard lot number 502552A). This standard has a Cd isotope composition of $\varepsilon^{114/110}Cd = -0.89 \pm 0.42$ relative to NIST SRM 3108 Cd (Abouchami et al., 2013).

Schmitt et al. (2009b) reported an estimated Cd isotope composition for the bulk silicate Earth of $\varepsilon^{112/110}Cd = -0.95 \pm 0.12$ relative to their own in house JMC standard and based on high-precision measurements of seven samples of MORB, OIBs and loess using TIMS coupled with the Cd double spike method. Relative to the NIST SRM 3108 Cd standard and using the epsilon notation adopted in this study, their value for the Cd isotope composition of the bulk silicate Earth is $\varepsilon^{114/110}Cd = -0.52 \pm 0.24$. They concluded from their measurements that there was little Cd isotopic heterogeneity between the major Earth silicate reservoirs represented by these 7 samples and that this data suggested that "little Cd isotope fractionation takes place during crust-mantle segregation". Schmitt et al. (2009b) acknowledge that these conclusions are based on a limited dataset which this study now aims to address directly by greatly extending the geological and geographical range of terrestrial samples measured.

In total, 44 different terrestrial samples were analysed in this study from a range of tectonic settings representing the major silicate reservoirs of the Earth, including nine peridotites and komatiites, rock types which were not represented at all in the dataset of Schmitt et al. (2009b), but which give insight into the Cd isotope composition of Earth's primitive mantle. Some rock samples were digested several times as indicated in Table 5.2 and the olivine fractions were aliquotted, with each aliquot processed independently through its own anion exchange separation. Including these repeat digestions and aliquots, a total of 55 samples were analysed resulting in the most comprehensive and globally widespread characterisation of the Cd isotope composition of Earth's silicate reservoirs to date.

The new Cd isotope data from this study have been plotted in Figure 5.2 on page 155 together with the seven above-mentioned samples analysed by Schmitt et al. (2009b), the global deep ocean water average from Xue et al. (2013), nine carbonaceous chondrites measured by Baker et al. (2010) and enstatite chondrite data from Chapter 3.

5.4.2 Peridotite xenoliths

5.4.2.1 Metasomatism in Cameroon Line spinel lherzolites

From Figure 5.2 we see that a main group of peridotites form a narrow range of Cd isotope compositions from $\varepsilon^{114/110}Cd \approx -2$ to 0, with the exception of one sample (Cameroon Line spinel lherzolite P13) which has a heavy isotope composition of $\varepsilon^{114/110}Cd = +8.71 \pm 0.49$ (2se). The other Cameroon Line spinel lherzolites P3 and C235D have isotope compositions ranging from $\varepsilon^{114/110}Cd = -1.62$ to -0.22.

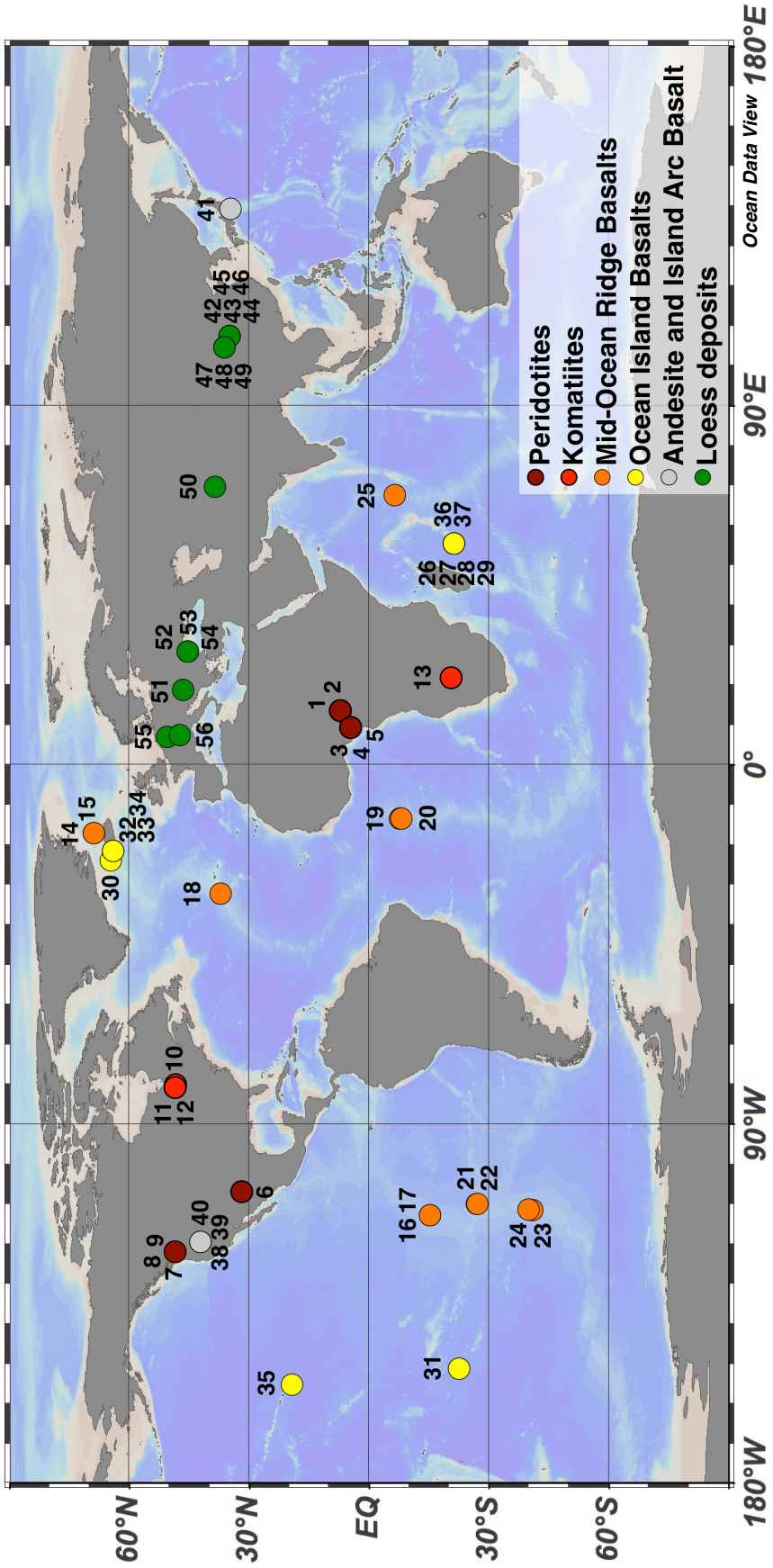


Figure 5.1. Map showing sample locations for this study. The numbers cross-reference to sample details in **Table 5.2**. Map produced using Ocean Data View (Schlitzer, 2016).

Table 5.2. Cadmium isotope compositions and concentrations for samples in this study

Sample name	Sample description	Digest	Weight (g)	$\varepsilon^{114/110}$Cd	2se	N	Cd ppb	Map
Peridotites								
P13 Cameroon Line xenolith	Spinel lherzolite, Ngaoundéré Plateau		2.649	8.71	0.49	2	41.63	1
P3 Cameroon Line xenolith	Spinel lherzolite, Ngaoundéré Plateau		2.824	–0.60	0.47	2	27.68	2
C235D Cameroon Line xenolith	Spinel lherzolite, Lake Barombi Mbo	1	2.571	–0.76	0.47	2	34.67	3
C235D Cameroon Line xenolith [1]	Spinel lherzolite, Lake Barombi Mbo	2	1.017	–1.62	1.11	2	35.68	4
C235D Cameroon Line xenolith [1]	Spinel lherzolite, Lake Barombi Mbo	3	0.809	–0.22	1.15	1	35.33	5
KH 96-2 Kilbourne Hole xenolith [1]	Spinel lherzolite, New Mexico, USA		0.803	–0.45	0.68	1	19.66	6
TS-1 Twin Sisters dunite [1]	Washington State, USA (USGS)		1.019	–1.79	0.56	1	5.25	7
TS-1 dunite – olivine fraction								
TS-1 olivine, Twin Sisters dunite	Aliquot 1 from single digest		4.629	1.89	0.94	1	5.35	8
TS-1 olivine, Twin Sisters dunite	Aliquot 2 from single digest		4.072	0.68	0.77	1	5.34	9
Komatiites								
MT20 Munro Township komatiite	Munro Township, Ontario, Canada		2.819	–3.22	0.80	3	47.27	10
M657 Alexo komatiite	Alexo Mine, Ontario, Canada		1.946	1.12	0.54	2	48.02	11
KAL-1 Alexo komatiite [1]	Alexo Mine, Ontario, Canada			–1.15	1.02	1		12
ZA-1 Belingwe komatiite [1]	Belingwe, Zimbabwe		0.523	0.28	0.34	2	77.28	13
Mid-Ocean Ridge Basalts								
POS 221 604 DS-1G MORB glass	S. Kolbeinsey Ridge	1	1.029	0.59	0.38	2	149.97	14
POS 221 604 DS-1G MORB glass [1]	S. Kolbeinsey Ridge	2	0.500	1.88	0.90	2	153.54	15
MW 87/2 87-6 MORB glass	E. Pacific Rise	1	1.038	0.80	0.60	2	157.74	16
MW 87/2 87-6 MORB glass [1]	E. Pacific Rise	2	0.514	1.64	0.90	2	161.84	17
A127 DR15 MORB glass	Azores Plateau		0.360	1.20	0.73	1	118.10	18
M41/2 130 DS-3 MORB glass*	S. Mid Atlantic Ridge		1.288	0.20	0.58	2	71.36	19
M41/2 142 DS-2 MORB glass*	Southern Mid Atlantic Ridge		1.670	0.71	0.74	2	115.23	20
SO80 37 DS-1 MORB glass*	Pukao Seamount		1.884	0.55	0.62	2	132.63	21
SO80 43 DS-1 MORB glass*	Seamount Pukao - Moai		1.349	0.01	0.53	2	131.68	22
SO157 54 DS-1 MORB glass*	Pacific Antarctic Rise		1.658	0.82	0.38	3	152.44	23
SO157 63 DS-1 MORB glass*	Pacific Antarctic Rise		2.095	0.57	0.80	4	301.94	24
MD57 D'10-1 MORB glass	Indian Ocean		0.198	2.38	0.97	1	132.35	25
Ocean Island Basalts								
RE 114 basalt	Réunion Island	1	1.599	4.77	0.38	2	82.85	26
RE 114 basalt [1]	Réunion Island	2	0.523	5.32	0.40	1	76.49	27
RE 114 basalt pure matrix	Réunion Island		1.663	4.38	0.39	2	101.04	28
RE 114 basalt matrix with inclusions	Réunion Island		2.290	4.20	0.34	3	97.61	29
SNS 24 alkali olivine basalt	Budahraun, West Iceland		1.892	2.62	0.49	2	119.34	30
120D Rurutu volcanic lava	Rurutu Island, Polynesia		1.876	2.29	0.80	5	181.82	31
BIR-1a basalt	Reykjavic dolerites, Iceland (USGS)		2.680	0.21	0.80	4	93.18	32
BTHO basalt [1]	Reykjanes Peninsula, Iceland (USGS)	1	1.004	1.12	1.04	3	92.38	33
BTHO basalt [1]	Reykjanes Peninsula, Iceland (USGS)	2	1.014	–0.43	1.19	1	92.86	34

Sample name	Sample description	Digest	Weight	$\varepsilon^{114/110}$Cd	2se	N	Cd ppb	Map
BHVO-2 [1]	Halemaumau crater, Hawaii (USGS)		0.800	1.09	0.90	2	86.08	35
Réunion basalt – olivine fraction								
RE 114 olivine, Réunion basalt	Aliquot 1 from single digest		2.555	1.63	0.64	2	22.19	36
RE 114 olivine, Réunion basalt	Aliquot 2 from single digest		2.766	2.01	0.53	2	22.15	37
Andesite and Island Arc Basalt								
AGV-2 Andesite	Guano Valley, Oregon (USGS)	1	1.603	1.17	0.58	1	67.73	38
AGV-2 Andesite	Guano Valley, Oregon (USGS)	2		1.52	0.80	2	67.71	39
AGV-2 Andesite [1]	Guano Valley, Oregon (USGS)	3	0.820	2.63	0.67	1	69.41	40
JB-2 Oshima tholeiitic basalt [1]	Oshima volcano, Japan (GSJ)		0.546	1.54	0.72	1	138.26	41
Loess deposits								
A1530 (L4) Lingtai loess	Central Loess Plateau, China (~350ka)		1.374	0.75	0.80	4	261.56	42
B0020 (L9) Lingtai loess [1]	Central Loess Plateau, China (~850ka)	1	0.490	–3.64	0.88	1	123.07	43
B0020 (L9) Lingtai loess[1]	Central Loess Plateau, China (~850ka)	2	0.295	–3.26	0.90	2	122.30	44
B0020 (L9) Lingtai loess [1]	Central Loess Plateau, China (~850ka)	3	0.490	–2.09	1.20	1	123.09	45
B5366 (L32) Lingtai loess	Central Loess Plateau, China (~2.5Ma)		1.144	–0.55	0.80	3	94.70	46
C0950 Jingyuan loess	Western Loess Plateau, China		1.138	0.78	0.45	2	136.52	47
J1864 Jingyuan loess	Western Loess Plateau, China		1.320	–0.27	0.80	4	128.25	48
J1865 Jingyuan loess	Western Loess Plateau, China		1.326	0.48	0.47	2	114.78	49
Do 031.035 Karamaidan loess [1]	Karamaidan, Tajikistan (~280ka)		0.764	0.97	0.87	1	153.93	50
P23.0m Paks loess	Paks, Hungary (~400ka)		1.932	0.10	0.80	5	132.19	51
2 - 8.10 Novaya Etuliya loess [1]	Novaya Etuliya, Moldova		0.788	2.29	1.10	1	196.62	52
2 - 8.20 Novaya Etuliya loess	Novaya Etuliya, Moldova		1.311	0.81	0.45	2	195.70	53
2 - 8.35 Novaya Etuliya loess	Novaya Etuliya, Moldova		1.201	0.80	1.10	4	210.97	54
Kreuzberg Bonn loess	Kreuzberg, Bonn, Germany		1.314	0.32	0.62	2	113.51	55
Basel loess [1]	Basel, Switzerland		0.496	0.81	1.20	1	147.84	56
Carbonaceous chondrites								
Ivuna (CI1)	Ivuna (CI1), Tanzania, Fall 1938		0.257	3.02	0.70	3	701.84	
Murchison (CM2)	Murchison (CM2, S1 – 2) no fusion crust		0.985	3.15	0.70	4	401.12	

The annotation [1] after the sample name indicates that digestion and analysis of the sample was carried out by Maria Schönbächler and included in this study with her permission. Analyses for multiple digestions of the same rock sample are shown separately, indicated by the numbers in the 'digest' column. Also shown separately are analyses of aliquots of a single digestion (olivine fractions), which have been passed through separate anion exchange separations. N refers to the number of separate measurement runs on the mass spectrometer carried out for the sample. The numbers in the 'Map' column refer to the sample locations plotted in **Figure 5.1** on page 151. All $\varepsilon^{114/110}$Cd values are reported relative to the NIST SRM 3108 Cd standard. MORB glasses indicated with * received as raw unprocessed chips from the dredges and were cleaned and leached as described in section 5.2.1.1 on page 136, the remaining MORB samples had already been cleaned and leached.

The range of Cd isotope compositions for the main group of peridotites is narrower than for komatiites, MORBs and OIBs. The more scattered Cd isotope compositions of those mantle-derived melts may result from mantle processes such as partial melting. Thus the narrow range of Cd isotope compositions is an indication that Cd isotope composition of the peridotites, apart from P13, has not been significantly fractionated by those processes.

The heavy isotope composition of sample P13, which is from the Ngaoundéré Plateau within the continental sector of the Cameroon Line, may at first sight seem to be the result of metasomatism by melts possibly derived from a mantle plume (Williams et al., 2005). However, Lee et al. (1996) indicate that reaction rims are absent from this sample apart from some secondary alteration which has replaced olivine. The presence of amphibole and other hydrous minerals in peridotites are a primary indicator of metasomatism (Boettcher and O'Neil, 1980; Boettcher et al., 1979) and, according to Lee et al. (1996), amphibole is absent in sample P13, but present in trace amounts in sample P3, along with spinel reaction rims and some olivine alteration.

Sample C235D, a spinel lherzolite from Lake Baronbi Mbo, is from the boundary zone between the oceanic and continental sections of the Cameroon Line, and, like sample P13, has no reaction rims, although fluid inclusions are present indicating contact with fluids or volatiles at some point (Lee et al., 1996). The average Cd isotope composition of this sample based on three different digestions is $\varepsilon^{114/110}Cd = -0.86 \pm 0.82$ (2se), which is identical within error to the isotope composition of the metasomatised sample P3 with a $\varepsilon^{114/110}Cd$ value of -0.60 ± 0.47 (2se).

Furthermore, Lee et al. (1996) report that sample P3 is enriched in the light rare earth elements (LREE), possibly from contamination with LREE-rich partial melts or fluids, and has a high μ value (60.4). This may be associated with enrichments in line with the U/Pb fractionation in the upper mantle of the Cameroon Line at about 125Ma, as suggested by (Halliday et al., 1990). According to Lee et al. (1996), however, samples P13 and C235D are depleted in LREE and have low μ values (<10). Based on sample petrology, P13 appears to be less metasomatised than P3, which is also from the Ngaoundéré Plateau, and yet has a much heavier Cd isotope composition indicating that (presumably) kinetic isotope fractionation resulted in the preferential loss of light Cd isotopes from the residue which now forms sample P13.

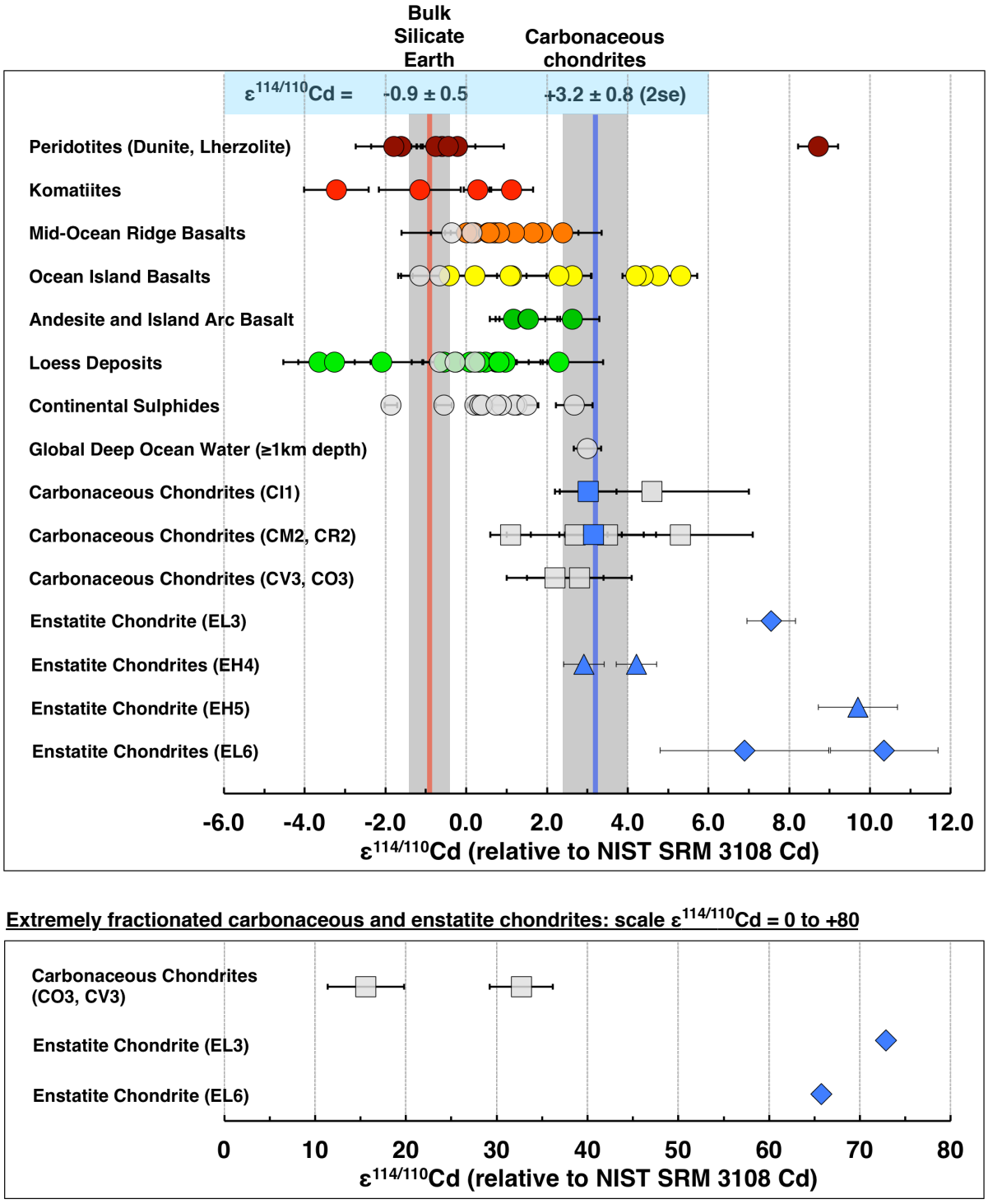


Figure 5.2. Cd isotope compositions of the bulk silicate Earth (BSE) and chondrites. Data analysed in this study are shown as solid coloured symbols and detailed in **Table 5.2** starting on page 152 and in Chapter 3 (enstatite chondrites). Literature data are shown as light grey symbols: 2 MORBs, 2 OIBs, 3 loess and all continental sulphides are from Schmitt et al. (2009b); Global Deep Ocean Water is from Xue et al. (2013); 9 carbonaceous chondrites are from Baker et al. (2010). The BSE isotope composition (red vertical line) is based on the average Cd isotope composition for peridotites and dunite excluding an anomalous highly fractionated sample (see text); the carbonaceous chondrite average Cd isotope composition (blue vertical line) excludes the highly fractionated samples included in the lower section of the figure. Error bars for data in this study are shown at the 2se level, with adjustments for scatter as explained in section 2.7.1 on page 43. Error bars for data from Schmitt et al. (2009b) and Xue et al. (2013) are shown at the 2se level, from Baker et al. (2010) at the 2sd level. The grey shaded areas represent uncertainties at the 2se level on the BSE and CC values.

5.4.2.2 Stable isotope fractionation in the mantle

There have been very few studies addressing Cd behaviour during mantle processes. Major studies involving Cd abundances are by Yi et al. (2000) and Witt-Eickschen et al. (2009) who studied the behaviour of Cd and other volatile chalcophile elements in MORB samples in the case of the former and spinel peridotite xenoliths in the case of the latter. More recently, Wang et al. (2016a) studied an extensive suite of mantle peridotites from a range of tectonic settings from which they were able to constrain the minimum Cd abundance in the bulk silicate Earth at 31 ± 6 ng/g. This is comparable with other estimates of 35 ± 7 ng/g (Witt-Eickschen et al., 2009) and 40 ±12 ng/g (McDonough and Sun, 1995) and consistent with the average Cd content for the Cameroon Line peridotite xenoliths of this study of 35 ± 4 ng/g (2se, n=5).

However, to date, there have been no studies specifically addressing Cd isotope fractionation in the mantle. Therefore, it would be useful to look at mantle processes which result in stable isotope fractionation in other non-traditional isotope systems, such as Li, Mg Fe and Zn in order to consider which mantle processes might cause Cd isotopic variations, in particular the heavy isotope composition of sample P13.

In cosmochemistry, Cd is classified as a labile element, which is easily mobilised by thermal and aqueous processes (e.g. Lipschutz, 1997; Lipschutz and Woolum, 1988). It is therefore relevant to consider the causes of lithium stable isotope fractionation in the mantle which might also result in Cd isotopic fractionation since Li, like Cd, is easily mobilised by low temperature alteration processes in the crust (Pearson and Wittig, 2014), with its mobility further evidenced by leaching experiments (Seitz et al., 2004).

Thermal and chemical diffusion have been recognised as processes which can result in kinetic isotope fractionation (e.g. Richter et al., 2009a; Richter et al., 2003; Richter et al., 2009b) and the large variations in Li isotopes found in mantle peridotites have been attributed mainly to diffusion processes by many authors (e.g. Aulbach and Rudnick, 2009; Ionov and Seitz, 2008; Jeffcoate et al., 2007; Lundstrom et al., 2005; Parkinson et al., 2007; Rudnick and Ionov, 2007). In contrast, the Li isotope composition of melts is lighter than mantle sources by only $\delta^7Li < 0.2 – 0.5$ ‰, indicating that fractionation of Li isotopes during partial melting is likely to be insignificant (Jeffcoate et al., 2007).

Aulbach and Rudnick (2009) suggested that two diffusion mechanisms could have resulted in the Li concentrations and isotope fractionations observed in Tanzanian mantle peridotite xenoliths. Firstly, diffusion of Li in melts along grain boundaries into peridotite

minerals during entrainment in the host magma or during an episode of metasomatism. Secondly, the subsolidus partitioning of Li between minerals, as controlled by temperature and pressure during heating (possibly plume-related), cooling, and decompression. Ionov and Seitz (2008) also suggested similar mechanisms, namely, diffusion of Li between minerals in peridotite xenoliths controlled by temperature and the infiltration of fluids during host magma crystallisation, although Yakob et al. (2012) concluded from their experiments that diffusion of Li was not dependant on temperature.

The range of Mg isotope variations in mantle peridotites is far more restricted than Li which indicates that Mg isotopes are not fractionated significantly by partial melting or fractional crystallisation (Teng et al., 2010), although Wiechert and Halliday (2007) observed that Mg isotope variations in lunar basalts were probably due to extensive olivine and pyroxene crystallisation during a magma ocean stage. In addition, thermal diffusion of Mg in olivine and pyroxene may also create small isotopic fractionations (Handler et al., 2009; Huang et al., 2010).

Iron isotope compositions of mantle peridotites are fairly homogeneous (Pearson and Wittig, 2014) with small isotopic variations attributable to peridotite melt depletion, inter-mineral diffusion and Fe enrichment from metasomatism (e.g. Weyer and Ionov, 2007; Williams et al., 2005; Zhao et al., 2012). Zhao et al. (2015) investigated the Fe isotope composition of peridotite xenoliths from beneath the North China Craton and found that large Fe isotopic variations in strongly metasomatised Fe-rich lherzolites resulted from kinetic isotope fractionation during interaction between wall-rock and melts, with little Fe isotopic variation in less metasomatised lherzolites.

The chemical behaviour of Zn is particularly relevant to Cd since both elements are in Group 12 (IUPAC classification) of the Periodic Table, mainly have an oxidation state of only +2 in nature and have similar volatilities. A very recent study by Doucet et al. (2016) analysed suites of fertile lherzolites and refractory harzburgites from Siberia and Mongolia and noted that the average Zn isotope composition of the former was $\delta^{66/64}Zn = +0.30 \pm 0.03‰$ and the latter was $\delta^{66/64}Zn = +0.14 \pm 0.03‰$. These workers attributed the light Zn isotope composition of the refractory harzburgites to the fractionation of Zn isotopes during high levels of partial melting (>30%) at high pressures (7 – 4 GPa), and suggested significant Zn isotopic heterogeneity may have arisen in the mantle of the early Earth from these processes. A further discussion of the results of Doucet et al. (2016) in the context of the Zn isotope composition of the bulk silicate Earth is contained in section 5.4.9 below. Wang et al. (2016b) also noted that the unaltered peridotites of their study had a light Zn isotope

composition ($\delta^{66/64}Zn = +0.17 \pm 0.06‰$) compared to basalts ($\delta^{66/64}Zn = +0.28 \pm 0.05‰$) and commented that this indicated isotope fractionation during partial melting of peridotites. They also noted that the metasomatised peridotites analysed showed a wide variation in Zn isotope compositions of $\Delta^{66/64}Zn \approx 0.9‰$ which they attributed to mantle metasomatism.

The insight gained from this work on the Li, Mg, Fe and Zn isotope systems is that kinetic isotope fractionation seems to be more significant in processes such as metasomatism, and in particular thermal and chemical diffusion, than it is in partial melting and fractional crystallisation. However, the influence of partial melting should not be dismissed, particularly in cases of high melt depletion. Examination of the Cd isotope compositions of komatiite, basalt and crustal samples in this study should, however, provide an indication of whether partial melting and fractional crystallisation have produced some fractionation in Cd isotopes.

The question of how peridotite xenolith P13 became fractionated, despite being less metasomatised than sample P3 from the petrological examination in Lee et al. (1996), remains unanswered.

5.4.3 Komatiites

As shown in Figure 5.2, the komatiite samples in this study show a far greater range of Cd isotope compositions ($\varepsilon^{114/110}Cd \approx -3$ to $+1$) than the peridotites ($\varepsilon^{114/110}Cd \approx -2$ to 0), however, the mean Cd isotope compositions are similar, as discussed in section 5.4.8 below. Maier et al. (2009) studied platinum group elements in a suite of komatiites ranging in age between about 3.5 and 2.7 Ga and concluded that material from the late chondritic veneer would have equilibrated with the mantle by 2.9 Ga. Therefore, it is unlikely that the scatter in the Cd isotope compositions of the fairly young (2.7 Ga) samples of this study were caused by incomplete mixing in the Archean mantle.

Given the high degree of partial melting during the formation of komatiite melt, it is possible that fractionation of Cd isotopes took place during this process leaving a lighter Cd isotope composition in the residue and a heavier composition in the melt. This has been recorded for Zn isotopes in conditions of extreme partial melting at high pressure (Doucet et al., 2016), as discussed in the previous section. However, Dauphas et al. (2010) argue that komatiite melt formed in a plume hotter than the surrounding mantle (Arndt et al., 1998) at high enough temperatures that, firstly, equilibrium isotope fractionation would have been reduced and, secondly, more rapid diffusion would have mitigated any kinetic isotope fractionation.

5.4.4 Basalts

Basalts from three major tectonic settings are represented in the dataset: mid-ocean ridge basalts (MORBs), ocean island basalts (OIBs), and an island arc basalt. The island arc basalt will be considered alongside the data for an andesite when the continental crust is discussed in section 5.4.6 below.

Figure 5.2 shows that Cd isotope compositions for MORBs are tightly clustered from $\varepsilon^{114/110}Cd \approx -0.4$ to +2.4 whereas OIBs show greater scatter with isotope compositions from $\varepsilon^{114/110}Cd \approx -1.2$ to +5.3. The mean values for these two categories are also significantly different: MORBs have a mean isotope composition of $\varepsilon^{114/110}Cd = +0.8 \pm 0.4$ (2se, n=14), with OIBs heavier at $\varepsilon^{114/110}Cd = +2.0 \pm 1.3$ (2se, n=12). However, the heaviest OIB isotopic compositions, ranging from $\varepsilon^{114/110}Cd \approx +4.2$ to +5.3, were measured for basalts (whole rock samples and matrix separates) from one location: Réunion Island. The remaining OIBs fall in the range $\varepsilon^{114/110}Cd \approx -1.2$ to +2.6, similar to the range of isotope compositions recorded for MORBs.

One MORB sample, SO157 65 DS-1 from the Pacific Antarctic Rise, has an anomalously high Cd content of 302 ng/g, compared to a Cd content of 152 ng/g for a dredge from another location on the Pacific Antarctic Rise and an average of 137 ng/g for the other MORB samples in the dataset (Table 5.2). It is possible that some residual ferromanganese coating remained on the sample after leaching (see section 5.2.1.2 on page 136). Such coatings are known to have a high Cd content ranging from 1.0 ppm to 21.6 ppm (Schmitt et al., 2009b). However, mass balance indicates that the sample would have had to have coatings comprising > 1.4 wt % of the bulk sample to generate its high Cd content, which is unrealistic since only sparse small reddish-brown coatings were present on the MORB chips of this sample during picking. Mass balance also indicates that any small residual ferromanganese coatings would not have altered the Cd isotope composition of this sample, or any other MORB sample, to any perceptible degree.

Since basalts are essentially mantle-derived melts, it would be useful to identify possible fractionation trends affecting Cd isotope compositions which might have taken place during partial melting, fractional crystallisation or degassing and which distinguish the basalts isotopically from the mantle rocks from which they are derived (Schönbächler et al., 2009). In Figure 5.3 the Cd isotope compositions of the samples are plotted against Cd content. The data is fairly scattered without any apparent fractionation trend, although it could be argued that a very loose partial melting trend might exist (indicated by the green

arrow) from peridotites through komatiites to basalts, and possibly a degassing trend (indicated by the red arrow) for some OIBs.

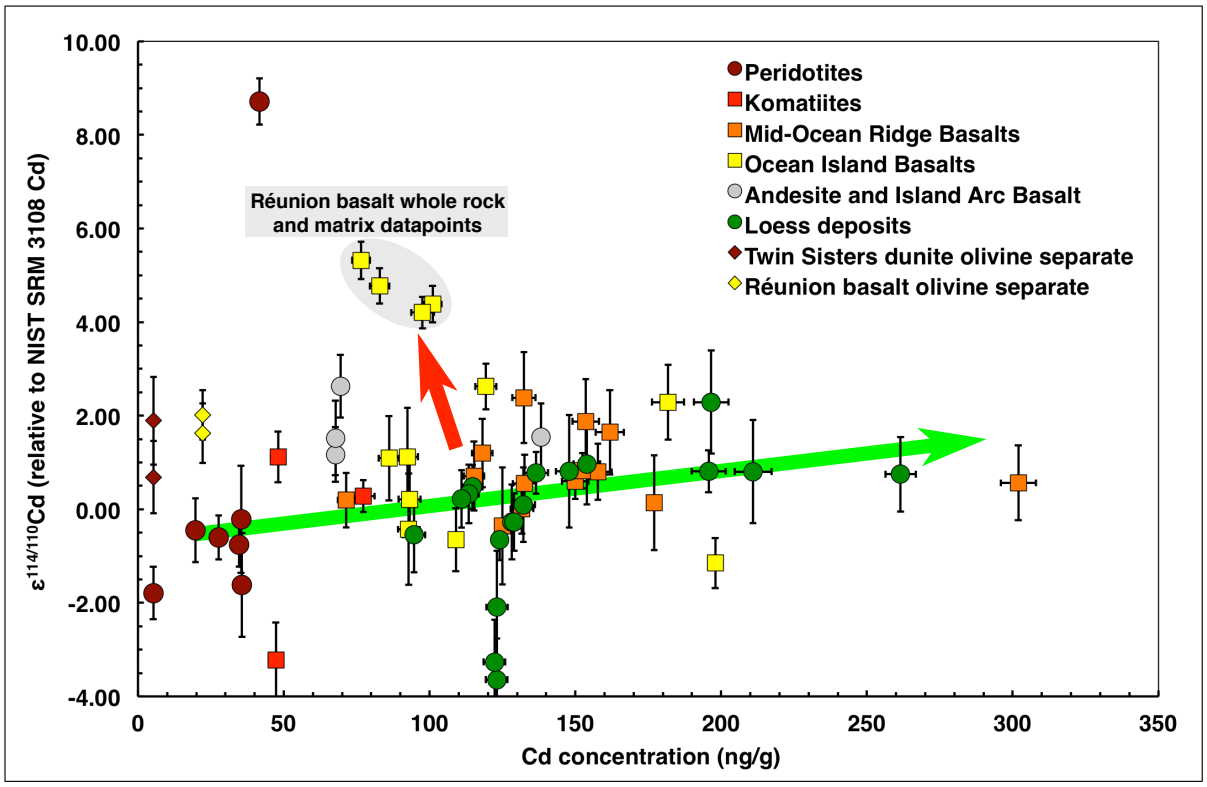


Figure 5.3. Plot of Cd isotope compositions expressed in $\varepsilon^{114/110}$Cd units against Cd concentrations in ppb. Data is from this study and 2 MORBs, 2 OIBs, 3 loess are from Schmitt et al. (2009b). Error bars for $\varepsilon^{114/110}$Cd values are at the 2se level. Uncertainties for Cd concentrations are unavailable for the data from Schmitt et al. (2009b), otherwise they are shown at the 2sd level unless smaller than the symbols. The red arrow indicates an approximate possible degassing trend and the green arrow indicates an approximate possible partial melting trend.

Regression analyses were carried out to further explore a possible partial melting trend in the data, as indicated by the green arrow in Figure 5.3. A linear regression applied to the Cd isotope compositions and contents of samples from all tectonic settings, with the exception of the anomalous Cameroon Line peridotite xenolith 'P13' referred to in section 5.4.2.1 above, shows a slight positive correlation, whereby $\varepsilon^{114/110}$Cd values increase with increasing Cd content. The coefficient of determination for the linear regression, R^2, is only 0.016, indicating the data is extremely scattered, obscuring any linear relationship.

However, if linear regression analysis is only applied to data for peridotites, komatiites and MORBs, a stronger positive correlation is evident with an R^2 value of 0.31, which improves to 0.43 if the MORB sample with the unusually high Cd content of 302 ppb, sample SO157 63 DS-1, is excluded. If this is interpreted as a linear partial melting trend for peridotites, komatiites and MORBs, the slope of this trend is approximately characterised by an increase in $\varepsilon^{114/110}$Cd of about 0.5 to 0.7 ε-units for an increase in Cd content of 100 ng/g.

It would hence appear that partial melting does slightly fractionate Cd isotopes resulting in heavier isotope compositions in basalts compared to their mantle sources. This finding is consistent with the fractionation of Zn isotopes during partial melting, discussed in section 5.4.2.2 above, particularly since Zn and Cd are chemically very similar.

5.4.5 Degassing behaviour in MORBs and OIBs

Ocean island basalts are excluded from the more strongly correlated dataset (peridotite, komatiites and MORBs) due to a possibly separate and competing degassing trend as indicated by the red arrow in Figure 5.3. When linear regression analysis is applied to the OIB data alone, there is a negative correlation, whereby $\varepsilon^{114/110}$Cd values decrease with increasing Cd content, although there is considerable scatter with an R^2 value of only 0.15. Heavier $\varepsilon^{114/110}$Cd values, corresponding to lower Cd contents, could indicate open system (Rayleigh) fractionation of the Cd isotope composition, possibly associated with Cd degassing in subaerial volcanic settings.

Six of the MORB samples (indicated with * in Table 5.2) were processed from raw sample chips by cleaning, leaching and picking as described in section 5.2.1.1 on page 136, whilst the remaining MORB samples had already been cleaned by other workers. All of the samples had chips with vesicles indicating degassing during eruption and solidification of the lavas. The vesicles varied in size up to about 1mm in diameter and some had evidence of grey or light brown clay alteration inside. Thus, based on a purely physical inspection of the samples, degassing has affected at least some MORB samples. This may account for some of the scatter apparent in the MORB data, as isotope fractionation from degassing would overprint the partial melting trend shown in Figure 5.3.

In studies of various elements in submarine and subaerial volcanic settings, Cd was found to be one of the most volatile during degassing of erupted lavas. The emanation coefficient is a simple measure by which the relative volatilities of elements during magmatism can be quantified and is defined by the proportional difference between the elemental concentrations in the lava before and after eruption (Gill et al., 1985; Lambert et al., 1985; Rubin, 1997). Consequently, an emanation coefficient of 0 would indicate no degassing of the element and a coefficient of 1 would indicate complete degassing. Early studies calculated an emanation coefficient of 0.19 – 0.27 for Cd, higher than the value for Zn (0.0026) and Tl (0.0022). According to this measure, very few metallic or metalloid elements are more mobile than Cd during magmatic degassing (Norman et al., 2004; Rubin, 1997),

although a more recent study identified Tl as more volatile than Cd, possibly due to its incompatible nature and ability to complex with Cl^- and S^{2-} ligands (Johnson and Canil, 2011)

Other studies also attest to the rapid diffusion of Cd into magmatic gases. Hinkley et al. (1994) reported that Cd and Tl were enriched in the Kilauea and Etna volcanic plumes compared to other chalcophile elements. MacKenzie and Canil (2008) measured the diffusivity of Cd and other trace metals in experimental CMAS (CaO-MgO-Al_2O_3-SiO_2) melts and concluded that Cd diffused faster across the magma-gas interface compared to Sb, Te, Pb, Tl and Re. They also found that the Cd/Re ratio of Kilauea volcanic gases increased rapidly from about 5 before the 1984 eruption to about 55 after.

Regarding isotope fractionation during volcanism, Toutain et al. (2008) found that mass-dependent isotope fractionation during evaporation and condensation controlled the Zn isotope compositions of melt, gases and condensates in fumerolic deposits from the Merapi volcano, although they concluded that degassing of Zn did not significantly change the Zn isotope composition of residual magmas.

The conclusion is that firstly, Cd is extremely mobile during magmatic degassing and this applies to both MORBs and OIBs. Secondly, the data show some evidence of isotope fractionation from partial evaporation and condensation during degassing (Schönbächler et al., 2009), as has been found for Zn. Notably, Cd is far more mobile than Zn, accounting for the variability found in the Cd isotope compositions of OIBs and, in particular, the relatively heavy isotope compositions of the Réunion basalt lavas.

5.4.6 Continental crust

The continental crust is characterised in this study by a large suite of loess samples from a variety of global loess deposits and the rock reference materials andesite AGV-2 (USGS) and island arc tholeiitic basalt JB-2 (GSJ). From Figure 5.2 on page 155, the loess samples exhibit $\varepsilon^{114/110}Cd$ values ranging from –3.6 to +2.3 and averaging –0.1 ± 0.7 (2se, n=18). Notably, this mean is lower than the averages determined for MORBs ($\varepsilon^{114/110}Cd$ = +0.8 ± 0.4) and OIBs ($\varepsilon^{114/110}Cd$ = +2.0 ± 1.3).

The USGS andesite reference material AGV-2 was analysed in connection with the samples of this chapter and the enstatite chondrites of Chapter 3, in order to monitor the reproducibility of the Cd (and Pb and Tl) isotope measurements. The Cd isotope composition of the AGV-2 samples associated with the enstatite chondrite analyses, shown in Table 5.2 (as

samples 41 and 47) and also Table 3.4 on page 71, is $\varepsilon^{114/110}Cd = +1.5 \pm 0.8$. Including the additional analyses of AGV-2 that were carried out together with the sample measurements of this chapter (Table 5.2), yields an overall mean Cd isotope composition for AGV-2 of $\varepsilon^{114/110}Cd = +1.7 \pm 0.9$, which is in line with the AGV-2 analyses of Wiggenhauser et al. (2016) which yielded a value of $\varepsilon^{114/110}Cd = +1.1 \pm 1.1$ (2sd, n=2).

The scatter in Cd isotope compositions and concentrations of the loess samples is similar to the scatter observed for OIBs (Figure 5.2, Figure 5.3), allowing speculation that one or more fractionation processes are responsible. For example, the loess deposits sample various cratonic source rocks with different petrogenetic partial melting and alteration histories, and these processes may be responsible for the generation of distinct and variable Cd isotope compositions.

5.4.7 Olivine separates

The Cd isotope compositions and concentrations of olivine separates from two bulk rock samples were analysed: the Twin Sisters dunite TS-1 and Réunion basalt (Table 5.2 and Figure 5.3). The average Cd isotope compositions of these two olivine separates were very similar with $\varepsilon^{114/110}Cd$ values of $+1.2 \pm 0.9$ for the TS-1 olivine and $+1.9 \pm 0.8$ for the Réunion basalt olivine. However, the isotopic offsets between the respective whole rock (WR) samples and the olivine separates (OL) are completely different. In the following, the capital delta-epsilon notation introduced in section 4.3.4.1 is used to define $\Delta\varepsilon^{114/110}Cd_{WR–OL} = \varepsilon^{114/110}Cd_{WR} - \varepsilon^{114/110}Cd_{OL}$. Thus, the observed $\Delta\varepsilon^{114/110}Cd_{WR–OL}$ values are –3.0 for TS-1 dunite and +2.8 for the Réunion basalt.

The Cd concentrations are virtually identical for the TS-1 whole rock and its olivine separate (5.3 ng/g), which is unsurprising given the high olivine content of dunites. For the Réunion basalt, the whole rock Cd concentration is 90 ng/g compared to 22 ng/g for the olivine separate. These Cd concentration results are entirely consistent with the preferential partitioning of Cd into clinopyroxene and possibly amphibole host phases rather than olivine and the moderate incompatibility of Cd during partial melting (Witt-Eickschen et al., 2007; Yi et al., 2000).

The observation of $\Delta\varepsilon^{114/110}Cd_{WR–OL}$ values that indicate a different direction of Cd isotope fractionation between the whole rock and olivine for the two samples likely reflects the very different petrogenic history of the two rocks. The negative $\Delta\varepsilon^{114/110}Cd_{WR–OL}$ value of the TS-1 dunite is thereby indicative of partitioning of isotopically light Cd into other phases

of this rock, particularly spinel and pyroxenes. In contrast, the positive $\Delta\varepsilon^{114/110}Cd_{WR-OL}$ value observed for the Réunion basalt is in accord with the observation that mantle melts generally prefer isotopically heavy Cd compared to mantle minerals, such as olivine. In addition, the positive $\Delta\varepsilon^{114/110}Cd_{WR-OL}$ of the Réunion basalt may reflect the fractionation of olivine followed by the loss of magmatic gas enriched in light Cd isotopes from the residual magma.

5.4.8 The Cd isotope composition of the bulk silicate Earth

Further to the reasoning in section 5.3.2 on page 146, that peridotites xenoliths sample the upper mantle and that evidence points to the mantle as a whole being fairly homogeneous, the average Cd isotope composition of the peridotites sampled in this study should provide an estimate of the Cd isotope composition of the mantle, and hence the bulk silicate Earth (BSE). Since the continental crust comprises just 0.585% of the BSE by mass (Lodders and Fegley, 1998), its average Cd isotope composition is not significant in determining the composition of BSE.

The fairly narrow spread of Cd isotope compositions of the peridotites, apart from the anomalous sample P13, from $\varepsilon^{114/110}Cd \approx -2$ to 0, particularly when compared with the greater spread of Cd isotope compositions for samples in other tectonic settings as illustrated in Figure 5.2, provides an indication that, generally, mantle processes such as metasomatism have not resulted in significant fractionation of Cd isotopes. The mean Cd isotope composition of peridotites measured in this study is $\varepsilon^{114/110}Cd = -0.9 \pm 0.5$ (2se, n=6), excluding anomalous sample P13, and this has been taken as the Cd isotope composition of the bulk silicate Earth and indicated in Figure 5.2 by the red vertical line.

Komatiites also provide an estimate of the composition of the upper mantle following the reasoning in sections 5.3.2 and 5.3.3 that they have not undergone a large degree of fractional crystallisation nor contamination from the continental crust (McDonough and Sun, 1995), and that they are representative of the composition of the Archean mantle due to the high degree of partial melting (Dauphas et al., 2010; Maier et al., 2009). In this study, the average Cd isotope composition of the komatiites is $\varepsilon^{114/110}Cd = -0.7 \pm 1.9$ (2se, n=4), which is very close to the Cd isotope composition of the peridotites, and the average composition of peridotites and komatiites taken together is $\varepsilon^{114/110}Cd = -0.8 \pm 0.8$ (2se, n=10). This additional data for komatiites therefore supports the estimate of the Cd isotope composition of the BSE provided by peridotites.

5.4.9 The Cd and Zn isotopic offset between the bulk silicate Earth and carbonaceous chondrites

A key finding for the dataset presented in this chapter is that there is a subtle but resolvable offset between the Cd isotope composition of BSE, $\varepsilon^{114/110}Cd = -0.9 \pm 0.5$ (2se), and that of carbonaceous chondrites, $\varepsilon^{114/110}Cd = +3.2 \pm 0.8$ (2se, n=9), calculated from the mean Cd isotope composition of carbonaceous chondrites analysed in this study, Ivuna (CI1) and Murchison (CM2) and carbonaceous chondrites analysed by Baker et al. (2010). The strongly fractionated carbonaceous chondrites of Baker et al. (2010), Leoville (CV3) and Kainsaz (CO3) with $\varepsilon^{114/110}Cd$ values of +32.7 and +15.6 respectively, were excluded from the mean as their very positive $\varepsilon^{114/110}Cd$ values probably arose from thermal processing or shock or both on the chondrite parent bodies. The weighted average Cd isotope composition of the CI1 chondrites Ivuna and Orgueil is $\varepsilon^{114/110}Cd = +3.1 \pm 0.7$ (2se), identical to the average for all carbonaceous chondrites within error.

This Cd isotopic offset is illustrated in Figure 5.2 with the red and blue vertical lines representing the mean Cd isotope compositions of BSE and carbonaceous chondrites respectively. Before exploring possible reasons for this Cd isotopic offset, it is worth investigating whether a similar offset also exists between the Zn isotope compositions of the BSE and carbonaceous chondrites, for which a reasonable dataset exists in the literature. The chemical behaviour of Zn is similar in many ways to Cd: both elements are in Group 12 (IUPAC classification) of the Periodic Table, have an oxidation state of +2 in most compounds and are volatile metals with 50% condensation temperatures (Lodders, 2003) 652 K for Cd and 726 K for Zn.

Accordingly, the Zn isotope compositions for terrestrial rocks from relevant tectonic settings, namely peridotites, various basalts and andesites and for carbonaceous chondrites are plotted in the lower panel of Figure 5.4, along with, in the upper panel, the Cd isotope compositions for similar rock and meteorite types from this study and literature already included in Figure 5.2 on page 155. The isotope data for both elements have been recast in terms of εCd per amu and εZn per amu using Eq. 2.2 on page 31 to allow for some comparison between the two stable isotope systems (Wombacher and Rehkämper, 2004) and the isotope composition of the BSE for both isotope systems has been aligned (single red vertical line) to compare the isotopic offset between the BSE and carbonaceous chondrites (blue vertical lines) directly.

In determining the Zn isotope composition of the BSE, Chen et al. (2013) argued that mantle-derived mafic and ultramafic melts represented the Zn isotope composition of their mantle source well since there would have been limited Zn fractionation resulting from high-temperature igneous processes. On that basis, they estimated the Zn isotope composition of the BSE to be $\delta^{66/64}Zn = +0.28 \pm 0.05‰$ based on their data for ultramafic and mafic rocks combined with some literature data.

However, Doucet et al. (2016), whilst acknowledging that the average Zn isotope composition of their suite of fertile spinel and garnet lherzolites at $\delta^{66/64}Zn = +0.30 \pm 0.03‰$ agreed with the BSE estimate of Chen et al. (2013), contended that the mantle of the early Earth was heterogeneous since their suite of refractory spinel harzburgites had a very light isotope composition ($\delta^{66/64}Zn = +0.14 \pm 0.03‰$). They attributed this fractionation to high levels of partial melting (> 30%) at high pressures (7 – 4 GPa). They also suggested that the range of isotope compositions found in basalts ($\delta^{66/64}Zn \approx 0.2 – 0.4$) was consistent with modelling Zn isotope fractionation in these melts at moderate levels of partial melting (up to 20%) at lower pressures (≤ 3 GPa). The Zn isotopic offset between fertile lherzolite and refractory harzburgite peridotites and the range of values for basalts can clearly be seen in the lower panel of Figure 5.4 below.

The Zn isotope dataset for mafic and ultramafic rocks has been extended in this study from that used by Chen et al. (2013) to include other mainly more recent literature data. Re-calculating the Zn isotope composition of the BSE with this additional data and on the same basis as these authors (ultramafic and mafic rocks: peridotites and ocean island basalts, all < 51 wt% SiO_2) but, importantly, excluding isotopically light depleted harzburgites, produces an identical average of $\delta^{66/64}Zn = +0.28 \pm 0.01‰$ (2se), or εZn per amu = +1.4 ± 0.1, depicted as the vertical red line in Figure 5.4.

The more intermediate rock types (about 53 to 58 wt% SiO_2), continental flood basalts, an island arc basalt (IAB) and andesites, have also been plotted on Figure 5.4 and their average Zn isotope compositions are clearly the same as that of the BSE within error: continental flood basalts produce an average $\delta^{66/64}Zn = +0.28 \pm 0.02‰$ and andesites an average $\delta^{66/64}Zn = +0.26 \pm 0.02‰$. In addition, $\delta^{66/64}Zn$ values of +0.2 to +0.3 (not plotted in Figure 5.4) have been reported for MORBs and loess (Ben Othman et al., 2001a; Ben Othman et al., 2001b; Ben Othman et al., 2003) further emphasising the apparent homogeneity of terrestrial Zn isotope compositions, supporting the contention of Chen et al. (2013), and also Albarède (2004), that igneous processes produce only limited fractionation of Zn isotopes.

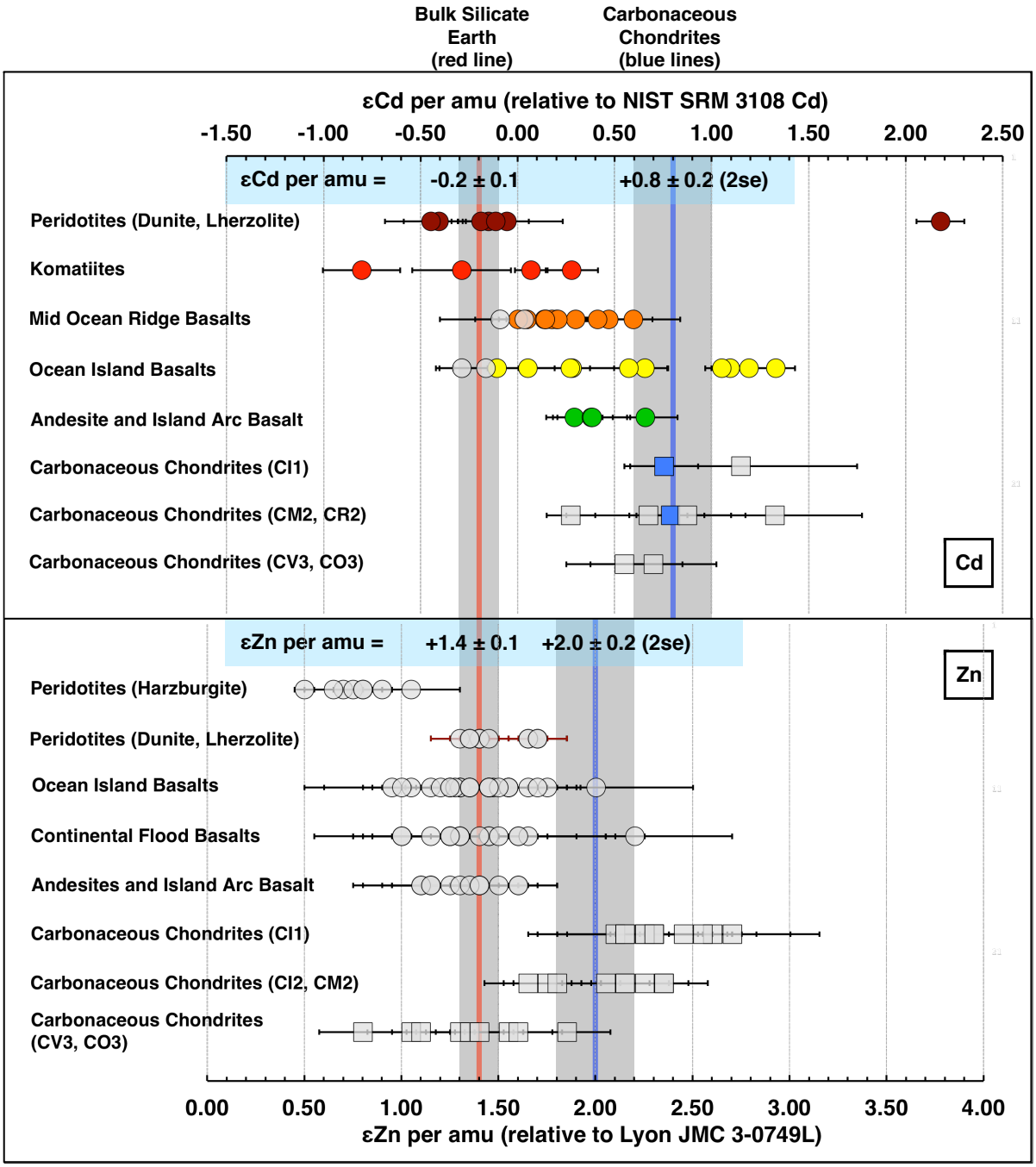


Figure 5.4. Cd and Zn isotope compositions (ICs) of bulk silicate Earth (BSE) and carbonaceous chondrites (CC) shown in ε-notation and normalised to a mass difference of 1 amu (Wombacher and Rehkämper, 2004) and with the ICs of the BSE aligned (red line) to allow direct comparison of the two isotope systems. The Zn IC of the BSE is the average of peridotites (dunite, lherzolites) and ocean island basalts, but excludes the refractory harzburgites. For the Cd IC of the BSE see **Figure 5.2**. Data from this study are plotted as solid coloured symbols, literature data as light grey symbols. Cd isotope data from this study (**Table 5.2** and **Figure 5.2**) and from Schmitt et al. (2009b) and Baker et al. (2010). Zn isotope data from Archer and Vance (2004), Barrat et al. (2012), Bigalke et al. (2010), Bridgestock et al. (2014), Chen et al. (2013), Chen et al. (2009), Chen et al. (2016), Chapman et al. (2006), Cloquet et al. (2006), Dolgopolova et al. (2006), Doucet et al. (2016), Herzog et al. (2009), Liu et al. (2016), Luck et al. (2005), Maréchal et al. (2000), Moynier et al. (2010), Moynier et al. (2011), Sonke et al. (2008), Sossi et al. (2015), Toutain et al. (2008), Viers et al. (2007), Zhou et al. (2014). For the Lyon JMC 3-0749 zero-delta standard see Maréchal et al. (1999). The CI2 chondrite is 'Tagish Lake' which can also be classified as C2 ungrouped. Error bars for data from this study and Cd ICs for MORBs and OIBs from Schmitt et al. (2009b) are reported at the 2se level. Error bars for other literature data are at the 2sd level. The grey shaded areas represent uncertainties at the 2se level on the BSE and CC values.

Further to this, Ben Othman et al. (2006) reported very little inter-mineral Zn isotope fractionation in a study of separates from peridotites and lherzolites, with the exception of spinel which displayed greater $\delta^{66/64}$Zn variability. Zinc displays very compatible behaviour partitioning into spinel crystallising from a melt (Horn et al., 1994; O'Reilly et al., 1991) and a study of the isotope compositions of Archean komatiites from Munro Township, Canada, found that chromites were strongly enriched in light Zn isotopes compared to silicate minerals, and that there was a smaller degree of Zn fractionation between silicate mineral separates with heavier Zn isotopes in minerals with lower Zn coordination numbers (Mattielli et al., 2012; Mattielli et al., 2014).

Several other investigations have also revealed that light Zn isotopes prefer the spinel phase, although these investigations concerned the Zn isotope composition of spinel in ordinary chondrites (Luck et al., 2005) and partitioning of Zn from metal into chromite during the cooling of iron meteorite parent bodies (Bridgestock et al., 2014).

Liu et al. (2016) reported significant Zn isotopic heterogeneity in continental basalts from Eastern China with $\delta^{66/64}$Zn values from +0.30 to +0.63 and concluded that these had incorporated Zn enriched and isotopically heavy carbonates ($\delta^{66/64}$Zn ≈ +0.91), although these authors reiterated the findings of Chen et al. (2013) that there was little Zn isotope fractionation during magmatic crystal-melt differentiation ($\Delta^{66/64}$Zn < 0.1‰).

The Zn isotope composition of carbonaceous chondrites show a distinct trend from heavier isotope compositions in the most primitive but most aqueously altered CI1 meteorite type (average $\delta^{66/64}$Zn = +0.47 ± 0.02‰) to lighter compositions in the less aqueously altered type 2 ($\delta^{66/64}$Zn = +0.41 ± 0.04‰) and the unequilibrated type 3 ($\delta^{66/64}$Zn = +0.27 ± 0.04‰), which shows Zn an isotope compositions identical to the BSE within error, although with slightly greater degree of scatter than the terrestrial rock groups (Figure 5.4). The overall average composition for carbonaceous chondrites is $\delta^{66/64}$Zn = +0.39 ± 0.04‰ (εZn per amu = +2.0 ± 0.2‰).

Comparing the offset in isotope compositions between the BSE and carbonaceous chondrites between the two isotope systems, represented by the red and blue vertical lines in Figure 5.4, the offset is greater for Cd (εCd per amu ≈ 1.0) than Zn (εZn per amu ≈ 0.6). This provides some evidence from two isotope systems that there might be some heterogeneity in the material from which the Earth originally accreted, assuming a component of that material was akin to carbonaceous chondrites, or that there was some mechanism which resulted in fractionation of Cd and Zn isotopes during accretion, such as fractionation during core partitioning, or indeed a combination of the two. These possibilities will be explored in

section 5.5 below by modelling elemental and isotopic behaviour during accretion and core formation. The model will use constraints provided in this chapter on the Cd isotope composition of material added to Earth during accretion and experimental evidence of Cd fractionation during core formation discussed in Chapter 4.

5.5 Modelling Cd behaviour during Earth's accretion and core partitioning

5.5.1 The late veneer

In order to begin constraining the reservoirs of material from which Earth accreted, it is useful to take an overall look at the abundances of elements present in the primitive mantle (PM) versus their volatility in the solar nebula at the approximate 1AU radial distance accretionary zone, as depicted in Figure 5.5.

There is excellent agreement between solar photospheric and CI chondrite abundances for most elements thus it is reasonable to assume that these abundances estimate the composition of the bulk solar system (e.g. Lodders et al., 2009; Palme et al., 2014).

The refractory lithophile elements (50% T_C > 1300 K see Figure 5.5 caption), which are assumed not to have partitioned to the core during accretion, form a reference point to determine the behaviour of other elements and, since they are in approximately CI chondritic proportions to one another, have (apart from Si, Mg and Nb) been assigned a CI-normalised PM abundance ratio (PM/CI) of 2.83 (Morbidelli and Wood, 2015; Palme and O'Neill, 2014).

The volatile lithophile elements (50% T_C < 1300 K) form an approximately linear trend of reducing PM/CI with increasing volatility, highlighted by the blue field of Figure 5.5. These elements are not partitioned to the core during accretion, but their abundances are primarily controlled by volatile depletion, which allows the simple deduction that the bulk Earth is mainly composed of material which would have condensed at higher temperatures in the inner solar system.

The remaining elements (circles in Figure 5.5) are weakly to strongly siderophile. The CI-normalised abundances of refractory siderophile elements are primarily controlled by the extent to which those elements have been partitioned to the core, and the volatile siderophile element abundances are controlled by volatility and partitioning behaviour, both very loosely following the same volatility trend as the lithophile elements.

Of particular interest are the highly siderophile elements (HSEs), depicted by red circles in Figure 5.5, which shows they are extremely depleted by partitioning to the core and, in the case of the most volatile HSEs (S, Se and Te; 50% $T_C \approx 700$ K), also due to Earth

accreting more refractory material. The eight most refractory HSEs (50% T_C > 1060 K), comprising the Platinum Group Elements (PGE: Ru, Rh, Pd, Os, Ir, Pt) plus Au and Re, have a narrow range of PM/CI ratios with an average of about 10^{-2} (Mg normalised PM/CI ≈ 4 x 10^{-3}) indicating, firstly, that they are present in the PM in approximately CI chondritic proportions but, secondly, they are more than two orders of magnitude more abundant in the BSE than if their abundances were governed solely by their known partitioning behaviour (Holzheid et al., 2000).

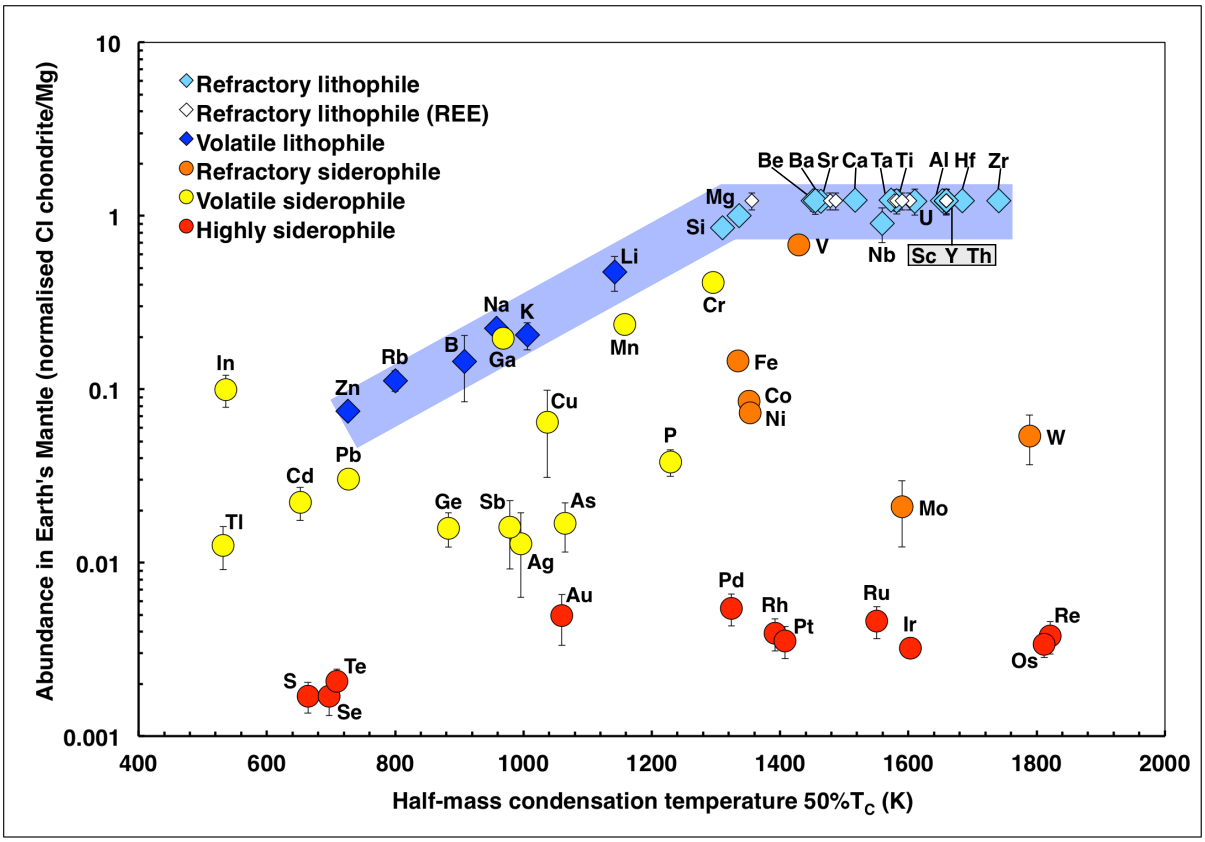


Figure 5.5. Estimated elemental abundances in the primitive mantle normalised to CI chondrite abundances and Mg versus elemental half-mass condensation temperatures, based on the data of Palme and O'Neill (2014) and references therein, and Lodders (2003). The more precise data of Wang and Becker (2013) has been used for the mantle abundances of S, Te and Se. Geochemical classification after McDonough and Sun (1995) modified by more recent metal-silicate partitioning data of Ballhaus et al. (2013) and Wang et al. (2016a). Lithophile elements = diamond symbols, weakly to strongly siderophile elements = circles. The 50% T_C is the temperature at which 50% of the element has condensed from a solar system composition gas at 10^{-4} bar, approximately the pressure at a solar radial distance of 1 AU (Fegley, 2000; Lodders, 2003). Refractory elements are those elements with 50% T_C > 1300 K. The blue field represents the volatility trend at 1 AU defined by lithophile elements. Error bars are shown at the 1sd level if larger than the symbols and take account of the uncertainties in mantle and CI contents for each element and in the Mg normalisation factor.

Kimura et al. (1974) noted that Au and Re were overabundant in the upper mantle and suggested that the part of the excess at least might have been delivered by a 'meteoritic infall' after planetary differentiation which would have 'trapped' these elements in the upper mantle

and crust. Chou (1978) went further and suggested that since the eight afore-mentioned PGEs plus Au and Re were present in the upper mantle in approximately chondritic ratios, varying by only a factor of 4, they were delivered by a 'meteoritic influx' after core formation resulting in a CI chondritic component of approximately 1% in the upper mantle. Other workers have since provided evidence of lowered metal-silicate partition coefficients for some HSEs under high pressure and temperature conditions. Whilst this might account for some of the 'excess' mantle abundances of these elements, their chondritic ratios cannot be reproduced solely by high P and T partition coefficients, leading to the suggestion of a 'hybrid' model combining the two mechanisms (Mann et al., 2012; Righter et al., 2008). Further to this, Laurenz et al. (2016) were able to reproduce HSE and sulphur concentrations in the mantle from core partitioning models using their experimental high P and T sulphide-silicate partition coefficients together with an addition of 0.4% bulk Earth mass (M_E) of chondritic material (CI or enstatite chondrites) as a late veneer.

This 'meteoritic influx' is commonly referred to as the 'late veneer' and many workers have since suggested different masses ranging from 0.3% – 4% M_E and different chondrite compositions (carbonaceous, ordinary and enstatite chondrite) for this component in the silicate Earth (e.g. Albarède et al., 2013; Ballhaus et al., 2013; Jacobsen et al., 2008; Marty, 2012; Meisel et al., 2001; Morgan, 1985; Morgan et al., 2001; O'Neill, 1991; Walker, 2009). Based on the PM/CI of the PGEs plus Au and Re plotted in Figure 5.5, but not taking into account possible increased retention of these elements in the primitive mantle by reduced high P and T partition coefficients (e.g. Mann et al., 2012), the late veneer delivery is calculated to have a mass of between about 0.4 and 0.9% M_E. If only the HSEs present in the BSE in the most CI-chondritic proportions, Rh, Pt, Ir, Os, Re, are taken into account, the late veneer mass required to account for this is about 0.5 to 0.6% M_E. These estimates are broadly in line with those of other workers favouring a small late veneer addition such as: 0.3 – 0.4% M_E (Jacobsen et al., 2008), 0.34% M_E (Walker, 2009), 0.48% ± 0.16% M_E (Jacobson et al., 2014), and 0.7% M_E (Holzheid et al., 2000).

5.5.2 Simple mass balance applied to the accretion of Cd and Zn to Earth

It is possible to make a mass balance of Cd and Zn isotopes and abundances for the budgets of these elements acquired by the BSE by using a simple two-component model comprising volatile-depleted main accretionary material from the inner solar system. This late veneer material is assumed to have a composition approximately akin to CI chondrites, based

on the evidence of approximately CI-chondritic abundances of HSEs demonstrated in the previous section. For the mass balance calculation and for the accretion modelling which follows, two hypotheses for the mass of late veneer material added will be tested. Firstly, 0.5% M_E, representing the mass required to account for HSE abundances in the mantle and, secondly, 1.7% M_E, or 2.5% of the BSE, as modelled by Ballhaus et al. (2013). The latter mass is representative of the lower end of a range of values for a more substantial late veneer including 2 ± 1% M_E (Marty, 2012) and up to 4% M_E (Albarède et al., 2013).

A critical value for the mass balance calculations and accretion modelling is the Cd abundance of the bulk silicate Earth. McDonough and Sun (1995) estimated the Cd content of the BSE to be 40 ng/g using the 'pyrolite model' (Ringwood, 1962). Witt-Eickschen et al. (2009) estimated the mantle Cd abundance to be 35 ± 7 ng/g and Wang et al. (2016a) estimated it to be a minimum of 31 ± 6 ng, both estimates based on the analyses of peridotite xenoliths from a range of different geological settings. In this study, the average Cd content of the Cameroon Line peridotite xenoliths (Table 5.2 on page 152) is 35 ± 4 ng/g (2se, n=5), which is consistent with the aforementioned literature data. Thus in this study, mass balance calculations and accretion modelling will use a low and high estimate for the Cd content of the BSE of 31 and 40 ng/g in order to constrain the range of possible outcomes.

The results of the mass balance calculations are shown in Table 5.3 using the low and high late veneer mass scenarios of 0.5% and 1.7% M_E. The calculations indicate that under the low-mass late veneer scenario, about 13 – 17% of the Cd budget of the BSE was delivered by the CI chondrite late veneer, but this increases to 44 – 57% under the high-mass late veneer scenario, with the remaining BSE budget supplied during the main accretion stage. In contrast, only 4% and 14% of the Zn budget of the BSE was supplied by the late veneer for the 0.5% M_E and 1.7% M_E scenarios, respectively.

In summary, the mass of the volatile-rich late veneer has a much greater impact on the Cd budget of the BSE than on the BSE Zn budget. This is further demonstrated when known Cd and Zn isotope compositions for the BSE and the late veneer are used in the mass balance calculations, as shown in Table 5.3. For the 0.5% M_E late veneer scenario, the main accretion component is estimated to have an $\varepsilon^{114/110}$Cd value of about –1.6, but for a 1.7% M_E late veneer, the main component is much lighter, with an $\varepsilon^{114/110}$Cd value of between –4 and –6. In contrast, there is little difference in the estimated Zn isotope composition of the main accretion component for the two scenarios.

Table 5.3. Mass balance results for Cd and Zn during Earth's accretion under low and high mass late veneer delivery scenarios.

		Proportion of Earth's mass delivered by late veneer			
	Units	**0.5 % M_E**		**1.7% M_E**	
Cd abundances					
Present day BSE	ng/g	31	40	31	40
Late veneer (CI chondrites)	ng/g	710	710	710	710
Proportion of Cd BSE budget delivered by					
Main accretion		83%	87%	43%	56%
Late veneer		17%	13%	57%	44%
Cd isotope compositions					
Main accretion	$\varepsilon^{114/110}$Cd	–1.7	–1.5	–6.3	–4.1
Late veneer	$\varepsilon^{114/110}$Cd	*+3.1*	*+3.1*	*+3.1*	*+3.1*
Present day BSE	$\varepsilon^{114/110}$Cd	*–0.9*	*–0.9*	*–0.9*	*–0.9*
Zn abundances					
Present day BSE	µg/g	55		55	
Late veneer (CI chondrites)	µg/g	310		310	
Proportion of Zn budget delivered by					
Main accretion		96%		86%	
Late veneer		4%		14%	
Zn isotope compositions					
Main accretion	$\delta^{66/64}$Zn	0.27		0.25	
Late veneer	$\delta^{66/64}$Zn	*0.47*		*0.47*	
Present day BSE	$\delta^{66/64}$Zn	*0.28*		*0.28*	

Cd BSE abundances are from Witt-Eickschen et al. (2009) and Wang et al. (2016a). CI chondrite abundances for Cd and Zn and BSE abundances for Zn are from McDonough and Sun (1995). Cd and Zn isotope compositions of the BSE and CI chondrites (italicised in table) are from this study (sections 5.4.8 and 5.4.9).

This mass balance demonstrates the prospect of using the BSE and CI chondrite Cd isotope compositions to derive the isotope composition of the volatile-depleted inner solar material likely to have accreted to form Earth and then using that data to constrain the late veneer mass delivered after core formation.

5.5.3 Accretion modelling strategy

The mass balance approach described in the previous section which derives the Cd isotope composition of the main accretionary component from the late veneer component and the resultant BSE isotope composition, does not account for fractionation of Cd isotopes during core-mantle partitioning, quantified by the parameter $\Delta\varepsilon^{114/110}Cd_{MET–SIL}$ (section 4.3.4.3 on page 128). In theory, if heavy Cd isotopes preferentially fractionated to the core and light Cd isotopes to the mantle during core partitioning, the same effect could be reproduced as seen in Table 5.3 whereby the BSE Cd isotope composition is lighter than the CI chondrite late veneer delivery.

The two component mass balance model for Cd has therefore been incorporated into a more complex accretion simulation, based on the model of Halliday (2004), which includes applying the $\Delta\varepsilon^{114/110}Cd_{MET-SIL}$ parameter quantitatively to Cd partitioned between the mantle and core during accretion, according to a set metal-silicate partition coefficient, $D_{Cd}^{MET/SIL}$ (Eq. 4.2). The Halliday (2004) model simulates accretion using a step function whereby mass is added to the Earth largely by impactors which grow in size: small impactors of 1% final M_E are added up to 10% M_E, 2% impactors added between 10% and 30% M_E, then 4% impactors added between 30% and 90% M_E. The final 10% of M_E is added as the Moon-forming giant impact (e.g. Canup and Asphaug, 2001) followed by a late veneer. This incremental increase in Earth mass during accretion formed by the addition of these impactors for the 0.5% M_E and 1.7% M_E late veneer scenarios of this study is shown by the red curve in Figure 5.6 panels (a) and (b).

The resultant exponential growth curve (black curve) is similar to the results of Monte Carlo simulations of impact-driven planetary accretion (e.g. Wetherill, 1986). The model assumes continuous core formation, growing in constant proportion to Earth's mass and simulates the tungsten isotope evolution resulting from complete mixing and equilibration of impactors between mantle and core in Figure 5.6 panels (c) and (d). Although an assumption of incomplete mixing and equilibration results in more realistic timescales for the age of the Moon from the Hf – W chronometer (Halliday, 2004), this is not important for the modelling of stable Cd isotopes and has not been adopted in this study.

In this study the model is used to simulate three main scenarios: the first two are 0.5% M_E and 1.7% M_E late veneer additions assuming no Cd isotope fractionation during core-mantle partitioning ($\Delta\varepsilon^{114/110}Cd_{MET-SIL} = 0$), and the third is a 1.7% M_E late veneer assuming Cd isotope fractionation take place during core-mantle partitioning.

For each scenario, the model has been run to produce Cd BSE abundances of 31 ng/g and 40 ng/g in order to determine the effect of this critical value on the modelled results, as explained in the previous section, producing a total of six model runs, A – F, in Table 5.4.

The model also simulates the isotopic and partitioning behaviour of other elements during accretion and core formation to ensure the integrity of the calculations behind the accretion model and compares the outcomes for these elements with literature values (references (a) to (l) in Table 5.4).

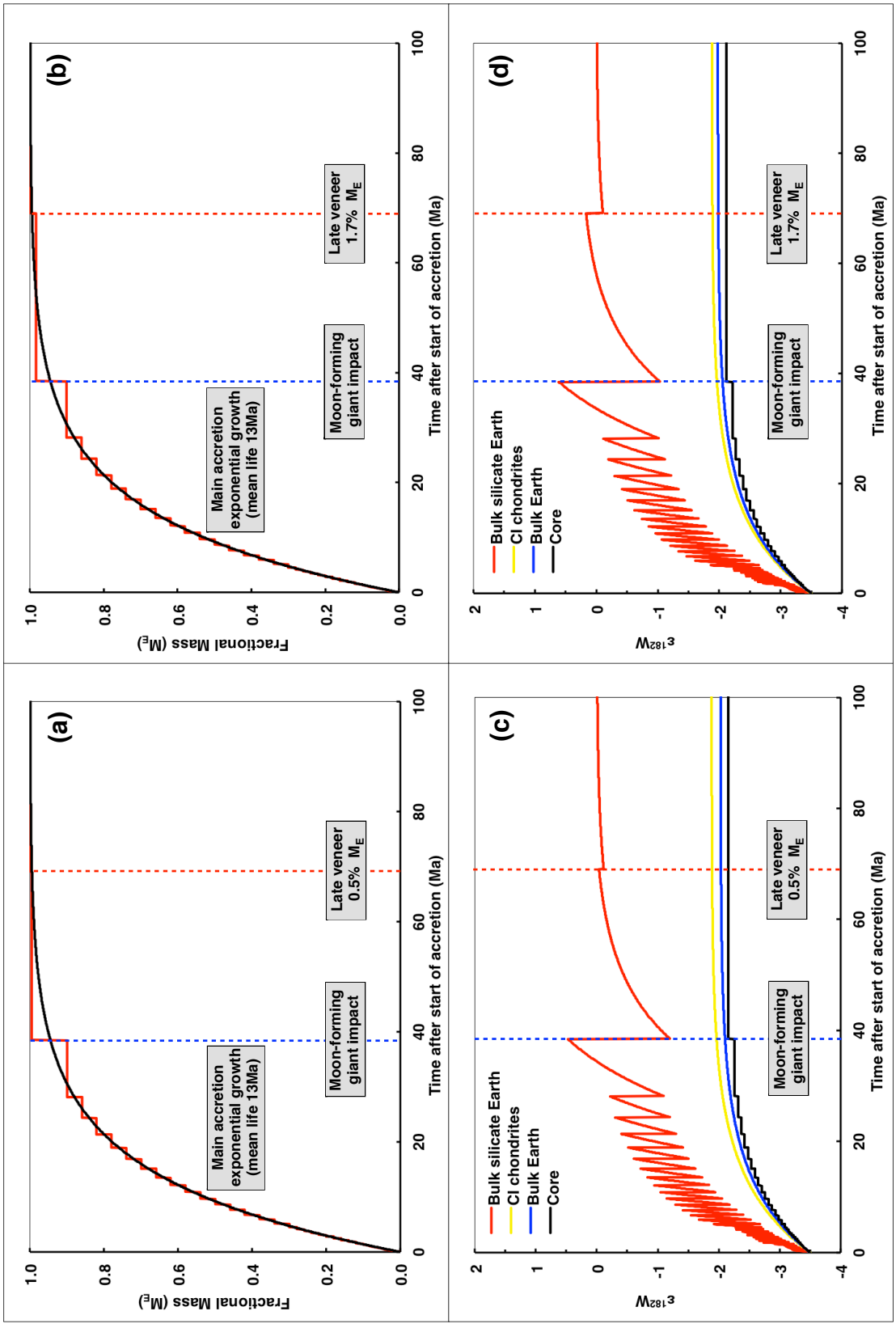


Figure 5.6. Results of accretion simulation (after Halliday, 2004) showing fractional mass and $\varepsilon^{182}W$ isotope evolution versus time after start of accretion for a low- and high-mass late veneer. Panels (a) and (c) show the fractional mass of bulk Earth (M_E) accreted and $\varepsilon^{182}W$ isotope evolution respectively for a late veneer of 0.5% M_E, panels (b) and (d) show the same for a late veneer of 1.7% M_E.

In addition, it is useful to compare the model outcomes to those obtained by Ballhaus et al. (2013) since the 0.5 M_E late veneer model is being compared to their 1.7% M_E late veneer model, although they use the continuous accretion model of Jacobsen and Harper (1996). In order to match the conditions of accretion and core formation simulated by the model of this study to those modelled by Ballhaus et al. (2013) as far as possible, the core-mantle partition coefficients derived in their paper were used (Table 5.4 bottom panel), apart from the partition coefficient for Pb, $D_{Pb}^{MET/SIL}$. It was found to be difficult to achieve reasonable outcomes for the Pb and Tl isotope compositions and abundances in the bulk silicate Earth, which are coupled by the initial solar system $^{205}Pb/^{204}Pb_{SS,0}$, by using the $D_{Pb}^{MET/SIL} = 50$ calculated by Ballhaus et al. (2013). Therefore the lower $D_{Pb}^{MET/SIL}$ derived by Wood et al. (2008) was used instead which is dependant on the evolving oxidation state of the accreting Earth.

5.5.4 Accretion modelling results and discussion

5.5.4.1 Accretion model elemental and isotopic constraints

The following is a brief summary of the more important outcomes of using the model to simulate the behaviour of elements, other than Cd, during accretion and core formation simulated in the six model runs, A – F, summarised in Table 5.4.

Firstly, the $\varepsilon^{182}W$ evolution of the bulk Earth, bulk silicate Earth, core and CI chondrites under both major alternative scenarios in the model of this study (0.5% and 1.7% M_E late veneer) is simulated and illustrated in Figure 5.6 panels (c) and (d). This broadly agrees with the outcome of Halliday (2004) using the same accretion model with slightly different constraints, as illustrated in figure 3 of that paper, and reproduces the present day W isotope composition of the bulk silicate Earth $\varepsilon^{182}W = 0$ (Kruijer et al., 2015).

Secondly, the model reproduces the Pb isotope composition and U/Pb ratio of the modern bulk silicate Earth ($^{207}Pb/^{204}Pb = 18.0$, $^{206}Pb/^{204}Pb = 15.6$ and $\mu = 8.5$) in agreement with literature values stated in Table 5.4. However, the evolution of μ values during accretion and core formation does not agree with the those modelled by Ballhaus et al. (2013), depicted in figure 8 of their paper.

Thirdly, the accretion model of this study reproduces the Tl isotope evolution of the Earth using similar initial solar system values for $^{205}Pb/^{204}Pb_{SS,0}$ and $\varepsilon^{205}Tl_{SS,0}$ discussed in section 3.5.2 on page 75.

Table 5.4. Parameters and results of accretion modelling.

	Units	Late veneer model						References
		0.5% M_E		1.7% M_E				
		A	B	C	D	E	F	Model runs
Key model parameters								
Cd content of the bulk silicate Earth	ng/g	**31**	**40**	**31**	**40**	**31**	**40**	(a) 31 ± 6 (1sd); (b) 35 ± 7; (c) 40
Cd isotope fractionation during during core-mantle partitioning	$\Delta\varepsilon^{114/110}Cd_{MET-SIL}$	*0.0*	*0.0*	*0.0*	*0.0*	**+4.7**	**+2.7**	$\Delta\varepsilon^{114/110}Cd_{MET-SIL} \approx 0$ (this study)
Cd isotope compositions								
Main accretion stage material	$\varepsilon^{114/110}Cd$	**-1.7**	**-1.5**	**-6.0**	**-4.0**	**-1.7**	**-1.5**	Modelled result
CI chondrite late veneer material	$\varepsilon^{114/110}Cd$	*+3.1*	*+3.1*	*+3.1*	*+3.1*	*+3.1*	*+3.1*	This study
Bulk silicate Earth	$\varepsilon^{114/110}Cd$	*-0.9*	*-0.9*	*-0.9*	*-0.9*	*-0.9*	*-0.9*	This study
Pb isotope compositions								
Initial solar system $^{205}Pb/^{204}Pb$	$^{205}Pb/^{204}Pb_{SS,0}$	1.8×10^{-3}	1.8×10^{-3}	1.8×10^{-3}	1.8×10^{-3}	1.8×10^{-3}	1.8×10^{-3}	(d) $(2 \pm 1) \times 10^{-3}$ (2sd); (e) $(1.0 \pm 0.4) \times 10^{-3}$ (2sd)
Bulk silicate Earth $^{207}Pb/^{204}Pb$		18.0	18.0	18.0	18.0	18.0	18.0	(f) 18
Bulk silicate Earth $^{206}Pb/^{204}Pb$		15.6	15.6	15.6	15.6	15.6	15.6	(f) 15.5
Evolution of $^{238}U/^{204}Pb$ (μ) in the bulk silicate Earth:								
Start of main accretion stage		38.6	38.6	70.3	70.3	70.3	70.3	
Start of late veneer stage		20.3	20.3	37.1	37.1	37.1	37.1	
End of late veneer stage		17.1	17.1	17.0	17.0	17.0	17.0	
Present day		8.5	8.5	8.5	8.5	8.5	8.5	(f) 8.5 ± 0.5
Tl isotope compositions								
Initial solar system $\varepsilon^{205}Tl$	$\varepsilon^{205}Tl_{SS,0}$	-10.5	-10.5	-10.5	-10.5	-10.5	-10.5	(d) -7.6 ± 2.1 (2sd); (e) 13 ± 6 (2sd)
Main accretion stage material	$\varepsilon^{205}Tl$	-1.7	-1.7	-2.0	-2.0	-2.0	-2.0	
CI chondrite late veneer material	$\varepsilon^{205}Tl$	-1.7	-1.7	-1.7	-1.7	-1.7	-1.7	(e) -1.7
Bulk silicate Earth	$\varepsilon^{205}Tl$	-2.0	-2.0	-2.0	-2.0	-2.0	-2.0	(g) -2
W isotope composition								
Bulk silicate Earth	$\varepsilon^{182}W$	0.0	0.0	0.0	0.0	0.0	0.0	(h) 0.0 ± 0.2 (2sd)
Elemental concentrations in the bulk silicate Earth								
Rb	ng/g	595	595	596	596	596	596	(c) 600; (f) 605
Hf	ng/g	276	276	273	273	273	273	(c) 283; (f) 301
W	ng/g	16.3	16.3	17.1	17.1	17.1	17.1	(c) 29; (f) 12
Tl	ng/g	6.96	6.96	6.73	6.73	6.73	6.73	(c) 3.5; (f) 4.1
Pb	ng/g	160	160	158	158	158	158	(c) 150; (f) 185
Th	ng/g	79.8	79.8	78.9	78.9	78.9	78.9	(c) 79.5; (f) 84.9
U	ng/g	21.7	21.7	21.5	21.5	21.5	21.5	(c) 20.3; (f) 22.9
CI normalised ratios for the bulk silicate Earth								
Rb/Pb_N		4.0	4.0	4.0	4.0	4.0	4.0	3.6 (f) and (i) 4.4 (c), (f) and (i)
Rb/Cd_N		5.9	4.6	5.9	4.6	5.9	4.6	5.8 (a), (c), (f) and (i) 4.5 (c), (f) and (i)
Core-mantle partitioning coefficients used								
Rb	$D_{Rb}^{MET/SIL}$	0.001	0.001	0.001	0.001	0.001	0.001	(j)
Cd	$D_{Cd}^{MET/SIL}$	22	22	22	22	22	22	(j), (k)
Hf	$D_{Hf}^{MET/SIL}$	0.001	0.001	0.001	0.001	0.001	0.001	(j)
W	$D_{W}^{MET/SIL}$	36	36	36	36	36	36	(j)
Tl	$D_{Tl}^{MET/SIL}$	12	12	12	12	12	12	(j)
Pb - low pressure	$D_{Pb}^{MET/SIL}$	30	30	30	30	30	30	(l)
Pb - high pressure	$D_{Pb}^{MET/SIL}$	13	13	13	13	13	13	(l)
Th	$D_{Th}^{MET/SIL}$	0.001	0.001	0.001	0.001	0.001	0.001	(j)
U	$D_{U}^{MET/SIL}$	0.001	0.001	0.001	0.001	0.001	0.001	(j)

References: (a) Wang et al. (2016a); (b) Witt-Eickschen et al. (2009); McDonough and Sun (1995); (d) Andreasen et al. (2012); (e) Baker et al. (2010); (f) Palme and O'Neill (2014); (g) Nielsen et al. (2005); (h) Kruijer et al. (2015); (i) Anders and Grevesse (1989); (j) Ballhaus et al. (2013); (k) Wood et al. (2014); (l) Wood et al. (2008). Data from this study is italicised and important Cd results are in bold.

5.5.4.2 The Cd isotope compositions of Earth's building blocks

As with the mass balance calculations of section 5.5.2 above, the model is constrained by the Cd isotope compositions of the BSE ($\varepsilon^{114/110}$Cd = –0.9 ± 0.5) and CI chondrites ($\varepsilon^{114/110}$Cd = +3.1 ± 0.7), as discussed in sections 5.4.8 and 5.4.9 starting on page 164. As with the mass balance calculations, the assumption is that the Earth's building blocks comprise a main accretion stage (> 98% M_E), including the moon-forming giant impact, sampling refractory inner solar system material (section 5.5.1) and a late veneer of CI chondrite material.

The main accretionary material is required to have a Cd isotope composition with a $\varepsilon^{114/110}$Cd value of –1.5 to –1.7 if a 0.5% M_E late veneer is delivered, but a much lighter main accretion material with a $\varepsilon^{114/110}$Cd value between –4.0 to –6.0 for a 1.7% M_E late veneer (Table 5.4 model runs A – D). The ranges quoted refer to the model results producing Cd contents of the BSE between 31 and 40 ng/g.

Since the step-wise accretion model assumes full equilibration between mantle and core of the impactors accreting to Earth, the results are identical to the simple mass balance approach of section 5.5.2. Although the results of the more sophisticated step-wise accretion model are dependent on the core-mantle partition coefficient for Cd ($D_{Cd}^{MET/SIL}$), unlike the simple mass balance approach, the accretion model assumes a constant Cd concentration for the BSE, whereby changes in $D_{Cd}^{MET/SIL}$ are offset by changes in the Cd content of the accreting material.

However, for comparison, an alternative 1.7% M_E late veneer scenario (Table 5.4 E and F) was also run allowing Cd isotope fractionation during core-mantle partitioning. For direct comparison with the 1.7% M_E scenario which assumes no fractionation but an isotopically lighter main accretionary material (Table 5.4 C and D), the Cd isotope compositions of the main accretionary material produced by the 0.5% M_E scenario were used as a baseline (Table 5.4 A and B). A core-mantle fractionation factor, $\Delta\varepsilon^{114/110}Cd_{MET–SIL}$, of between +2.7 and +4.7 is required if the main accretionary material has a Cd isotope composition with a $\varepsilon^{114/110}$Cd value between –1.5 and –1.7 and the BSE Cd abundance is between 31 and 40 ng/g. This scenario requires heavier Cd isotopes to preferentially partition into the core leaving lighter isotopes in the mantle.

The results of runs E and F depend on the metal-silicate partitioning coefficient which has been set at $D_{Cd}^{MET/SIL}$ = 22, modelled by Ballhaus et al. (2013), and agreeing with results obtained Wood et al. (2014). The $D_{Cd}^{MET/SIL}$ values increase with temperature (section 4.3.3.4

on page 123) and S content in the metal phase (Wood et al., 2014). However, increasing the $D_{Cd}^{MET/SIL}$ values has very little effect on the modelled core-mantle isotope fractionation. For example, the modelled $\Delta\varepsilon^{114/110}Cd_{MET-SIL}$ values decrease by only 0.1 to 0.2 ε-units if the partition coefficient is increased to $D_{Cd}^{MET/SIL} = 40$. Lower $D_{Cd}^{MET/SIL}$ values of less than 22 would correspondingly increase the $\Delta\varepsilon^{114/110}Cd_{MET-SIL}$ factors slightly.

However, the conclusion from the results of the Cd metal-silicate partitioning experiments of Chapter 4 was that Cd isotopes were not significantly fractionated between metal and silicate phases, or $\Delta\varepsilon^{114/110}Cd_{MET-SIL} \approx 0$ (section 4.3.4.3 on page 128). The average result from the equilibrated time series experiments at constant temperature and pressure in graphite capsules was $\Delta\varepsilon^{114/110}Cd_{MET-SIL} = -0.46 \pm 0.46$ (2se, n=3) and for all equilibrated experiments at constant pressure, $\Delta\varepsilon^{114/110}Cd_{MET-SIL} = -0.14 \pm 0.35$ (2se, n=7). Thus the modelled core-mantle fractionation factors for runs E and F are well outside the uncertainties of the experimental results and therefore the evidence does not support such partitioning behaviour. If anything, the experimental results may hint at a very slight opposite trend in which *lighter* Cd isotopes preferentially partition into the metal phase although, as explained in section 4.3.4.3, this trend is not statistically significant.

Accordingly, models E and F, which require that Cd isotope fractionation accompanies core-mantle partitioning, can be dismissed as unrealistic indicating that the reason for the difference between the isotope compositions of the BSE and the late veneer is more likely due to the isotope composition of the main accretionary material alone, as modelled by A – D in Table 5.4.

In summary, the Cd isotope compositions of the main accretionary material in this model are controlled by the following constraints: the difference in Cd isotope composition and abundance between the BSE and CI-chondrite late veneer material, the core-mantle partition coefficient, the core-mantle isotope fractionation factor and the proportion of M_E comprised by the late veneer. Constraints have been established in this study on the Cd isotope compositions of the BSE ($\varepsilon^{114/110}Cd = -0.9 \pm 0.5$) and CI chondrites ($\varepsilon^{114/110}Cd = +3.1 \pm 0.7$), respectively, together with the core-mantle fractionation factor ($\Delta\varepsilon^{114/110}Cd_{MET-SIL} \approx 0$). The Cd abundance of the BSE and the core-mantle partition coefficient are fairly well-constrained from literature, leaving the mass of late veneer delivered as the remaining control on the isotope composition of the main accretionary material.

With a 0.5% M_E late veneer, which satisfies the chondritic HSE abundances in the BSE, the main accretionary component would have a Cd isotope composition of $\varepsilon^{114/110}Cd \approx -1.6$. However, a 1.7% M_E late veneer, which would result in highly suprachondritic HSE

abundances in the BSE, would require the main accretionary material to have a Cd isotope composition of $\varepsilon^{114/110}Cd \approx -4$ to -6. The question thus becomes whether it is reasonable to have a main accretionary component about 0.7 and 4.7 ε-units lighter than the BSE and CI chondrites respectively (0.5% M_E late veneer), or a component approximately 4 and 8 ε-units lighter than the BSE and CI chondrites respectively (1.7% M_E late veneer).

5.5.4.3 Chondritic Earth building blocks

Various models have been suggested for the composition of the Earth's building blocks and it is useful at this point to evaluate whether these claims are realistic in terms of the likely Cd isotope compositions of those building blocks in the light of the accretion modelling of this study. Most of the models have proposed some form of chondritic composition for the building blocks, such as carbonaceous chondrites (e.g. Allègre et al., 2001; Allègre et al., 1995), enstatite chondrites (Javoy, 1995; Javoy et al., 2010) or models suggesting a combination of different chondritic components (e.g. Jagoutz et al., 1979; Lodders, 2000), although difficulties remain since the bulk composition of the Earth simply does not match a specific group of meteorites (McDonough and Sun, 1995). However, the Cd isotope compositions of bulk chondrites do not appear to show any trend towards light epsilon values (this study, Wombacher et al., 2008) although they are difficult to interpret in many cases due to fractionation caused by parent body processes obscuring isotopic signatures from the solar nebula.

As an illustration, the step-wise accretion model was run assuming that the main accretion component was akin to average carbonaceous chondrites, for which the mean Cd isotope composition is $\varepsilon^{114/110}Cd = +3.2 \pm 0.8$ (2se) (section 5.4.8, Figure 5.2). The only way to achieve a BSE isotope composition of $\varepsilon^{114/110}Cd = -0.9 \pm 0.5$, using a CI-chondrite late veneer composition of $\varepsilon^{114/110}Cd = +3.1 \pm 0.7$, is to invoke fractionation during core-mantle partitioning. For a 0.5% M_E late veneer, the Cd core-mantle fractionation factor would need to be $\Delta\varepsilon^{114/110}Cd_{MET-SIL} \approx +5$ and for the 1.7% M_E late veneer it would need to be $\Delta\varepsilon^{114/110}Cd_{MET-SIL} \approx +8$ to $+10$ and both are simply not supported by the results from metal-silicate partitioning experiments which indicate no significant fractionation.

The lack of pervasive bulk light isotope compositions in the main chondrites groups, which authors have argued may be major components in Earth's building blocks, offers little hope in solving the mass balance without core-mantle fractionation. In order to arrive at a

BSE isotope composition of $\varepsilon^{114/110}Cd = -0.9 \pm 0.5$ with a Cd content of between 31 and 40 ng/g, a light main accretionary component is required.

5.5.4.4 Comparison with other isotope systems

From the comparative Cd and Zn mass balance calculations set out in Table 5.3 and discussed in section 5.5.2, a significant proportion of the budget of these elements in Earth is delivered during the main accretionary phase, regardless of the mass of late veneer subsequently delivered. Thus, it is reasonable to conclude that the isotope composition of the main component exerts a major influence on the final isotope composition of the BSE. It is particularly useful to look briefly at lithophile elements, which are not significantly entrained in the core during accretion. A major part of Earth's budget of lithophile elements is in the mantle and thus lithophile element isotope compositions of the mantle are unlikely to have been significantly affected by any fractionation during core-mantle partitioning. Accordingly, the isotope composition of the BSE for these elements should provide a reliable indication of the isotope composition of Earth's main accretionary material.

Zinc is lithophile or slightly siderophile with $D_{Zn}^{MET/SIL}$ values mostly in the range 0.02 to 7 under various temperature and pressure conditions, and is thus consistently less siderophile than Cd (Ballhaus et al., 2013; Wang et al., 2016a; Wood et al., 2014). As with Cd, there is also no significant fractionation of Zn isotopes during core-mantle partitioning (Bridgestock et al., 2014). The Zn isotope composition of the BSE ($\delta^{66/64}Zn = +0.28 \pm 0.01$‰ (2se) and type 3 carbonaceous chondrites 3 ($\delta^{66/64}Zn = +0.27 \pm 0.04$‰) are identical within error (section 5.4.9 on page 165). There is an offset between the Zn isotope composition of the BSE and CI chondrites ($\delta^{66/64}Zn = +0.47 \pm 0.02$‰), however, mass balance indicates that the main accretionary material would have a Zn isotope composition of $\delta^{66/64}Zn = +0.25$ to +0.27, hardly distinguishable from the isotope composition of the BSE (section 5.5.2). Furthermore, there is no significant difference between the stable isotope composition of chondrites and the BSE for the refractory lithophile elements Mg, K and Ba (Moynier et al., 2015; Teng et al., 2010; Wang and Jacobsen, 2016).

The variability of Zn in solar system materials should be similar to that of Cd since the two elements are chemically very similar: both are in Group 12 (IUPAC classification) of the Periodic Table, they are divalent in most compounds and have similar volatilities, although Cd is more siderophile than Zn. The range of $\delta^{66/64}Zn$ values for the BSE, CI chondrites and the modelled main accretionary material spans about 0.2‰, equivalent to

about 0.1‰ per amu. In comparison, the $\delta^{114/110}$Cd values for the same materials (note the delta notation is used for comparison) span a range of about 0.5‰ or about 0.12‰ per amu for a 0.5% M_E late veneer. However, for a 1.7% M_E late veneer, the range in values required in these materials increases to approximately 0.7 to 0.9‰ or about 0.2‰ per amu. The 0.5% M_E late veneer model thus seems more reasonable.

Based on this evidence, it is possible to speculate that large isotope contrasts between the main accretionary material, a chondritic late veneer, and the resultant BSE are unlikely. This leads to the suggestion that the relatively large differences in the Cd isotope composition of these reservoirs, which are required by a larger late veneer (1.7% M_E), represent a less likely scenario than the more uniform isotope compositions that are associated with a smaller late veneer (0.5% M_E).

5.5.4.5 The light Cd isotope composition of the main accretionary material

Earth's main accretionary material was volatile-depleted on the basis that the CI chondrite-normalised abundances of volatile lithophile elements (50% T_C < 1300 K) decrease with decreasing 50% T_C (Figure 5.5 blue field). Similar depletion trends are observed in chondritic meteorites, apart from CI chondrites (Palme et al., 1988; Wasson and Kallemeyn, 1988), and may be explained by the condensation and coagulation of hot nebular gases in a cooling solar nebula, forming initially refractory solids which started accreting into planetesimals, effectively decoupling from volatile elements still present in vapour form (Cassen, 1996).

Ciesla (2008) modelled the thermal evolution of the solar nebula and found that the Cassen (1996) model required rapid accretion and therefore differentiation of planetesimals, which did not occur in the chondrite parent bodies, but may have occurred for Earth. His model required a longer formation time for planetesimals and envisaged that solids in the outer solar nebula, which had cooled sufficiently to contain volatiles, would have been carried into the now cooler inner solar nebula to reduce the depletion trends.

Essentially, evaporation and condensation processes play a major part in controlling the depletion trend of volatile elements in the solar nebula. However, this abundance trend could in theory reflect either partial evaporation residues or partial condensation products, and isotopic data provide a means to gain further insight into which of these processes might be primarily responsible for the observed volatile signatures (Davis and Richter, 2014; Humayun and Cassen, 2000).

If solids and gases decouple in a cooling solar nebula, as envisaged by Cassen (1996), the isotopic behaviour of the condensing vapour in the solar nebula may be determined principally by Rayleigh condensation, whereby condensates are constantly removed in an open system and no longer have contact with the gas phase. Under such conditions equilibrium isotope fractionation ensures that the removed condensate has a heavier isotope composition than the original vapour. However, the isotope compositions of successive condensates from the ever smaller vapour reservoir progressively become lighter, as does the vapour itself (Kehm et al., 2003).

Examples of large-scale forces prevalent in the solar nebula are: (i) mixing and outward radial transport of material in the evolving solar nebula (e.g. Boss, 2004; Ciesla, 2007; Gail, 2001; Keller and Gail, 2004); (ii) strong mixing of material near the nascent sun and its redistribution to outer parts of the accretion disk, as envisaged by the X-wind model (Shu et al., 1994; Shu et al., 2001; Shu et al., 1996); and (iii) turbulence resulting from shearing between gas and dust layers in a rotating nebula (Weidenschilling, 1980). Forces such as these would have helped to redistribute the condensing vapour allowing it to be widely available in the accretion disk, whilst its isotope composition became progressively lighter.

Some authors suggest that the accretion of the carbonaceous chondrites predated the ordinary and enstatite chondrites (Chambers, 2000; Jacquet et al., 2012). On that basis, early in the evolution of the solar nebula, condensates from nebula gas from which components of the carbonaceous chondrites accreted, would have been isotopically heavier than later condensates from a more depleted nebula gas reservoir, which are more likely to have accreted to form other chondrites and the terrestrial planets. This scenario is consistent with the relatively heavy (compared to bulk silicate Earth) Cd isotope composition of the carbonaceous chondrites (averaging $\varepsilon^{114/110}Cd = +3.2 \pm 0.8$), forming in the cooler outer solar system at a solar radial distance of 3 – 4 AU (Wasson, 1988). The enstatite chondrites appear to show consistently *heavier* Cd isotope compositions than the carbonaceous chondrites (Figure 5.2 on page 155), which would not be expected if they accreted after the carbonaceous chondrites. However, from the discussion in section 3.5.4.1 and elsewhere in Chapter 3, the greater variability in Cd isotope compositions of the enstatite chondrites compared to the carbonaceous chondrites most likely reflects that they have undergone significant stable isotope fractionation due to parent body processes. Therefore, proto-enstatite chondrite material that has a lighter Cd isotope composition than carbonaceous chondrite material cannot be ruled out.

As a precursor to terrestrial planetary accretion, coagulated and growing dust aggregates settled towards the solar nebula mid-plane allowing runaway accretion to take place in denser layers (Weidenschilling, 1980; Weidenschilling, 2000). Due to the diminishing nebular gas reservoir from which the coagulating dust had condensed, material clumping together in the mid-plane would have become progressively lighter in isotope composition. In addition, smaller condensate particles would have had a tendency to migrate inwards toward the inner solar system due to gas drag (Weidenschilling, 1977). In all, it is likely that such isotopically light material was dominant in the 1 AU inner solar system feeding zone from which Earth accreted.

Wombacher et al. (2008) analysed the Cd isotope compositions of separate fractions of matrix, chondrules and Ca-Al inclusions (CAI) from the chondrite Allende (CV3) and reported εCd per amu values for chondrules and CAIs in the range –1.5 to –10 and an enriched Cd content of about 1200 ng/g in a CAI. Similarly, a CAI from Allende was found to have a εZn per amu value of –13 (Luck et al., 2005). In comparison, the εCd per amu and εZn per amu values recorded for bulk carbonaceous chondrites are heavier in the ranges +0.27 to +1.3 and +0.80 to +2.7 respectively (Figure 5.4 on page 167) and the Cd content of the bulk Allende meteorite is 366 ng/g (Makishima et al., 2011).

The light Cd and Zn isotope compositions and enrichment of Cd abundance in CAIs may be an indication that these components incorporated volatile-rich vapour with a light Cd (and Zn) isotope composition before accretion to the Allende parent body (Wombacher et al., 2008). This may be a very tentative indication of isotopically lighter vapour or re-evaporated material migrating to the inner solar system, or it may be a more localised process. Further analyses of chondrite separates are required to determine if the light isotope composition is widespread.

In conclusion, the Cd isotope composition of the main accretionary material is estimated to have a $\varepsilon^{114/110}$Cd value of about –1.6 for a 0.5% M_E late veneer and –4 to –6 for a 1.7% M_E late veneer. It is not possible to definitively determine which scenario is correct although the more extreme light isotope composition for the larger mass late veneer is more unlikely since such a light isotope composition not commonly observed in primitive meteorites.

5.6 Conclusions

This investigation presents new accurate and precise Cd isotope measurements for a comprehensive suite of terrestrial rocks from a wide range of global tectonic settings together with analyses of several carbonaceous chondrites, including the rare CI chondrite Ivuna, using the well-tested and reliable analytical protocols for Cd set out in Chapter 2. From this data, the bulk silicate Earth is estimated to have a Cd isotope composition of $\varepsilon^{114/110}Cd = -0.9 \pm 0.5$ (2se, n=6) based on the average Cd isotope composition of peridotites, which broadly agree with the average Cd isotope composition of komatiites.

The analysis of the Cd isotope compositions and concentrations of partial mantle-derived melts, including komatiites, MORBs and OIBs reveals a tentative trend in which slightly heavier Cd isotope compositions form a loose correlation with increasing Cd content. This putative partial melting trend for Cd resembles similar findings of other workers for Zn, an element which is similar to Cd chemically. A competing trend arising from kinetic isotope fractionation during degassing of OIBs and possibly some MORBs was identified and these trends together with possibly other mantle processes such as metasomatism create significant scatter on plots of Cd isotope compositions versus Cd contents.

The finding in this investigation of a difference in Cd isotope composition between the BSE ($\varepsilon^{114/110}Cd = -0.9 \pm 0.5$) and carbonaceous chondrites ($\varepsilon^{114/110}Cd = +3.2 \pm 0.8$) has led to the hypothesis that Earth's main accretionary materials are isotopically lighter than the BSE, confirmed by simple mass balance modelling. Furthermore, the calculated Cd isotope composition of this main accretion component is dependent on the mass of late veneer material of CI chondrite composition delivered to Earth after the Moon-forming giant impact. Accordingly, this relationship can be used to assess various estimates for the mass of the late veneer.

An accretion simulation based on the model of Halliday (2004) was run to test alternative late veneer scenarios comprising 0.5% and 1.7% of bulk Earth mass (M_E). The main accretionary material was required to have a Cd isotope composition with a $\varepsilon^{114/110}Cd$ value of about –1.6 for a 0.5% M_E late veneer of CI chondrite material, but a much lighter composition with a $\varepsilon^{114/110}Cd$ value of between –4 to –6 for a 1.7% M_E late veneer. Both scenarios assume no Cd isotope fractionation took place during core-mantle partitioning ($\Delta\varepsilon^{114/110}Cd_{MET-SIL} = 0$).

If the 1.7% M_E late veneer assumed a main accretion component with a Cd isotope composition similar to the one required for a 0.5% M_E late veneer, then Cd isotope fractionation during core-mantle partitioning is necessary for mass balance and the fractionation factor required would be $\Delta\varepsilon^{114/110}Cd_{MET-SIL}$ = +2.7 to + 4.7. However, the results of this accretion scenario were discounted because Cd metal-silicate partition experiments described in Chapter 4 showed that no significant Cd isotope fractionation is expected during core-mantle partitioning.

An assessment was made of likely solar nebula scenarios which could produce a main accretionary component with a light Cd isotope composition. Using evidence from other workers, it was noted that (i) nebular gases and solids were decoupled during nebular evolution due to condensation of refractory components in a cooling solar nebula, (ii) condensing nebular gases were well-mixed due to turbulence and migration of materials in the solar nebula, and (iii) condensation of the nebular gases were governed by equilibrium partitioning during open system Rayleigh fractionation due to the continuous removal of coagulating solids from the gas phases.

Accordingly, the nebular gas reservoir became lighter and lighter in its Cd isotope composition. Early condensates in the cooler outer solar system, such as carbonaceous chondrites, would hence have acquired a heavier Cd isotope composition than later condensates in the inner solar system, which formed the building blocks of Earth. Such a scenario can thus account for the measured Cd isotope offset between the BSE and carbonaceous chondrites and the light Cd isotope composition of the main accretionary material.

Based on the (i) the similarity between the isotope compositions of meteoritic and terrestrial materials for elements other than Cd and (ii) the modelled Cd isotope compositions of the main accretionary component, a 0.5% M_E late veneer is more likely than a 1.7% M_E late veneer, although it is acknowledged that the latter cannot be ruled out at present.

5.7 Declaration

The study detailed in this chapter was completed as part of collaborative research efforts to which the author of this thesis contributed most of the Cd isotope composition measurements and associated data reduction. Dr Maria Schönbächler was responsible for the Cd isotope composition measurements and data reduction for the samples annotated [1] in Table 5.2 and supported data interpretation. The author was primarily responsible for data

analysis and developing the interpretations that are presented here. Professor Kevin Burton is thanked for the donation of MORB sample MD57 D'10-1 and Dr Caroline Smith is thanked for the donation of the sample of the CI chondrite Ivuna from the Natural History Museum collection.

Chapter 6 Summary and outlook

6.1 Major research findings

6.1.1 ^{205}Pb – ^{205}Tl and volatile element systematics in enstatite and L- and LL-chondrites

It is clear from the analyses of Chapter 3 that the Pb abundances and isotope compositions of many samples are altered by pervasive contamination by terrestrial Pb. In addition, Tl isotope compositions are likely affected by stable isotope fractionation, as evidenced by the Cd isotope data. These issues severely restrict the search for evidence of ^{205}Pb in enstatite and ordinary chondrites, more so than in the previous study by Baker et al. (2010) of carbonaceous chondrites. As such, only speculative isochrons can be constructed from the results, which indicate cooling ages approximately in the range 50 to 90 Ma for both L- and LL-chondrites relative to carbonaceous chondrites.

The Cd isotope compositions of the enstatite chondrites are highly variable with $\varepsilon^{114/110}$Cd values of +3.0 to +72.9, but show evidence of decoupling from the Tl isotope systematics in three samples. The exact mechanism for this decoupling is not known although it is likely related to the complex multi-event and impact-driven evaporation and condensation processes that took place on the enstatite chondrite parent bodies.

The abundances of Cd and Tl reveal considerable variability in enstatite and ordinary chondrites, with higher petrological types generally showing depletions in these elements, except for the LL-chondrites, which do not display systematic variations with petrological type. This suggests that the variable concentrations of these volatile and labile elements are controlled to a significant degree by volatilisation and mobilisation from thermal and impact metamorphism.

6.1.2 Cd isotope fractionation during core-mantle partitioning

The metal-silicate partitioning experiments of Chapter 4, carried out at temperatures between 1235 °C and 1570 °C and at 1.5 GPa, indicate that, within analytical uncertainties, no fractionation of Cd isotopes takes place between metal and silicate phases. The experiments included a time series with run times of between 4 and 200 minutes, carried out in graphite capsules and at a constant temperature and pressure of 1235 °C and 1.5 GPa, respectively. The average $\Delta\varepsilon^{114/110}Cd_{MET-SIL}$ value for the equilibrated time series experiments was –0.46 ± 0.46 (2se, n=3). Although most of the experiments (n=6) exhibited slightly

negative $\Delta\varepsilon^{114/110}Cd_{MET-SIL}$ values ranging from about –0.1 to –0.9, possibly hinting at a very slight preference of heavy Cd isotopes for the silicate phase, the average $\Delta\varepsilon^{114/110}Cd_{MET-SIL}$ value for all experiments together was –0.19 ± 0.21 (2se, n=8). This indicates that the negative trend was not significant considering the analytical uncertainties.

In all, these results provide evidence that Cd partitioning between the mantle and the core of the early Earth was most likely not accompanied by any significant Cd isotope fractionation.

6.1.3 The Cd isotope composition of the bulk silicate Earth

New accurate and precise Cd isotope measurements for a comprehensive suite of terrestrial rocks from a wide range of global tectonic settings are presented in Chapter 5. Based on the average results for peridotites (spinel lherzolites and a dunite) from this dataset, the Cd isotope composition of the bulk silicate Earth (BSE) is estimated to be $\varepsilon^{114/110}Cd = –0.9 \pm 0.5$ (2se, n=6). The average Cd isotope composition of komatiites is $\varepsilon^{114/110}Cd = –0.7 \pm 1.9$ (2se, n=4) and the mean composition of peridotites and komatiites taken together is $\varepsilon^{114/110}Cd = –0.8 \pm 0.8$ (2se, n=10). Since komatiites are formed by high-degree partial melting of the mantle, they can be taken as representative for the composition of the Archean mantle (Dauphas et al., 2010; Maier et al., 2009). As such, the komatiite data support the estimate of the BSE Cd isotope composition, which is based on the results for peridotites.

A detailed analysis of the Cd isotope composition and concentration data for partial mantle-derived melts, including komatiites, MORBs and OIBs, reveals a tentative partial melting trend and possibly a second competing trend that may arise from kinetic isotope fractionation during degassing of OIBs and some MORBs.

6.1.4 The Cd isotope composition of Earth's building blocks

This final major finding of this study follows from the application of the data that is presented in Chapters 4 and 5. The constraints that are provided by these results are thereby employed in terrestrial accretion and core formation models to better understand the origin of Earth's volatile inventory.

The key results of the accretion modelling are as follows: (i) Earth's main accretion component is estimated to have a Cd isotope composition of $\varepsilon^{114/110}Cd \approx –1.6$ if the late veneer component comprises 0.5% of Earth's mass (M_E), whereas (ii) the main accretion component is estimated to have a Cd isotope composition of $\varepsilon^{114/110}Cd \approx –4$ to –6 if the late

veneer component is larger at 1.7% M_E. Both scenarios assume the late veneer has a Cd isotope composition approximately akin to CI chondrites and that there is no Cd isotope fractionation between core and mantle during core formation, in accord with the results of the metal-silicate partitioning experiments (section 6.1.2 above).

Assuming gases and solids were decoupled during nebular evolution with condensing refractory components and thorough mixing in a turbulent but cooling solar nebula, the condensation of nebular gas would be governed by equilibrium partitioning during open system Rayleigh fractionation, due to the continuous removal of coagulating solids from the gas phase. As a result, the diminishing nebular gas reservoir would become lighter and lighter in its Cd isotope composition. This is consistent with carbonaceous chondrites, which were early condensates, having a relatively heavy mean Cd isotope composition of $\varepsilon^{114/110}Cd = +3.2 \pm 0.8$ (2se) compared to the modelled main terrestrial accretion component, which condensed later in the inner solar system. Direct evidence for the lighter Cd isotope composition of inner solar system material is provided by the inferred BSE isotope composition of $\varepsilon^{114/110}Cd = -0.9 \pm 0.5$.

Although it is possible for Earth to have accreted from material with an unusually light Cd isotope composition of $\varepsilon^{114/110}Cd \approx -4$ to -6, there is little evidence from meteorites that such isotopically light material was prevalent or even present in the inner solar system during Earth's accretion. In addition, such significant isotopic differences between meteorites and the BSE are also not seen for chemically similar elements such as Zn. Together, the evidence thus favours a main terrestrial accretionary component with a less extreme light composition of $\varepsilon^{114/110}Cd \approx -1.6$. This is in accord with a smaller late veneer comprising about 0.5% M_E, and also agrees with most current thinking on the origin of the highly siderophile element abundances in the BSE.

6.2 Future directions

The terrestrial Pb contamination commonly encountered in meteorites and the stable isotope fractionation of Tl resulting from meteorite parent body processes have made the application of the $^{205}Pb - ^{205}Tl$ chronometer challenging, even with strategies to identify and adjust for these interfering processes. It is therefore difficult to foresee whether the $^{205}Pb - ^{205}Tl$ chronometer will prove to be more successful in the future. Of particular interest are studies of rare meteorite groups but such investigations are especially problematic as sample

numbers may be insufficient to allow the 'weeding out' of contaminated samples and those affected by parent body processes that drive stable isotope fractionation.

The data obtained in coupled analyses of Cd and Tl isotope compositions for enstatite chondrites have raised the question of how such volatile and labile elements are affected by multiple fractionation events. Further studies in this area would be helpful, in particular to identify the causes of both coupled and decoupled variations in Cd and Tl isotope compositions, as seen in this study. In addition, novel insights might be obtained from investigations that employ coupled isotope analyses for other combinations of elements that exhibit a range of volatile and labile characteristics, for example Cd, Zn and K.

The modelling that was carried out to constrain the Cd isotope composition of Earth's building blocks has opened the way for similar investigations of other bodies for which meteoritic or direct samples exist, including the Moon, Mars and Vesta. The improvements in precision that will be offered by future MC-ICP-MS instruments may furthermore allow finer differences in isotope compositions to be resolved and this may enable studies similar to that performed here for other volatile elements. Importantly, such investigations will be able to verify (or possibly question) the conclusions that were derived in this thesis and provide novel insights into the volatile element delivery to Earth and large-scale fractionation processes in the evolving solar nebula.

6.3 Closing remarks

A recurring theme of this thesis is how useful the volatility and lability of Cd has been in identifying magmatic, planetary and solar nebular processes, despite the tendency for multiple fractionation events to overprint previous isotopic signatures, particularly those which originated in the solar nebula. In particular, this was possible through the use of improved analytical techniques and instrumentation, which allowed much smaller differences of the Cd isotope compositions in terrestrial and meteoritic materials to be resolved in comparison to previous studies.

Bibliography

Abouchami, W., Galer, S.J.G., Horner, T.J., Rehkämper, M., Wombacher, F., Xue, Z., Lambelet, M., Gault-Ringold, M., Stirling, C.H., Schönbächler, M., Shiel, A.E., Weis, D., Holdship, P.F., 2013. A Common Reference Material for Cadmium Isotope Studies – NIST SRM 3108. Geostand. Geoanal. Res. 37, 5-17.

Ahrland, S., Chatt, J., Davies, N.R., 1958. The relative affinities of ligand atoms for acceptor molecules and ions. Quarterly Reviews, Chemical Society 12, 265-276.

Albarède, F., 2004. The Stable Isotope Geochemistry of Copper and Zinc. Rev. Mineral. Geochem. 55, 409-427.

Albarède, F., 2009. Volatile accretion history of the terrestrial planets and dynamic implications. Nature 461, 1227-1233.

Albarède, F., Ballhaus, C., Blichert-Toft, J., Lee, C.-T., Marty, B., Moynier, F., Yin, Q.-Z., 2013. Asteroidal impacts and the origin of terrestrial and lunar volatiles. Icarus 222, 44-52.

Albarède, F., Bunch, T.E., Moynier, F., Douchet, C., 2007. Isotope Fractionation during Impact: Earth versus The Moon. Meteorit. Planet. Sci. 42, 8 , Supplement. #A11 (abstr.).

Allègre, C., Manhès, G., Lewin, É., 2001. Chemical composition of the Earth and the volatility control on planetary genetics. Earth Planet. Sci. Lett. 185, 49-69.

Allègre, C.J., Poirier, J.-P., Humler, E., Hofmann, A.W., 1995. The chemical composition of the Earth. Earth Planet. Sci. Lett. 134, 515-526.

Anders, E., Grevesse, N., 1989. Abundances of the Elements - Meteoritic and Solar. Geochim. Cosmochim. Acta 53, 197-214.

Anders, E., Stevens, C.M., 1960. Search For Extinct Lead 205 In Meteorites. J. Geophys. Res. 65, 3043-3047.

Andersen, T., Knutsen, A.B., 1962. Anion-Exchange Study. I. Adsorption of some Elements In HBr-solutions. Acta Chem. Scand. 16, 849-854.

Andreasen, R., Rehkämper, M., Benedix, G.K., Theis, K.J., Schönbächler, M., Smith, C.L., 2012. Lead-Thallium Chronology of IIAB and IIIAB Iron Meteorites and the Solar System Initial Abundance of Lead-205. 43rd Lunar and Planetary Science Conference. Lunar Planet. Inst., Houston. #2902 (abstr.).

Andreasen, R., Schönbächler, M., Rehkämper, M., 2009. The 205Pb-205Tl and Cd isotope systematics of ordinary chondrites. Geochim. Cosmochim. Acta. 73, 13, Supplement 1. #A43 (abstr.).

Archer, C., Vance, D., 2004. Mass discrimination correction in multiple-collector plasma source mass spectrometry: an example using Cu and Zn isotopes. J. Anal. At. Spectrom. 19, 656-665.

Arden, J.W., 1983. Distribution of lead and thallium in the matrix of the Allende meteorite and the extent of terrestrial lead contamination in chondrites. Earth Planet. Sci. Lett. 62, 395-406.

Arndt, N., 2003. Komatiites, kimberlites, and boninites. J. Geophys. Res. 108, n/a-n/a.

Arndt, N., Ginibre, C., Chauvel, C., Albarède, F., Cheadle, M., Herzberg, C., Jenner, G., Lahaye, Y., 1998. Were komatiites wet? Geology 26, 739-742.

Arnould, M., Meynet, G., Mowlavi, N., 2000. Some selected comments on cosmic radioactivities. Chem. Geol. 169, 83-105.

Arnould, M., Paulus, G., Meynet, G., 1997. Short-lived radionuclide production by non-exploding Wolf-Rayet stars. Astron. Astrophys. 321, 452-464.

Asplund, M., Grevesse, N., Sauval, A.J., Scott, P., 2009. The Chemical Composition of the Sun. Annu. Rev. Astron. Astrophys. 47, 481-522.

Aulbach, S., Rudnick, R.L., 2009. Origins of non-equilibrium lithium isotopic fractionation in xenolithic peridotite minerals: Examples from Tanzania. Chem. Geol. 258, 17-27.

Baker, R.G.A., Rehkämper, M., Hinkley, T.K., Nielsen, S.G., Toutain, J.P., 2009. Investigation of thallium fluxes from subaerial volcanism–Implications for the present and past mass balance of thallium in the oceans. Geochim. Cosmochim. Acta 73, 6340-6359.

Baker, R.G.A., Schönbächler, M., Rehkämper, M., Williams, H.M., Halliday, A.N., 2010. The thallium isotope composition of carbonaceous chondrites -- New evidence for live 205Pb in the early solar system. Earth Planet. Sci. Lett. 291, 39-47.

Ballhaus, C., Laurenz, V., Münker, C., Fonseca, R.O.C., Albarède, F., Rohrbach, A., Lagos, M., Schmidt, M.W., Jochum, K.-P., Stoll, B., Weis, U., Helmy, H.M., 2013. The U/Pb ratio of the Earth's mantle—A signature of late volatile addition. Earth Planet. Sci. Lett. 362, 237-245.

Barrat, J.A., Zanda, B., Moynier, F., Bollinger, C., Liorzou, C., Bayon, G., 2012. Geochemistry of CI chondrites: Major and trace elements, and Cu and Zn Isotopes. Geochim. Cosmochim. Acta 83, 79-92.

Ben Othman, D., Luck, J.M., Arndt, N.T., Bodinier, J.L., Albarède, F., 2001a. Cu-Zn isotopic variations in Precambrian and present-day mantle. Geophysical Research Abstracts. 7. #06732 (abstr.).

Ben Othman, D., Luck, J.M., Bodinier, J.L., Arndt, N.T., Albarède, F., 2006. Cu–Zn isotopic variations in the Earth's mantle. Geochim. Cosmochim. Acta. 70, 18, Supplement. #A46 (abstr.).

Ben Othman, D., Luck, J.M., Tchalikian, A., 2001b. Cu, Zn (and Pb) Isotopes in Aerosols and Loesses. European Union of Geosciences XI. Cambridge Publications. #PCM7 SUpm27 G25 (abstr.).

Ben Othman, D., Luck, J.M., Tchalikian, A., Albarède, F., 2003. Cu-Zn Isotope Systematics in Terrestrial Basalts. Geophysical Research Abstracts. 5. #09669 (abstr.).

Bennett, M.E., McSween, H.Y., 1996. Shock features in iron-nickel metal and troilite of L-group ordinary chondrites. Meteorit. Planet. Sci. 31, 255-264.

Bigalke, M., Weyer, S., Kobza, J., Wilcke, W., 2010. Stable Cu and Zn isotope ratios as tracers of sources and transport of Cu and Zn in contaminated soil. Geochim. Cosmochim. Acta 74, 6801-6813.

Bigeleisen, J., 1996. Nuclear Size and Shape Effects in Chemical Reactions. Isotope Chemistry of the Heavy Elements. JACS 118, 3676-3680.

Blake, J.B., Lee, T., Schramm, D.N., 1973. Chronometer for s-process nucleosynthesis. Nature Physical Science 242, 98-100.

Blake, J.B., Schramm, D.N., 1976. A possible alternative to the r-process. Astrophys. J. 209, 846-849.

Boelrijk, N.A.I.M., 1968. A general formula for "double" isotope dilution analysis. Chem. Geol. 3, 323-325.

Boettcher, A.L., O'Neil, J.R., 1980. Stable isotope, chemical, and petrographic studies of high-pressure amphiboles and micas: evidence for metasomatism in the mantle source regions of alkali basalts and kimberlites. Am. J. Sci. 280, 594-621.

Boettcher, A.L., O'Neil, J.R., Windom, K.E., Stewart, D.C., Wilshire, H.G., 1979. Metasomatism of the Upper Mantle and the Genesis of Kimberlites and Alkali Basalts, The Mantle Sample: Inclusion in Kimberlites and Other Volcanics. American Geophysical Union, pp. 173-182.

Bollhöfer, A., Rosman, K.J.R., 2000. Isotopic source signatures for atmospheric lead: the Southern Hemisphere. Geochim. Cosmochim. Acta 64, 3251-3262.

Bollhöfer, A., Rosman, K.J.R., 2001. Isotopic source signatures for atmospheric lead: the Northern Hemisphere. Geochim. Cosmochim. Acta 65, 1727-1740.

Bonnand, P., Williams, H.M., Parkinson, I.J., Wood, B.J., Halliday, A.N., 2016. Stable chromium isotopic composition of meteorites and metal–silicate experiments: Implications for fractionation during core formation. Earth Planet. Sci. Lett. 435, 14-21.

Boss, A.P., 2004. Evolution of the Solar Nebula. VI. Mixing and Transport of Isotopic Heterogeneity. Astrophys. J. 616, 1265-1277.

Bouvier, A., Blichert-Toft, J., Moynier, F., Vervoort, J.D., Albarède, F., 2007. Pb-Pb dating constraints on the accretion and cooling history of chondrites. Geochim. Cosmochim. Acta 71, 1583-1604.

Boyd, F.R., England, J.L., 1960. Apparatus for phase-equilibrium measurements at pressures up to 50 kilobars and temperatures up to 1750°C. J. Geophys. Res. 65, 741-748.

Brearley, A.J., Jones, R.H., 1998. Chondritic meteorites, in: Papike, J.J. (Ed.), Planetary Materials, Reviews in Mineralogy and Geochemistry 36. Mineralogical Society of America, Washington, DC, pp. 1-398.

Bridgestock, L.J., Williams, H., Rehkämper, M., Larner, F., Giscard, M.D., Hammond, S., Coles, B., Andreasen, R., Wood, B.J., Theis, K.J., Smith, C.L., Benedix, G.K., Schönbächler, M., 2014. Unlocking the zinc isotope systematics of iron meteorites. Earth Planet. Sci. Lett. 400, 153-164.

Buggle, B., Glaser, B., Zöller, L., Hambach, U., Marković, S., Glaser, I., Gerasimenko, N., 2008. Geochemical characterization and origin of Southeastern and Eastern European loesses (Serbia, Romania, Ukraine). Quat. Sci. Rev. 27, 1058-1075.

Burbidge, E.M., Burbidge, G.R., Fowler, W.A., Hoyle, F., 1957. Synthesis of the Elements in Stars. Rev. Mod. Phys. 29, 547-650.

Canup, R.M., Asphaug, E., 2001. Origin of the Moon in a giant impact near the end of the Earth's formation. Nature 412, 708-712.

Cassen, P., 1996. Models for the fractionation of moderately volatile elements in the solar nebula. Meteorit. Planet. Sci. 31, 793-806.

Chabot, N.L., Campbell, A.J., McDonough, W.F., Draper, D.S., Agee, C.B., Humayun, M., Watson, H.C., Cottrell, E., Saslow, S.A., 2008. The Fe–C system at 5 GPa and implications for Earth's core. Geochim. Cosmochim. Acta 72, 4146-4158.

Chambers, J., 2000. Meteoritic Diversity and Planetesimal Formation, in: Lauretta, D., McSween Jr, H.Y. (Eds.), Meteorites and the Early Solar System II. University of Arizona Press, Tucson, pp. 487-497.

Chao, T.T., Sanzolone, R.F., 1992. Decomposition techniques. J. Geochem. Explor. 44, 65-106.

Chapman, J.B., Mason, T.F.D., Weiss, D.J., Coles, B.J., Wilkinson, J.J., 2006. Chemical Separation and Isotopic Variations of Cu and Zn From Five Geological Reference Materials. Geostand. Geoanal. Res. 30, 5-16.

Chen, H., Savage, P.S., Teng, F.-Z., Helz, R.T., Moynier, F., 2013. Zinc isotope fractionation during magmatic differentiation and the isotopic composition of the bulk Earth. Earth Planet. Sci. Lett. 369–370, 34-42.

Chen, J., Gaillardet, J., Louvat, P., Huon, S., 2009. Zn isotopes in the suspended load of the Seine River, France: Isotopic variations and source determination. Geochim. Cosmochim. Acta 73, 4060-4076.

Chen, J.H., Wasserburg, G.J., 1983. A Search for Primordial Pb in Iron-Meteorites. Meteoritics. 18, 4. #279-280 (abstr.).

Chen, J.H., Wasserburg, G.J., 1987. A search for Evidence of Extinct Lead 205 in Iron Meteorites. Lunar and Planetary Science XVIII. Lunar Planet Inst., Houston. #165-166 (abstr.).

Chen, M., El Goresy, A., 2000. The nature of maskelynite in shocked meteorites: not diaplectic glass but a glass quenched from shock-induced dense melt at high pressures. Earth Planet. Sci. Lett. 179, 489-502.

Chen, S., Liu, Y., Hu, J., Zhang, Z., Hou, Z., Huang, F., Yu, H., 2016. Zinc Isotopic Compositions of NIST SRM 683 and Whole-Rock Reference Materials. Geostand. Geoanal. Res. 40, 417-432.

Chipman, J., 1972. Thermodynamics and phase diagram of the Fe-C system. Metall. Trans. 3, 55-64.

Chou, C.-L., 1978. Fractionation of Siderophile Elements in the Earth's Upper Mantle, Proceedings of the 9th Lunar and Planetary Science Conference. Lunar and Planetary Institute, Houston. pp. 219-230.

Ciesla, F.J., 2007. Outward Transport of High-Temperature Materials Around the Midplane of the Solar Nebula. Science 318, 613-615.

Ciesla, F.J., 2008. Radial transport in the solar nebula: Implications for moderately volatile element depletions in chondritic meteorites. Meteorit. Planet. Sci. 43, 639-655.

Cloquet, C., Carignan, J., Libourel, G., 2006. Isotopic Composition of Zn and Pb Atmospheric Depositions in an Urban/Periurban Area of Northeastern France. Environ. Sci. Technol. 40, 6594-6600.

Cloquet, C., Rouxel, O., Carignan, J., Libourel, G., 2005. Natural Cadmium Isotopic Variations in Eight Geological Reference Materials (NIST SRM 2711, BCR 176, GSS-1, GXR-1, GXR-2, GSD-12, Nod-P-1, Nod-A-1) and Anthropogenic Samples, Measured by MC-ICP-MS. Geostand. Geoanal. Res. 29, 95-106.

Coggon, R.M., Rehkämper, M., Atteck, C., Teagle, D.A.H., Alt, J.C., Cooper, M.J., 2014. Controls on thallium uptake during hydrothermal alteration of the upper ocean crust. Geochim. Cosmochim. Acta 144, 25-42.

Compston, W., Oversby, V.M., 1969. Lead isotopic analysis using a double spike. J. Geophys. Res. 74, 4338-4348.

Connolly Jr, H.C., Smith, C., Benedix, G., Folco, L., Righter, K., Zipfel, J., Yamaguchi, A., Chennaoui Aoudjehane, H., 2005. The Meteoritical Bulletin, No. 92, 2007 September. Meteorit. Planet. Sci. 42, 1647-1694.

Corfu, F., 1993. The evolution of the southern Abitibi greenstone belt in light of precise U-Pb geochronology. Econ. Geol. 88, 1323-1340.

Corgne, A., Liebske, C., Wood, B.J., Rubie, D.C., Frost, D.J., 2005. Silicate perovskite-melt partitioning of trace elements and geochemical signature of a deep perovskitic reservoir. Geochim. Cosmochim. Acta 69, 485-496.

Corgne, A., Wood, B.J., 2002. CaSiO3 and CaTiO3 perovskite-melt partitioning of trace elements: Implications for gross mantle differentiation. Geophys. Res. Lett. 29, 39-31-39-34.

Dauphas, N., Teng, F.-Z., Arndt, N.T., 2010. Magnesium and iron isotopes in 2.7 Ga Alexo komatiites: Mantle signatures, no evidence for Soret diffusion, and identification of diffusive transport in zoned olivine. Geochim. Cosmochim. Acta 74, 3274-3291.

Davis, A.M., Richter, F.M., 2014. 1.10 - Condensation and Evaporation of Solar System Materials, in: Turekian, H.D., Holland, K.K. (Eds.), Treatise on Geochemistry (Second Edition). Elsevier, Oxford, pp. 335-360.

Ding, Z.L., Xiong, S.F., Sun, J.M., Yang, S.L., Gu, Z.Y., Liu, T.S., 1999. Pedostratigraphy and paleomagnetism of a ~7.0 Ma eolian loess–red clay sequence at Lingtai, Loess Plateau, north-central China and the implications for paleomonsoon evolution. Palaeogeogr., Palaeoclimatol., Palaeoecol. 152, 49-66.

Dodson, M.H., 1963. A theoretical study of the use of internal standards for precise isotopic analysis by the surface ionization technique: Part I - General first-order algebraic solutions. J. Sci. Instrum. 40, 289.

Dodson, M.H., 1970. Simplified equations for double-spiked isotopic analyses. Geochim. Cosmochim. Acta 34, 1241-1244.

Dolgopolova, A., Weiss, D.J., Seltmann, R., Kober, B., Mason, T.F.D., Coles, B., Stanley, C.J., 2006. Use of isotope ratios to assess sources of Pb and Zn dispersed in the environment during mining and ore processing within the Orlovka–Spokoinoe mining site (Russia). Appl. Geochem. 21, 563-579.

Doucet, L.S., Mattielli, N., Ionov, D.A., Debouge, W., Golovin, A.V., 2016. Zn isotopic heterogeneity in the mantle: A melting control? Earth Planet. Sci. Lett. 451, 232-240.

Dreibus, G., Wänke, H., 1980. On the origin of the excess of volatile trace elements in the dark portion of gas-rich chondrites. 43rd Annual Meeting of the Meteoritical Society. #100 (abstr.).

Dunstan, L.P., Gramlich, J.W., Barnes, I.L., Purdy, W.C., 1980. Absolute isotopic abundance and the atomic weight of a reference sample of thallium. J. Res. Natl. Bur. Stand. 85, 1-10.

Errandonea, D., 2010. The melting curve of ten metals up to 12 GPa and 1600 K. J. Appl. Phys. 108, 033517.

Falahi-Ardakani, A., 1984. Contamination of environment with heavy metals emitted from automotives. Ecotoxicol. Environ. Saf. 8, 152-161.

Faris, J.P., Buchanan, R.F., 1964. Anion Exchange Characteristics of the Elements in Nitric Acid Medium. Anal. Chem. 36, 1157-1158.

Fegley, B., Jr., 2000. Kinetics of Gas-Grain Reactions in the Solar Nebula. Space Sci. Rev. 92, 177-200.

Fitton, J.G., Dunlop, H.M., 1985. The Cameroon line, West Africa, and its bearing on the origin of oceanic and continental alkali basalt. Earth Planet. Sci. Lett. 72, 23-38.

Forster, T., Heller, F., 1994. Loess deposits from the Tajik depression (Central Asia): Magnetic properties and paleoclimate. Earth Planet. Sci. Lett. 128, 501-512.

Franchi, I.A., 2008. Oxygen isotopes in asteroidal materials, in: MacPherson, G.J., Mittlefehldt, D.W., Jones, J.H., Simon, S.B. (Eds.), Oxygen in the Solar System, Reviews in Mineralogy & Geochemistry 68. Mineralogical Soc Amer, Chantilly, pp. 345-397.

Frechen, M., Oches, E.A., Kohfeld, K.E., 2003. Loess in Europe—mass accumulation rates during the Last Glacial Period. Quat. Sci. Rev. 22, 1835-1857.

Friedrich, J.M., Bridges, J.C., Wang, M.-S., Lipschutz, M.E., 2004. Chemical studies of L chondrites. VI: variations with petrographic type and shock-loading among equilibrated falls. Geochim. Cosmochim. Acta 68, 2889-2904.

Fujii, T., Moynier, F., Agranier, A., Ponzevera, E., Abe, M., Uehara, A., Yamana, H., 2013. Nuclear field shift effect in isotope fractionation of thallium. J. Radioanal. Nucl. Chem. 296, 261-265.

Fujii, T., Moynier, F., Albarède, F., 2009. The nuclear field shift effect in chemical exchange reactions. Chem. Geol. 267, 139-156.

Gail, H.-P., 2001. Radial mixing in protoplanetary accretion disks I. Stationary disc models with annealing and carbon combustion. Astronomy & Astrophysics 378, 192-213.

Galer, S.J.G., 1999. Optimal double and triple spiking for high precision lead isotopic measurement. Chem. Geol. 157, 255-274.

Galer, S.J.G., Abouchami, W., 1998. Practical application of lead triple spiking for correction of instrumental mass discrimination. Mineral. Mag. 62A, 1. #491-492 (abstr.).

Gallet, S., Jahn, B.-m., Van Vliet Lanoë, B., Dia, A., Rossello, E., 1998. Loess geochemistry and its implications for particle origin and composition of the upper continental crust. Earth Planet. Sci. Lett. 156, 157-172.

Ganapathy, R., Anders, E., 1974. Bulk compositions of the moon and earth, estimated from meteorites, Proceedings of the 5th Lunar Science Conference. Pergamon Press, Inc., New York. pp. 1181-1206.

Gannoun, A., Burton, K.W., Parkinson, I.J., Alard, O., Schiano, P., Thomas, L.E., 2007. The scale and origin of the osmium isotope variations in mid-ocean ridge basalts. Earth Planet. Sci. Lett. 259, 541-556.

Gattacceca, J., Rochette, P., Denise, M., Consolmagno, G., Folco, L., 2005. An impact origin for the foliation of chondrites. Earth Planet. Sci. Lett. 234, 351-368.

Gault-Ringold, M., Stirling, C.H., 2012. Anomalous isotopic shifts associated with organic resin residues during cadmium isotopic analysis by double spike MC-ICPMS. J. Anal. At. Spectrom. 27.

Georgiev, S.V., Horner, T.J., Stein, H.J., Hannah, J.L., Bingen, B., Rehkämper, M., 2015. Cadmium-isotopic evidence for increasing primary productivity during the Late Permian anoxic event. Earth Planet. Sci. Lett. 410, 84-96.

Gill, J., Williams, R., Bruland, K., 1985. Eruption of basalt and andesite lava degasses 222Rn and 210Po. Geophys. Res. Lett. 12, 17-20.

Göpel, C., Manhès, G., Allègre, C.J., 1985. U-Pb Systematics in Iron-Meteorites - Uniformity of Primordial Lead. Geochim. Cosmochim. Acta 49, 1681-1695.

Göpel, C., Manhès, G., Allègre, C.J., 1994. U-Pb Systematics of Phosphates from Equilibrated Ordinary Chondrites. Earth Planet. Sci. Lett. 121, 153-171.

Grossman, L., 1972. Condensation in the primitive solar nebula. Geochim. Cosmochim. Acta 36, 597-619.

Grossman, L., Larimer, J.W., 1974. Early chemical history of the solar system. Rev. Geophys. 12, 71-101.

Gudfinnsson, G.H., Presnall, D.C., 2000. Melting Behaviour of Model Lherzolite in the System CaO–MgO–Al2O3–SiO2–FeO at 0·7–2·8 GPa. J. Petrol. 41, 1241-1269.

Gylesjö, S., Arnold, E., 2006. Clay mineralogy of a red clay–loess sequence from Lingtai, the Chinese Loess Plateau. Global Planet. Change 51, 181-194.

Haase, D., Fink, J., Haase, G., Ruske, R., Pécsi, M., Richter, H., Altermann, M., Jäger, K.D., 2007. Loess in Europe—its spatial distribution based on a European Loess Map, scale 1:2,500,000. Quat. Sci. Rev. 26, 1301-1312.

Halliday, A.N., 2004. Mixing, volatile loss and compositional change during impact-driven accretion of the Earth. Nature 427, 505-509.

Halliday, A.N., Davidson, J.P., Holden, P., DeWolf, C., Lee, D.-C., Fitton, J.G., 1990. Trace-element fractionation in plumes and the origin of HIMU mantle beneath the Cameroon line. Nature 347, 523-528.

Halliday, A.N., Dickin, A.P., Fallick, A.E., Fitton, J.G., 1988. Mantle Dynamics: A Nd, Sr, Pb and O Isotopic Study of the Cameroon Line Volcanic Chain. J. Petrol. 29, 181-211.

Hamelin, B., Manhès, G., Albarede, F., Allègre, C.J., 1985. Precise lead isotope measurements by the double spike technique: A reconsideration. Geochim. Cosmochim. Acta 49, 173-182.

Handler, M.R., Baker, J.A., Schiller, M., Bennett, V.C., Yaxley, G.M., 2009. Magnesium stable isotope composition of Earth's upper mantle. Earth Planet. Sci. Lett. 282, 306-313.

Hart, S.R., Zindler, A., 1986. In search of a bulk-Earth composition. Chem. Geol. 57, 247-267.

Heber, V.S., Brooker, R.A., Kelley, S.P., Wood, B.J., 2007. Crystal–melt partitioning of noble gases (helium, neon, argon, krypton, and xenon) for olivine and clinopyroxene. Geochim. Cosmochim. Acta 71, 1041-1061.

Helffrich, G.R., Wood, B.J., 2001. The Earth's mantle. Nature 412, 501-507.

Herzberg, C., 1992. Depth and degree of melting of komatiites. J. Geophys. Res. 97, 4521-4540.

Herzog, G.F., Moynier, F., Albarède, F., Berezhnoy, A.A., 2009. Isotopic and elemental abundances of copper and zinc in lunar samples, Zagami, Pele's hairs, and a terrestrial basalt. Geochim. Cosmochim. Acta 73, 5884-5904.

Hettmann, K., Marks, M.A.W., Kreissig, K., Zack, T., Wenzel, T., Rehkämper, M., Jacob, D.E., Markl, G., 2014. The geochemistry of Tl and its isotopes during magmatic and hydrothermal processes: The peralkaline Ilimaussaq complex, southwest Greenland. Chem. Geol. 366, 1-13.

Hin, R.C., Burkhardt, C., Schmidt, M.W., Bourdon, B., Kleine, T., 2013. Experimental evidence for Mo isotope fractionation between metal and silicate liquids. Earth Planet. Sci. Lett. 379, 38-48.

Hin, R.C., Fitoussi, C., Schmidt, M.W., Bourdon, B., 2014. Experimental determination of the Si isotope fractionation factor between liquid metal and liquid silicate. Earth Planet. Sci. Lett. 387, 55-66.

Hin, R.C., Schmidt, M.W., Bourdon, B., 2012. Experimental evidence for the absence of iron isotope fractionation between metal and silicate liquids at 1 GPa and 1250–1300°C and its cosmochemical consequences. Geochim. Cosmochim. Acta 93, 164-181.

Hinkley, T.K., Le Cloarec, M.F., Lambert, G., 1994. Fractionation of families of major, minor, and trace metals across the melt-vapor interface in volcanic exhalations. Geochim. Cosmochim. Acta 58, 3255-3263.

Hofmann, A., 1971. Fractionation corrections for mixed-isotope spikes of Sr, K, and Pb. Earth Planet. Sci. Lett. 10, 397-402.

Holloway, J.R., Pan, V., Gudmundsson, G., 1992. High-pressure fluid-absent melting experiments in the presence of graphite; oxygen fugacity, ferric/ferrous ratio and dissolved CO2. Eur. J. Mineral. 4, 105.

Holzheid, A., Sylvester, P., O'Neill, H.S.C., Rubie, D.C., Palme, H., 2000. Evidence for a late chondritic veneer in the Earth's mantle from high-pressure partitioning of palladium and platinum. Nature 406, 396-399.

Hopp, J., Trieloff, M., Ott, U., 2016. I–Xe ages of enstatite chondrites. Geochim. Cosmochim. Acta 174, 196-210.

Hopp, J., Trieloff, M., Ott, U., Korochantseva, E.V., Buykin, A.I., 2014. 39Ar-40Ar chronology of the enstatite chondrite parent bodies. Meteorit. Planet. Sci. 49, 358-372.

Horn, I., Foley, S.F., Jackson, S.E., Jenner, G.A., 1994. Trace-element Partitioning with Application to Magmatic Processes Experimentally determined partitioning of high field strength- and selected transition elements between spinel and basaltic melt. Chem. Geol. 117, 193-218.

Horner, T.J., Schönbächler, M., Rehkämper, M., Nielsen, S.G., Williams, H., Halliday, A.N., Xue, Z., Hein, J.R., 2010. Ferromanganese crusts as archives of deep water Cd isotope compositions. Geochem. Geophys. Geosyst. 11, n/a-n/a.

Huang, F., Chakraborty, P., Lundstrom, C.C., Holmden, C., Glessner, J.J.G., Kieffer, S.W., Lesher, C.E., 2010. Isotope fractionation in silicate melts by thermal diffusion. Nature 464, 396-400.

Huey, J.M., Kohman, T.P., 1972. Search for extinct natural radioactivity of 205Pb via thallium-isotope anomalies in chondrites and lunar soil. Earth Planet. Sci. Lett. 16, 401-412.

Huff, E.A., Huff, D.R., 1993. TRU-spec and RE-spec chromatography - basic studies and applications. 34th ORNL/DOE Conference Analytical Chemistry in Energy Technology. Oak Ridge National Laboratory/U.S. Department of Energy, Gatlinburg, Tennessee. # 58 (abstr.).

Humayun, M., Cassen, P., 2000. Processes Determining the Volatile Abundances of the Meteorites and Terrestrial Planets, in: Canup, R.M., Righter, K. (Eds.), Origin of the Earth and Moon. University of Arizona Press, Tucson, AZ, pp. 3-23.

Huston, T.J., Lipschutz, M.E., 1984. Chemical studies of L chondrites—III. Mobile trace elements and 40Ar39Ar ages. Geochim. Cosmochim. Acta 48, 1319-1329.

Hyung, E., Huang, S., Petaev, M.I., Jacobsen, S.B., 2016. Is the mantle chemically stratified? Insights from sound velocity modeling and isotope evolution of an early magma ocean. Earth Planet. Sci. Lett. 440, 158-168.

Ionov, D.A., Seitz, H.-M., 2008. Lithium abundances and isotopic compositions in mantle xenoliths from subduction and intra-plate settings: Mantle sources vs. eruption histories. Earth Planet. Sci. Lett. 266, 316-331.

Izawa, M.R.M., Flemming, R.L., Banerjee, N.R., McCausland, P.J.A., 2011. Micro-X-ray diffraction assessment of shock stage in enstatite chondrites. Meteorit. Planet. Sci. 46, 638-651.

Jacobsen, S.B., Harper, C.L., 1996. Accretion and Early Differentiation History of the Earth Based on Extinct Radionuclides, Earth Processes: Reading the Isotopic Code. American Geophysical Union, pp. 47-74.

Jacobsen, S.B., Ranen, M.C., Petaev, M.I., Remo, J.L., Connell, R.J., Sasselov, D.D., 2008. Isotopes as clues to the origin and earliest differentiation history of the Earth. Philos. Trans. R. Soc. A 366, 4129-4162.

Jacobson, S.A., Morbidelli, A., Raymond, S.N., O'Brien, D.P., Walsh, K.J., Rubie, D.C., 2014. Highly siderophile elements in Earth's mantle as a clock for the Moon-forming impact. Nature 508, 84-87.

Jacquet, E., Gounelle, M., Fromang, S., 2012. On the aerodynamic redistribution of chondrite components in protoplanetary disks. Icarus 220, 162-173.

Jaffey, A.H., Flynn, K.F., Glendenin, L.E., Bentley, W.C., Essling, A.M., 1971. Precision Measurement of Half-Lives and Specific Activities of 235U and 238U. Phys. Rev. C 4, 1889-1906.

Jagoutz, E., Palme, H., Baddenhausen, H., Blum, K., Cendales, M., Dreibus, G., Spettel, B., Lorenz, V., Wänke, H., 1979. The abundances of major, minor and trace elements in the earth's mantle as derived from primitive ultramafic nodules, Proceedings of the 10th Lunar and Planetary Science Conference. Pergamon Press, Inc., New York. pp. 2130-2050.

Jakobsson, S., 2012. Oxygen fugacity control in piston-cylinder experiments. Contrib. Mineral. Petrol. 164, 397-406.

Javoy, M., 1995. The Integral Enstatite Chondrite Model of the Earth. Geophys. Res. Lett. 22, 2219-2222.

Javoy, M., Kaminski, E., Guyot, F., Andrault, D., Sanloup, C., Moreira, M., Labrosse, S., Jambon, A., Agrinier, P., Davaille, A., Jaupart, C., 2010. The chemical composition of the Earth: Enstatite chondrite models. Earth Planet. Sci. Lett. 293, 259-268.

Jeffcoate, A.B., Elliott, T., Kasemann, S.A., Ionov, D., Cooper, K., Brooker, R., 2007. Li isotope fractionation in peridotites and mafic melts. Geochim. Cosmochim. Acta 71, 202-218.

Jochum, K.P., Nohl, U., Herwig, K., Lammel, E., Stoll, B., Hofmann, A.W., 2005. GeoReM: A New Geochemical Database for Reference Materials and Isotopic Standards. Geostand. Geoanal. Res. 29, 333-338.

Johnson, A., Canil, D., 2011. The degassing behavior of Au, Tl, As, Pb, Re, Cd and Bi from silicate liquids: Experiments and applications. Geochim. Cosmochim. Acta 75, 1773-1784.

Johnson, C.M., Beard, B.L., 1999. Correction of instrumentally produced mass fractionation during isotopic analysis of Fe by thermal ionization mass spectrometry. Int. J. Mass spectrom. 193, 87-99.

Kaczaral, P.W., Dennison, J.E., Verkouteren, R.M., Lipschutz, M.E., 1988. On Volatile/Mobile Trace Element Trends in E3 Chondrites, Twelfth Symposium on Antarctic Meteorites, Proceedings of the NIPR Symposium 1. National Institute of Polar Research, Tokyo. pp. 113-121.

Kato, T., Ringwood, A.E., Irifune, T., 1988. Experimental determination of element partitioning between silicate perovskites, garnets and liquids: constraints on early differentiation of the mantle. Earth Planet. Sci. Lett. 89, 123-145.

Keays, R.R., Ganapathy, R., Anders, E., 1971. Chemical fractionations in meteorites--IV abundances of fourteen trace elements in L-chondrites; implications for cosmothermometry. Geochim. Cosmochim. Acta 35, 337-363.

Kehm, K., Hauri, E.H., Alexander, C.M.O.D., Carlson, R.W., 2003. High precision iron isotope measurements of meteoritic material by cold plasma ICP-MS. Geochim. Cosmochim. Acta 67, 2879-2891.

Keil, K., 1989. Enstatite Meteorites and their Parent Bodies. Meteoritics 24, 195-208.

Keller, C., Gail, H.-P., 2004. Radial mixing in protoplanetary accretion disks VI. Mixing by large-scale radial flow. Astronomy & Astrophysics 415, 1177-1185.

Kimura, K., Lewis, R.S., Anders, E., 1974. Distribution of gold and rhenium between nickel-iron and silicate melts: implications for the abundance of siderophile elements on the Earth and Moon. Geochim. Cosmochim. Acta 38, 683-701.

Kiseeva, E.S., Wood, B.J., 2013. A simple model for chalcophile element partitioning between sulphide and silicate liquids with geochemical applications. Earth Planet. Sci. Lett. 383, 68-81.

Kiseeva, E.S., Wood, B.J., 2015. The effects of composition and temperature on chalcophile and lithophile element partitioning into magmatic sulphides. Earth Planet. Sci. Lett. 424, 280-294.

Kondev, F.G., 2004. Nuclear Data Sheets for A=205. Nuclear Data Sheets 101, 521-662.

Kong, P., Mori, T., Ebihara, M., 1997. Compositional continuity of enstatite chondrites and implications for heterogeneous accretion of the enstatite chondrite parent body. Geochim. Cosmochim. Acta 61, 4895-4914.

Korkisch, J., 1989. Handbook of Ion Exchange Resins: Their Application to Inorganic Analytical Chemistry (Vols. 1-6). CRC Press, Inc., Boca Raton, Florida.

Kraus, K.A., Nelson, F., 1956. Proc. Intern. Conf. Peaceful Uses Atomic Energy, Geneva 1955 7. United Nations, New York. p. 118.

Krogh, T.E., Hurley, P.M., 1968. Strontium isotope variation and whole-rock isochron studies, Grenville Province of Ontario. Journal of Geophysical Research 73, 7107-7125.

Krot, A.N., Keil, K., Scott, E.R.D., Goodrich, C.A., Weisberg, M.K., 2014. 1.1 - Classification of Meteorites and Their Genetic Relationships, Treatise on Geochemistry (Second Edition). Elsevier, Oxford, pp. 1-63.

Kruijer, T.S., Kleine, T., Fischer-Godde, M., Sprung, P., 2015. Lunar tungsten isotopic evidence for the late veneer. Nature advance online publication.

Kruijer, T.S., Sprung, P., Kleine, T., Leya, I., Wieler, R., 2013. The abundance and isotopic composition of Cd in iron meteorites. Meteorit. Planet. Sci. 48, 2597-2607.

Lagos, M., Ballhaus, C., Munker, C., Wohlgemuth-Ueberwasser, C., Berndt, J., Kuzmin, D.V., 2008. The Earth's missing lead may not be in the core. Nature 456, 89-92.

Lambelet, M., Rehkämper, M., van de Flierdt, T., Xue, Z., Kreissig, K., Coles, B., Porcelli, D., Andersson, P., 2013. Isotopic analysis of Cd in the mixing zone of Siberian rivers with the Arctic Ocean—New constraints on marine Cd cycling and the isotope composition of riverine Cd. Earth Planet. Sci. Lett. 361, 64-73.

Lambert, G., Le Cloarec, M.F., Ardouin, B., Le Roulley, J.C., 1985. Volcanic emission of radionuclides and magma dynamics. Earth Planet. Sci. Lett. 76, 185-192.

Larimer, J.W., 1967. Chemical fractionations in meteorites—I. Condensation of the elements. Geochim. Cosmochim. Acta 31, 1215-1238.

Laurenz, V., Rubie, D.C., Frost, D.J., Vogel, A.K., 2016. The importance of sulfur for the behavior of highly-siderophile elements during Earth's differentiation. Geochim. Cosmochim. Acta 194, 123-138.

Lee, D.-C., Halliday, A.N., Davies, G.R., Essene, E.J., Fitton, J.G., Temdjim, R., 1996. Melt Enrichment of Shallow Depleted Mantle: a Detailed Petrological, Trace Element and Isotopic Study of Mantle-Derived Xenoliths and Megacrysts from the Cameroon Line. J. Petrol. 37, 415-441.

Lee, D.-C., Halliday, A.N., Fitton, J.G., Poli, G., 1994. Isotopic variations with distance and time in the volcanic islands of the Cameroon line: evidence for a mantle plume origin. Earth Planet. Sci. Lett. 123, 119-138.

Lee, K.J., Lee, Y.J., Choi, Y.R., Kim, J.S., Kim, Y.S., Heo, S.B., 2013. Development of new reference materials for the determination of cadmium, chromium, mercury and lead in polycarbonate. Anal. Chim. Acta 758, 19-27.

Lin, Y., Goresy, A.E., 2002. A comparative study of opaque phases in Qingzhen (EH3) and MacAlpine Hills 88136 (EL3): Representatives of EH and EL parent bodies. Meteorit. Planet. Sci. 37, 577-599.

Lipschutz, M., 1997. Nebular and Parent-Body Processes in Chondrites: Labile Trace Elements as Indicators and Thermometers, in: Zolensky, M.E., Krot, A.N., Scott, E.R.D. (Eds.), Workshop on Parent-Body and Nebular Modification of Chondritic Materials. Lunar and Planetary Institute, Houston. p. 38.

Lipschutz, M.E., Woolum, D.S., 1988. Highly Labile Elements, in: Kerridge, J.F., Matthews, M.S. (Eds.), Meteorites and the Early Solar System. University of Arizona Press, Tucson, pp. 462-487.

Liu, C.-Q., Masuda, A., Okada, A., Yabuki, S., Fan, Z.-L., 1994. Isotope geochemistry of Quaternary deposits from the arid lands in northern China. Earth Planet. Sci. Lett. 127, 25-38.

Liu, C.-Q., Masuda, A., Okada, A., Yabuki, S., Zhang, J., Fan, Z.-L., 1993. A geochemical study of loess and desert sand in northern China: Implications for continental crust weathering and composition. Chem. Geol. 106, 359-374.

Liu, L.-G., Bassett, W.A., 1975. The melting of iron up to 200 kbar. J. Geophys. Res. 80, 3777-3782.

Liu, S.-A., Wang, Z.-Z., Li, S.-G., Huang, J., Yang, W., 2016. Zinc isotope evidence for a large-scale carbonated mantle beneath eastern China. Earth Planet. Sci. Lett. 444, 169-178.

Lodders, K., 2000. An Oxygen Isotope Mixing Model for the Accretion and Composition of Rocky Planets, in: Benz, W., Kallenbach, R., Lugmair, G.W. (Eds.), From Dust to Terrestrial Planets, Space Sciences Series of ISSI 9. Springer Netherlands, pp. 341-354.

Lodders, K., 2003. Solar System Abundances and Condensation Temperatures of the Elements. Astrophys. J. 591, 1220-1247.

Lodders, K., 2010. Solar System Abundances of the Elements, in: Goswami, A., Reddy, B.E. (Eds.), Principles and Perspectives in Cosmochemistry, Astrophysics and Space Science Proceedings. Springer Berlin Heidelberg, pp. 379-417.

Lodders, K., Fegley, B., Jr., 1998. The planetary scientist's companion. Oxford University Press, New York, 371 pp.

Lodders, K., Palme, H., Gail, H.-P., 2009. Chapter 4.4 Abundances of the elements in the Solar System, in: Trümper, J.E. (Ed.), Subvolume B 'Solar System' of Volume 4 'Astronomy, Astrophysics, and Cosmology' of Landolt-Börnstein - Group VI 'Astronomy and Astrophysics'. Springer Berlin Heidelberg, Berlin, Heidelberg, pp. 560-598.

Luck, J.-M., Othman, D.B., Albarède, F., 2005. Zn and Cu isotopic variations in chondrites and iron meteorites: Early solar nebula reservoirs and parent-body processes. Geochim. Cosmochim. Acta 69, 5351-5363.

Ludwig, K.R., 2003. User's Manual for Isoplot 3.0, A Geochronological Toolkit for Microsoft Excel. Berkeley Geochronology Center Special Publication No. 4, Berkeley, CA, 70 pp.

Lundstrom, C.C., Chaussidon, M., Hsui, A.T., Kelemen, P., Zimmerman, M., 2005. Observations of Li isotopic variations in the Trinity Ophiolite: Evidence for isotopic fractionation by diffusion during mantle melting. Geochim. Cosmochim. Acta 69, 735-751.

Maaløe, S., Aoki, K.-i., 1977. The major element composition of the upper mantle estimated from the composition of lherzolites. Contrib. Mineral. Petrol. 63, 161-173.

MacKenzie, J.M., Canil, D., 2008. Volatile heavy metal mobility in silicate liquids: Implications for volcanic degassing and eruption prediction. Earth Planet. Sci. Lett. 269, 488-496.

Maier, W.D., Barnes, S.J., Campbell, I.H., Fiorentini, M.L., Peltonen, P., Barnes, S.-J., Smithies, R.H., 2009. Progressive mixing of meteoritic veneer into the early Earth/'s deep mantle. Nature 460, 620-623.

Makishima, A., Kitagawa, H., Nakamura, E., 2011. Simultaneous Determination of Cd, In, Tl and Bi by Isotope Dilution-Internal Standardisation ICP-QMS with Corrections Using Externally Measured MoO+/Mo+ Ratios. Geostand. Geoanal. Res. 35, 57-67.

Malhotra, S., Chang, L., Schlesinger, M.E., 1998. Liquid Solution Thermodynamics in the Alumina-saturated Fe–C–Pb System. ISIJ Int. 38, 1-8.

Manhès, G., Allègre, C.J., 1978. Time Differences as Determined from the Ratio of Lead 207 to Lead 206 in Concordant Meteorites. Meteoritics. 13. #543 (abstr.).

Manhès, G., Minster, J.F., Allègre, C.J., 1978. Comparative uranium-thorium-lead and rubidium-strontium study of the Saint Sèverin amphoterite: consequences for early solar system chronology. Earth Planet. Sci. Lett. 39, 14-24.

Mann, U., Frost, D.J., Rubie, D.C., 2009. Evidence for high-pressure core-mantle differentiation from the metal–silicate partitioning of lithophile and weakly-siderophile elements. Geochim. Cosmochim. Acta 73, 7360-7386.

Mann, U., Frost, D.J., Rubie, D.C., Becker, H., Audétat, A., 2012. Partitioning of Ru, Rh, Pd, Re, Ir and Pt between liquid metal and silicate at high pressures and high temperatures - Implications for the origin of highly siderophile element concentrations in the Earth's mantle. Geochim. Cosmochim. Acta 84, 593-613.

Maréchal, C., Albarède, F., 2002. Ion-exchange fractionation of copper and zinc isotopes. Geochim. Cosmochim. Acta 66, 1499-1509.

Maréchal, C.N., Nicolas, E., Douchet, C., Albarède, F., 2000. Abundance of zinc isotopes as a marine biogeochemical tracer. Geochem. Geophys. Geosyst. 1, 1015.

Maréchal, C.N., Télouk, P., Albarède, F., 1999. Precise analysis of copper and zinc isotopic compositions by plasma-source mass spectrometry. Chem. Geol. 156, 251-273.

Marin, N., Righter, K., Danielson, L., Pando, K., Lee, C.T., 2013. Metal-silicate partitioning of Bi, In, and Cd as a function of temperature and melt composition. 44th Lunar and Planetary Science Conference. Lunar and Planetary Institute, Houston. #1848 (abstr.).

Marsh, S.F., Alarid, J.E., Hammond, C.F., McLeod, M.J., Roensch, F.R., Rein, J.E., 1978. Anion exchange of 58 elements in hydrobromic acid and in hydriodic acid. Los Alamos Scientific Laboratory of the University of California, Los Alamos, New Mexico, 18 pp.

Marty, B., 2012. The origins and concentrations of water, carbon, nitrogen and noble gases on Earth. Earth Planet. Sci. Lett. 313, 56-66.

Matsukage, K.N., Kubo, K., Chromian spinel during melting experiments of dry peridotite (KLB-1) at 1.0–2.5 GPa, Am. Mineral. 88, 2003, p. 1271.

Matsukage, K.N., Oya, M., 2010. Petrological and chemical variability of peridotite xenoliths from the Cameroon volcanic line, West Africa: an evidence for plume emplacement. Journal of Mineralogical and Petrological Sciences 105, 57-69.

Mattielli, N., Haenecour, P., Debaille, V., 2012. Zn isotope fractionation in Archean komatiites and associated lava-flows. Mineral. Mag. 76, 6. #2080 (abstr.).

Mattielli, N., Haenecour, P., Hublet, G., Duchemin, C., Debaille, V., 2014. Correlated Mg-Zn isotope fractionation in archaen komatiitic lava flows. Geological Soceiety of America Annual Meeting. 46, 6, Vancouver. #197 (abstr.).

Mattinson, J.M., 2010. Analysis of the relative decay constants of 235U and 238U by multi-step CA-TIMS measurements of closed-system natural zircon samples. Chem. Geol. 275, 186-198.

McDade, P., Wood, B.J., Van Westrenen, W., Brooker, R., Gudmundsson, G., Soulard, H., Najorka, J., Blundy, J., 2002. Pressure corrections for a selection of piston-cylinder cell assemblies. Mineral. Mag. 66, 1021-1028.

McDonough, W.F., Sun, S.s., 1995. The composition of the Earth. Chem. Geol. 120, 223-253.

McFarlane, E.A., Drake, M.J., Rubie, D.C., 1994. Element partitioning between Mg-perovskite, magnesiowüstite, and silicate melt at conditions of the Earth's mantle. Geochim. Cosmochim. Acta 58, 5161-5172.

Médard, E., McCammon, C.A., Barr, J.A., Grove, T.L., 2008. Oxygen fugacity, temperature reproducibility, and H2O contents of nominally anhydrous piston-cylinder experiments using graphite capsules. Am. Mineral. 93, 1838-1844.

Meisel, T., Walker, R.J., Irving, A.J., Lorand, J.-P., 2001. Osmium isotopic compositions of mantle xenoliths: a global perspective. Geochim. Cosmochim. Acta 65, 1311-1323.

Menzies, M.A., Halliday, A.N., Palacz, Z., Hunter, R.H., Upton, B.G.J., Aspen, P., Hawkesworth, C.J., 1987. Evidence from mantle xenoliths for an enriched lithospheric keel under the Outer Hebrides. Nature 325, 44-47.

Milelli, L., Fourel, L., Jaupart, C., 2012. A lithospheric instability origin for the Cameroon Volcanic Line. Earth Planet. Sci. Lett. 335-336, 80-87.

Mills, K.C., Hayashi, M., Wang, L., Watanabe, T., 2014. Chapter 2.2 - The Structure and Properties of Silicate Slags, in: Seetharaman, S., McLean, A., Guthrie, R., Sridhar, S. (Eds.), Treatise on Process Metallurgy, Volume 1: Process Fundamentals. Elsevier, Oxford, pp. 149-286.

Mills, K.C., Yuan, L., Jones, R.T., 2011. Estimating the physical properties of slags. The Journal of The Southern African Institute of Mining and Metallurgy 111, 649-658.

Morbidelli, A., Wood, B.J., 2015. Late Accretion and the Late Veneer, in: Badro, J., Walter, M. (Eds.), The Early Earth, AGU Monograph. John Wiley & Sons, Inc, Hoboken, New Jersey, pp. 71-82.

Morgan, J.W., 1985. Osmium isotope constraints on Earth's late accretionary history. Nature 317, 703-705.

Morgan, J.W., Walker, R.J., Brandon, A.D., Horan, M.F., 2001. Siderophile elements in Earth's upper mantle and lunar breccias: Data synthesis suggests manifestations of the same late influx. Meteorit. Planet. Sci. 36, 1257-1275.

Mowlavi, N., 1998. The survival of 205Pb in intermediate-mass AGB stars. Astron. Astrophys. 330, 206.

Moynier, F., Albarède, F., Herzog, G.F., 2006. Isotopic composition of zinc, copper, and iron in lunar samples. Geochim. Cosmochim. Acta 70, 6103-6117.

Moynier, F., Beck, P., Jourdan, F., Yin, Q.-Z., Reimold, U., Koeberl, C., 2009. Isotopic fractionation of zinc in tektites. Earth Planet. Sci. Lett. 277, 482-489.

Moynier, F., Beck, P., Yin, Q.-Z., Ferroir, T., Barrat, J.-A., Paniello, R., Telouk, P., Gillet, P., 2010. Volatilization induced by impacts recorded in Zn isotope composition of ureilites. Chem. Geol. 276, 374-379.

Moynier, F., Paniello, R.C., Gounelle, M., Albarède, F., Beck, P., Podosek, F., Zanda, B., 2011. Nature of volatile depletion and genetic relationships in enstatite chondrites and aubrites inferred from Zn isotopes. Geochim. Cosmochim. Acta 75, 297-307.

Moynier, F., Pringle, E.A., Bouvier, A., Moureau, J., 2015. Barium stable isotope composition of the Earth, meteorites, and calcium–aluminum-rich inclusions. Chem. Geol. 413, 1-6.

Murphy, K., Rehkämper, M., Kreissig, K., Coles, B., van de Flierdt, T., 2015. Improvements in Cd stable isotope analysis achieved through use of liquid-liquid extraction to remove organic residues from Cd separates obtained by extraction chromatography. J. Anal. At. Spectrom.

Mysen, B.O., 1983. The Structure of Silicate Melts. Annu. Rev. Earth Planet. Sci. 11, 75-97.

Mysen, B.O., 1990. Relationships between silicate melt structure and petrologic processes. Earth-Sci. Rev. 27, 281-365.

NASA Johnson Space Centre, Antarctic Meteorite Newsletter, March 1993, in: Score, R., Lindstrom, M. (Eds.) 16, NASA Johnson Space Centre, Houston, 1993.

NASA Johnson Space Centre, Antarctic Meteorite Newsletter, February 2004, in: Satterwhite, C., Righter, K. (Eds.) 27, NASA Johnson Space Centre, Houston, 2004.

Neal, C.W., Dodd, R.T., Jarosewich, E., Lipschutz, M.E., 1981. Chemical studies of L-chondrites—I. A study of possible chemical sub-groups. Geochim. Cosmochim. Acta 45, 891-898.

Nielsen, S.G., Prytulak, J., Wood, B.J., Halliday, A.N., 2014. Vanadium isotopic difference between the silicate Earth and meteorites. Earth Planet. Sci. Lett. 389, 167-175.

Nielsen, S.G., Rehkämper, M., 2012. Thallium Isotopes and Their Application to Problems in Earth and Environmental Science, in: Baskaran, M. (Ed.), Handbook of Environmental Isotope Geochemistry. Springer-Verlag, Berlin, Heidelberg, pp. 247-269.

Nielsen, S.G., Rehkämper, M., Baker, J., Halliday, A.N., 2004. The precise and accurate determination of thallium isotope compositions and concentrations for water samples by MC-ICPMS. Chem. Geol. 204, 109-124.

Nielsen, S.G., Rehkämper, M., Brandon, A.D., Norman, M.D., Turner, S., O'Reilly, S.Y., 2007. Thallium isotopes in Iceland and Azores lavas -- Implications for the role of altered crust and mantle geochemistry. Earth Planet. Sci. Lett. 264, 332-345.

Nielsen, S.G., Rehkämper, M., Halliday, A.N., 2006a. Large thallium isotopic variations in iron meteorites and evidence for lead-205 in the early solar system. Geochim. Cosmochim. Acta 70, 2643-2657.

Nielsen, S.G., Rehkämper, M., Norman, M.D., Halliday, A.N., Harrison, D., 2006b. Thallium isotopic evidence for ferromanganese sediments in the mantle source of Hawaiian basalts. Nature 439, 314-317.

Nielsen, S.G., Rehkämper, M., Porcelli, D., Andersson, P., Halliday, A.N., Swarzenski, P.W., Latkoczy, C., Günther, D., 2005. Thallium isotope composition of the upper continental crust and rivers--An investigation of the continental sources of dissolved marine thallium. Geochim. Cosmochim. Acta 69, 2007-2019.

Nielsen, S.G., Rehkämper, M., Teagle, D.A.H., Butterfield, D.A., Alt, J.C., Halliday, A.N., 2006c. Hydrothermal fluid fluxes calculated from the isotopic mass balance of thallium in the ocean crust. Earth Planet. Sci. Lett. 251, 120-133.

Nisbet, E.G., Arndt, N.T., Bickle, M.J., Cameron, W.E., Chauvel, C., Cheadle, M., Hegner, E., Kyser, T.K., Martin, A., Renner, R., Roedder, E., 1987. Uniquely fresh 2.7 Ga komatiites from the Belingwe greenstone belt, Zimbabwe. Geology 15, 1147-1150.

Norman, M.D., Garcia, M.O., Bennett, V.C., 2004. Rhenium and chalcophile elements in basaltic glasses from Ko'olau and Moloka'i volcanoes: Magmatic outgassing and composition of the Hawaiian plume. Geochim. Cosmochim. Acta 68, 3761-3777.

Nriagu, J.O., 1990. The rise and fall of leaded gasoline. Sci. Total Environ. 92, 13-28.

Nriagu, J.O., Pacyna, J.M., 1988. Quantitative assessment of worldwide contamination of air, water and soils by trace metals. Nature 333, 134-139.

O'Neill, H.S.C., 1991. The origin of the moon and the early history of the earth—A chemical model. Part 2: The earth. Geochim. Cosmochim. Acta 55, 1159-1172.

O'Neill, H.S.C., Palme, H., 2008. Collisional erosion and the non-chondritic composition of the terrestrial planets, 4205-4238 pp.

O'Reilly, S.Y., Griffin, W.L., Ryan, C.G., 1991. Residence of trace elements in metasomatized spinel lherzolite xenoliths: a proton-microprobe study. Contrib. Mineral. Petrol. 109, 98-113.

Ostic, R.G., El-Badry, H.M., Kohman, T.P., 1969. Isotopic composition of meteoritic thallium. Earth Planet. Sci. Lett. 7, 72-76.

Pacyna, J.M., Pacyna, E.G., 2001. An assessment of global and regional emissions of trace metals to the atmosphere from anthropogenic sources worldwide. Environ. Rev. 9, 269-298.

Palme, H., Larimer, J., Lipschutz, M., 1988. Moderately volatile elements, in: Kerridge, J.F., Matthews, M.S. (Eds.), Meteorites and the early solar system. University of Arizona Press, Tucson, Arizona, pp. 436-461.

Palme, H., Lodders, K., Jones, A., 2014. 2.2 - Solar System Abundances of the Elements, in: Turekian, H.D., Holland, K.K. (Eds.), Treatise on Geochemistry (Second Edition). Elsevier, Oxford, pp. 15-36.

Palme, H., Nickel, K.G., 1985. CaAl ratio and composition of the Earth's upper mantle. Geochim. Cosmochim. Acta 49, 2123-2132.

Palme, H., O'Neill, H.S.C., 2014. 3.1 - Cosmochemical Estimates of Mantle Composition, in: Turekian, H.D., Holland, K.K. (Eds.), Treatise on Geochemistry (Second Edition). Elsevier, Oxford, pp. 1-39.

Parkinson, I.J., Hammond, S.J., James, R.H., Rogers, N.W., 2007. High-temperature lithium isotope fractionation: Insights from lithium isotope diffusion in magmatic systems. Earth Planet. Sci. Lett. 257, 609-621.

Patzer, A., Schultz, L., 2002. Noble gases in enstatite chondrites II: The trapped component. Meteorit. Planet. Sci. 37, 601-612.

Pearson, D.G., Wittig, N., 2014. 3.6 - The Formation and Evolution of Cratonic Mantle Lithosphere – Evidence from Mantle Xenoliths, in: Turekian, H.D., Holland, K.K. (Eds.), Treatise on Geochemistry (Second Edition). Elsevier, Oxford, pp. 255-292.

Pearson, R.G., 1968. Hard and soft acids and bases, HSAB, part 1: Fundamental principles. J. Chem. Educ. 45, 581.

Pécsi, M., 1990. Loess is not just the accumulation of dust. Quat. Int. 7, 1-21.

Peucker-Ehrenbrink, B., Jahn, B.-m., 2001. Rhenium-osmium isotope systematics and platinum group element concentrations: Loess and the upper continental crust. Geochem. Geophys. Geosyst. 2, 1061.

Pietruszka, A.J., Reznik, A.D., 2008. Identification of a matrix effect in the MC-ICP-MS due to sample purification using ion exchange resin: An isotopic case study of molybdenum. Int. J. Mass spectrom. 270, 23-30.

Poirier, A., Doucelance, R., 2009. Effective Correction of Mass Bias for Rhenium Measurements by MC-ICP-MS. Geostand. Geoanal. Res. 33, 195-204.

Poitrasson, F., Roskosz, M., Corgne, A., 2009. No iron isotope fractionation between molten alloys and silicate melt to 2000 °C and 7.7 GPa: Experimental evidence and implications for planetary differentiation and accretion. Earth Planet. Sci. Lett. 278, 376-385.

Polyakov, V.B., 2009. Equilibrium Iron Isotope Fractionation at Core-Mantle Boundary Conditions. Science 323, 912-914.

Presnall, D.C., Dixon, S.A., Dixon, J.R., O'Donnell, T.H., Brenner, N.L., Schrock, R.L., Dycus, D.W., 1978. Liquidus phase relations on the join diopside-forsterite-anorthite from 1 atm to 20 kbar: Their bearing on the generation and crystallization of basaltic magma. Contrib. Mineral. Petrol. 66, 203-220.

Prytulak, J., Nielsen, S.G., Plank, T., Barker, M., Elliott, T., 2013. Assessing the utility of thallium and thallium isotopes for tracing subduction zone inputs to the Mariana arc. Chem. Geol. 345, 139-149.

Pye, K., 1987. Aeolian Dust and Dust Deposits. Academic Press, 334 pp.

Pye, K., 1995. The nature, origin and accumulation of loess. Quat. Sci. Rev. 14, 653-667.

Pye, K., Zhou, L.-P., 1989. Late Pleistocene and Holocene aeolian dust deposition in North China and the Northwest Pacific Ocean. Palaeogeogr., Palaeoclimatol., Palaeoecol. 73, 11-23.

Quirico, E., Bourot-denise, M., Robin, C., Montagnac, G., Beck, P., 2011. A reappraisal of the metamorphic history of EH3 and EL3 enstatite chondrites. Geochim. Cosmochim. Acta 75, 3088-3102.

Rehkämper, M., Frank, M., Hein, J.R., Halliday, A., 2004. Cenozoic marine geochemistry of thallium deduced from isotopic studies of ferromanganese crusts and pelagic sediments. Earth Planet. Sci. Lett. 219, 77-91.

Rehkämper, M., Frank, M., Hein, J.R., Porcelli, D., Halliday, A., Ingri, J., Liebetrau, V., 2002. Thallium isotope variations in seawater and hydrogenetic, diagenetic, and hydrothermal ferromanganese deposits. Earth Planet. Sci. Lett. 197, 65-81.

Rehkämper, M., Halliday, A.N., 1999. The precise measurement of Tl isotopic compositions by MC-ICPMS: Application to the analysis of geological materials and meteorites. Geochim. Cosmochim. Acta 63, 935-944.

Rehkämper, M., Halliday, A.N., Barfod, D., Fitton, J.G., Dawson, J.B., 1997. Platinum-Group Element Abundance Patterns in Different Mantle Environments. Science 278, 1595-1598.

Rehkämper, M., Halliday, A.N., Fitton, J.G., Lee, D.C., Wieneke, M., Arndt, N.T., 1999. Ir, Ru, Pt, and Pd in basalts and komatiites: new constraints for the geochemical behavior

of the platinum-group elements in the mantle. Geochim. Cosmochim. Acta 63, 3915-3934.

Rehkämper, M., Mezger, K., 2000. Investigation of matrix effects for Pb isotope ratio measurements by multiple collector ICP-MS: verification and application of optimized analytical protocols. J. Anal. At. Spectrom. 15, 1451-1460.

Rehkämper, M., Schönbächler, M., Stirling, C.H., 2001. Multiple Collector ICP-MS: Introduction to Instrumentation, Measurement Techniques and Analytical Capabilities. Geostandards Newsletter 25, 23-40.

Rehkämper, M., Wombacher, F., Horner, T.J., Xue, Z., 2011. Natural and Anthropogenic Cd Isotope Variations, in: Baskaran, M. (Ed.), Handbook of Environmental Isotope Geochemistry, Advances in Isotope Geochemistry. Springer-Verlag Berlin Heidelberg, pp. 125-154.

Reusch, A.M., Nyblade, A.A., Tibi, R., Wiens, D.A., Shore, P.J., Bekoa, A., Tabod, C.T., Nnange, J.M., 2011. Mantle transition zone thickness beneath Cameroon: Evidence for an upper mantle origin for the Cameroon Volcanic Line. Geophys. J. Int. 187, 1146-1150.

Reusch, A.M., Nyblade, A.A., Wiens, D.A., Shore, P.J., Ateba, B., Tabod, C.T., Nnange, J.M., 2010. Upper mantle structure beneath Cameroon from body wave tomography and the origin of the Cameroon Volcanic Line. Geochem. Geophys. Geosyst. 11, Q10W07.

Richter, F.M., Dauphas, N., Teng, F.-Z., 2009a. Non-traditional fractionation of non-traditional isotopes: Evaporation, chemical diffusion and Soret diffusion. Chem. Geol. 258, 92-103.

Richter, F.M., Davis, A.M., DePaolo, D.J., Watson, E.B., 2003. Isotope fractionation by chemical diffusion between molten basalt and rhyolite. Geochim. Cosmochim. Acta 67, 3905-3923.

Richter, F.M., Watson, E.B., Mendybaev, R., Dauphas, N., Georg, B., Watkins, J., Valley, J., 2009b. Isotopic fractionation of the major elements of molten basalt by chemical and thermal diffusion. Geochim. Cosmochim. Acta 73, 4250-4263.

Righter, K., 2011. Prediction of metal–silicate partition coefficients for siderophile elements: An update and assessment of PT conditions for metal–silicate equilibrium during accretion of the Earth. Earth Planet. Sci. Lett. 304, 158-167.

Righter, K., 2015. Modeling siderophile elements during core formation and accretion, and the role of the deep mantle and volatiles. Am. Mineral. 100, 1098-1109.

Righter, K., Danielson, L., Drake, M.J., Domanik, K., 2014. 3.12 - Partition Coefficients at High Pressure and Temperature, in: Turekian, H.D., Holland, K.K. (Eds.), Treatise on Geochemistry (Second Edition). Elsevier, Oxford, pp. 449-477.

Righter, K., Drake, M.J., Yaxley, G., 1997. Prediction of siderophile element metal-silicate partition coefficients to 20 GPa and 2800°C: the effects of pressure, temperature, oxygen fugacity, and silicate and metallic melt compositions. Phys. Earth Planet. Inter. 100, 115-134.

Righter, K., Humayun, M., Danielson, L., 2008. Partitioning of palladium at high pressures and temperatures during core formation. Nat. Geosci. 1, 321-323.

Ringwood, A.E., 1962. A model for the upper mantle. J. Geophys. Res. 67, 857-867.

Ripperger, S., Rehkämper, M., 2007. Precise determination of cadmium isotope fractionation in seawater by double spike MC-ICPMS. Geochim. Cosmochim. Acta 71, 631-642.

Roe, G., 2009. On the interpretation of Chinese loess as a paleoclimate indicator. Quatern. Res. 71, 150-161.

Rosman, K.J.R., 1980. Isotope composition of Cd, Ca and Mg in the Brownfield chondrite. Geochem. J. 14, 269.

Rosman, K.J.R., De Laeter, J.R., 1975. The isotopic composition of cadmium in terrestrial minerals. International Journal of Mass Spectrometry and Ion Physics 16, 385-394.
Rubin, A.E., 1983. The Atlanta Enstatite Chondrite Breccia. Meteoritics 18, 113-121.
Rubin, A.E., 1994. Metallic copper in ordinary chondrites. Meteoritics 29, 93-98.
Rubin, A.E., 1995. Petrologic Evidence for Collisional Heating of Chondritic Asteroids. Icarus 113, 156-167.
Rubin, A.E., 2004. Postshock annealing and postannealing shock in equilibrated ordinary chondrites: Implications for the thermal and shock histories of chondritic asteroids. Geochim. Cosmochim. Acta 68, 673-689.
Rubin, A.E., 2015. Impact features of enstatite-rich meteorites. Chem. Erde 75, 1-28.
Rubin, A.E., Huber, H., Wasson, J.T., 2009. Possible impact-induced refractory-lithophile fractionations in EL chondrites. Geochim. Cosmochim. Acta 73, 1523-1537.
Rubin, A.E., Scott, E.R.D., 1997. Abee and related EH chondrite impact-melt breccias. Geochim. Cosmochim. Acta 61, 425-435.
Rubin, A.E., Scott, E.R.D., Keil, K., 1997. Shock metamorphism of enstatite chondrites. Geochim. Cosmochim. Acta 61, 847-858.
Rubin, A.E., Wasson, J.T., 2011. Shock effects in "EH6" enstatite chondrites and implications for collisional heating of the EH and EL parent asteroids. Geochim. Cosmochim. Acta 75, 3757-3780.
Rubin, K., 1997. Degassing of metals and metalloids from erupting seamount and mid-ocean ridge volcanoes: Observations and predictions. Geochim. Cosmochim. Acta 61, 3525-3542.
Rudge, J.F., 2011. Double spike cocktail lists June 2011. http://www.johnrudge.com/doublespike/ (Excel spreadsheet downloaded 6 May 2015).
Rudge, J.F., Reynolds, B.C., Bourdon, B., 2009. The double spike toolbox. Chem. Geol. 265, 420-431.
Rudnick, R.L., Ionov, D.A., 2007. Lithium elemental and isotopic disequilibrium in minerals from peridotite xenoliths from far-east Russia: Product of recent melt/fluid–rock reaction. Earth Planet. Sci. Lett. 256, 278-293.
Russell, R.D., 1971. The systematics of double spiking. J. Geophys. Res. 76, 4949-4955.
Russell, W.A., Papanastassiou, D.A., 1978. Calcium isotope fractionation in ion-exchange chromatography. Anal. Chem. 50, 1151-1154.
Savage, P.S., Moynier, F., 2013. Silicon isotopic variation in enstatite meteorites: Clues to their origin and Earth-forming material. Earth Planet. Sci. Lett. 361, 487-496.
Schaefer, L., Fegley, B., Jr., 2010. Volatile element chemistry during metamorphism of ordinary chondritic material and some of its implications for the composition of asteroids. Icarus 205, 483-496.
Schauble, E.A., 2007. Role of nuclear volume in driving equilibrium stable isotope fractionation of mercury, thallium, and other very heavy elements. Geochim. Cosmochim. Acta 71, 2170-2189.
Schlitzer, R., Ocean Data View, Alfred-Wegener-Institute for Polar and Marine Research, http://odv.awi.de, 2016.
Schmitt, A.D., Galer, S.J.G., Abouchami, W., 2009a. High-precision cadmium stable isotope measurements by double spike thermal ionisation mass spectrometry. J. Anal. At. Spectrom. 24, 1079-1088.
Schmitt, A.D., Galer, S.J.G., Abouchami, W., 2009b. Mass-dependent cadmium isotopic variations in nature with emphasis on the marine environment. Earth Planet. Sci. Lett. 277, 262-272.

Schönbächler, M., Fehr, M.A., 2014. 15.7 - Basics of Ion Exchange Chromatography for Selected Geological Applications, in: Turekian, H.D., Holland, K.K. (Eds.), Treatise on Geochemistry (Second Edition). Elsevier, Oxford, pp. 123-146.

Schönbächler, M., Rehkämper, M., Williams, H.M., Halliday, A.N., 2009. The cadmium isotope composition of the Earth. Geochim. Cosmochim. Acta. 73, 13, Supplement 1. #A1183 (abstr.).

Sears, D.W., Kallemeyn, G.W., Wasson, J.T., 1982. The compositional classification of chondrites: II The enstatite chondrite groups. Geochim. Cosmochim. Acta 46, 597-608.

Seifert, F.A., Mysen, B.O., Virgo, D., 1981. Structural similarity of glasses and melts relevant to petrological processes. Geochim. Cosmochim. Acta 45, 1879-1884.

Seitz, H.-M., Brey, G.P., Lahaye, Y., Durali, S., Weyer, S., 2004. Lithium isotopic signatures of peridotite xenoliths and isotopic fractionation at high temperature between olivine and pyroxenes. Chem. Geol. 212, 163-177.

Shahar, A., Hillgren, V.J., Young, E.D., Fei, Y., Macris, C.A., Deng, L., 2011. High-temperature Si isotope fractionation between iron metal and silicate. Geochim. Cosmochim. Acta 75, 7688-7697.

Shi, P., Yang, T., Tian, Q., Jiang, S., Fan, Z., Wang, J., 2013. Loess record of climatic changes during MIS 12–10 in the Jingyuan section, northwestern Chinese Loess Plateau. Quat. Int. 296, 149-159.

Shiel, A.E., Barling, J., Orians, K.J., Weis, D., 2009. Matrix effects on the multi-collector inductively coupled plasma mass spectrometric analysis of high-precision cadmium and zinc isotope ratios. Anal. Chim. Acta 633, 29-37.

Shu, F., Najita, J., Ostriker, E., Wilkin, F., Ruden, S., Lizano, S., 1994. Magnetocentrifugally driven flows from young stars and disks. 1: A generalized model. Astrophys. J. 429, 781-796.

Shu, F.H., Shang, H., Gounelle, M., Glassgold, A.E., Lee, T., 2001. The Origin of Chondrules and Refractory Inclusions in Chondritic Meteorites. Astrophys. J. 548, 1029-1050.

Shu, F.H., Shang, H., Typhoon, L., 1996. Toward an Astrophysical Theory of Chondrites. Science 271, 1545-1552.

Shukolyukov, A., Lugmair, G.W., 2004. Manganese-chromium isotope systematics of enstatite meteorites. Geochim. Cosmochim. Acta 68, 2875-2888.

Siebert, C., Nägler, T.F., Kramers, J.D., 2001. Determination of molybdenum isotope fractionation by double-spike multicollector inductively coupled plasma mass spectrometry. Geochem. Geophys. Geosyst. 2, 1032.

Siebert, J., Corgne, A., Ryerson, F.J., 2011. Systematics of metal-silicate partitioning for many siderophile elements applied to Earth's core formation. Geochim. Cosmochim. Acta 75, 1451-1489.

Smalley, I., Marković, S.B., Svirčev, Z., 2011. Loess is [almost totally formed by] the accumulation of dust. Quat. Int. 240, 4-11.

Smalley, I., O'Hara-Dhand, K., Wint, J., Machalett, B., Jary, Z., Jefferson, I., 2009. Rivers and loess: The significance of long river transportation in the complex event-sequence approach to loess deposit formation. Quat. Int. 198, 7-18.

Smalley, I.J., 1966. The properties of glacial loess and the formation of loess deposits. J. Sediment. Res. 36, 669-676.

Smalley, I.J., Leach, J.A., 1978. The origin and distribution of the loess in the Danube basin and associated regions of East-Central Europe — A review. Sediment. Geol. 21, 1-26.

Sonke, J.E., Sivry, Y., Viers, J., Freydier, R., Dejonghe, L., André, L., Aggarwal, J.K., Fontan, F., Dupré, B., 2008. Historical variations in the isotopic composition of atmospheric zinc deposition from a zinc smelter. Chem. Geol. 252, 145-157.

Sossi, P.A., Halverson, G.P., Nebel, O., Eggins, S.M., 2015. Combined Separation of Cu, Fe and Zn from Rock Matrices and Improved Analytical Protocols for Stable Isotope Determination. Geostand. Geoanal. Res. 39, 129-149.

Stevens, T., Palk, E., Carter, A., Lu, H., Clift, P.D., 2010. Assessing the provenance of loess and desert sediments in northern China using U-Pb dating and morphology of detrital zircons. Geol. Soc. Am. Bull. 122, 1331 - 1344.

Stöffler, D., Keil, K., Edward R.D, S., 1991. Shock metamorphism of ordinary chondrites. Geochim. Cosmochim. Acta 55, 3845-3867.

Strelow, F.W.E., 1978. Distribution coefficients and anion exchange behavior of some elements in hydrobromic-nitric acid mixtures. Anal. Chem. 50, 1359.

Sun, J., 2002. Provenance of loess material and formation of loess deposits on the Chinese Loess Plateau. Earth Planet. Sci. Lett. 203, 845-859.

Takahashi, E., Irvine, T.N., 1981. Stoichiometric control of crystal/liquid single-component partition coefficients. Geochim. Cosmochim. Acta 45, 1181-1185.

Taylor, J.R., 1982. An Introduction to Error Analysis. The Study of Uncertainties in Physical Measurements. University Science Books, Sausalito, California, 327 pp.

Taylor, M., Brown, G.E., Fenn, P.M., 1980. Structure of mineral glasses—III. NaAlSi3O8 supercooled liquid at 805°C and the effects of thermal history. Geochim. Cosmochim. Acta 44, 109-117.

Taylor, S.R., McLennan, S.M., McCulloch, M.T., 1983. Geochemistry of loess, continental crustal composition and crustal model ages. Geochim. Cosmochim. Acta 47, 1897-1905.

Taylor, T.I., Urey, H.C., 1938. Fractionation of the Lithium and Potassium Isotopes by Chemical Exchange with Zeolites. The Journal of Chemical Physics 6, 429-438.

Temdjim, R., 2012. Ultramafic xenoliths from Lake Nyos area, Cameroon volcanic line, West-central Africa: Petrography, mineral chemistry, equilibration conditions and metasomatic features. Chem. Erde 72, 39-60.

Teng, F.-Z., Li, W.-Y., Ke, S., Marty, B., Dauphas, N., Huang, S., Wu, F.-Y., Pourmand, A., 2010. Magnesium isotopic composition of the Earth and chondrites. Geochim. Cosmochim. Acta 74, 4150-4166.

Toutain, J.-P., Sonke, J., Munoz, M., Nonell, A., Polvé, M., Viers, J., Freydier, R., Sortino, F., Joron, J.-L., Sumarti, S., 2008. Evidence for Zn isotopic fractionation at Merapi volcano. Chem. Geol. 253, 74-82.

Trémillon, B., 1965. Valeurs Expérimentales Des Coefficients-Limites de Partage des Élements Métalliques, Les Séparations par les Résines Échangeuses d'Ions. Gauthier-Villars, Paris, p. 400.

Trieloff, M., Jessberger, E.K., Herrwerth, I., Hopp, J., Fieni, C., Ghelis, M., Bourot-Denise, M., Pellas, P., 2003. Structure and thermal history of the H-chondrite parent asteroid revealed by thermochronometry. Nature 422, 502-506.

Tuff, J., Wood, B.J., Wade, J., 2011. The effect of Si on metal–silicate partitioning of siderophile elements and implications for the conditions of core formation. Geochim. Cosmochim. Acta 75, 673-690.

Twyman, R.M., 2005. Sample Dissolution for Elemental Analysis - Wet Digestion, Encyclopaedia of Analytical Science 8. Elsevier Academic Press, pp. 146 - 153.

Unruh, D.M., 1982. The U-Th-Pb age of equilibrated L chondrites and a solution to the excess radiogenic Pb problem in chondrites. Earth Planet. Sci. Lett. 58, 75-94.

Urey, H.C., 1947. The thermodynamic properties of isotopic substances. J. Chem. Soc., 562-581.

van der Hilst, R.D., Widiyantoro, S., Engdahl, E.R., 1997. Evidence for deep mantle circulation from global tomography. Nature 386, 578-584.

Van der Walt, T.N., Strelow, F.W.E., Verheij, R., 1985. The influence of crosslinkage on the distribution coefficients and anion exchange behaviour of some elements in hydrochloric acid. Solvent Extr. Ion Exch. 3, 723.

van Keken, P., Zhong, S., 1999. Mixing in a 3D spherical model of present-day mantle convection. Earth Planet. Sci. Lett. 171, 533-547.

Viers, J., Oliva, P., Nonell, A., Gélabert, A., Sonke, J.E., Freydier, R., Gainville, R., Dupré, B., 2007. Evidence of Zn isotopic fractionation in a soil–plant system of a pristine tropical watershed (Nsimi, Cameroon). Chem. Geol. 239, 124-137.

Wade, J., Wood, B.J., 2005. Core formation and the oxidation state of the Earth. Earth Planet. Sci. Lett. 236, 78-95.

Walker, R.J., 2009. Highly siderophile elements in the Earth, Moon and Mars: Update and implications for planetary accretion and differentiation. Chem. Erde 69, 101-125.

Walker, R.J., Shirey, S.B., Stecher, O., 1988. Comparative ReOs, SmNd and RbSr isotope and trace element systematics for Archean komatiite flows from Munro Township, Abitibi Belt, Ontario. Earth Planet. Sci. Lett. 87, 1-12.

Walsh, T.M., Lipschutz, M.E., 1982. Chemical studies of L chondrites—II. Shock-induced trace element mobilization. Geochim. Cosmochim. Acta 46, 2491-2500.

Walter, M.J., Presnall, D.C., 1994. Melting Behavior of Simplified Lherzolite in the System CaO-MgO-Al2O3-SiO2-Na2O from 7 to 35 kbar. J. Petrol. 35, 329-359.

Wang, K., Jacobsen, S.B., 2016. Potassium isotopic evidence for a high-energy giant impact origin of the Moon. Nature 538, 487-490.

Wang, X., Tsuchiya, T., Hase, A., 2015. Computational support for a pyrolitic lower mantle containing ferric iron. Nat. Geosci. 8, 556-559.

Wang, Z., Becker, H., 2013. Ratios of S, Se and Te in the silicate Earth require a volatile-rich late veneer. Nature 499, 328-331.

Wang, Z., Laurenz, V., Petitgirard, S., Becker, H., 2016a. Earth's moderately volatile element composition may not be chondritic: Evidence from In, Cd and Zn. Earth Planet. Sci. Lett. 435, 136-146.

Wang, Z.-Z., Liu, S.-A., Liu, J., Yan, X., 2016b. Zinc isotope fractionation during partial melting of the Earth's upper mantle. 26th Annual V.M. Goldschmidt Conference. Yokohama, Japan. #3361 (abstr.).

Wasson, J., Kallemeyn, G., 1988. Compositions of chondrites. Philos. Trans. R. Soc. Lond. A 325, 535-544.

Wasson, J.T., 1988. The building stones of the planets, in: Vilas, F., Chapman, C.R., Matthews, M.S. (Eds.), Mercury. University of Arizona Press, Tucson, pp. 622-650.

Wasylenki, L.E., 2012. Establishing the Basis for Using Stable Isotope Ratios of Metals as Paleoredox Proxies, in: Vanhaecke, F., Degryse, P. (Eds.), Isotopic Analysis: Fundamentals and Applications Using ICP-MS. Wiley-VCH Verlag GmbH & Co. KGaA, Weinheim, Germany, pp. 317-350.

Weidenschilling, S.J., 1977. Aerodynamics of solid bodies in the solar nebula. Mon. Not. R. Astron. Soc. 180, 57-70.

Weidenschilling, S.J., 1980. Dust to planetesimals: Settling and coagulation in the solar nebula. Icarus 44, 172-189.

Weidenschilling, S.J., 2000. Formation of Planetesimals and Accretion of the Terrestrial Planets. Space Sci. Rev. 92, 295-310.

Wetherill, G.W., 1986. Accumulation of the terrestrial planets and implications concerning lunar origin, in: Hartmann, W.K., Phillips, R.J., Taylor, G.J. (Eds.), Origin of the Moon. Lunar and Planetary Institute, Houston, TX, pp. 519-550.

Weyer, S., Ionov, D.A., 2007. Partial melting and melt percolation in the mantle: The message from Fe isotopes. Earth Planet. Sci. Lett. 259, 119-133.

Wiechert, U., Halliday, A.N., 2007. Non-chondritic magnesium and the origins of the inner terrestrial planets. Earth Planet. Sci. Lett. 256, 360-371.

Wiggenhauser, M., Bigalke, M., Imseng, M., Müller, M., Keller, A., Murphy, K., Kreissig, K., Rehkämper, M., Wilcke, W., Frossard, E., 2016. Cadmium Isotope Fractionation in Soil–Wheat Systems. Environ. Sci. Technol. 50, 9223-9231.

Williams, H.M., Peslier, A.H., McCammon, C., Halliday, A.N., Levasseur, S., Teutsch, N., Burg, J.P., 2005. Systematic iron isotope variations in mantle rocks and minerals: The effects of partial melting and oxygen fugacity. Earth Planet. Sci. Lett. 235, 435-452.

Witt-Eickschen, G., Palme, H., O'Neill, H.S.C., Allen, C.M., 2007. The abundances of nominally chalcophile trace elements in the main minerals of upper mantle rocks. Geochim. Cosmochim. Acta. 71, 15. #A120 (abstr.).

Witt-Eickschen, G., Palme, H., O'Neill, H.S.C., Allen, C.M., 2009. The geochemistry of the volatile trace elements As, Cd, Ga, In and Sn in the Earth's mantle: New evidence from in situ analyses of mantle xenoliths. Geochim. Cosmochim. Acta 73, 1755-1778.

Wolff, E.W., Peel, D.A., 1985. The record of global pollution in polar snow and ice. Nature 313, 535-540.

Wombacher, F., Rehkämper, M., 2003. Investigation of the mass discrimination of multiple collector ICP-MS using neodymium isotopes and the generalised power law. J. Anal. At. Spectrom. 18, 1371-1375.

Wombacher, F., Rehkämper, M., 2004. Problems and suggestions concerning the notation of cadmium stable isotope compositions and the use of reference materials. Geostand. Geoanal. Res. 28, 173-178.

Wombacher, F., Rehkämper, M., Mezger, K., 2004. Determination of the mass-dependence of cadmium isotope fractionation during evaporation. Geochim. Cosmochim. Acta 68, 2349-2357.

Wombacher, F., Rehkämper, M., Mezger, K., Bischoff, A., Muenker, C., 2008. Cadmium stable isotope cosmochemistry. Geochim. Cosmochim. Acta 72, 646-667.

Wombacher, F., Rehkämper, M., Mezger, K., Münker, C., 2003. Stable isotope compositions of cadmium in geological materials and meteorites determined by multiple-collector ICPMS. Geochim. Cosmochim. Acta 67, 4639-4654.

Wood, B.J., 1993. Carbon in the core. Earth Planet. Sci. Lett. 117, 593-607.

Wood, B.J., Halliday, A.N., 2010. The lead isotopic age of the Earth can be explained by core formation alone. Nature 465, 767-770.

Wood, B.J., Halliday, A.N., Rehkämper, M., 2010. Volatile accretion history of the Earth. Nature 467, E6-E7.

Wood, B.J., Kiseeva, E.S., Mirolo, F.J., 2014. Accretion and core formation: The effects of sulfur on metal–silicate partition coefficients. Geochim. Cosmochim. Acta 145, 248-267.

Wood, B.J., Nielsen, S.G., Rehkämper, M., Halliday, A.N., 2008. The effects of core formation on the Pb- and Tl- isotopic composition of the silicate Earth. Earth Planet. Sci. Lett. 269, 326-336.

Xue, Z., Rehkämper, M., Horner, T.J., Abouchami, W., Middag, R., van de Flierd, T., de Baar, H.J.W., 2013. Cadmium isotope variations in the Southern Ocean. Earth Planet. Sci. Lett. 382, 161-172.

Xue, Z., Rehkämper, M., Schönbächler, M., Statham, P., Coles, B., 2012. A new methodology for precise cadmium isotope analyses of seawater. Anal. Bioanal. Chem. 402, 883-893.

Yakob, J.L., Feineman, M.D., Deane Jr, J.A., Eggler, D.H., Penniston-Dorland, S.C., 2012. Lithium partitioning between olivine and diopside at upper mantle conditions: An experimental study. Earth Planet. Sci. Lett. 329–330, 11-21.

Yi, W., Halliday, A.N., Alt, J.C., Lee, D.-C., Rehkämper, M., Garcia, M.O., Langmuir, C.H., Su, Y., 2000. Cadmium, indium, tin, tellurium, and sulfur in oceanic basalts: Implications for chalcophile element fractionation in the Earth. J. Geophys. Res. 105, 18927-18948.

Yokoi, K., Takahashi, K., Arnould, M., 1985. The production and survival of 205Pb in stars, and the 205Pb-205Tl s-process chronometry. Astron. Astrophys. 145, 339-346.

Young, E.D., Galy, A., Nagahara, H., 2002. Kinetic and equilibrium mass-dependent isotope fractionation laws in nature and their geochemical and cosmochemical significance. Geochim. Cosmochim. Acta 66, 1095-1104.

Zhang, Y., Wen, H., Zhu, C., Fan, H., Luo, C., Liu, J., Cloquet, C., 2016. Cd isotope fractionation during simulated and natural weathering. Environ. Pollut. 216, 9-17.

Zhao, X., Zhang, H., Zhu, X., Tang, S., Yan, B., 2012. Iron isotope evidence for multistage melt–peridotite interactions in the lithospheric mantle of eastern China. Chem. Geol. 292–293, 127-139.

Zhao, X.-M., Zhang, H.-F., Zhu, X.-K., Zhu, B., Cao, H.-h., 2015. Effects of melt percolation on iron isotopic variation in peridotites from Yangyuan, North China Craton. Chem. Geol. 401, 96-110.

Zhou, J.-X., Huang, Z.-L., Zhou, M.-F., Zhu, X.-K., Muchez, P., 2014. Zinc, sulfur and lead isotopic variations in carbonate-hosted Pb–Zn sulfide deposits, southwest China. Ore Geol. Rev. 58, 41-54.

Ziegler, K., Young, E.D., Schauble, E.A., Wasson, J.T., 2010. Metal–silicate silicon isotope fractionation in enstatite meteorites and constraints on Earth's core formation. Earth Planet. Sci. Lett. 295, 487-496.